NYU POLYTECHNIC SCHOOL OF ENGINEERING

NYU WIRELESS

NYU WIRELESS TR 2014-001

Technical Report

Characterization of the 28 GHz Millimeter-Wave Dense Urban Channel for Future 5G Mobile Cellular

Mathew K. Samimi, Theodore S. Rappaport

mks@nyu.edu, tsr@nyu.edu

NYU WIRELESS
NYU Polytechnic School of Engineering
2 MetroTech Center
Brooklyn, NY 11201

June 24, 2014

Abstract

Characterization of the 28 GHz Millimeter-Wave Dense Urban Channel for Future 5G Mobile Cellular

By

Mathew K. Samimi and Theodore S. Rappaport

This technical report presents ultra-wideband statistical spatial and omnidirectional channel models for 28 GHz millimeter-wave cellular dense urban line-of-sight and non-line-of-sight environments, developed from wideband measurements in New York City that used synthesized timing from 3-D ray-tracing. An accurate 3GPP-like channel model has been developed, where model parameters are based on empirical distributions for time cluster and spatial (lobe) channel parameters. A statistical simulator capable of reproducing the joint temporal and spatial measured channel statistics is given here. A step-by-step procedure for generating channel coefficients is shown to validate measured statistics from 28 GHz field measurements, thus validating the statistical channel model.

Contents

List of Figures

List of Tables

Chapter 1

Previous Measurements at Millimeter-Wave Frequencies Above 6 GHz

1.1 Introduction

The wireless spectrum below 6 GHz in the United States, and throughout the world, has become congested as a result of the widespread use of smartphones and tablets. Wireless network usage is further expected to increase by a factor of 1000 over the next decade [1]. While 4G Long Term Evolution (LTE) focuses on optimizing spectral efficiency in today's conventional cellular frequency bands using multiple-input multiple-output (MIMO) and coordinated multipoint (CoMP) systems, heterogeneous networks (HetNets), and carrier aggregation (CA) algorithms, many researchers believe that the incredible demand for broadband wireless communications can be supplied by scaling up to the millimeter-wave (mmWave) spectrum, where a massive amount of raw bandwidth can accommodate the ever-expanding consumption for wireless. A new and appropriate wireless infrastructure must however be established to support giga-bit per second (Gbps) data

rates between a radio transmitter (TX) and a stationary or moving receiver (RX) which conventional Ultra-High Frequency (UHF) and Microwave systems and networks cannot offer today. The mmWave spectrum offers 30 - 50 GHz of raw available bandwidth that can be exploited to supply multi-Gbps data rates. A number of viable frequency candidates are currently being considered for delivering multi-Gbps data rates to meet the demand for broadband communications: the 28 and 38 GHz bands have recently become available through LMDS and LMCS auctions and are currently considered for mobile cellular, the 60 GHz band is already in use for short-range indoor wireless broadband systems, and the 70 - 80 GHz E-band is currently under study for broadband backhaul-to-backhaul, backhaul-to-mobile and short-range indoor communications.

This chapter presents a comprehensive literature survey of past mmWave measurements and channel models for frequencies above 6 GHz from the past three decades, to provide the necessary background against which to evaluate the performance of mmWave broadband communications in dense urban environments, the subject of this thesis. The measurement campaigns described in this section have been divided into the IEEE US frequency bands, namely the X, K_u, K, K_a, V and W bands spanning the 8 - 110 GHz spectrum, offering a convenient classification unit for sub-dividing past mmWave propagation measurements. The following table summarizes the frequency ranges for each frequency band [2] .

Table 1.1: The IEEE frequency bands and their corresponding spectrum.

Band	**Frequencies (GHz)**
X	8 - 12
K_u	12 - 18
K	18 - 27
K_a	27 - 40
V	40 - 75
W	75 - 110

Each section in this chapter describes the propagation characteristics and material properties obtained from RF propagation measurements for each frequency band. The main propagation characteristics studied are the effects of the atmosphere, vegetation and different weather conditions such as rain, snow, and hail on RF signal propagation such as path loss and RMS delay spreads. Material properties such as electromag-

netic (EM) reflection and transmission coefficients, indices of refraction, and dielectric constants are highly dependent on frequency of propagation, and hence are an important aspect of mmWave channel characterization. Propagation channel characteristics and material properties must be understood for proper wireless communication system design.

It must be noted that a number of measurement campaigns have simultaneously been conducted in different frequency bands, especially the X and K_u bands in conjunction with the K_a and V bands. For those few cases, the measurement campaigns are described once (typically in the band section for the lowest frequency studied) and results at all studied frequencies are given together in order to provide a proper comparison analysis. Each sub-section ends with a comprehensive table summarizing all measurement campaigns presented, such as the goals of the measurement campaign, the frequencies studied, the typical T-R separation distances measured, the signal bandwidths, the types of antennas used and the principal results discovered. These tables are meant to provide quick and easy access to measurement results.

1.2 X - Band: 8 - 12 GHz

The X-Band has received little research or commercial interest, but rather, has been studied for comparison against the performance of communication channels in other frequency bands. This section provides a detailed description of three measurement campaigns performed at 9.6 GHz, and 11.4 GHz in comparison to the 30 GHz and 60 GHz band channel performances to glean insight into radio-wave propagation subject to fading from the atmosphere (atmospheric fading), and from densely foliated (foliage-induced fading) and urban multipath (multipath-fading) environments.

1.2.1 Channel Characterization

1.2.1.1 Propagation Characteristics in the X - Band

Allen *et al.* studied the propagation mechanisms giving rise to atmospheric fading at 9.6 GHz, 11.4 GHz, and 28.8 GHz by observing signal performance on a 23 km transmitter-to-receiver link in a rural

and suburban environment. The receiver (RX) remained fixed while the transmitter (TX) ascended and descended a 300 m high tower, transmitting a narrowband signal with a highly directional horn antenna in the direction of the RX, to investigate signal fading phenomena such as ground reflections, atmosphere-induced signal scintillation (random fluctuations of signal amplitude and phase), and radio holes (caused by a change in index of refraction between adjacent atmospheric layers). The signals were propagated over gently rolling terrain in a rural and suburban area consisting mainly of grass land and a few houses. Ground reflections and atmospheric fading were reported to induce 8 dB and 20 - 40 dB fades, respectively, while atmospheric ray bending (anti-radio holes) was seen to enhance signals by as much as 10 dB. These results were observed at all three frequencies [3].

Violette *et al.* investigated point-to-point signal propagation at street level in an urban environment to characterize the 9.6 GHz, 11.4 GHz, 28.8 GHz, 30.3 GHz and 57.6 GHz narrowband and broadband (1 GHz RF bandwidth) radio-wave communication channels, as well as reflection and penetration losses through various outdoor building materials using highly directional horn antennas [4]. The street-level propagation channel was studied by recording power delay profiles (PDP) at a fixed location, while the TX moved towards the RX at near constant speed over distances of 0.1 to 0.9 km [4].

It was discovered that reflected signals are an important part of the channel description. Multipath signals from street surfaces produced fades in excess of 30 dB, while reflected multipath components arriving at the RX had amplitudes 15 dB below the line-of-sight (LOS) component. The dependence on antenna linear co-polarization was observed to be insignificant on received power levels [4]. Table 1.2 contains a summary of campaign parameters and important results.

1.2.1.2 Effects of Vegetation in the X - Band

Schwering *et al.* have investigated the effects of radio-wave propagation through densely foliated environments at 9.6 GHz, 28.8 GHz and 57.6 GHz to understand the signal propagation range and frequency dependence on tree depth, and depolarization of signals propagating through vegetation [5]. A narrowband continuous-wave (CW) signal was propagated through a regularly, well groomed stand of trees of the same

Table 1.2: Summary of measurement campaigns at 9.6 GHz, 11.4 GHz, 28.8 GHz, 30.3 GHz, and 57.6 GHz.

Measurements	**Frequency**	**T-R Dist.**	**BW**	**Antennas**	**Results**
Study atmospheric fading in rural and suburban context [3].	9.6 GHz 11.4 GHz 28.8 GHz	22.8 km	2 kHz	Narrow; Wide	Ground reflections: 8 dB fades; Scintillation: 1 dB fades; Atmospheric multipath: 20 to 40 dB fading; Atmospheric bending: 10 dB enhancement.
Study point-to-point transmission at street level in urban environment [4].	9.6 GHz 11.4 GHz 28.8 GHz 30.3 GHz 57.6 GHz	0.9 km	5 kHz	Narrow; Wide	Reflected signals are strong; Multipath from street surfaces produce fades > 30 dB; Multipath reflections from building walls and other reflecting surfaces have amplitudes of 15 dB below LOS component; No dependence on polarization in RX power levels.

species in the summer time (with a fully grown canopy of leaves), and early spring (trees that had lost their leaves) using highly directional horn antennas at all three frequencies. The TX was placed 300 m away from a tree orchard, and the RX was placed inside the same orchard facing the TX so that a line of tree trunks was in between the TX and the RX. Power delay profiles were obtained for different T-R separation distances ranging from 0.1 to 0.9 km, or equivalently, for a number of trees in between the TX and RX ranging between 1 and 35 trees, and for TX heights of 1, 4, and 6 m.

A clear transition in the rate of signal attenuation between short and long range distances was discovered. The break usually happened at three and eight trees in the presence and absence of leaves, respectively. The attenuation rate through trees with leaves was 12 - 20 dB/tree for the first three trees, and 0.5 - 0.7 dB/tree for larger vegetation depths, observed at all frequencies. A 15 - 20 dB difference in received power levels was observed for co- and cross-polarization measurements, exhibiting potential frequency re-use applications. Received power levels were very similar for vertical-to-vertical (VV) and horizontal-to-horizontal (HH) polarization measurements. The path loss at 9.6 GHz was observed to be significantly less than the path losses incurred at 28.8 GHz and 57.6 GHz. Table 1.3 gives more results pertaining to this

campaign.

Table 1.3: Summary of measurement results for signal propagation through densely foliated environments [5].

Measurements	**Frequency**	**T-R Dist.**	**BW**	**Antennas**	**Results**
Study range dependence, depolarization and frequency dependence in foliated environments [5].	9.6 GHz 28.8 GHz 57.6 GHz	0.1 - 0.9 km	Narrowband CW Source	Narrow	12 - 20 dB/tree attenuation for distances < 30 m; 0.5 - 0.7 dB/tree attenuation for distances > 30 m; Flat received signal in azimuth at depth of 8 - 11 trees; No dependence on linear co-polarization.

1.2.2 Material Properties in the X - Band

1.2.2.1 Penetration and Reflection Measurements

Penetration and reflection narrowband measurements of common outside building structures were conducted with a channel sounder at 9.6 GHz, 28.8 GHz, and 57.6 GHz using highly directional horn antennas with beamwidths of 4.8° at 9.6 GHz, and 1.2° at both 28.8 GHz and 57.6 GHz [4]. For the penetration measurements, the TX and RX were placed on either side of a large building, on a straight line perpendicular to the building surfaces. Reflection measurements were performed with the transmitter and receiver located in a line perpendicular to the building wall, with both transmit and receive antennas pointing at normal incidence to the surface building, for combined T-R distances of 41 m to 135 m. The receiver sensitivity (lowest detectable RF signal) was -110 dBm and the dynamic range of the whole system (range of measurable path loss) was 60 dB. A system calibration was performed with an aluminum metal plate to ensure that the system was working properly. The reflection loss from this metal plate was found to be -1 dB compared to a LOS path loss measurement, a reasonable approximation that this metal conductor was a perfect conductor. It was found that reflection power losses were considerably lower for metal surfaces than for brick and concrete walls. The measured penetration and reflection losses at 9.6 GHz can be found in Table 1.4 and Table 1.5.

Table 1.4: Penetration losses through common building structures common to an urban city. For additional penetration losses, refer to Section III.B in [4].

Reference	**Material**	**Path Length (m)**	**Penetration Loss [dB] at 9.6 GHz**
[4]	Solid Cement	42	-84
		53	-55
	Solid Pre-Cast Concrete	200	< -95
		260	-65
	Brick with Windows	120	-72
	Chromatic Glass	72	-60

Table 1.5: Some reflection losses through common building structures common to an urban city. For additional reflection losses, refer to Section III.B in [4].

Reference	**Material**	**Path Length (m)**	**Reflection Loss [dB] at 9.6 GHz**
[4]	Metal	50	0
		109	-6
	Brick (Solid)	95	< -2
		47	-6
	Concrete (Ribbed)	64	-6
		93	-9
	Brick (Windows, Doorway)	93	-9
		135	-12
	Concrete (Aggregate)	75	-6
		75	-12

For all buildings measured, the penetration losses decreased as the transmitter and receiver were placed farther away from the building walls, indicating a strong dependence upon T-R distance. The penetration loss through the solid cement building for a T-R separation distance of 42 m was greater than 84 dB, but was decreased to 55 dB for a T-R separation distance of 53 m. Violette *et al.* attribute this decrease in penetration loss to a double-edge diffraction mode, where the EM waves can get diffracted on the two rooftop edges, on both the transmitter side and the receiver side. This was confirmed when tilting the transmit and receive antennas directly towards the rooftop edges, where the penetration loss was significantly reduced.

The penetration loss through solid pre-cast concrete for a T-R distance of 200 m with both TX and RX antennas pointed at each other was greater than 95 dB, but was reduced to 65 dB when increasing the T-R distance to 260 m and tilting both antennas towards the rooftop edges. Violette *et al.* note that the

chromatic glass building had an unusually high penetration loss of 60 dB because the glass was metal-coated on the exterior side, but transparent from the inside, thus acting as a perfect conductor with high reflection coefficient.

The metal surface measured had an average reflection loss of 3.2 dB (over all metal surface measurements performed, see [4]) and exhibited the largest variability in measured reflection loss with respect to path length. The solid brick and ribbed concrete surfaces had an average reflection loss of 10.5 dB and 8.6 dB (over all brick and concrete surface measurements performed, see [4]), respectively, and moderate variability with respect to path length. Finally, the brick and aggregate concrete surfaces had an average reflection loss of 14.5 dB and 10.9 dB (over all brick and concrete surface measurements performed, see [4]), respectively, with small variability with respect to path length. Violette *et al.* attribute this variability dependence on T-R distance to surface roughness of the materials tested.

1.3 K_u - Band: 12 - 18 GHz

The K_u - Band, like the X - Band, has been studied simultaneously with other frequency bands to provide communication channel comparisons.

1.3.1 Channel Characterization

1.3.1.1 Propagation Characteristics in the K_u - Band

Vannucci *et al.* conducted narrowband indoor propagation measurements at 17 GHz to assess the feasibility of frequency re-use with and without antenna diversity [6]. Three indoor environments were investigated: a typical office, a laboratory and a long hallway. The TX had an open-ended rectangular waveguide of effective 20 dBi gain, and the RX was a biconical omnidirectional horn in the azimuth plane, with overall 4.5 dBi gain in the elevation plane. The TX was fixed 2 m above the floor in a reference room facing the center of the room, while the RX swept around the room or corridor to simulate a mobile scenario in both static and time-varying environments (i.e., with a person moving in front of the transmitter). The

measurements were repeated with a 20 dBi receiver horn antenna to compare the effects of antenna diversity gains upon the indoor communication channel.

The path loss exponent for non-line-of-sight (NLOS) conditions is visually estimated from the received power as a function of distance plot to lie between 2 and 4. Received signal levels were observed to vary by 40 dB when the RX was placed in a neighboring room from the TX. Finally, outage curves are computed and it is concluded that frequency re-use is a definite possibility at 17 GHz [6].

A wideband (2 GHz RF bandwidth) indoor propagation measurement campaign was performed at 17 GHz and 60 GHz to characterize indoor radio-propagation in a corridor, and a small room with and without furniture [7], with the TX kept fixed while the RX was rotated at constant angular speed about a fixed point from a NLOS to a LOS condition.

For the 60 GHz channel, multipath arrivals were observed to arrive between 10 - 80 ns excess time delay, with RMS delay spreads ranging from 4 to 5 ns and from 5 to 13 ns for LOS and NLOS conditions, respectively. Most of the RF power was contained in multipath components arriving between 0 - 42 ns. For the 17 GHz channel, the longest multipath arrival was found at 240 ns excess time delay. Each incoming ray was easily tracked in both time delay and azimuth angle of arrival by matching up the received power levels on an omnidirectional PDP and the corresponding polar plot, showing the azimuthal distribution of received power [7]. A summary of results reported in [6] and [7] can be found in Table 1.6.

Table 1.6: Summary of indoor propagation campaigns and results in the 17-18 GHz band [6][7].

Measurements	**Frequency**	**T-R Dist.**	**BW**	**Antennas**	**Results**
Assess the feasibility of short-range frequency re-use in office and lab [6].	17.5 GHz	1-30 m	Narrowband CW Source	Open-ended waveguide; Widebeam	Path loss exponent between 2 and 4; 40 dB variation in received power levels in neighboring rooms; Outage curves are given.
Characterize indoor radio-propagation in room and corridor [7].	17 GHz 60 GHz	1-10 m	2 GHz RF	Not Stated	Largest observed multipath at 240 ns excess time delay (17 GHz); Graphs of received power levels given.

Table 1.7: Penetration losses through common office building materials at 17 GHz as measured in [6][8].

Reference	Material	Thickness (cm)	Penetration Loss [dB] at 17 GHz
[6]	Ceiling Tile	-	-0.9
	Sheetrock	1.59	-1.25
	Plain Glass	0.32	-1.3
	Aluminum Sheet	0.32	< -42
	Steel	0.16	< -42
	Plywood	1.27	-2.85
	Fiberglass Insulation, Paper Backed	7.62	-0.33
	Fiber Insulation, Foil Backed	2.54	< -42
	Thermal Windows	-	-20.2
[8]	Uniform Plasterboard Wall	12	-11
	Slightly Reinforced Non-Uniform Concrete	12	-33

1.3.2 Material Properties in the K_u - Band

1.3.2.1 Penetration Measurements

Two penetration measurement campaigns in the 17 GHz band were performed on typical office building materials [6][8]. Measurement procedures were not provided. The results are reported in Table 1.7.

1.4 K - Band: 18 - 27 GHz

1.4.1 Channel Characterization

1.4.1.1 Propagation Characteristics in the K - Band

Kalivas *et al.* investigated the received envelope fading and large scale attenuation properties of a narrowband signal with and without antenna diversity at 21.6 GHz and 37.2 GHz in the rooms and hallways of a university building using a biconical omnidirectional transmit and receive antennas of 0 dBi gain, as well as highly directional 15 dBi antennas at the RX [9]. The receiver always remained stationary while the transmitter moved around the room or hallway at constant speed during the measurements. NLOS measurements were also taken with the RX placed in a neighboring room, separated by walls internally made of double plasterboard. Both TX and RX antennas were located 1.5 m above ground.

The LOS and NLOS path loss exponents (PLE) were 1.2 and 2.95 at 21.6 GHz, and 1.65 and 3.3 at 37.2 GHz, respectively. The computed LOS PLE was typically better than free space propagation (PLE in free space being 2), suggesting multipath constructive interference in the corridor, acting as a waveguide structure in helping the RF energy to reach the RX. The partition loss was computed to be 3.7 dB/wall and 5.4 dB/wall at 21.6 GHz and 37.2 GHz respectively. The received power levels followed a Rayleigh and Rician distribution for the NLOS and LOS measurements respectively, implying the presence a large number of approximately equal power multipath in the NLOS conditions, and the presence of a much stronger LOS component relative to first- or second-order reflected components in the LOS conditions [9].

A simulation study at 25 GHz and 40 GHz was performed to determine the area coverage of three base stations, located 190 - 202 m above sea level, based on their height in an outdoor urban environment, consisting of multistoried buildings, apartments, and shopping centers. The simulation proceeded by placing three transmitter base stations 1.2 - 1.5 km apart, each located at the apex of a triangle. The T-R separation distances measured were between 0.5 km to 3 km [10]. It was found that for cell radii of 1 km, 2 km, and 3 km, cell coverage ranged from 6.4 - 50%, 2.53 - 29.8% and 1.80 - 23.9% respectively, for TX heights ranging from 10 - 50 m.

It was found that raising the transmit antenna from 10 m to 50 m (above its designated 0 m height) provided a 23% increase in coverage, whereas raising the receive antenna from 1 m to 5 m increased coverage by 8.7%. Rain and atmospheric oxygen gas attenuations were estimated using the measured rainfall rate and annual atmospheric attenuation curves and the ITU models [11][12]. It was found that rain and oxygen gas attenuations are 5 dB and 0.32 dB/km at 25 GHz, and 11 dB and 0.26 dB/km at 40 GHz, respectively. The results reported in [9] and [10] are summarized in Table 1.8.

Table 1.8: Summary of results at 21.6 GHz and 25 GHz as reported in [9][10].

Measurements	Frequency	T-R Dist.	BW	Antennas	Results
Study radio propagation in university rooms and hallways [9].	21.6 GHz 37.2 GHz	15 - 30 m	Narrowband 3 kHz IF	Omni; Wide	LOS Corridor at 21.6/37.2 GHz: $n = 1.2$ /1.65; NLOS at 21.6/37.2 GHz: $n = 2.95/3.3$; Wall penetration loss at 21.6/37.2 GHz = 3.7/5.4 dB/wall (the wall is made of double plasterboard); Many more multipath fades at 37.2 GHz than at 21.6 GHz (not quantified).
Simulate outdoor urban area coverage of three transmitter base stations [10].	25 GHz 40 GHz	3 km; TX height: 190-202 m	Not Stated	Not Stated	Raising TX from 10 m to 50 m increases coverage by 23%; Raising RX from 1 m to 5 m increases coverage by 8.7%; Rain and gas attenuations are estimated using ITU models and are found to be 5 dB and 0.32 dB/km respectively, at 25 GHz.

1.5 K_a - Band: 27 - 40 GHz

1.5.1 Channel Characterization

1.5.1.1 Propagation Characteristics in the K_a - Band

Allen *et al.* studied the propagation mechanisms giving rise to atmospheric fading at 9.6 GHz, 11.4 GHz, and 28.8 GHz by observing signal performance on a 23 km transmitter-to-receiver link in a rural and suburban environment. The receiver remained fixed while the transmitter ascended and descended a 300 m high tower, transmitting a narrowband signal with a highly directional horn antenna in the direction of the RX, to investigate signal fading phenomena such as ground reflections, scintillation, and radio holes. Among the results, it was found that ground reflections and atmospheric fading induced up to 8 dB and 20 - 40 dB fades, respectively [3].

Violette *et al.* investigated point-to-point signal propagation at street level in an urban environment

to characterize the 9.6 GHz, 11.4 GHz, 28.8 GHz, 30.3 GHz, and 57.6 GHz radio-wave communication channels, with both the TX and the RX located on the streets [4]. It was discovered that reflected signals are an important part of the channel description. Multipath signals from street surfaces produced fades in excess of 30 dB, while multipath components having been reflected had amplitudes 15 dB below the line-of-sight (LOS) component.

The LMDS 28 GHz channel has been extensively studied [13][14][15][16][17][18][19][20]. Elrefaie *et al.* performed an extensive propagation measurement campaign to characterize the LMDS communication channel in a suburban environment [13]. Cell coverage was studied as a function of TX and RX height, cell radius and link margin for TX heights of 40 ft and 80 ft, and RX distances between 0.5 - 2 km from the TX. They found a coverage of 70% and 84% for TX heights of 40 ft and 80 ft, respectively. The outage was 11% and 8% worse than 10^{-3} for TX heights of 40 ft and 80 ft, respectively.

Seidel *et al.* investigated the LMDS propagation channel in a LOS condition with two TX locations placed at heights of 50 ft and 165 ft. The transmitter-to-receiver distances went as far as 8 km. The results of the study show that received power levels strongly depend on RX height [14]. The LOS component at the RX was shown to decrease from -99 dBm, to -105 dBm, to -112 dBm, as the height of the RX antenna decreased from 11.3 m, 7.3 m and 4 m. When the RX was located at lower heights, reflected components suddenly became more prominent.

A wideband (200 MHz RF bandwidth) outdoor measurement campaign was conducted at 27.4 GHz at two specific hub sites in Singapore, the suburban National University of Singapore (NUS) area and the urban area near Clementi, to investigate the characteristics of the LMDS communication channel [15][16][21]. At each hub location, the transmitter was located on the rooftop of a tall building surrounded by 13 - 25 story high buildings while the RX locations were placed on surrounding rooftops within a radius ranging from 0.5 - 6 km. The RX locations were surrounded by several residential blocks, business centers and hilly terrain. The transmit antenna was a widebeam vertically polarized 11 dBi horn, and the receive antenna had a gain of 31 dBi with half-power beamwidth of 4° in both the azimuth and elevation planes. A power delay profile was obtained at the RX for each 5° step increment in the azimuth plane [15][16][21].

It was found that signal impairment mostly comes from surrounding vegetation, blockage by adjacent buildings and the density of surrounding buildings. Received signal at NUS was observed to follow a Nakagami-Rician distribution. The LOS links showed strong Rician behavior with K-factor ranging from -4 dB to 12 dB. Different types of environments were classified according to the excess loss beyond free space path loss caused by buildings, vegetation, and atmospheric attenuation. The table below summarizes the different environments based on the excess loss incurred.

Table 1.9: Summary of different types of environments classified according to excess path loss incurred at 27.4 GHz [15].

Environment Type	**Excess Loss (dB)**
Clear LOS	25 - 35
Partial Blockage	35 - 45
Single Blockage/Multiple Foliage	45 - 55
Multiple Blocks	> 55

The average excess delay and RMS delay spread were below 150 ns and 200 ns respectively, for more than 90% of all measured RX sites. The maximum average excess delay and RMS delay spread were 300 ns and 250 ns, respectively. The RX signal level fluctuated by ± 5 dB about the mean signal level, and the excess path loss ranged from 25 dB to 65 dB. These measurements became the basis for the static and time-varying channel impulse responses, developed for theoretical studies and enabling radio-system design (See Section 1.5.1.5).

A number of propagation channel parameters have been classified according to statistical heights and widths distributions of an urban area, which was divided into four types of environments including a business area with high buildings and strong multipath fading environment, a residential building area with low rooftops, a historical and shopping center, and a residential area with new individual houses [17]. This wideband measurement campaign at 27.4 GHz was performed by placing the TX on high buildings or towers, and placing the RX between 0.5 - 5 km in range on a rooftop, so that there was a clear LOS path between TX and RX. The transmit and receive antennas had gains of 20 dBi and 25 dBi, respectively. The received power levels followed a Rician distribution with K-factor ranging from -13 dB to 25 dB. The mean and RMS delay spreads ranged from 40 - 580 ns and 50 - 300 ns, respectively. Table 1.10 below summarizes

the parameterization and obtained results in an urban environment [17].

Table 1.10: Statistical parameterization of a typical urban environment [17].

Location	**Zone 1**	**Zone 2**	**Zone 3**	**Zone 4**
General Description	Business area, very high buildings	Residential area, old buildings with few stores	Historical and shopping center	Residential area, new individual houses
Distribution	Normal $\mu = 21.4$ m, $\sigma = 8.9$ m	Normal $\mu = 12.5$ m, $\sigma = 3.7$ m	Normal $\mu = 10$ m, $\sigma = 2$ m	h < 9 m, 5% h $= 9$ m, 70% h $= 12$ m, 20% h > 12 m, 5%
Received Power	-50 to -100 dBm	-50 to -100 dBm	-50 to -100 dBm	-50 to -100 dBm
Mean Delay	60 - 380 ns	140 - 680 ns	40 - 150 ns	150 - 580 ns
Delay Spread	50 - 200 ns	150 - 300 ns	50 - 60 ns	100 - 150 ns
K-Factor	-3 to 12 dB	-13 to 25 dB	-8 to 15 dB	-12 to 21 dB
Excess Path Loss	10 - 60 dB	3 - 6 dB	8 - 12 dB	4 - 6 dB

A measurement campaign was performed to investigate the 38 GHz and 60 GHz peer-to-peer, cellular and intra-vehicular channels using a 750 mega-chips per second (Mcps) broadband sliding correlator channel sounder, with a pair of 25 dBi horn antennas, on the UT Austin campus [19][20][18][22]. Of all peer-to-peer measurements performed, 51% and 31% of links were completed with extreme off-boresight transmit and receive antenna combinations (relative angle between transmit and receive antennas greater than 50°) at 38 GHz and 60 GHz, respectively. Peer-to-peer measurements yielded an average of 1 to 2 completed links at 60 GHz, and 1 to 3 links at 38 GHz. Cellular channel measurements yielded 2 to 4 links for a given transmitter-receiver location and angle-pointing combination at 38 GHz. Vehicular measurements at 60 GHz yielded 3 to 5 links for a given transmitter-receiver location. It was found that NLOS links (obstructed paths between transmitter and receiver) path losses ranged from 15 to 40 dB greater than LOS path losses. Additionally, NLOS links achieved RMS delay spreads ranging from 1 ns to 122 ns at 38 GHz, and from 1 ns to 36.6 ns at 60 GHz (for more detail on each TX location, see Figs. 15-16 of [20]). Table 1.11 below summarizes the path loss exponents measured using the minimum mean square error best line fit with a 5 m free space reference distance at 38 GHz and 60 GHz for both peer-to-peer and cellular (rooftop to ground) measurements. An important trend observed was that higher excess path loss was found to be positively

correlated with higher RMS delay spreads for both peer-to-peer and cellular measurements of the 38 GHz and 60 GHz channels. It was empirically found that the RMS delay spread per dB of excess path loss was 0.73 ns/dB and 0.27 ns/dB at 38 GHz and 60 GHz, respectively, for peer-to-peer measurements, and 0.47 ns/dB at 38 GHz for cellular measurements [19]. High delay spreads were shown to be less likely at T-R separation distances greater than 50 m for the 60 GHz peer-to-peer and vehicular channels. A more detailed breakdown of all path loss exponents found for each TX location can be found in Table IV of [20].

Table 1.11: Summary of path loss exponents for the 38 GHz and 60 GHz peer-to-peer and cellular channels at UT Austin as a function of RX antennas gain [19][20].

Antenna Gains		**13 dBi RX Ant.**		**25 dBi RX Antenna**					
Path Loss Exponents		38 GHz		60 GHz	38 GHz	60 GHz	38 GHz	60 GHz	38 GHz
		LOS	NLOS-Best	LOS		NLOS		NLOS-Best	
Peer-to-Peer	PLE	-		2.25	2.0	4.22	4.57	3.76	3.71
	σ (dB)			2.0	3.79	10.12	11.72	10.16	8.57
Cellular	PLE	2.21	3.18	-	2.22	N/A	3.88	-	3.26
	σ (dB)	9.4	11.0		6.38		11.43		11.76
Vehicular	PLE	-		2.66	-	7.17	-	-	
	σ (dB)			5.4		23.8			

Table 1.12: Summary of RMS delay spreads for the 38 GHz and 60 GHz peer-to-peer and cellular channels at UT Austin [19].

RMS Delay Spreads		60 GHz	38 GHz	60 GHz	38 GHz	60 GHz
		LOS		NLOS		All
Peer-to-Peer	Mean (ns)	0.8	1.2	7.4	23.6	6.02
	Max (ns)	0.9	1.3	36.6	122	-
Cellular	Mean (ns)	-	1.1	-	12.2	-
	Max (ns)	-	1.4	-	117	-
Vehicular	Mean (ns)	-	-	-	-	2.73
	Max (ns)	0.9	-	-	-	12.3

An outage study was conducted for the 38 GHz cellular channel. For T-R distances less than 150 m, outages ranged from 42.6% to 70.7%, 43% to 76%, and 43% to 84.5% for angle of arrivals less than 45°, 65° and 85° off boresight respectively. It was found that TX antennas of 25 dBi gain required an azimuth scan of 60° for elevated heights of 2 to 8 stories above ground. A more detailed breakdown of outages for each TX location as a function of TX antenna height can be found in Tables II and V of [20]. Elevated TX antennas

could cover 73% of RX locations in a range of 200 m, and TX antennas located at lower base station heights could cover 90% of all RX locations [18][20]. Table 1.13 below summarizes the results of each propagation campaign in this section.

Table 1.13: Summary of measurement campaigns performed in the 21 GHz, 28 GHz, and 38 GHz frequency bands.

Measurements	**Frequency**	**T-R Dist.**	**BW**	**Antennas**	**Results**
Study atmospheric fading in rural and suburban context [3].	28.8 GHz	22.8 km	Narrowband 2 kHz IF	Narrow; Wide	Ground reflections: 8 dB fades; Scintillation: 1 dB fades; Atmospheric multipath: 20 to 40 dB fading; Atmospheric bending: 10 dB enhancement.
Study point-to-point transmission at street level in urban environment [4].	9.6 GHz 11.4 GHz 28.8 GHz 30.3 GHz 57.6 GHz	0.9 km	5 kHz	Narrow; Wide	Reflected signals are strong; Multipath from street surfaces produce fades $>$ 30 dB; Multipath reflections from building walls and other reflecting surfaces have amplitudes of 15 dB below LOS component; No dependence on polarization in RX power levels.
Study range dependence, depolarization and frequency dependence in foliated environments [5].	9.6 GHz 28.8 GHz 57.6 GHz	0.1 - 0.9 km	Narrowband CW Source	Narrow	12 - 20 dB/tree attenuation for distances $<$ 30 m; 0.5 - 0.7 dB/tree attenuation for distances $>$ 30 m; Flat received signal in azimuth at depth of 8 - 11 trees; No dependence on linear co-polarization.
Characterize radio-wave propagation for LMDS in suburban environment [13].	28 GHz	1 - 2 km; TX height: 40 - 80 ft	Not Stated	Not Stated	TX height of 40 ft: 70% coverage, outage is less than 11% worse than 10^{-3}; TX height of 80 ft: 84% coverage, outage is less than 8% worse than 10^{-3}.

Measurements	Frequency	T-R Dist.	BW	Antennas	Results
Describe the LMDS channel and its broadband applications [14].	28 GHz	Up to 8 km	Not Stated	Not Stated	Received power levels significantly depend on RX height; As RX is lowered, LOS component decreases in amplitude, NLOS multipath components become more prominent.
Investigate the performance of LMDS band in urban and suburban areas [15][16].	27.4 GHz	0.5 - 6 km	Wideband 200 MHz RF with BPSK Modulation	Narrow; Wide	Measured excess loss: 24 - 60 dB; Mean/Max excess delay: 150/300 ns; Mean/Max RMS delay: 200/250 ns; LOS RX signal followed Nakagami-Rician distribution with K-factor ranging from -4 dB to 12 dB; Linear relationship between delay spread and excess loss.
Parameterization of propagation channel based on statistical height and widths distributions of urban areas [17].	27.4 GHz	0.5 - 5 km	Wideband 50 MHz RF	Narrow; Wide	Mean delays: 40 - 580 ns; Delay spreads: 50 - 300 ns; Rician K-factor: -13 dB to 25 dB; Excess path loss: 10 - 60 dB.

Measurements	Frequency	T-R Dist.	BW	Antennas	Results
Study the peer-to-peer and cellular communication channels in urban campus environment [19][22].	38 GHz 60 GHz	15 - 120 m	Wideband 1.5 GHz RF	Narrow; Wide	Peer-to-peer: 51% of links completed with extreme off-boresight TX and RX antenna combinations; 1 to 3 completed links; Cellular: 2 to 4 completed links for a given TX-RX location. NLOS link path losses ranged from 15 - 40 dB in excess loss; RMS delay spreads ranged from 1 - 122 ns; Path loss exponents P2P/C: • LOS: 2.0/ 2.22 • NLOS All: 4.57/3.88 • NLOS-Best: 3.71/ -3.26 Max RMS delay spreads P2P/C(ns): • LOS: 1.3/1.4 • NLOS All: 122/117 P2P: $DS[ns] = 0.73 \times EPL$ C: $DS[ns] = 0.47 \times EPL$

1.5.1.2 Diffraction in the 28 GHz Frequency Band

The propagation mechanism of diffraction models the bending effects of propagating electromagnetic waves traveling close to obstruction corners. This mechanism is greatly dependent on carrier frequency, more pronounced at low frequencies (less than 6 GHz), and increasingly less as the frequency of propagation increases. Wireless devices operating in the low GHz spectrum range benefit from diffraction, allowing an increase in signal coverage in areas shadowed by large obstructions.

Diffraction around brick and concrete corners was studied at 28 GHz [23] using a continuous wave (single frequency) source channel sounder and a highly directional 2.5° parabolic transmit antenna. The receiver had a spectrum analyzer and a 17° horn antenna, capturing the transmitted signal while rejecting unwanted energy. The range of measurable path loss of the channel sounder was 97 dB. An initial reference LOS measurement was taken, against which later diffracted measurements were compared. The difference between the reference LOS received power and the diffracted received power constituted the diffraction loss

from the building corner. The TX and RX antennas were aligned with the corner of the building, and this configuration was denoted as the $\theta_D = 0°$ angle. The RX was moved along an arc of constant radius towards the shadowing region of the building, from 0° to 40°.

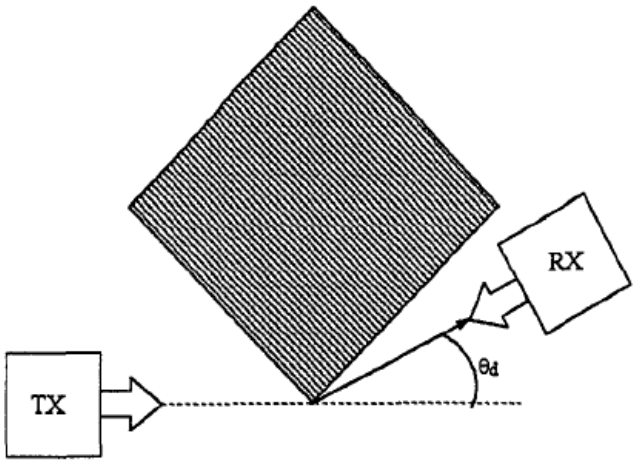

Figure 1.1: Diffraction measurement setup used in [23]. The $\theta_D = 0°$ corresponds to the TX and RX aligned with the obstruction corner. The RX sweeps an arc of constant radius counterclockwise as θ_D increases.

The concrete corner attenuated the diffracted signals 3 dB more than for brick for $0° < \theta_D < 40°$. Polarization only affected the loss very slightly, a 0 to 1.5 dB change in received power levels. The loss at $\theta_D = 0°$ was found to be 6-7 dB. The model is logarithmic in the 0° to 5° range, and linear in the 5° to 40° range. The T-R path length did not significantly affect diffraction loss. Below is the model that predicts diffraction for both concrete and brick as found in [23].

Table 1.14: Model predicting diffraction losses around brick and corner buildings at 28 GHz [23].

Diffraction Angle (°)	**Diffraction Loss [dB]**
$0° \leq \theta_D < 0.1°$	6.5
$0.1° \leq \theta_D < 5°$	$5 \times \ln(\theta_D) + 18$
$5° \leq \theta_D \leq 40°$	$0.74 \times \ln(\theta_D) + 25$

1.5.1.3 Effects of Vegetation in the K_a - Band

A number of propagation measurement campaigns have been conducted to study the 28 GHz and 38 GHz LMDS communication channel obscured by vegetation [5][24][25][26][27]. For a description of the propagation study in [5], refer to Section 1.2.1.2.

Papazian *et al.* conducted a 28.8 GHz wideband (1.5 GHz RF bandwidth) propagation measurement campaign to study the seasonal variability of the propagation channel obscured by two deciduous trees with and without leaves [25], using 43 dBi and 30 dBi transmit and receive horn antennas, respectively, over a link distance of 957 m. The attenuation due to the expansive leaf canopy was measured to be 26 - 28 dB, and 16 - 18 dB in the absence of leaves.

A measurement campaign was performed to investigate the effects of vegetation for 28 GHz propagation [26] by comparing received power levels over a LOS path and the equivalent single tree-obstructed NLOS path for a given distance of 370 m. A 14 GHz narrowband CW source was frequency-doubled to 28 GHz, fed at 8 dBm through a 15 dBi (half-power beamwidth of 90°) sectorial horn, and analyzed on the receiver end with a 50 GHz spectrum analyzer hooked up to a PC for automatic data acquisition. Two receive antennas, a 15 dBi sectorial horn and a 28 dBi circular lens (6° half-power beamwidth), were swapped to study the effects of vertical and horizontal co-polarizations (V/V and H/H), and vertical-circular (V/C) as well as horizontal-circular (H/C) cross-polarizations on received power levels through vegetation. The vertical-horizontal cross-polarizations (V/H and H/V) were found to have a cross-polarization attenuation greater than 35 dB (allowing for orthogonal frequency reuse), and were thus not studied. The transmit and receive antennas were placed on a pan-and-tilt mast to control azimuth and elevation angles. Table 1.15 shows the mean and standard deviations of the received power levels in both the LOS and tree-obstructed NLOS paths.

The measured power levels for the LOS path were within experimental errors of the theoretical values with standard deviations less than 0.5 dB, which ensured that the hardware was functioning correctly. The foliage-induced loss for the NLOS path was found to be 19 to 26 dB depending on the polarization scheme used. The vertical co-polarization scheme benefitted from an extra 3 dB of gain over the horizontal co-

Table 1.15: Mean and standard deviations of received power levels for an unobstructed LOS and its equivalent tree-obstructed NLOS path [26].

	Received Power	**H/H**	**V/V**	**H/C**	**V/C**
LOS Path	Measured (dBm)	-71.53	-72.95	-61.28	-60.66
	Stand. Dev. (dB)	0.47	0.65	0.39	0.28
	Theoretical (dBm)	-74.71	-74.71	-61.71	-61.71
NLOS Path	Measured (dBm)	-95.33	-92.01	-87.59	–85.43
	Stand. Dev. (dB)	3.90	3.88	2.66	3.11
	Theoretical (dBm)	-74.71	-74.71	-61.71	-61.71
Foliage-Induced Attenuation	Measured (dB)	23.80	19.06	26.31	24.78

polarization scheme, indicating that horizontally polarized plane waves suffered roughly twice as much loss from vegetation scattering than vertically polarized plane waves. The high standard deviations of roughly 3 dB in all polarization schemes for the NLOS received powers indicated the random nature of EM wave penetration through vegetation. The V/V, H/H and H/C polarizations received signal levels followed a Gaussian random distribution, while the V/C received signal levels were found to best match a Rayleigh distribution using the Smirnov-Kolmogorov test, a test designed to numerically find the best distribution fit.

The following distributions may be used to statistically recreate the path loss observed over a path link obstructed by one tree for a given T-R separation distance at 28 GHz:

$$PL[dB] = PL_{FS}(d) + \chi_p \tag{1.1}$$

$$PL_{FS}[dB](d) = 20 \times \log_{10}\left(\frac{4\pi d}{\lambda}\right) \tag{1.2}$$

where PL_{FS} is the free space path loss in dB, d (m) is the T-R separation distance, λ (m) is the carrier wavelength (0.0107 m at 28 GHz), and χ_p is a random variable modeling vegetation loss depending on the polarization scheme used (see Table 1.16). These statistical models are valid for the antenna patterns used in the experiment.

Table 1.16: Single tree-induced vegetation loss distributions depending on the polarization scheme used. The vertically and horizontally polarized antennas had 90° half-power beamwidths (15 dBi), and the circular lens antennas had 6° half-power beamwidths (28 dBi) [26].

Polarization Scheme	**Mean μ [dB]**	**Stand. Dev. σ [dB]**	**Distribution χ_p**
H/H	23.80	3.90	Gaussian
V/V	19.06	3.88	Gaussian
H/C	26.31	2.66	Gaussian
V/C	24.78	3.11	Rayleigh

A narrowband measurement campaign was performed at 2.45 GHz, 5.5 GHz, 29 GHz, and 60 GHz to compare temporal and statistical characteristics of communication channels obscured by foliated and non-foliated deciduous trees, and coniferous trees with leaves over link distances and foliage depths ranging from 64 - 110 m and 7 - 25 m, respectively [27]. The received RF power through foliage was observed to vary considerably with wind speeds, increasingly more attenuated as the wind speed decreases. Table 1.17 below summarizes the mean and variance of signal attenuations for the different trees.

Table 1.17: Mean and standard deviations of vegetation loss through deciduous and coniferous trees [27].

Reference	**Type of Foliage**	**Loss [dB] at 29 GHz**	
		Mean [dB]	σ [dB]
[27]	Deciduous with Leaves	-32.8	37.4
	Deciduous without Leaves	-8.7	10.9
	Coniferous with Leaves	-21.7	10

The mean attenuations through the coniferous tree, and the deciduous tree in presence and absence of leaves was 21.7 dB, 8.7 dB and 32.8 dB respectively, with corresponding standard deviations of 10 dB, 10.9 dB and 37.4 dB. In rare instances, the 29 GHz and 60 GHz signal did not suffer any attenuation through the leafless tree (i.e., 0 dB attenuation). The variance in received power levels was observed to decrease with increasing frequency. The received power levels were best described with the Extreme Value and Lognormal distributions. The duration of fades is best modeled with a Log-exponential distribution [27]. Table 1.18 below summarizes the results discussed in this section.

Table 1.18: Summary of measurement campaigns studying the effects of vegetation on LMDS 28 GHz frequency bands.

Measurements	**Frequency**	**T-R Dist.**	**BW**	**Antennas**	**Results**
Study range dependence, depolarization and frequency dependence in foliated environments [5].	9.6 GHz 28.8 GHz	0.1-0.9 km	Narrowband CW Source	Narrow	12 - 20 dB/tree attenuation for T-R distance < 30 m; 0.5 - 0.7 dB/tree attenuation for T-R distance > 30 m; Flat received signal in azimuth at depth of 8 - 11 trees; RX power has no dependence on polarization.
Investigate seasonal variability in signal attenuation for LMDS radio channel [25].	28.8 GHz	957 m	Wideband 1.5 GHz IF	Widebeam	Attenuation without leaves: 16 - 18 dB; Attenuation with leaves: 26 - 28 dB.
Characterize a single-tree obstructed NLOS communication channel [26].	28 GHz	370 m	Narrowband CW	Narrow; Widebeam	19 - 26 dB foliage-induced attenuation; Received power levels follow Rayleigh distribution.

Measurements	Frequency	T-R Dist.	BW	Antennas	Results
Characterize the radio-wave foliated channel through deciduous tree (with and without leaves) and coniferous tree with leaves [27].	29 GHz 60 GHz	64-110 m; Foliage Thickness: 7-25 m	Narrowband CW Source	Not Stated	RF power received depends on wind speeds, reduced speeds induce greater attenuations; 29 GHz and 60 GHz foliage channels are similar in their fading statistics; Mean attenuation through coniferous tree is visually estimated at 11 dB and 13 dB at 29 GHz and 60 GHz, respectively; Small variation of RX power through leafless deciduous tree at both 29 GHz and 60 GHz with attenuation visually estimated at 3 dB and 9 dB respectively. In rare instances, signal is not affected by tree (0 dB attenuation); Mean attenuation for tree with leaves and without leaves is 16 - 33 dB and 5 - 9 dB, respectively; RX power can be modelled with Extreme Value or Log-normal distributions; Duration of fades can be modelled with Log-Exponential distribution.

1.5.1.4 Effects of Rain and Hail in the K_a - Band

Xu *et al.* conducted a measurement campaign at 38 GHz to characterize the influence of rain, hail, glass and foliage on average RF signal attenuation [28]. Their results are shown in Table 1.19.

1.5.1.5 LMDS 28 GHz Impulse Response Channel Models

A channel model has been implemented to estimate channel impulse responses in different types of urban environments based on an extensive 28 GHz propagation measurement campaign [29]. It is presented

Table 1.19: Summary of measurement campaigns studying the effects of rain on LMDS 28 GHz frequency band and reported reports [28].

Measurements	**Frequency**	**T-R Dist.**	**BW**	**Antennas**	**Results**
Characterize influence of LMDS LOS and NLOS links during different weather events [28].	38 GHz	LOS: 605 m NLOS: 262 m	Wideband 200 MHz	Widebeam	Mean / Max Delay spreads: • L1: 3.4 - 6.4 ns / 6.1 - 9.7 ns • L2: 3.9 - 7.5 ns / 8.1 - 15.4 ns • L3: 3.2 - 5.9 ns / 5.9 - 15.9 ns Glass/Dry leaves/Hail attenuation: 25.5 dB/17 dB/25.7 dB; Received power levels follow Rician distribution with $K[dB] = 16.88 - 0.04 \times R[mm/h]$.

in this section.

1.5.1.5.1 Soma *et al.* Channel Model

This channel model provides impulse responses for the LMDS static and time-varying channels, applicable to urban, suburban and rural environments for LMDS 28 GHz propagation. The measurements that provided the basis for this channel model were performed with the transmitter located well above surrounding rooftops, and the receiver located on surrounding rooftops at distances ranging from 1 to 5 km away. Vegetation was the main obstruction [21][29]. Below is a comprehensive description of the LMDS static and time-varying channel impulse response as described in [29]. The average received power P_r is computed as follows:

$$P_r[dBm](d) = EIRP[dBm] + G_r - 32.44 - 20 \times \log_{10}(d \times f_{GHz}) - L_{cab} - L_{env} \tag{1.3}$$

where $EIRP$ is the effective isotropic radiated power in dBm at the transmitter side, f_{GHz} is the operating frequency in GHz, d (m) is the transmitter-receiver separation distance, and G_r (dBi) is the gain of the receive antenna. L_{cab} denotes the cable loss in dB at the receiver side, and L_{env} represents the environment

loss in dB in addition to free space path loss due to the local blockage by buildings and vegetation, the rainy climate, and the multipath fading environment.

The environment loss is modeled with the following expression:

$$L_{env}[dB] = 20 \times \log_{10}\left(\frac{2.25}{d_{km}}\right) \tag{1.4}$$

where d_{km} is the T-R separation distance in km.

Upon computing the environment loss, the RMS delay spread is modeled with the following expression:

$$DS[ns] = 215.75 + 1.5 \times L_{env}[dB] \tag{1.5}$$

The static-channel impulse response is modeled for three types of channels: the good, the moderate, and the bad channels. Each channel type is further sub-divided into several models to account for the degree of the multipath-fading environment. Table 1.20 summarizes the different channel types and models as a function of mean delay, delay spread and excess loss.

Table 1.20: Mean excess delays, RMS delay spreads and excess losses for different models for different time-invariant (i.e., static) channel types based on measurements obtained at 27.4 GHz [29].

Channel Type	**Model #**	**Mean Delay (ns)**	**Delay Spread (ns)**	**Excess Loss (dB)**
Good	Model 1	15.46	11.96	0 - 12
	Model 2	22.46	14.61	
	Model 3	31.72	18.16	
	Model 4	27.1	16.65	
Moderate	Model 1	28.97	16.67	12 - 26
	Model 2	35.27	50.89	
Bad	Model 1	18.97	13.69	26 - 40
	Model 2	85.35	75.84	

The N-tap static impulse response is modeled as follows:

$$h(\tau) = \sum_{n=0}^{N-1} a_n \delta(\tau - \tau_n) \tag{1.6}$$

where N is the total number of multipath components arriving at the receiver, and a_n and τ_n are the tap gain and excess time delay of the n^{th} multipath arrival, respectively. Tables 2.1 and 2.2 below provide values for the number of multipath components N, the tap gains a_n, and the excess time delays τ_n. The tap gain values have been normalized to the first arriving LOS multipath component power, computed using Eq. (1.3).

Table 1.21: Tap gains (relative to the first arriving multipath power) for different models based on measurements at 27.4 GHz made in [29]. Models 1 and 2 are applicable in environments with good signal reception with less multipath arriving to the RX. Models 3 and 4 are applicable in environments with good signal reception and moderate multipaths arriving to the RX. All models are for static channels.

Good Reception	**Tap Gains a_n [dB]**			
Excess Delay τ_n [ns]	Model 1	Model 2	Model 3	Model 4
0	-2.65	-6.31	-18.18	-10.86
20	0	0	-0.69	0
40	-8.05	-3.67	0	-2
60	-		-13.45	-21.86
80			-24.54	-19.68
100			-20	-20.79

Table 1.22: Tap gains for different models based on measurements at 27.4 GHz made in [29]. Models 1 and 2 are applicable in environments with moderate signal reception to the RX. All models are for static channels.

Moderate Reception	**Tap Gains a_n [dB]**	
Excess Delay τ_n [ns]	Model 1	Model 2
0	-12.36	-6.37
20	0	0
40	-0.5	-4.7
60	-15.56	-18.16
80	-	-20.00
200		-19.91
280		-18.71
300		-16.74
340		-18.68
360		-17.65

Table 1.23: Tap gains for different models based on measurements at 27.4 GHz made in [29]. Models 1 and 2 are applicable in environments with poor signal reception to the RX. All models are for static channels.

Poor Reception	**Tap Gains a_n [dB]**	
Excess Delay τ_n [ns]	Model 1	Model 2
0	-3.05	-3.12
20	0	0
40	-4.1	-5.68
60	-15.56	-12.31
80	-	-9.24
100		-8.64
120		-12.34
140		-13.43
200		-12.7
220		-14.1
260		-11.32
280		-7.27
300		-7.44
320		-11.3

The time-varying response impulse is modeled with the following equation:

$$h(t_k, \tau) = c_k \sum_{n=0}^{N-1} m(t_k, \tau_n)\delta(\tau - \tau_n)e^{-j(\omega_c \tau_n + \phi_n)} \tag{1.7}$$

where n is the tap index of the n^{th} arriving multipath component, N is the total number of taps, ω_c (rad/s) is the carrier angular frequency, τ_n (ns) and ϕ_n (rad) are the excess time delay and random phase in the range [0, 2π] of the n^{th} arriving multipath component. The factor c_k is a random variable that models the time-varying nature of the peak of the impulse response. The peak signal level variations were observed to follow a Rician distribution with K-factor ranging from -4 dB to 12 dB. The function $m(t_k, \tau_n)$ represents the distribution of the tap gains of various multipath components of the channel impulse response. A general equation for m is given below:

$$m(\tau_n) = \alpha \times \exp\left(-\beta\left(\frac{\tau_n - \tau_p}{100}\right)^2\right) \tag{1.8}$$

where β (ns^{-2}) controls the rate of decay of tap gains, α is the attenuation amplitude, and τ_p is the peak time (ns) of a particular multipath cluster. The parameters α and β are randomly distributed variables. Tables 2.4 and 2.5 give the values of τ_p, α, β and the range for the excess time delay τ:

Table 1.24: Summary of parameters needed to compute the time-varying channel impulse response as described in [29].

Parameter	**Urban**	**Suburban**	**Rural**
c_k (dB)	-10 to 6	-5 to 3	-5 to 3
β_1	20 - 100	50 - 120	50 - 120
β_2	6 - 20	10 - 25	10 - 25
β_3	0.5 - 10	1 - 10	0
β_4	5 - 50	0	0
t_{max} (ns)	400	250	100
Mean Excess Delay (ns)	50 - 70	40 - 50	30 - 40
RMS Delay Spread	20 - 80	10 - 20	< 10
K-Factor (dB)	-4 to 3	3 - 6	6 - 12

Table 1.25: Summary of peak times, attenuation factors, decay factors and range of excess time delays as described in [29].

Peak Time τ_p (ns)	**Attenuation Factor α**	**Decay Factor β**	**Excess Delay τ**
40	1	β_1	0 - 40
40	1	β_2	0 - 40
100	0.1	β_3	40 - 100
320	0.1	β_4	250 - 400

Once the impulse response has been generated as described above, the received signal can be generated as follows:

$$r(t) = s(t) \bigotimes h(t, \tau) + n(t) \tag{1.9}$$

where $r(t)$ is the received signal, $s(t)$ is the transmitted signal, $h(t, \tau)$ is the time-varying two-sided complex channel impulse response, and $n(t)$ is the complex Additive White Gaussian Noise given by:

$$n(t) = \sum_{n=\frac{M-1}{2}}^{\frac{M+1}{2}} a_n e^{-j(\omega_c \tau_n + \phi_n)} \tag{1.10}$$

where a_n, ω_n, and ϕ_n are amplitude, frequency, and phase of the individual sinusoidal components that contribute to noise, respectively. The amplitude a_n is a uniform random number in the range (0,1) and the phase term ϕ_n is also uniformly distributed through $[0, 2\pi]$. The angular frequency ω_n (rad/s) is given by $\omega_n = 2B/M$ where B (Hz) is the channel bandwidth and M is the number of sinusoidal components that contribute to noise.

1.5.2 Material Properties in the K_a - Band

1.5.2.1 Penetration Measurements

Two penetration measurement campaigns have been performed at 28 GHz to recover penetration losses through common outside building materials, such as metal and concrete buildings [4], tinted and clear glass, brick and drywall [30]. Penetration measurements in [30] were performed with a 400 Mcps sliding correlator channel sounder at 28 GHz, with a pair of 24.5 dBi horn antennas at a height of 1.5 m. The transmitter and receiver were placed on either side of the surface material on a straight line normal to the material surface, each 2.5 m away from the material, so that the total T-R separation distance was 5 m. The greatest measurable penetration loss allowed by the measurement system was 64 dB, allowing for a 10 dB margin. The excess channel loss (ECL) (i.e., penetration loss) was computed as the excess loss over free space path loss due to building penetration. For the penetration measurement procedure used in [4], refer to Section 1.2.1.1 The results are listed in Table 2.6.

Table 1.26: Penetration losses through common building structures common to an urban city at 28 GHz [4].

Reference	**Material**	**Building Width/Height (m)**	**Path Length (m)**	**Penetration Loss [dB] at 28 GHz**
[4]	Solid Cement	17/6	42	> 112
		17/6	53	108
		17/6	90	72
		17/6	53	58
	Solid Pre-Cast Concrete	100/7	200	> 100
		100/7	200	84
		100/7	260	69
	Brick with Windows	40/16	120	101
		40/16	120	85
	Chromatic Glass	53/9	72	65

Table 1.27: Penetration losses through common indoor and outdoor materials at 28 GHz [30].

Reference	**Material**	**Thickness (cm)**	**Penetration Loss [dB] at 28 GHz**
[30]	Tinted Glass (Outdoor)	3.8	-40.1
	Brick (Outdoor)	185.4	-28.3
	Clear Glass (Outdoor)	< 1.3	-3.9
	Tinted Glass (Indoor)	< 1.3	-24.5
	Clear Glass (Indoor)	< 1.3	-3.6
	Dry Wall (Indoor)	38.1	-6.8

1.5.2.2 Reflection Measurements

Two reflection measurement campaigns have been performed at 28 GHz to investigate the properties of common outside building materials [4][30]. The vertically-polarized transmitter and receiver 24.5 dBi horn antennas were oriented at equal incident angles with respect to the material surface normal and at equal distances of 2.5 m from the surface material. The reflection coefficient $\Gamma_{//}$ in [30] was obtained by taking the ratio of the total received power to the transmit power, for incident angles of 10° and 45°. The reflection losses (RL) were obtained as follows:

$$RL[dB] = 10 \times \log_{10}(|\Gamma_{//}|) \tag{1.11}$$

Note that the reflection coefficient $\Gamma_{//}$ relates the received power to transmit power, and not the received electric field to transmit electric field, and hence there is no need to square the reflection coefficient (in the linear scale) before taking the decibel value. For the reflection measurement procedure used in [4], refer to Section 1.2.1.1.

Table 1.28: Penetration losses through common building structures common to an urban city at 28 GHz [4].

Reference	**Material**	**Path Length (m)**	**Reflection Loss [dB] at 28.8 GHz**
[4]	Metal	50	-1
		109	-1
	Brick (Solid)	95	-7
		47	-14
	Concrete (Ribbed)	64	-11
		65	-7
	Brick (Windows, Doorway)	93	-14
		135	-15
	Concrete (Aggregate)	75	-12
		75	-10

The outdoor materials measured in [30] exhibited the smallest reflection losses of 0.48 dB and 0.89 dB at 10° incidence for tinted glass and concrete, respectively. Since tinted glass and concrete are typical materials found in dense urban environments, these measured reflection losses suggest that 28 GHz signals will remain relatively confined to the outside environment. Similarly, the indoor reflection losses are also relatively small, 1.31 dB and 1.52 dB for clear glass and drywall respectively, suggesting again that 28 GHz signals will remain confined to indoor environments. Inter-cell interference between indoor and outdoor cells will therefore be negligible, allowing the possibility of frequency reuse.

Table 1.29: Reflection losses of common building materials at 28 GHz for two incident angles [30].

Reference	**Material**	**Thickness (cm)**	**Reflection Loss [dB] at 28 GHz**	
			$\boldsymbol{\theta = 10°}$	$\boldsymbol{\theta = 45°}$
[30]	Tinted Glass (Outdoor)	3.8	-0.48	-
	Concrete (Outdoor)	-	-0.89	-2.06
	Clear Glass (Indoor)	< 1.3	-1.31	-
	Drywall (Indoor)	38.1	-1.52	-2.02

The discussion pertaining to the results of reflection losses in [4] are identical to those presented in Section 1.2.1.1.

1.5.2.3 Index of Refraction of Concrete at 28 GHz and 38 GHz

A 28 GHz and 38 GHz measurement campaign investigated the reflection properties of a cement block typical of construction to recover its indices of refraction at the two studied frequencies [31]. The transmit and receive antennas were oriented at the same angle with respect to the surface normal, and incremented from 5° to 70° in 5° steps using a vector network analyzer at the receiver side, and a pair of 25 dBi horn antenna with half-power beamwidth of 10°. Fig. 1.2 shows the measurement setup used.

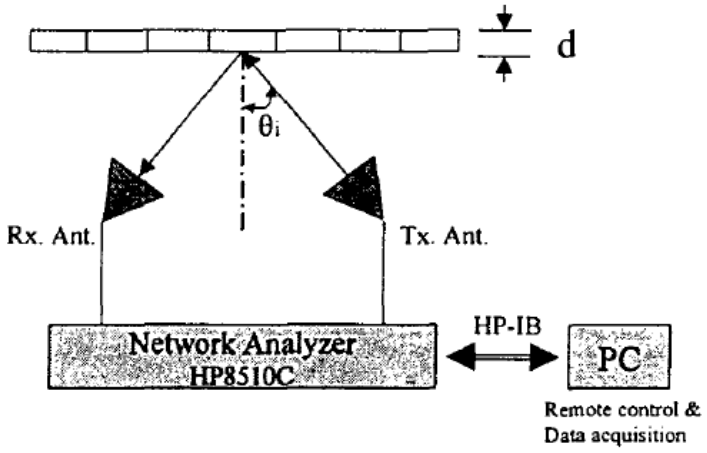

Figure 1.2: Measurement set up used to determine the TE and TM reflection coefficients of a cement block typical of construction [31].

The TE and TM reflection coefficients were computed as the ratio of reflected to transmitted electric fields, and the index of refraction of the sample material was recovered using a non-linear least square best line fit to the Fresnel coefficient equations. Table 1.30 shows the indices of refraction found at 28 GHz and 38 GHz for the cement block studies in [31].

Table 1.30: Refractive indices of cement block studied in [31] at 28 GHz. The indices of refraction are found from the Fresnel coefficients using a non-linear least square method.

Material	**Frequency**	**Thickness**	**Refractive Index**
Cement Block	28 GHz	50 mm	2.2443 - j0.0597
Cement Block	38 GHz	50 mm	2.1848 - j0.0475

The imaginary part of the refractive index at 38 GHz was found to be 20.4% smaller (in absolute value) than the one for 28 GHz, indicating that the cement block is more lossy at 28 GHz than at 38 GHz.

1.5.2.4 Scattering Properties of Brick and Limestone at 28 GHz

An important difference between mmWaves (frequencies greater than 6 GHz) and traditional low-frequency radio-waves is that the former respond fundamentally differently to reflections from material surfaces. Traditional low-frequency radio-waves typically follow the law of reflection, which states that the impinging angle of incidence of the wave equals the outgoing angle after reflection, also called specular reflection. Low-frequency waves see rough surfaces as smooth because the corresponding wavelengths are much greater than the surface imperfection heights which are typically on the order of millimeters for a typical surface. However, higher-frequency waves (greater than 6 GHz) tend to react differently to reflections from building materials. For mmWaves, the specular reflection component remains, but more pronounced diffuse components will appear as well. The Law of Reflection accounts for the specular reflected component and the diffuse reflected components appear from the radiation impinging on surface imperfections on the order of the wavelength of propagation.

A study of the properties of reflected signals from brick and limestone walls was performed in which diffuse scattering was quantified and reflection coefficients were computed for various incident angles and TX and RX distances from the materials [32][33]. The brick dimensions were 7.6 cm x 20 cm, and the limestone dimensions were in between 15 cm x 20 cm and 30 cm x 61 cm. Using a sliding correlator channel sounder, a short 7.5 ns RF pulse centered at 28 GHz was illuminated onto a test material, and the reflected signal was captured and processed as a power delay profile. Diffuse scattering of brick and limestone materials was studied by determining the excess delay of the diffuse scattering component -15 dB down from the maximum peak of the power delay profile, that is, taken to represent the duration of the diffuse scattering. Dillard *et al.* also considered excess pulse duration at -3 dB and -10 dB from maximum peak, that is, the difference in durations between the received diffuse pulse width and the LOS received pulse width (via antenna sidelobes).

As the material tends to exhibit greater diffuse scattering, the excess delay will increase. Fig. 1.3 and

Fig. 3.4 display the excess delay durations (-15 dB down from maximum power peak) as a function of EM wave incident angle, for various T-R distances ranging between 3 m and 21 m, for brick and limestone.

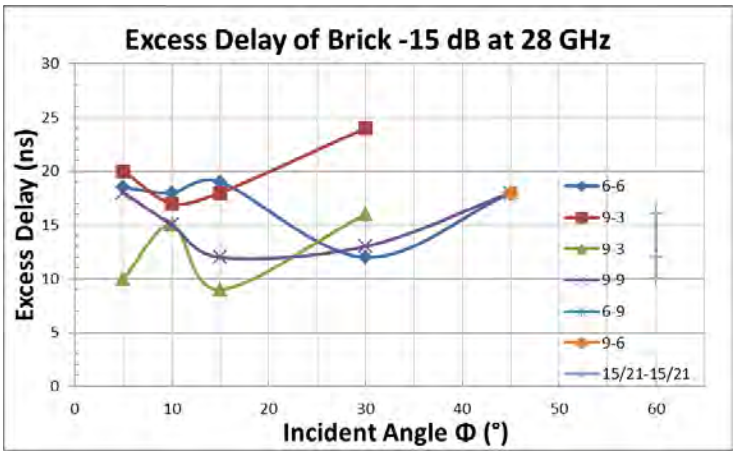

Figure 1.3: Diffuse scattering excess delay durations -15 dB down from maximum power delay profile peak for brick as a function of incident angle at 28 GHz. The legend lists the distances from TX and RX antennas to the measured materials dTx and dRx in meters from left to right, respectively [32].

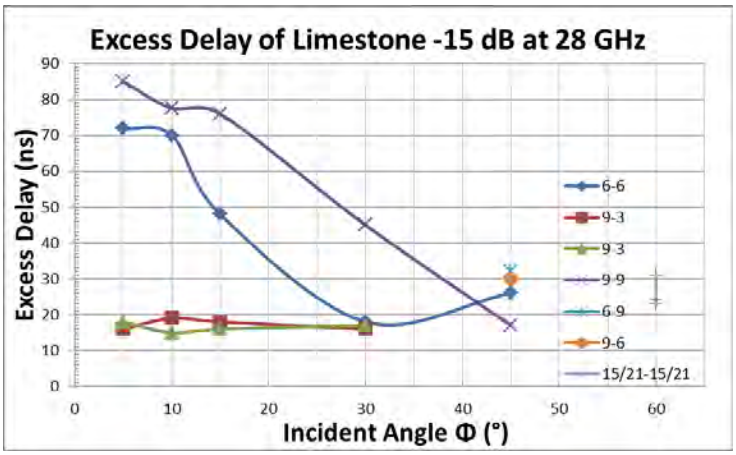

Figure 1.4: Diffuse scattering excess delay durations -15 dB down from maximum peak for limestone as a function of incident angle at 28 GHz. The legend lists the distances from TX and RX antennas to the measured materials dTx and dRx in meters from left to right, respectively [32].

The brick sample exhibited excess delays spread over at most 7 ns for a given dTx-dRx pair and all values ranged from 9 ns to 25 ns, indicating that brick excess delay is relatively independent of incident angle. This observation reflects the relatively small surface height imperfections of brick.

The limestone sample exhibited a radically different behavior than the brick sample. For equal dTx and dRx (i.e., dTx-dRx = 6-6, and dTx-dRx = 9-9), the excess delay is strongly negatively correlated with

incident angle, going from approximately 80 ns at $\Phi = 5^\circ$ down to 20 ns at $\Phi = 45^\circ$. For unequal dTx and dRx, the excess delay durations are relatively constant over incident angles between 5° and 60°, and ranging from 17 ns to 30 ns. This observation reflects large surface height imperfections of limestone.

Dillard *et al.* reports an average excess delay (averaged over all angles and all dTx-dRx distance pairs) of 15.7 ns and 34.7 ns for the brick and limestone samples, respectively. Limestone exhibits diffuse scattering that lasts twice as long as brick on average. The study does not quantify diffuse component power levels. However, the provided power delay profile waveforms suggest that the brick diffuse power component is much weaker than the specular component (at least 15 dB weaker), whereas the limestone diffuse power component contains several multipath component peaks 5 dB to 12 dB down from the specular component. This observation suggests that brick exhibits short and weak diffuse scattering, whereas limestone exhibits longer and stronger diffuse scattering.

1.6 V - Band: 40 - 75 GHz

The V - Band has been mainly studied for the 41 - 43 GHz and 57 - 66 GHz bands, the former for the performance of communication systems called multimedia wireless systems (MWS), and the latter for wireless broadband communication systems. This section describes measurement campaigns pertaining to these bands. The 60 GHz band has become available in different countries, motivating the research community and industry to understand the propagation mechanisms as the standardization of wireless systems throughout the world becomes possible. The 57 - 66 GHz band was allocated in Europe by the European Conference of Postal and Telecommunications Administration (ECPTA), the 57 - 64 GHz band was made available in the United States, Canada and Korea, the 59 - 66 GHz band was made available in Japan, and the 59 - 63 GHz band was made available in Australia. The great overlap in frequency band is motivating research and industry to understand the propagation mechanisms at 60 GHz allowing for the global standardization of wireless devices.

1.6.1 Channel Characterization

1.6.1.1 Propagation Characteristics in the V - Band

A number of measurement campaigns have studied the 60 GHz band [4][19][22][34][35][36][37][38][39][40][41][42]. Wideband propagation measurements were conducted to study path loss characteristics of the 60 GHz channel in an outdoor to indoor fashion, with the TX located on a one-way 120 m by 10 m road on a campus environment, surrounded by 3 to 7 storey high buildings, and the RX housed in a building and placed on the ground, first and second floors. Measurements were performed with the TX behind buildings, in a static (i.e., stationary) and time-varying (i.e., moving cars) environment. The building housing the RX had windows, and as such a LOS condition between TX and RX could be established. The TX was a hand-held horizontally polarized 6 dBi gain horn antenna, placed between 20 - 100 m away from the RX [34].

The path loss exponents found were 1.4, 2.3, and 2.1 when the RX was placed on the second, first and ground floors, respectively. It was discovered that a stationary and moving car reduces received power levels by 3 dB and 10 dB, respectively. The pedestrian-induced attenuation was 7 dB. Overall, the standard deviation of received power levels was between 3.4 - 5.7 dB with a 2 dB variation. In a NLOS condition, the received signal level was attenuated by 20 dB to below noise floor when the TX was placed behind a brick building blocking the RX. Fades in excess of 15 dB and 20 dB occurred for 20% and 1% of the collected data, respectively. Hawkins *et al.* concluded that 6 to 7 dBm of power with a 5 dB safety margin is enough to cover a 100 m street cell where a single co-channel interferer (i.e., cars, pedestrians) is expected.

A wideband 55 GHz propagation measurement campaign was performed to investigate the usable bandwidth in a heavily built-up urban multipath environment. The RX was placed on the rooftop of a moving car, and signal was acquired for different vehicle speeds using a sensor attached to a speedometer. The TX and RX antennas provided 25 dBi (10° beamwidth) and 6 dBi (120° beamwidth) gain. The lowest detectable RF signal was -100 dBm, which corresponded to a fading loss of 36.3 dB. The coherent bandwidth was estimated to be 25 MHz for T-R distances of 50 - 300 m [35].

A 59.9 GHz propagation measurement campaign was performed to study a corridor, a laboratory and an office environment inside a brick and reinforced concrete three-storey building to recover received signal

envelope distributions in a LOS and NLOS configuration with stationary RX and moving TX [40]. The TX and RX antennas used were omnidirectional in the azimuth and had a 7 dBi gain in the elevation plane. Edge-diffraction measurements were conducted with a standard 20 dBi gain aerial horn (18°) at the RX, and a 37 dBi (2.4°) lens-horn at the TX. The path loss exponents measured were 1.32, 1.2 and 1.7 for the lab, and 2.17 for the office. The received signal levels were observed to follow a Rician and Rayleigh distribution in the LOS and NLOS conditions, respectively. Penetration measurements yielded a 7 dB and 27 dB loss through a wooden door (4 cm) and plaster-covered concrete wall (40 cm), respectively. Diffraction measurements conducted over an aluminum sheet yielded a loss of 22 dB at a diffracted angle of 11°. The diffraction loss over a metal covered wall was too great to be observed as reflected multipath waves dominated the received signal at a diffracted angle of 3°. Tharek *et al.* conclude that attaching a radio transmitter near the middle of a room ceiling will improve the signal strength behind obstructions. The screening effect of concrete suggests that one radio transmitter will be required for every room. Chipwood walls attenuated signals by 7 dB and thus allowed signal to get through to enhance cell coverage.

A wideband 60.4 GHz measurement campaign was conducted to characterize the fading characteristics and the effectiveness of a selection frequency diversity scheme of a portable radio link in a long narrow corridor and an empty square room to recover power delay profiles and distributions of fading envelope [36][41]. The RX remained stationary while the TX was moving at a nearly constant speed of 0.2 m/s. The TX and RX antennas were omnidirectional in the azimuth plane, and had a net 8.5 dBi gain in the elevation (8° beamwidth). The majority of received power was concentrated in lower frequency components, and reflected components (high frequencies) arrived with relatively low power levels. The received power level distribution did not quite follow a Rayleigh distribution because of the small number of multipath components induced in the corridor and room. In a confined environment with small time delays such as the corridor and room studied, there was a 3.2 to 12 dB link budget improvement with a 5 to 15 MHz spacing in frequency selection combining at 99.9% reliability [36][41].

A wideband (200 MHz) 59 GHz outdoor measurement campaign was conducted to characterize the microcellular city street environment, with 4 to 7 storey high buildings made of concrete and steel [43]. The

TX remained stationary while the RX moved towards the TX for T-R distances of 5 - 200 m. The transmit and receive antennas used were a 90° horn and an omnidirectional biconical horn with vertical half-power beamwidth of 20°, respectively. There was always a LOS path between TX and RX, with an occasional line of leafless trees obstructing the LOS path. The measured RMS delay spreads remained consistently below 20 ns in 90% of measurements. Wideband and narrowband received power typically incurred 3 - 6 dB and 15 - 20 dB fades, respectively. The city street was found to be relatively free of multipath fading when the TX was pointed at the RX, but the multipath-fading effect became severe when the antennas were off-boresight [43].

A wideband 60 GHz (960 MHz) indoor measurement campaign investigated the indoor LOS environment for channel modeling purposes [44]. A channel model was developed to predict channel impulse responses based on a set of measurements performed inside a library. It was found that 10 dB fades in the LOS received component occurred when the TX was not pointed at the RX. Reflected multipath components were 30 dB below the LOS peak. Multipath power contributions were found to follow a Gaussian distribution with an exponential amplitude decay and Poisson-distributed inter-arrival times. The Saleh and Valenzuela one-cluster model was used to model and predict channel impulse responses in this environment.

A 60 GHz narrowband measurement campaign was conducted to characterize an indoor corridor and big college room, as well as an outdoor parking lot LOS communication channel to study the effects of receiver location on frequency fading, in order to determine radio-coverage and data-rate limitations [45]. The frequency of propagation was swept over 100 MHz in bandwidth and frequency profiles were recorded as the RX moved towards the TX. The TX remained fixed for T-R distances less than 50 m. The K-factors and path loss exponents ranged from 16 - 423 and 0.78 - 2.54, respectively. Table 3.1 below shows the K-factors and path loss exponents measured in the different types of environments investigated.

Table 1.31: Summary of K-factors and corresponding standard deviations, path loss exponents and mean attenuations found in several environments at 60 GHz as measured in [45].

Environment	**Antenna Type**	**K-Factor [dB]**	σ_k **[dB]**	**PLE**	**Attenuation (dB)**
Corridor	Directional	169	101	1.88	-74.05
	Omni.	16.79	19.38	1.87	-59.65
College Room	TX up	28.36	29.04	0.78	-102.23
	TX down	56.61	78.11	1.27	-81.92
Grassfield	Omni.	84.25	87.94	1.9	-72.21
Parking	Omni.	80.71	79.89	2.1	-71.8
	Directional	423.85	165.35	2.54	-48.03

A 62.4 GHz wideband propagation measurement was performed to estimate the instantaneous coherence bandwidth as a function of T-R separation distance in a corridor and room of a university building [46][47]. The TX was mounted on a box and left stationary while the RX was displaced at different locations along the center line of the corridor for T-R distances ranging from 5 - 40 m. The transmit and receive antennas had 10 dBi and 6 dBi gains, respectively. The 90^{th} percentile coherence bandwidths at 0.9 correlation coefficient level with respect to the 1.5 m probe curve were 38 MHz and 72 MHz for the corridor and the room, respectively. The coherence bandwidth was observed to vary significantly between 1.1 MHz and 84.5 MHz for T-R separation distances of 2 to 40 m in the corridor reflecting multipath interference. Table 3.2 shows a summary of measured coherence bandwidth in the corridor and the room.

Table 1.32: Minimum, maximum, mean, standard deviation (MHz) and 90^{th} percentile of the coherence bandwidths at 0.9 correlation level in a corridor and room as measured in [46][47].

Environment	**Setup**	**Minimum**	**Maximum**	**Mean**	σ	**90%**
Corridor	Horn-horn	1.3	84.5	14.1	16	38
	Horn-omni	1.1	103.5	11.5	16.4	31.5
Room	With Furniture	5.8	75.6	31.3	21.5	62.8
	Empty	6.8	82.6	23.3	23.3	72

A wideband (200 MHz RF bandwidth) 61 GHz propagation measurement campaign was performed to characterize the dispersion and fading effects of a corridor and hall in LOS and NLOS conditions using highly directional (22.7 dBi gain) and omni-directional (5 dBi gain) horn antennas [48][49]. The RMS delay spread was found to follow a Lognormal distribution in all three environments, ranging from 2.8 ns to 81 ns

in the corridor, and from 4.2 ns to 38 ns in the LOS hall environment. The median RMS delay spreads were found to be 15.8 ns, 16.1 ns and 21.7 ns in the corridor (LOS) and hall (LOS and NLOS), respectively. Table 3.3 below summarizes the RMS delay spreads for the 10^{th}, 50^{th} and 90^{th} percentile. The path loss exponents were found to be 1.64, 2.17, and 3.01 in the corridor, LOS hall and NLOS hall, respectively. Table 3.4 below summarizes the results.

Table 1.33: The 10^{th}, 50^{th}, and 90^{th} percentile delay spreads measured in a corridor and a hall [48][49].

RMS Delay Spreads	$\sigma_{10\%}$	$\sigma_{90\%}$	$\sigma_{50\%}$
Corridor	2.8	80.5	15.8
LOS Hall	4.2	37.8	16.1
NLOS Hall	10.8	38.2	21.7

Table 1.34: Path loss exponents and standard deviations with respect to a 1 m free space reference measured in a corridor and hall [48].

Environment	**PL in free space at 1 m (dB)**	**PLE**	σ **(dB)**
Corridor	68	1.64	2.53
LOS Hall	68	2.17	0.88
NLOS Hall	68	3.01	1.55

The number of paths in the LOS hall was found to be Poisson-distributed with an average number of paths equal to 3.5, and a maximum number of paths equal to 17 paths. In the case of the corridor, the number of paths followed a combination of a Poisson and exponential distributions, with an average number of paths equal to 2.2, and a maximum number of paths equal to 13.

The direct LOS path and the first-order reflected components from smooth surfaces formed the main contributions of received power in the corridor, while diffracted components were found to be significant contributors to the total received power in the NLOS hall environment. A linear relationship with a correlation coefficient of nearly 1 was found between the RMS delay spread and the number of paths measured, and an exponential relationship between the worst RMS delay spread as a function of large scale path loss (See Section 1.6.1.5).

A wideband (1 GHz RF bandwidth) 61 GHz propagation measurement campaign was performed in an aircraft passenger cabin in both LOS and NLOS environments to characterize the dispersive nature of an

indoor in-vehicular wireless channel [50]. A total of 17 RX locations in both LOS, obstructed and NLOS conditions were measured for a fixed TX location with T-R distances ranging from 1.43 - 6.15 m. The effects of small-scale fading and human blockage were investigated using vertically polarized omnidirectional transmit and receive antennas of 5 dBi and 2 dBi gains, respectively. The path loss exponent with respect to a 1 m free space reference distance was found to be 1.65 with a standard deviation of 1.76. The average RMS delay spreads ranged from 3.4 - 12.5 ns and 5.9 - 16.8 ns for the LOS and NLOS conditions, respectively. The maximum RMS delay spread observed was 24 ns. Human blockage was found to cause a 16.4 dB fade on the received LOS component with insignificant effect on NLOS components. Finally, the coherent bandwidth was measured to be 4.4 MHz.

A wideband (800 MHz bandwidth) 70 GHz propagation measurement campaign was performed in a conference room and cubicle in a modern office environment to investigate the channel characteristics for wireless local area network deployment [51]. The TX and RX antennas used were 18 dBi 20° half-power beamwidth directional antennas placed 1 m above floor level, and both antennas were rotated in 10° increments in the azimuth and elevation planes to detect multipath components arriving from all possible incoming directions. First- and second-order clusters were found to have a -10 dB reflection loss (with standard deviation of 4 dB), and a -16 dB reflection loss (with standard deviation of 5 dB), respectively, in the conference room. Cross-polarization attenuation was found to lie in the range 10 - 20 dB for first- and second-order reflected waves. A time-domain cluster model was created based on the measurements obtained (See Section 1.6.1.5). Finally, 2 to 3 clusters were observed in the cubicle environment.

A number of propagation campaigns in the 60 - 66 GHz band have been summarized in [52] and provide path loss exponents in different types of outdoor environment. Table 3.5 below summarizes the results. Additional measurements in the 73 GHz band were conducted in Manhattan, New York to investigate the propagation characateristics and outage probabilities of dense urban environments for wideband signals spanning 800 MHz null-to-null RF bandwidth, and more details can be found in the following references [53][54][55]. The above measurement campaigns are summarized in Table 1.36.

Table 1.35: A summary of the path loss exponents measured in various outdoor environments as reported in [52]. The stars in the PLE column indicate that the values for the path loss exponents were estimated from the provided figure in the corresponding reference.

Scenario	**Ant. Gain (dBi)**		**Ant. Gain (dBi)**		**Dist. (m)**	**PLE**
	TX	**RX**	**TX**	**RX**		
Open Area (Grass) [40]	20	6	1.5	1.5	200	2.23
Open Area (Asphalt) [56]	17	15	5	1.5	200	2.0*
Open Area [57]	-	-	-	-	-	2.2*
Urban Street [56]	17	15	5	1.5	120	2.2*
Campus Street [34]	6	20	1.5	2 / 5.5	120	2.1 / 2.3
Tunnel [56]	17	15	1.5	1.5	200	2.5*

Table 1.36: Summary of measurement campaigns studying the 60 GHz band.

Measurements	**Frequency**	**T-R Dist.**	**BW**	**Antennas**	**Results**
Propagation measurements to study path loss from outdoor (TX) urban and rural areas to indoors (RX) [34].	60 GHz	20-100 m	Wideband 100 MHz	Wide	Path loss exponents: n = 1.4, 2.3, and 2.1 when RX is placed on 2nd, 1st and ground floors respectively; Stationary and moving cars reduced RX signal levels by 3 dB and 10 dB respectively. Signal attenuation due to blocking pedestrians was 7 dB; Fades in excess of 15 dB and 20 dB occurred 20% and 1% of the time, respectively.
Investigate usable bandwidth in heavily built-up outside urban microcell area [35].	55 GHz	50-300 m	Wideband 320 MHz	Wide	Coherence bandwidth of 25 MHz.

Measurements	Frequency	T-R Dist.	BW	Antennas	Results
Propagation and BER measurements within corridors, laboratory and office environments [40].	59.9 GHz	Not Stated	Not Stated	Omni; Wide; Narrow	Path loss exponents: $n = 1.32$ and 1.2 in corridors; $n = 1.7$ in lab, $n = 2.17$ in office; Penetration losses through wooden door (4 cm thick) and plaster-covered concrete wall (40 cm thick) were 7 dB and 27 dB, respectively; Diffraction losses over aluminum sheet was -22 dB for 11° diffracted angle.
Study point-to-point transmission at street level in urban environment [4].	57.6 GHz	0.9 km	5 kHz	Narrow; Wide	Reflected signals are strong; Multipath from street surfaces produce fades > 30 dB; Multipath reflections from building walls and other reflecting surfaces have amplitudes of 15 dB below LOS component; No dependence on polarization in RX power levels.
Investigate fading characteristics of radio link in corridor and square room [41].	60.4 GHz	10-30 m	Not Stated	Wide	Small number of multipath components observed, resulting in distribution of RX signal levels not being Rayleigh; Power in the fading envelope is concentrated at lower frequencies; Reflected components are present at relatively low power levels (compared to LOS component).
Investigate effectiveness of frequency selection diversity scheme in corridor and square room [36].	60 GHz	5-20 m	Wideband 115 MHz IF	Omni; Wide	Small time delays observed (unquantified); Frequency selection improvement of 3.2 - 12 dB with 5 - 15 MHz spacing in selection combining at 99.9% reliability.

Measurements	Frequency	T-R Dist.	BW	Antennas	Results
Characterizing indoor radio propagation in corridor, medium and large-sized lab [37].	60 GHz	5-30 m	Wideband 200 MHz RF	Narrow; Semi-Omni; Omni	Path loss exponent in corridor is visually approximated as 2 (from received power over distance); RMS delay spreads ranging from 10 - 40 ns; Small to no dependence on wave polarization; Number of multipath components and received power levels follow Poisson and Exponential distributions in corridor(LOS), respectively.
Characterize indoor radio-wave propagation in single room, corridor and hall [38].	58 GHz	2-10 m	Wideband 2 GHz RF	Omni	Path loss exponent reported as 0.5 (LOS conditions, and high antenna elevation gain); RMS delay spreads ranging from 13 - 98 ns.
Characterize dispersive nature of urban outdoor area in presence of moving traffic [42].	55 GHz	0-400 m	Wideband	Narrow	Path loss exponent: • n = 2 in LOS conditions • n = 3.6 in obstructed NLOS • n = 10 behind base station Reflection and scattering dominates over diffraction; Coherence bandwidth ranging from 20 - 150 MHz.
Characterize indoor radio propagation in room and corridor [7].	60 GHz	1-10 m	Wideband 2 GHz RF	Not Stated	Largest observed multipath at 240 ns excess time delay; Graphs of received power levels given.

Measurements	Frequency	T-R Dist.	BW	Antennas	Results
Study the peer-to-peer and vehicular communication channels in urban campus environment [19][22].	60 GHz	15-120 m	Wideband 1.5 GHz RF	Narrow	Peer-to-peer: 31% of links completed with extreme off-boresight TX and RX antenna combinations; 1 to 2 completed links; Vehicular: 3 to 5 completed links for a given T-R location. NLOS link path losses ranged from 15 - 40 dB in excess loss; RMS delay spreads ranged from 1 - 36.6 ns; Path loss exponents P2P/V: • LOS: 2.25/ 2.66 • NLOS All: 4.22/7.17 • NLOS-Best: 3.76/ - Max RMS delay spreads P2P/V(ns): • LOS: 0.9/0.9 • NLOS All: 36.6/- • All: 36.6/12.3 DS [ns] = 0.27*EPL [dB]
Study the city street multipath environment, with 4 - 7 storey concrete and steel buildings [43].	59 GHz	5-200 m	Narrowband Wideband 200 MHz	Omni; Biconical	RMS delay spreads less than 20 ns in 90% of measurements; Wideband and narrowband measurements show typical fades of 3 - 6 dB and 15 - 20 dB, respectively; Tree induces 8 - 12 dB fade; Not a severe multipath environment when TX is pointed at RX.
Study and estimate library channel impulse responses based on measurements [44].	60 GHz	2-5 m	Wideband 920 MHz	Dielectric Lens; Narrow	10 dB fades observed in LOS component if TX does not point towards RX; Reflected multipath components are 30 dB below LOS component; Multipath contributions show Gaussian behavior with exponential decay and Poisson-distributed inter-arrival times; Saleh-Valenzuela model fits the measurement well.

Measurements	Frequency	T-R Dist.	BW	Antennas	Results
Characterize the indoor corridor and large room, and outdoor parking lot communication channels, determine radio-coverage and data-rate limitations [45].	60 GHz	5-50 m	Narrowband CW	Omni; Narrow	Average K-factor ranges from 16 - 169 and 80 - 423 in indoor and outdoor environment, respectively; PLE ranges from 0.78 - 1.88 and 1.9 - 2.54 in indoor and outdoor environment, respectively.
Estimate the coherence bandwidth for indoor corridor and room environment [46][47].	62.4 GHz	5-40 m	Wideband	Omni Wide	90^{th} percentile of the coherence bandwidth at 0.9 correlation coefficient (w.r.t. reference curve) was below 38 MHz and 72 MHz for the corridor and room respectively; Coherence bandwidth varies significantly over distance between 1.1 MHz and 84.5 MHz in the corridor reflecting multipath interference at RX; Lowest-value coherence bandwidth for design is 5 MHz.

Measurements	Frequency	T-R Dist.	BW	Antennas	Results
Characterize dispersion and fading effects on a corridor and hall communication channel [48] [49].	61 GHz	2-50 m	Wideband 200 MHz RF	Omni; Wide	For corridor (LOS), hall (LOS and NLOS), respectively: PLE: 1.64, 2/1.7 and 3.0; 90^{th} percentile RMS delay spread: 80.5 ns, 37.8 ns and 38.2 ns; Average/Maximum number of paths: 2.2/13, 3.5/17, not stated; Received power comes mainly from LOS component and first-order reflected waves in LOS. Diffraction is found to be important in NLOS indoor environment; Linear relationship between RMS delay spread and number of paths: Corridor (LOS): RMS DS [ns] = 14.5*#of paths - 12.4 (correlation coeff. = 0.93); Hall (LOS): RMS DS [ns] = 6.03*# of paths - 6.9 (correlation coeff. = 0.95); Worst RMS delay spread model: RMS DS [ns]= $e^{0.055*PL} - 100$, PL > 84 dB
Characterize the dispersive nature of in-vehicular wireless channel [50].	61 GHz	1.4-6.2 m	Wideband 1 GHz	Omni	PLE of 1.65 with respect to 1 m FS reference distance, standard deviation of 1.76 dB; Human blockage caused 16.4 dB on LOS component, but not much effect on NLOS components; Average RMS delay spread ranges from 3.4 - 12.5 ns and 5.9 - 16.8 ns in LOS and NLOS respectively. Max RMS delay spread of 24 ns; Coherent bandwidth below 4.4 MHz (frequency flat channel).

Measurements	Frequency	T-R Dist.	BW	Antennas	Results
Characterize a typical conference room and cubicle in a modern indoor office environment [51].	60 GHz	Not Stated	Wideband 800 MHz	Narrow	Conference room: First- and second-order reflected clusters have 10 dB and 16 dB reflection loss respectively; Cross-polarization attenuation of LOS and NLOS components is 10 - 20 dB; Cubicle: 2-3 essential clusters at each RX location.
Characterize in-building office propagation [58].	60 GHz	3.5 - 27.4 m	Wideband 800 MHz	Narrow	Path loss exponent $n = 2.1$ and $\sigma = 7.9$ dB.

1.6.1.2 Diffraction in the V - Band

Alejos *et al.* report a diffraction model based on a diffraction measurement campaign at 42 GHz around brick corners using standard gain pyramidal horn antennas and a vector network analyzer [59]. Table 1.37 summarizes the diffraction model obtained.

Table 1.37: Diffraction model at 42 GHz for brick corners [59].

Reference	Diffraction Angle (°)	Diffraction Loss [dB]
[59]	$10° \leq \theta \leq 30°$	$-1.51 \times \theta - 61.33$
	$40° \leq \theta \leq 60°$	$-1.64 \times \theta - 67.55$

1.6.1.3 Effects of Vegetation in the V - Band

Two measurement campaigns have investigated the radio-wave foliated channel characteristics in the 60 GHz band [5][27]. For a campaign description, refer to Sections 1.2.1.1 and 1.2.1.2.

Table 1.38: Summary of campaigns studying the effects of vegetation on RF signal propagation in the 60 GHz band.

Measurements	**Frequency**	**T-R Dist.**	**BW**	**Antennas**	**Results**
Study range dependence, depolarization and frequency dependence in foliated environments [5].	9.6 GHz 28.8 GHz 57.6 GHz	0.1 - 0.9 km	Narrowband CW Source	Narrow	12 - 20 dB/tree attenuation for distances < 30 m; 0.5 - 0.7 dB/tree attenuation for distances > 30 m; Flat received signal in azimuth at depth of 8 - 11 trees; No dependence on linear co-polarization.
Characterize the radio-wave foliated channel through deciduous tree (with and without leaves) and coniferous tree with leaves [32].	29 GHz 60 GHz	64 - 110 m; Foliage thickness: 7-25 m	Narrowband CW Source	Not Stated	RF power received depends on wind speeds, reduced speeds induce greater attenuations; 29 GHz and 60 GHz foliage channels are similar in their fading statistics; Mean attenuation for tree with leaves and without leaves is 16 - 33 dB and 5 - 9 dB, respectively; RX power can be modelled with Extreme Value or Log-normal distributions; Duration of fades can be modelled with Log-Exponential distribution.

1.6.1.4 Effects of Polarization in the V - Band

The effects of polarization on a mmWave multipath-fading environment are not well known. Two measurement campaigns investigated the polarization dependence on a multipath fading environment in an indoor empty conference room in a modern office building using linearly (vertical and horizontal) and circularly polarized antennas, as well as the effects of radiation patterns in the 60 GHz band [60][61]. The TX and RX were placed in the same room while the RX antenna swept the azimuth plane in 5° increments and recorded a power delay profile for each polarization type. The measurements were taken with the TX and RX having the same type of antenna. The TX and RX used a widebeam and narrowbeam scalar horn antenna

with 60° and 4.6° 3 dB beamwidth respectively, each manually switchable between vertical, horizontal and right-handed circular polarizations. The cross-polarization isolation ratio was better than 17 dB. Both the TX and RX were placed 1.46 m above the ground floor. Power delay profiles were also obtained using four different antennas: an omnidirectional antenna, widebeam, medium-sized beam, narrowbeam antennas with 60°, 10° and 5° half-power beamwidth.

Table 1.39: Summary of campaigns investigating the effects of polarization on RF propagation in the 60 GHz band.

Measurements	**Frequency**	**T-R Dist.**	**BW**	**Antennas**	**Results**
Study a modern empty office indoor multipath environment for different antenna beamwidths and polarizations [61][60].	60 GHz	10 - 15 m	Not Stated	Narrow Wide	RMS delay spreads: VV and HH: ranging from 9.9 - 11.1 ns; Circular Polarization: ranging from 4.6 - 5.7 ns; First-order reflected waves are significantly reduced in amplitude when using circularly polarized antennas; RMS delay spreads using different antenna beamwidths: - Omni: 18.08 ns - Widebeam: 13.59 ns - Medium: 4.7 ns - Narrowbeam: 1.05 ns

The horizontal (HH), vertical (VV) and circular (RR) polarization PDPs showed very similar multipath-dependence in time delay but the power amplitudes diverged significantly between linear and circular polarizations. The RMS delay spreads ranged from 9.9 - 11.1 ns and 4.6 - 5.7 ns for linearly and circularly polarized antennas respectively, indicating that the circularly polarized antenna did not pick up later arriving multipath as efficiently as the linearly polarized antennas. Manabe *et al.* explain this phenomenon by noting that a right-handed polarized wave reflecting off a surface will reverse its polarization direction and therefore get rejected by the receive antenna. The receive antenna thus completely rejected first-order reflected waves. Higher-order reflected waves lost a significant amount of power from reflections and hence did not contribute a significant amount to the LOS component. Multipath-delayed waves are then effectively suppressed by

a factor of 2 when using circularly polarized antennas, allowing for a doubling of the intended transmitted signal bandwidth in indoor environments. The RMS delay spreads observed were 18.08 ns, 13.59 ns, 4.7 ns and 1.05 ns for the omni, widebeam, medium-sized beam and narrowbeam antennas respectively. Table 1.39 summarizes the campaign parameters and results found.

1.6.1.5 60 GHz Channel Models

1.6.1.5.1 Geng *et al.* Indoor Channel Models

A wideband (200 MHz RF bandwidth) 61 GHz propagation measurement campaign was performed to characterize the dispersion and fading effects of a corridor and hall in LOS and NLOS conditions using highly directional (22.7 dBi gain) and omnidirectional (5 dBi gain) horn antennas [48][49]. From the measurements obtained, RMS delay spread models as a function of the number of multipath components and large scale path loss were developed, where the number of paths and the path loss exponents for the LOS corridor and hall are given in Table 1.40. The number of paths can be generated with a Poisson distribution and a combination of Poisson-Exponential distributions with means of 3.5 and 2.2 for the LOS corridor and hall environments respectively, and the large scale path loss can be determined with the path loss exponents and the standard deviations from Table 1.40.

Table 1.40: Statistical distributions for the number of paths and path loss exponents measured in a LOS corridor and hall [49].

	# of Paths			**Path Loss Parameters**	
	Mean	Max	Distribution	PLE	σ (dB)
LOS Corridor	3.5	17	Poisson	1.64	2.53
LOS Hall	2.2	13	Poisson/Exponential	2.17	0.88
NLOS Hall	-			3.01	1.55

Once the number of paths and path loss has been determined, the RMS delay spread is computed from the channel models shown in Table 4.1.

Table 1.41: RMS delay spreads channel models as a function of the number of paths and the path loss for a LOS corridor and hall [49].

Channel Model	**LOS Corridor**	**LOS Hall**
RMS Delay Spread	*RMS DS [ns] = 6.03 × # of paths - 6.9*	*RMS DS [ns] = 14.5 × # of paths - 12.4*
	(worst) *RMS DS [ns]* = $\exp(0.055 \times PL[dB])$ *- 100, PL > 84 dB*	

1.6.1.5.2 Maltsev *et al.* Indoor Channel Models

A wideband (800 MHz bandwidth) 70 GHz propagation measurement campaign was performed in a conference room and cubicle in a modern office environment to investigate the channel characteristics for wireless local area network deployment [51]. From the measurements obtained, a time-domain cluster model for reflected clusters was developed to reproduce the impulse response observed in a LOS conference room configuration. A cluster is characterized by its intra-cluster parameters, such as the number of rays contained within the cluster, the power decay time, the arrival rate and amplitude distribution of rays. Cluster were observed to have a central ray with maximum amplitude, which is proceeded by two pre-cursor rays and followed by four post-cursor rays, whose amplitudes are Rayleigh-distributed. These are summarized in Table 1.42.

Table 1.42: Intra-cluster parameters for a conference room channel impulse response in a LOS environment as measured in [51].

Parameter	**Pre-cursor Rays**	**Post-cursor Rays**
Ray K-Factor	5 dB	10 dB
Power Decay Time	1.3 ns	2.8 ns
Arrival Rate	0.2 ns^{-1}	0.12 ns^{-1}
Amplitude Distribution	Rayleigh	Rayleigh
Number of Rays	2	4

1.6.1.5.3 Smulders *et al.* Indoor Channel Models

The 60 GHz band indoor radio channel impulse model was developed based on propagation measurements obtained at 58 GHz in a room, corridor and hall [38][62]. The rays are modeled as a discrete uncorrelated scattering process. The impulse response is modeled as a summation of arriving multipath as follows:

$$h(t) = \sum_{n} \beta_n e^{j\theta_n} \delta(t - \tau_n) \tag{1.12}$$

where β_n, τ_n and θ_n are the real ray amplitude, propagation delay and phase of ray n, respectively. These quantities are time-variant as the channel is constantly varying due to motion of people and objects in the environment. However, Smulders *et al.* note that the relatively low speed of motion does not significantly change over many bit periods. It is thus appropriate to assume a quasi-static channel.

The ray amplitudes β_n are modeled with the Rayleigh-distribution continuous time function $\beta(t)$ as follows:

$$f(\beta(t)) = \frac{2\beta(t)}{\overline{\beta^2}(t)} e^{-\frac{\beta(t)}{\overline{\beta^2}(t)}} \tag{1.13}$$

$$\overline{\beta^2}(t) = \frac{1}{K} \sum_{k=1}^{K} \frac{|h_k(t)|^2}{G_k} \tag{1.14}$$

$$G_k = \sum_{n=1}^{N} \beta_{kn}^2 \tag{1.15}$$

where $t = 0, 0.5, 1, ...,$ ns, K is the total number of impulse responses, and N is the total number of multipath components in the k^{th} impulse response.

In order to generate the β_n, $\overline{\beta^2}(t)$ is estimated as follows:

$$10 \times \log_{10}(\overline{\beta^2}(t)) = \begin{cases} 10 \times \log_{10}(\overline{\beta^2}(t_1)), & \text{if } t \leq t_1 \\ 10 \times \log_{10}(\overline{\beta^2}(t_1)) + A \times (t - t_1), & \text{otherwise} \end{cases}$$

where $t_1 = 50$ ns is the excess delay over which the average power delay profile is approximately constant, and varies for each environment considered. The parameter A is estimated to lie between -0.06 dB/ns and -0.3 dB/ns using the minimum mean square error criterion. The average amplitude of the first arriving

multipath can be approximated using the Friis Free Space Transmission equation as follows:

$$\overline{\beta^2}(t=0) = G_r G_t \left(\frac{\lambda}{4\pi r}\right)^2 \tag{1.16}$$

where G_r and G_t are the receive and transmit antenna gains respectively, λ (m) is the wavelength and r (m) is the T-R separation distance. The value of $\overline{\beta^2}(t_1)$ can be taken to be equal to $\overline{\beta^2}(0)$ if the multipath components are expected to reflect off of metallic objects, and 5 - 15 dB below $\overline{\beta^2}(0)$ if the multipath components are expected to reflect off of boundaries with significant reflection loss like wooden walls. It is be noted that the LOS component can be completely omitted in an obstructed environment.

The excess time delays are modeled a as Poisson distribution with mean arrival rate of λ ranging from 0.93 ns to 1.96 ns, and a mean inter-arrival rate $\Delta\tau$ ranging from 0.7 ns to 1.0 ns.

1.6.1.6 Oxygen Absorption and Rain Attenuation Channel Models

The CCIR provides a mathematical expression for the oxygen absorption γ_0 and rain attenuation γ_r in the 60 - 66 GHz frequency band [63][64].

The oxygen absorption is expressed in dB/km and has the following form:

$$\gamma_0[dB/km] = \begin{cases} 15.10 - 0.104(f-60)^{3.26}, & \text{if } 60 \le f < 63 \\ 11.35 + (f-63)^{2.25} - (f-63)^{1.27}, & \text{if } 63 \le f \le 66 \end{cases}$$

where f is the frequency in GHz.

The rain attenuation (dB/km) has the following form:

$$\gamma_r[dB/km] = k(f) \times R^{a(f)} \tag{1.17}$$

$$k(f) = \begin{cases} 10^{1.296 \times \log_{10}(f) - 2.497}, & \text{VP} \\ 10^{1.204 \times \log_{10}(f) - 2.290}, & \text{VH} \end{cases}$$

$$a(f) = \begin{cases} 10^{1.647-0.463\times\log_{10}(f)}, & \text{VP} \\ 10^{1.703-0.463\times\log_{10}(f)}, & \text{VH} \end{cases}$$

where f is the frequency in GHz, and R is the rainfall rate in mm/hr.

1.6.2 Material Properties in the V - Band

1.6.2.1 Penetration Measurements

A number of penetration measurement campaigns have been performed at 42 GHz and in the 60 GHz band, specifically between 57 GHz and 66 GHz [4][59][65][66][67][68]. The following tables show the penetration coefficients measured in the V - band.

Table 1.43: Penetration losses through common materials at 42 GHz for horizontally and vertically polarized EM wave [59].

Reference	**Material**	**Thickness (cm)**	**Penetration Loss [dB] at 42 GHz**	
			H-Pol	**V-Pol**
[59]	Chipwood	16	-7.9	-8.6
	Glass	4	-3.2	-2.5
	Wood	7	-2.6	-3.5
	Plasterboard	15	-2.7	-2.9
	Mortar	100	-160	-159.3
	Brick Wall	100	-177.9	-195
	Concrete	100	-175	-178

Table 1.44: Penetration losses through common building structures common to an urban city. For additional penetration losses, refer to Section III.B in [4].

Reference	**Material**	**Path Length (m)**	**Penetration Loss [dB] at 57.6 GHz**
[4]	Solid Cement	42	> 94
		53	53
	Solid Pre-Cast Concrete	200	> 80
		260	76
	Brick with Windows	120	79
	Chromatic Glass	72	64

Table 1.45: Penetration losses through various materials in the 60 GHz band.

Reference	**Material**	**Thickness (cm)**	**Penetration Loss [dB] in 60 GHz Band**
[40]	Wooden Door	4	-7
	Plaster Covered Concrete	40	-27
[38]	Granite	3	< -30
	Quartzite	2	-3.4
	Marble	1.7	-5.2
	Limestone	3	< -30
	Concrete	5	< -30
	Brick	11	-16.9
	Plasterwork (rough)	1	< -30
	Plasterwork (smooth)	1	-4.5
	Glass (smooth)	0.6	-3.1
[66]	Composite Wall with Studs (not in path)	-	-8.8
	Composite Wall with Studs (in path)	-	-35.5
	Glass Door	-	-2.5
	Concrete Wall 14 Months after Concreting	-	-28.1
	Plasterboard Wall	-	-5.4 to -8.1
	Partition of Glass Wool and Plywood Surfaces	-	-9.2 to -10.1
	Partition of Cloth-covered Plywood	-	-3.9 to -8.7
	Granite	3 -	< -30
	Metalized Glass	-	< -30
	Wooden Panels	-	-6.2 to -8.6
[66]	Brick	11	-17
	Limestone	3	< -30
	Concrete	-	< -30
[67]	Double Glass	1.5	-4.5
	Simple Glass	0.5	-3.5
	Wooden Closet	2	-13.8
	Metal Closet	0.8	-8
	Whiteboard	1.5	-11.6
	Plywood Panels	0.5	-6
	Brick Wall with Plasterboard on both sides and paint	23	-48

Reference	Material	Thickness (cm)	Penetration Loss [dB] in 60 GHz Band
	Iron Door Covered with thin layer of plywood panels	8	-49
[68]	Drywall	2.5	-6
	Office Whiteboard	1.9	-9.6
	Clear Glass	0.3	-3.6
	Mesh Glass	0.3	-10.2
	Clutter	-	-1.2
[69]	Hollow 12 mm thick plasterboard wall with 96 mm air gap	12	-5.1 to -8.1
	5-cm thick partition made of 5.5 mm-thick cloth-covered plywood with glass wool in between	-	-7.9 to -10.1
	4.3-cm thick wooden partition made of 2.5 mm thick cloth-covered plywood surfaces	-	-3.4 to -8.7

1.6.2.2 Reflection Measurements

A number of reflection measurement campaigns have been performed in the 60 GHz band to study common indoor and outdoor building materials [4][65][70][71][72][73]. The following tables show the reflection coefficients measured in the V - band.

Table 1.46: Reflection losses from common indoor materials at 57.6 GHz [4].

Reference	Material	Path Length (m)	Reflection Loss [dB] at 57.6 GHz
[4]	Metal	50	-1
		109	-9
	Brick (Solid)	95	-7
		47	-8
	Concrete (Ribbed)	64	-19
		65	-18
	Brick (Windows, Doorway)	93	-18
		135	-15
	Concrete (Aggregate)	75	-17
		75	-20

Table 1.47: Reflection losses from indoor materials in the 60 GHz band.

Reference	Material	Thickness (cm)	Reflection Loss [dB] in 60 GHz Band
[65]	Granite	3	-17.5
	Quartzite	2	-5.8
	Marble	1.7	-3.8
	Limestone	3	-6.5
	Concrete	5	-7.5
	Brick	11	-14.8
	Plasterwork (rough)	1	< -30
	Plasterwork (smooth)	1	-6.9
	Glass (smooth)	0.6	-8.8
[71][73]	Metal	-	0
	Wooden Panels	-	-8
	Concrete	-	-2

1.6.2.3 Index of Refraction Measurements

A number of measurement campaigns have investigated the index of refraction by performing reflection measurements and deducing the index of refraction using the best line fit through the Fresnel coefficients in the 60 GHz band [70][74]. The results are summarized below.

Table 1.48: Indices of refraction for common indoor materials in the 60 GHz band.

Reference	Material	Thickness (mm)	Refractive Index at 60 GHz
[70]	Concrete	30	2.55 - j0.084
	Plasterboard	9	1.5 - j0.01
	Floor Board (Synthetic Resin)	25	1.98 - j0.083
	Ceiling Board (Rock Wool)	9	1.26 - j0.005
[74]	Soda-lime Glass	8 - 12	2.61 - j0.0318
[69]	Soda-lime Glass with Wire Mesh	8 - 12	2.74 - j0.0354

1.6.2.4 Relative Permittivity Measurements

A number of measurement campaigns have investigated the relative permittivity, attenuation coefficients and tangent losses of common indoor and outdoor building materials at 42 GHz and in the 60 GHz band [75][76][77]. The following tables show the permittivities measured for different materials in the V - band.

Table 1.49: Complex permittivity and attenuation coefficients of common indoor materials at 42 GHz and in the 60 GHz band.

Reference	Material	Complex Permittivity	Attenuation Coeff. (dB/cm)	Frequency
[77]	Glass	7 - j0.001	-	42 GHz
	Concrete	7 - j0.1	-	
	Wood	3 - j0.1	-	
[75]	Stone	6.81 - j0.273	5.73	60 GHz
	Marble	11.56 - j0.077	1.25	
	Concrete	6.14 - j0.301	6.67	
	Aerated Concrete	2.26 - j0.101	3.7	
	Tiles	6.3 - j0.358	7.81	
	Glass	5.29 - j0.254	6.05	
	Acrylic Glass	2.53 - j0.03	1.03	
	Plasterboard	2.81 - j0.046	1.51	
	Wood	1.57 - j0.096	4.22	
	Chipboard	2.86 - j0.159	5.15	
[76]	Plasterboard	2.58 - j0.021	0.071	
	Chipboard	2.95 - j0.19	0.6	

1.7 W - Band: 75 - 110 GHz

The W - Band has so far received little attention for its channel propagation properties. It has mostly been studied to understand material characteristics.

1.7.1 Material Properties in the W - Band

1.7.1.1 Index of Refraction Measurements

A measurement campaign has investigated the indices of refraction of several indoor building materials by performing reflection measurements and deducing the index of refraction using the best line fit through the Fresnel coefficients at 78.5 GHz and 95.9 GHz [72]. The results are summarized in Table 1.50.

Table 1.50: Indices of refraction of common indoor materials in the W - Band.

Reference	**Material**	**Thickness (mm)**	**Index of Refraction**	
			78.5 GHz	**95.9 GHz**
[72]	Concrete	30	-	2.49 - j0.068
	Plaster Board	9	1.54 - j0.033	1.5 - j0.02
	Floor Board (Synthetic Resin)	25	1.91 - j0.096	1.78 - j0.11
	Ceiling Board (Rock Wool)	9	1.25 - j0.009	1.25 - j0.016

1.8 Conclusion

A comprehensive literature survey was presented describing mmWave propagation measurement campaign details and corresponding measured results above 6 GHz. It is apparent from this section that mmWave propagation has been extensively conducted and studied to understand the effects of the indoor and outdoor environments over the past three decades to implement a number of applications, ranging from short-range indoor to satellite communications. To this date, however, mmWave propagation for outdoor broadband mobile cellular and backhaul communications has not been investigated, as a result of recurring myths from the wireless industry in that mmWave propagation can only perform well enough in LOS environments where there is a direct propagation path between TX and RX, while NLOS links are too weak to support connectivity over ultra-high bandwidths. While it is true that mmWave propagation suffers from greater

free space path loss and increased atmospheric and rain attenuation over conventional UHF/Microwave frequency bands for a given T-R separation, these effects become negligible over small distances, that is, less than 200 - 300 m, and are easily accounted for using high gain directional horn antennas at the TX and RX. This thesis investigates the capabilities of outdoor dense urban wideband mmWave channels to assess their viability and develop a channel modeling framework for current and future mmWave channel modeling that faithfully accounts for the unique stochastic properties of dense urban mmWave channels, that will allow for the design of mmWave radio-systems used for delivering multi-Gbps data rates in dense LOS and NLOS environments. Measurements like those presented in this chapter were performed in the lower frequency bands below 6 GHz, and have been used in building statistical spatial channel models needed to estimate channel coefficients. Chapter 2 presents a detailed analysis of the 3GPP and WINNER II spatial channel models that are currenlty used in designing radio-system for the UHF/Microwave spectrum.

Chapter 2

Geometry-Based Stochastic Spatial Channel Models for Frequencies Below 6 GHz: 3GPP and WINNER II

2.1 Introduction

It is in theory possible to determine the propagation characteristics of a wireless channel using Maxwell's set of differential equations. In practice, however, a number of limitations arise which make this impossible to achieve. For instance, it is extremely difficult to describe the wireless environment as a set of boundary conditions, and even if this were possible, it would still take an enormous amount of time to solve for the channel impulse responses as numerical solutions to Maxwell's equations. Instead, the environment is considered as a black box ruled by statistical distributions, and the task at hand is to determine these distributions using real-world collected propagation measurements. The set of statistical distributions describing the wireless channel is usually referred to as a statistical spatial channel model (SSCM).

Many of the current 3G and 4G MIMO radio systems are designed using the geometry-based stochastic

3GPP and WINNER II SSCMs, which provide important statistical channel parameters such as path delays, powers, angle of arrival (AOA) and angle of departure (AOD) information, and path loss models based on real-world measurements, ultimately providing statistical complex channel coefficients allowing to recover channel impulse responses. These two very important and widespread channel models allow for calibration, link-level and system-level simulations for computing theoretical channel capacities, outage probabilities and determining optimum coding and modulation schemes. The 3GPP and WINNER II channel models are based on real-world propagation measurements in many types of environments conducted between 1 GHz and 6 GHz and for RF signal bandwidths spanning 5 MHz to 100 MHz using several channel sounders and a variety of multiple element antenna arrays, such as rectangular, uniform or semi-spherical arrays [78][79][80]. In this section, the micro-cellular channel models provided by the 3GPP and WINNER II channel models are presented and explained so as to compare and contrast them in the light of future 5G mmWave channel models for dense urban environments (See Chapter 5).

The 3GPP and WINNER II models use slightly different terminology to refer to a group of multipath components traveling close in both time and space. The 3GPP model defines such a group of traveling multipath as a ray or path, composed of sub-rays or path components, while the WINNER II channel model defines a group of traveling multipath as a cluster, composed of closely-spaced traveling rays. The 3GPP models provided are valid for $N = 6$ paths, which are each sub-divided into $M = 20$ path components (irrespective of LOS or NLOS conditions), while the WINNER II model proposes to use $N = 8$ and $N = 16$ clusters in LOS and NLOS conditions respectively, each cluster sub-divided into $M = 20$ rays (identical to 3GPP) for the micro-cellular scenario.

2.2 The 3GPP Spatial Channel Model

2.2.1 3GPP NLOS Micro-Cellular Channel Models

The 3GPP Spatial Channel Model (SCM) for Multiple-Input Multiple-Output (MIMO) has come out with numerous releases since Release 1 in 2003, and is currently up to Release 11 (September 2012). This

section outlines the 3GPP SCM micro-cellular channel models from the latest release, that is, Release 11, specified for 1-2 GHz RF propagation, and systems with 5 MHz bandwidth or less. The micro-cellular environment is assumed to be a dense grid-like urban environment where the T-R separation distance is less than 1 km, and the base station is located at rooftop height (12 m). The 3GPP channel model specifies $N = 6$ paths for systems with 5 MHz bandwidth or less.

The steps for generating channel parameters and channel coefficients (i.e., the taps of an omni-directional power delay profiles) outlined in the 3GPP channel models for the LOS and NLOS microcellular environment are presented below. Note: The step procedure outlined in this section does not follow the same order as the one presented in [78].

Step 1: Calculate the path loss using the following path loss formulas [78]:

$$LOS : PL[dB] = -35.4 + 26 \times \log_{10}(d) + 20 \times \log_{10}(f_c) + X_{\sigma,LOS} \tag{2.1}$$

$$NLOS : PL[dB] = -55.9 + 38 \times \log_{10}(d) + (24.5 + 1.5 \times f_c/925) \times \log_{10}(f_c) + X_{\sigma,NLOS} \tag{2.2}$$

where X_σ is the usual lognormal random variable with 0 dB mean, $\sigma_{LOS} = 4\ dB$ and $\sigma_{NLOS} = 10\ dB$. Note: These path loss formulas are taken from the COST231 [56] Walfisch-Ikegami NLOS path loss model, and street canyon LOS model, specified for a BS antenna height of 12.5 m, building height of 12 m, building-to-building distance of 50 m, street width of 25 m, MS antenna height of 1.5 m, orientation of 30° for all paths, and the selection of metropolitan center scenario.

Step 2: Generate the path delays τ_n [78]:

$$LOS\ and\ NLOS : \tau_n' \sim Uniform(0, 1.2\mu s) \tag{2.3}$$

$$\tau_n = sort(\tau_n' - \min(\tau_n')) \tag{2.4}$$

where *sort()* indicates that the path delays should be ordered from smallest to largest delay.

Step 3: Generate the fractional path powers P_n [78]:

$$LOS\ and\ NLOS: P'_n = 10^{-(\tau_n + z_n/10)} \tag{2.5}$$

where z_n is i.i.d. $N(\mu = 0 \text{ dB}, \sigma = 3 \text{ dB})$.

For LOS:

$$P_{n,LOS} = \frac{P'_{n,LOS}}{(K+1)\sum_{k=1}^{N} P'_{k,LOS}}, n \geq 2 \tag{2.6}$$

$$P_{1,LOS} = \frac{K}{K+1} \tag{2.7}$$

where: $K[dB] = 13 - 0.03d$ is the Rician K-factor, and d (m) is the T-R separation distance.

For NLOS:

$$P_{n,NLOS} = \frac{P'_{n,NLOS}}{(K+1)\sum_{k=1}^{N} P'_{k,LOS}} \tag{2.8}$$

Note: $P_{n,LOS}$ is easily derived by noting the constraint on the LOS direct path power P_D and the additional constraint that the sum of the P'_n must equal to unity (normalization), as shown below:

$$\begin{cases} P_{1,LOS} = \frac{P_D}{\sum_{k=2}^{N} P'_{k,LOS}} \\ \sum_{n=1}^{N} P'_{n,LOS} = 1 \end{cases}$$

Putting the two constraints above together yields:

$$P_{1,LOS} + \sum_{n=2}^{N} P'_{n,LOS} = 1 \tag{2.9}$$

$$P_{1,LOS} + \frac{P_{1,LOS}}{K} = 1 \tag{2.10}$$

$$P_{1,LOS} = \frac{K}{K+1} \tag{2.11}$$

Step 4.a: Generate the path azimuth AOD's $\delta_{n,AOD}$ folllowed by the intra-cluster subpath AOD's $\delta_{n,m,AOD}$ [78]:

$$LOS\ and\ NLOS: \delta_{n,AOD} \sim Uniform(-40^\circ, +40^\circ) \tag{2.12}$$

Note: in LOS, the direct path azimuth AOD is set to the LOS path direction θ_{BS}.

Step 4.b: Generate the subpath ray angles $\delta_{n,m,AOD}$ [78]:

$$LOS\ and\ NLOS: \delta_{n,m,AOD} = \delta_{n,AOD} + \Delta_{n,m,AOD} \tag{2.13}$$

Note: See Table 2.1 for the offsets $\Delta_{n,m,AOD}$.

Step 5.a: Generate the path azimuth AOA's $\delta_{n,AOA}$ folllowed by intra-cluster subpath AOA's $\delta_{n,m,AOA}$ [78]:

$$LOS\ and\ NLOS: \delta_{n,AOA} \sim N(0, \sigma^2_{n,AOA}) \tag{2.14}$$

Note: in LOS, the direct path azimuth AOA is set to the LOS path direction $\theta_{BS} - 180^\circ$, and there are no intra-cluster subpath offsets.

Step 5.b: Generate the subpath ray angles $\delta_{n,m,AOA}$ [78]:

$$LOS\ and\ NLOS: \delta_{n,m,AOA} = \delta_{n,AOA} + \Delta_{n,m,AOA} \tag{2.15}$$

Note: See Table 2.1 for the offsets $\Delta_{n,m,AOA}$.

Table 2.1: The angle offsets needed to generate the intra-cluster angles of departure and arrival. Note that for both departure and arrival offsets, the mean is 0°, while the standard deviations (RMS) are equal to 5° and 35° for departure offsets and arrival offsets, respectively [78].

Subpath # m	**Offset $\Delta_{n,m,AOD}$ for a 5° AS at BS**	**Offset $\Delta_{n,m,AOA}$ for a 35° AS at MS**
1,2	±0.2236	±1.5649
3,4	±0.7064	±4.9447
5,6	±1.2461	±8.7224
7,8	±1.8578	±13.0045
9,10	±2.5642	±17.9492
11,12	±3.3986	±23.7899
13,14	±4.4220	±30.9538
15,16	±5.7403	±40.1824
17,18	±7.5974	±53.1816
19,20	±10.7753	±75.4274

Step 6: Generate the intra-cluster subpath absolute AOD's and AOA's (with respect to the BS antenna array broadside [78]:

$$\theta_{m,n,AOD} = \theta_{BS} + \delta_{n,AOD} + \Delta_{n,m,AOD} \tag{2.16}$$

$$\theta_{m,n,AOA} = \theta_{BS} + \delta_{n,AOA} + \Delta_{n,m,AOA} \tag{2.17}$$

Step 7: Determine directive gains $G_{BS}(\theta_{m,n,AOD})$ and $G_{MS}(\theta_{m,n,AOA})$ of the subpaths based on subpath AOD's and AOA's [78]:

The BS antenna pattern is given by $A(\theta)$ below, and the MS antenna pattern is an omnidirectional pattern with -1 dBi gain. Note that the antenna patterns are assumed to be aligned with the BS and MS antenna array broadsides.

$$A(\theta) = -\min\left[12\left(\frac{\theta}{\theta_{3dB}}\right)^2, A_m\right], |\theta| \leq 180^\circ \tag{2.18}$$

where θ_{3dB} is the HPBW in degrees, A_m is the maximum attenuation. For a 3 sector scenario, $\theta_{3dB} = 70^\circ$ and $A_m = 20$ dB. For a 6 sector scenario, $\theta_{3dB} = 35^\circ$ and $A_m = 23$ dB. The gains of the 3 sector and 6 sector antennas are 14 dBi and 17 dBi, respectively.

Step 8: Generate the initial subpath phases $\Phi_{n,m}$ [78]:

$$LOS\ and\ NLOS: \Phi_{n,m} \sim Uniform(-\pi, +\pi) \tag{2.19}$$

Step 9: Generate the channel coefficients (complex voltage levels of each path) for the n^{th} *path travelling between the (u,s)*th *RX-TX antenna pair (see Fig. 2.1) [78]:*

$$h_{u,s,n}(t) = \sqrt{P_{n,m}\sigma_{SF}} \sum_{m=1}^{M} \sqrt{G_{BS}(\theta_{n,m,AOD})G_{MS}(\theta_{n,m,AOA})} e^{j(k_0 d_s sin(\theta_{n,m,AOD})+\Phi_{n,m})} \cdot e^{jk_0 d_u sin(\theta_{n,m,AOA})} e^{jk_0||v||cos(\theta_{n,m,AOA}-\theta_v)t} \tag{2.20}$$

where:

- $P_{n,m} = P_n/M$, the power of the m^{th} subpath within the n^{th} path;
- σ_{SF} is the lognormal shadow factor applied to each subpath m;
- $M = 20$ is the number of subpaths in each path;
- $\theta_{n,m,AOD}$ is the AOD for the m^{th} subpath of the n^{th} path;
- $\theta_{n,m,AOA}$ is the AOA for the m^{th} subpath of the n^{th} path;
- $G_{BS}(\theta_{n,m,AOD})$ is the BS antenna directive gain for the m^{th} subpath of the n^{th} path;
- $G_{MS}(\theta_{n,m,AOA})$ is the MS antenna directive gain for the m^{th} subpath of the n^{th} path;
- k_0 is the wavenumber equal to $2\pi/\lambda$;
- d_s is the distance (m) from BS antenna element s from the reference ($s = 1$) antenna.

  For the reference antenna, $s = 1$, $d_1 = 0$;
- d_u is the distance (m) from MS antenna element s from the reference ($u = 1$) antenna

  For the reference antenna, $u = 1$, $d_1 = 0$;
- $||\mathbf{v}||$ is the magnitude (m/s) of the MS velocity vector;

– θ_v is the angle of the MS velocity vector.

Note that the complex voltage level of the n^{th} tap, i.e., $h_{u,s,n}$, corresponding to the $(u,s)^{\text{th}}$ TX-RX antenna pair is the coherent sum of the individual $M = 20$ subpath complex voltages (square root of the power levels), each weighted by the TX and RX antenna patterns, the departure and arriving phases of the path, and the additional phase term arising from the Doppler shift (for non-stationary MS, i.e., $||\mathbf{v}|| \neq 0$). In order to recover a normalized power delay profile, one must take the magnitude squared of the $h_{u,s,n}$ coefficients as computed in Eq. 2.20, since $h_{u,s,n}$ only specifies the complex voltage coefficients, that is, the in-phase I and quadrature Q components of the PDP.

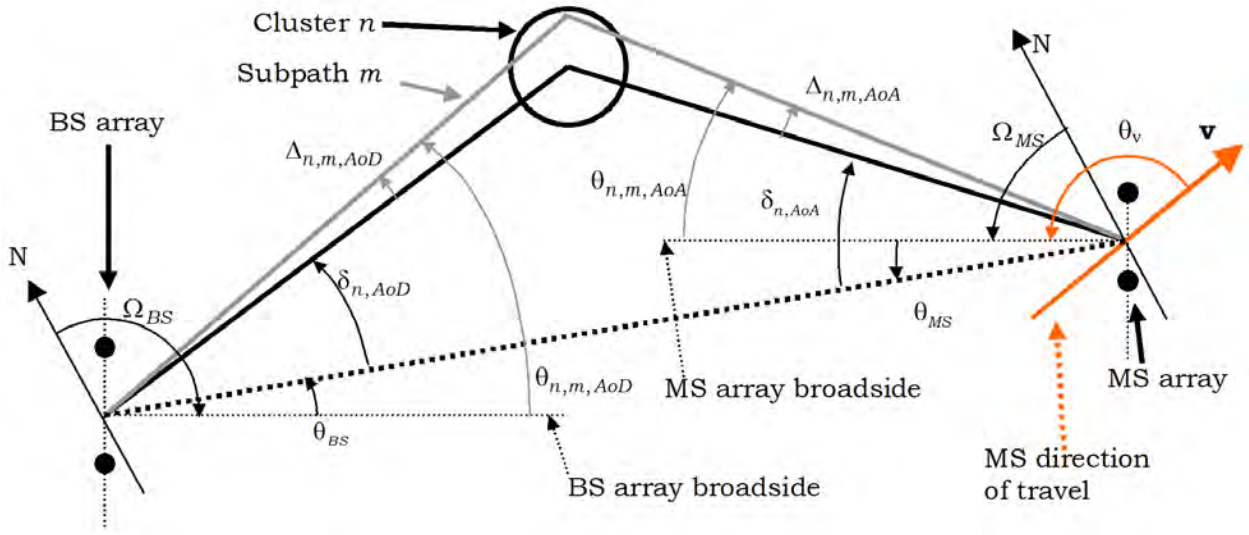

Figure 2.1: This figure shows a BS and MS broadside arrays separated by the wireless channel. One path emerges from the BS array, and is broken up into M subpaths, where each subpath has a distinct AOD and contains $\frac{1}{M}^{\text{th}}$ of the total path power. The MS array captures the path as it travels with velocity $\mathbf{v}$ [78].

2.2.2 LOS Probability

The LOS probability as a function of the T-R separation distance d (m) is shown in the following equation:

$$P_{LOS}(d) = \begin{cases} (300 - d)/300, & 0 < d < 300 \text{ m} \\ 0, & d > 300 \text{ m} \end{cases}$$

The NLOS probability is easily estimated as follows:

$$P_{NLOS}(d) = 1 - P_{LOS}(d) \tag{2.21}$$

2.3 The WINNER II Spatial Channel Model

2.3.1 WINNER II Hardware Equipment Specifications

The WINNER II channel models are an extension to the 3GPP models, and are based on a set of narrowband and wideband propagation measurements at 2 GHz and 5 GHz for RF signal bandwidths spanning 5 MHz to 100 MHz using several channel sounders with various degrees of angular resolution, providing a minimum multipath time resolution of 20 ns (at 100 MHz RF bandwidth). The three main channel sounders used to collect the measurements are the Propsound channel sounder (a product of the Elektrobit Corporation), the RUSK TUI-FAU channel sounder (designed by Medav), and the CRC Chanprobe channel sounder. Table 2.2 summarizes the specifications of the channel sounders used during the measurements.

Various multiple-element antennas were used, such as rectangular, circular and linear arrays. Table 2.3 summarizes the typical types of antennas and corresponding angular resolution (i.e., angle range where power levels drop by 3 dB and 10 dB from maximum boresight gain) used with the RUSK TUI-FAU channel sounder during propagation measurements in the 5-6 GHz band [79]. The 3 dB and 10 dB beamwidths were obtained by considering the array factor of the antenna types and finding the half-power and one tenth power beamwidth angular range in the azimuth plane. These antennas were used to recover energy from multiple incoming directions at the receiver, and absolute timing PDPs were obtained with absolute timing rubidium clock standards.

Table 2.2: Channel sounder specifications used for the WINNER II measurements. For further detail, refer to pp. 21-25 in [79].

Property	**Propsound**	**RUSK TUI-FAU Sounder**	**CRC-Chanprobe**
RF Band (GHz)	1.7 - 2.1, 2.0 - 2.7 3.2 - 4.0, 5.1 - 5.9	5 - 6	0.95, 2.25, 5.8, 30, 40, 60
Chip Rate	Up to 100 MChips/s	-	Up to 50 MChips/s
Available Code Lengths	31 - 4095	256 - 8192	127 - 1021
Sustained Measurement Rate	Up to 30,000 CIR/s (Code Length: 255 Chips)	-	40,000 CIR/s
Number of Measurement Channels	Up to 8,448	Up to 65,536	Up to 32 Switched RX Antennas, 1 TX Antenna
Measurement Modes	SISO, SIMO, MIMO	SISO, SIMO, MIMO	SISO, SIMO
Spurious IR Free Dynamic Range	35 dB	48 dB	40 dB
Maximum TX Output Power	26 dBm	33 dBm	42 dBm (2.25 GHz), 30 dBm (other)
Minimum Detectable Signal	-	-88 dBm	-89 dBm
Synchronization	Rubidium Clock with Stability of 10^{-11}	Rubidium Clock with Stability of 10^{-11}	Rubidium Clock with Stability of 10^{-11}

Table 2.3: Antenna types and specifications used with the Medav RUSK TUI-FAU channel sounder [79].

Antenna Type	**Uniform Linear Array**	**Uniform Circular Array**	**Rectangular Array**
Center Frequency (GHz)	5.2	5.2	5.2
Bandwidth (MHz)	120	120	120
Number of Elements	8	16	32
3 dB Beamwidth (°)	25°	32°	5°
10 dB Beamwidth (°)	40°	48°	10°

The antenna beamwidths used in the TUI measurements are on the order of 30° (except for the rectangular array which had 5° angular resolution). The minimum multipath time resolution in the WINNER II measurements was on the order of 20 ns (100 MHz RF bandwidth).

2.3.2 WINNER II NLOS Micro-Cellular Channel Models

The steps for generating channel parameters and channel coefficients (i.e., complex voltage tap values) outlined in the WINNER II channel models for the LOS and NLOS microcellular environment are presented below.

Step 1: Calculate the path loss using the following path loss formulas [79]:

$$PL[dB] = A \times \log_{10}(d[m]) + B + C \times \log_{10}\left(\frac{f_c[GHz]}{5.0}\right) + X_\sigma \tag{2.22}$$

Table 2.4: WINNER II path loss models for the LOS and NLOS microcellular urban environments [79].

Environment	**Path Loss [dB]**	**Shadow Fading [dB]**	**Applicability Range**
LOS	$A = 22.7, B = 41, C = 21$ $PL = 40 \times \log_{10}(d_1) + 9.45$ $-17.3 \times \log_{10}(h_{BS}/h_{MS})$ $+2.7 \times \log_{10}(f_c/5)$	$\sigma = 3$	$10m < d_1 < d_{BP}$ $d_{BP} < d_1 < 5km$ $h_{BS} = 10m$ $h_{MS} = 1.5m$
NLOS	$PL = \min\Big(PL(d_1, d_2),$ $PL(d_2, d_1)\Big)$ where: $PL(d_k, d_l) = PL_{LOS}(d_k)$ $+20 - 12.5n_j + 10n_j \log_{10}(d_l)$ $+3\log_{10}(f_c/5)$ and $n_j =$ $\max(2.8 - 0.0024d_k, 1.84)$ P_{LOS} is the LOS PL with $C = 23$	$\sigma = 4$	$10m < d_1 < 5km$ $w/2 < d_2 < 2km$ $w = 20m$ $h_{BS} = 10m$ $h_{MS} = 1.5m$ When $0 < d_2 < w/2$, the LOS PL is applied

In the above table,

– h_{BS}: base station height (m);

– h_{MS}: mobile station height (m);

– w: street width (m);

– f_c: center frequency (Hz);

– d_{BP}: breakpoint distance, where $d_{BP} = 4h_{BS}h_{MS}f_c/c$, and $c = 3 \times 10^8$ m/s;

– d_1: distance from base station to the center of the perpendicular street (See Fig. 2.2);

– d_2: distance from the mobile station along the perpendicular street, measured from;

the center of the LOS street (See Fig. 2.2).

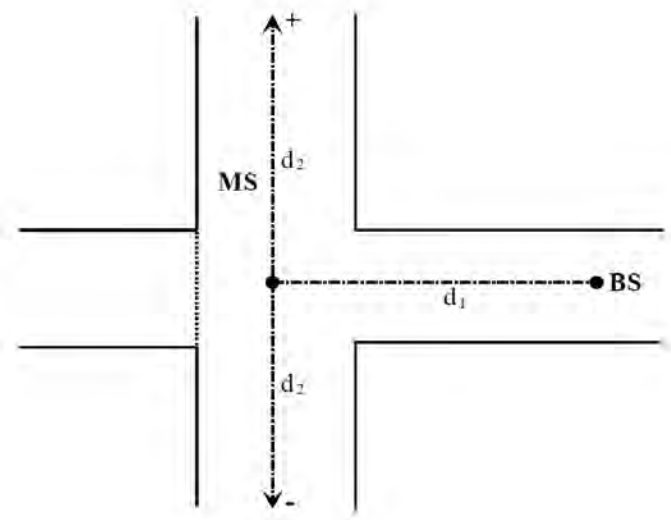

Figure 2.2: Geometry for d_1 and d_2 path loss model [79].

Step 2: Calculate the cluster delays τ_n:

$$LOS: \begin{cases} \tau_n'' = -r_\tau \sigma_\tau \ln(X_n) \\ \tau_n' = \frac{\tau_n''}{D} \end{cases}$$

$$NLOS: \tau_n' \sim Uniform(0, 800 \text{ ns}) \tag{2.23}$$

$$\tau_n = sort(\tau_n' - \min(\tau_n')) \tag{2.24}$$

where:

– The delay distribution proportionality factor $r_\tau = 3.2$;

– The delay spread $\log_{10}(\sigma_\tau) = -7.12$;

– $X_n \sim Uniform(0, 1)$;

– $D = 0.07705 - 0.0433K + 0.0002K^2 + 0.000017K^3$;

– The Rician Factor $K \sim N(\mu = 9 \text{ dB}, \sigma = 6 \text{ dB})$.

Step 3: Generate the fractional cluster powers P_n and ray powers $P_{n,m}$:

$$LOS : P'_n = 10^{\frac{-Z_n}{10}} e^{-\tau_n \frac{r_\tau - 1}{r_\tau \sigma_\tau}} \tag{2.25}$$

$$NLOS : P'_n = 10^{\frac{-Z_n}{10}} e^{-\frac{\tau_n}{\sigma_\tau}} \tag{2.26}$$

$$P_n = \frac{P'_n}{\sum P'_j} \tag{2.27}$$

$$P_{n,m} = \frac{P_n}{M} \tag{2.28}$$

where:

– The delay distribution proportionality factor $r_\tau = 3.2$;

– The cluster delays τ_n are generated in Step 2;

– The delay spread $\log_{10}(\sigma_\tau) = -7.12$ in LOS, and -7.44 in NLOS;

– $Z_n \sim N(\mu = 0 \text{ dB}, \zeta = 3 \text{ dB})$;

– $M = 20$.

Step 4.a: Generate the cluster azimuth AOD's ϕ_n:

$$LOS : \phi_n = \phi'_n X_n + Y_n - (X_n \phi'_1 + Y_1 - \phi_{LOS}) \tag{2.29}$$

$$NLOS : \phi_n = \phi'_n X_n + Y_n + \phi_{LOS} \tag{2.30}$$

$$\phi'_n = \frac{2\sigma_{AOD}\sqrt{-ln(\frac{P_n}{max(P_n)})}}{C'} \tag{2.31}$$

where:

- P_n are the fractional cluster powers generated in Step 3;
- $\sigma_{AOD} = \frac{\sigma_\phi}{\sqrt{2}}$;
- $\log_{10}(\sigma_\phi) = 0.37$ in LOS, and 0.21 in NLOS;
- $C' = C \times (1.1035 - 0.028K - 0.002K^2 + 0.0001K^3)$ in LOS;
- $C' = C$, in NLOS, See Table 2.5;
- $K \sim N(\mu = 9 \text{ dB}, \sigma = 6 \text{ dB})$;
- $Y_n \sim N(0, \frac{\sigma_{AOD}}{5})$;
- $X_n = (-1, +1)$ with probabiliy 1/2;
- ϕ_{LOS} is the LOS direction.

Step 4.b: Generate the ray azimuth AOD's $\phi_{n,m}$:

$$LOS \text{ and } NLOS : \phi_{n,m} = \phi_n + c_{AOD}\alpha_m \tag{2.32}$$

where:

- The cluster-wise RMS azimuth spread AOD $c_{AOD} = 3$ in LOS, and 10 in NLOS;
- The ray angle offsets α_m are obtained from the Table 2.6.

Table 2.5: The constant scaling factor C related to the total number of clusters used to appropriately scale the azimuth angle of arrivals.

# of Clusters	4	5	8	10	11	12	14	15	16	20
C	0.779	0.86	1.018	1.09	1.123	1.146	1.19	1.211	1.223	1.289

Table 2.6: The angle offsets that are applied to the cluster angle of arrivals to recover the angle of arrivals of intra-cluster rays. Note that the angle offsets are generated such that the mean of the set is equal to 0, and the standard deviation (RMS) is equal to 1°.

Ray Number m	**Angle Offset α_m**
1,2	±0.0447
3,4	±0.1413
5,6	±0.2492
7,8	±0.3715
9,10	±0.5129
11,12	±0.6797
13,14	±0.8844
15,16	±1.1481
17,18	±0.5195
19,20	±2.1551

Step 5.a: Generate the cluster azimuth AOD's ϕ_n:

$$LOS : \phi_n = \phi'_n X_n + Y_n - (X_n \phi'_1 + Y_1 - \phi_{LOS}) \tag{2.33}$$

$$NLOS : \phi_n = \phi'_n X_n + Y_n + \phi_{LOS} \tag{2.34}$$

$$\phi'_n = \frac{2\sigma_{AOA}\sqrt{-ln(\frac{P_n}{max(P_n)})}}{C'} \tag{2.35}$$

where:

– P_n are the fractional cluster powers generated in Step 3;

– $\sigma_{AOA} = \frac{\sigma_\phi}{\sqrt{2}}$;

– $\log_{10}(\sigma_\phi) = 0.37$ in LOS, and 0.21 in NLOS;

– $C' = C \times (1.1035 - 0.028K - 0.002K^2 + 0.0001K^3)$ in LOS;

– $C' = C$, in NLOS, See Table 2.5;

– $K \sim N(\mu = 9 \text{ dB}, \sigma = 6 \text{ dB})$;

– $Y_n \sim N(0, \frac{\sigma_{AOA}}{5})$;

– $X_n = (-1, +1)$ with probabiliy 1/2;

– ϕ_{LOS} is the LOS direction.

Step 5.b: Generate the ray azimuth AOD's $\phi_{n,m}$:

$$LOS \text{ and } NLOS : \phi_{n,m} = \phi_n + c_{AOA}\alpha_m \tag{2.36}$$

where:

– The cluster-wise RMS azimuth spread AOA $c_{AOA} = 18$ in LOS, and 22 in NLOS

– The ray angle offsets α_m are obtained from the Table 2.6

Step 6: Generate the cross-polarization ratios $\kappa_{n,m}$:

$$LOS \text{ and } NLOS : \kappa_{n,m} = 10^{\frac{X}{10}} \tag{2.37}$$

$$X \sim N(\mu, \sigma) \tag{2.38}$$

where:

– $(\mu = 9 \text{ dB}, \sigma = 3 \text{ dB})$ in LOS

– $(\mu = 8 \text{ dB}, \sigma = 3 \text{ dB})$ in NLOS

Step 7: Generate the initial phases of each ray:

$$LOS \text{ and } NLOS : \phi_{n,m}^{\beta} \sim Uniform(-\pi, +\pi) \tag{2.39}$$

where:

$$-\beta = vv, vh, hv, hh \tag{2.40}$$

Step 8: Generate the intra-cluster power mappings:

The two strongest clusters are further sub-divided into three sub-clusters, composed of 10 sub-rays, 6 sub-rays and 4 sub-rays. The mapping is shown in the Table 2.7:

Table 2.7: Intra-cluster mapping of rays for the two strongest clusters. The two strongest clusters are further sub-divided into 3 sub-clusters, offset by 5 ns in excess time delay.

Sub-cluster #	**Mapping to Rays**	**Power**	**Delay Offset**
1	1,2,3,4,5,6,7,8,19,20	10/20	0 ns
2	9,10,11,12,17,18	6/20	5 ns
3	13,14,15,16	4/20	10 ns

Step 9: Generate the channel coefficient matrix for the n^{th} cluster (for Uniform Linear Array):

$$LOS: H_{u,s,n}(t) = \left\{ \sqrt{\frac{P_n}{K_R+1}} \sum_{m=1}^{M} \begin{bmatrix} F_{tx,s,V}(\phi_{n,m}) \\ F_{tx,s,H}(\phi_{n,m}) \end{bmatrix}^T \begin{bmatrix} e^{j\Phi_{n,m}^{vv}} & \sqrt{\kappa_{m,n}} e^{j\Phi_{n,m}^{vh}} \\ \sqrt{\kappa_{m,n}} e^{j\Phi_{n,m}^{hv}} & e^{j\Phi_{n,m}^{hh}} \end{bmatrix} \begin{bmatrix} F_{rx,s,V}(\varphi_{n,m}) \\ F_{rx,s,H}(\varphi_{n,m}) \end{bmatrix} \right.$$
$$+$$
$$\left. \delta(n-1) \sqrt{\frac{K_R}{K_R+1}} \sum_{m=1}^{M} \begin{bmatrix} F_{tx,s,V}(\phi_{n,m}) \\ F_{tx,s,H}(\phi_{n,m}) \end{bmatrix}^T \begin{bmatrix} e^{j\Phi_{n,m}^{vv}} & 0 \\ 0 & e^{j\Phi_{n,m}^{hh}} \end{bmatrix} \begin{bmatrix} F_{rx,s,V}(\varphi_{n,m}) \\ F_{rx,s,H}(\varphi_{n,m}) \end{bmatrix} \right\}$$
$$\cdot e^{jd_s k_0 sin(\phi_{n,m})}$$

$$NLOS: H_{u,s,n}(t) = \sqrt{P_n} \sum_{m=1}^{M} \begin{bmatrix} F_{tx,s,V}(\phi_{n,m}) \\ F_{tx,s,H}(\phi_{n,m}) \end{bmatrix}^T \begin{bmatrix} e^{j\Phi_{n,m}^{vv}} & \sqrt{\kappa_{m,n}} e^{j\Phi_{n,m}^{vh}} \\ \sqrt{\kappa_{m,n}} e^{j\Phi_{n,m}^{hv}} & e^{j\Phi_{n,m}^{hh}} \end{bmatrix} \begin{bmatrix} F_{rx,s,V}(\varphi_{n,m}) \\ F_{rx,s,H}(\varphi_{n,m}) \end{bmatrix}$$
$$\cdot e^{jd_s k_0 sin(\phi_{n,m})} e^{jd_u k_0 sin(\varphi_{n,m})} e^{j2\pi \nu_{n,m} t}$$

where:

- $P_{n,LOS}$ is the fractional power in the n^{th} cluster;
- K_R is the Rician K-Factor in linear units;
- $F_{tx,s,V}$ and $F_{tx,s,H}, F_{rx,s,V}$ and $F_{rx,s,H}$: transmitter and receiver antenna gain patterns;

  for vertical and horizontal polarizations, respectively;
- d_s and d_u: distances (m) of transmitter and receiver antenna elements from reference

  element respectively;
- $k_0 = 2\pi/\lambda_0,$ where λ_0 is the carrier wavelength;
- $\nu_{n,m} = \dfrac{||\mathbf{v}||cos(\phi_{n,m} - \theta_v)}{\lambda_0}$ is the Doppler frequency shift, where $||\mathbf{v}||$ is the absolute velocity of

  the MS, and θ_v is the direction of travel with respect to the broadside of the antenna.

2.3.3 LOS Probability

The LOS probability as a function of the T-R separation distance d (m) is shown in the following equation:

$$P_{LOS}(d) = \min\left(\frac{18}{d}, 1\right)(1 - e^{-\frac{d}{36}} + e^{-\frac{d}{36}}) \tag{2.41}$$

The NLOS probability is easily estimated as follows:

$$P_{NLOS}(d) = 1 - P_{LOS}(d) \tag{2.42}$$

2.4 Conclusion

This section provided current 3GPP and WINNER II SSCM step procedures for generating channel coefficients, that is, PDPs that embody the statistics of the measured urban microcellular channels for 1 - 6 GHz RF propagation and systems with 100 MHz RF bandwidth or less. A key feature of these two widespread channel models is the ability to recreate the measured channel statistics with relatively simple step procedures and equations, and this simplicity must be maintained when developing next generation mmWave channel models.

Chapter 3

28 GHz Wideband Propagation Measurement Campaign in New York City - Summer 2012

3.1 Introduction

A 28 GHz wideband propagation measurement campaign was performed from June to August of 2012 in Manhattan and Brooklyn, New York City to investigate dense urban mmWave channels and assess the viability of broadband communications for mobile cellular. A 400 mega-chips-per-second (Mcps) broadband sliding correlator channel sounder and highly directional 24.5 dBi (10.9° and 8.6° 3 dB beamwidths in azimuth and elevation, respectively) and 15 dBi (28.8° and 30° 3 dB beamwidths in azimuth and elevation, respectively) horn antennas were used to recover angle of departure (AOD) and angle of arrival (AOA) statistics. Over 8,000 PDPs were collected, which provide the means to develop the necessary statistical channel models for an accurate description and characterization of the 28 GHz urban communication channel for next generation mmWave mobile applications. This chapter describes the details of the measurement

campaign conducted in the summer of 2012 in New York City.

3.2 Environment Definitions

A 28 GHz wideband propagation measurement campaign was performed with a broadband sliding correlator channel sounder using a pair of 15 dBi and 24.5 dBi highly directional horn antennas in order to recover channel impulse responses in a highly populated, dense urban environment in New York City in the summer of 2012. Typical measurements included:

- *Line-of-Sight Boresight (LOS-B):* both the TX and RX antennas were pointed directly toward each other (i.e., on boresight) and aligned in both azimuth and elevation angles with no obstructions between the antennas in an outdoor environment.
- *Line-of-Sight Non-Boresight (LOS-NB):* both the TX and RX are in an environment with no obstructions between the antennas, however, the antennas were not necessarily pointed directly towards each other in both azimuth and elevation angles in an outdoor environment.
- *Non-Line-of-Sight (NLOS):* the TX and RX are in an outdoor environment with obstructions between the antennas. A NLOS environment with moderate obstructions includes trees between TX and RX or when the RX is slightly behind a building corner. A NLOS environment with heavy obstruction includes the RX completely behind buildings.
- *Outdoor-to-Indoor (O-to-I):* the TX is located outdoors, and the RX is located inside a building at mobile level, such that any received signal must come from penetration through the building.

3.3 Brooklyn Measurements

The Brooklyn sites used 11 different antenna pointing angle combinations and also different antennas and polarizations as seen in Table 3.1. The 360° rotation of the TX was not used in the Brooklyn sites, however the TX was always pointed in the direction of the strongest received power. For all angle pointing combinations, the RX rotated 360° with angular steps of 10°, and a power delay profile was acquired for each

measured angle. Note that the TX antenna in configurations #7-9 was a widebeam 15 dBi horn antenna with 28.8° (≈ 30°) beamwidth, thus a TX elevation of "-1/2" would be 15° below horizon. Additional small-scale linear track measurements were obtained at RX locations. The linear track was made of 21 track increments, each separated by a distance of $\lambda/2 = 5.35$ mm so as to obtain small-scale statistics.

Table 3.1: The different antenna pointing angle combinations used for all outdoor Brooklyn measurements at 28 GHz. "Narrow" means 24.5 dBi horn antenna with 10.9° beamwidth and "Wide" means 15 dBi with 28.8° beamwidth. The Elevation column represents the number of beamwidths above or below horizon

Measurement #	**TX Pol.**	**RX Pol.**	**TX Ant. BW**	**RX Ant. BW**	**TX EL. (# of BW)**	**RX EL. (# of BW)**
1	Vertical	Narrow	Vertical	Narrow	0	0
2	Vertical	Narrow	Vertical	Narrow	0	-1
3	Vertical	Narrow	Vertical	Narrow	0	-2
4	Vertical	Narrow	Vertical	Narrow	0	1
5	Vertical	Narrow	Vertical	Narrow	0	2
6	Vertical	Narrow	Vertical	Narrow	0	3
7	Vertical	Wide	Vertical	Narrow	-1/2	0
8	Vertical	Wide	Vertical	Narrow	-1/2	-1
9	Vertical	Wide	Vertical	Narrow	-1/2	1
10	Vertical	Narrow	Horizontal	Narrow	0	0
11	Vertical	Narrow	Horizontal	Narrow	-1	0

3.3.1 Brooklyn RX Locations and TX AODs

In total, signal was successfully detected and acquired at 5 RX locations in the MetroTech Commons area in Brooklyn for one TX location, Rogers Hall 1 (ROG1), located on the rooftop of the building, 40 m above ground level. The breakdown of the locations, T-R separation distances, type of environments, and angle conventions used are explained in this section. This section also presents a map of the measured Brooklyn area, identifying all RX locations, the 0° RX azimuth angle as well as the TX 0° angle (AOD) used in the field. The RX locations at which a signal was detected and recorded can be found in Table 3.2.

Table 3.2: Table showing the T-R separation distances and propagation conditions of all Brooklyn locations at which a signal was detected and recorded. The TX height for ROG1 was 40 m above ground level. The propagation conditions are designated according to Section 3.2.

TX ID	RX ID	T-R Separation (m)	Propagation Conditions
ROG1	RX1	133	NLOS
ROG1	RX1	134	NLOS
ROG1	RX3	135	NLOS
ROG1	RX9	110	NLOS
ROG1	RX11	128	NLOS

Additional small-scale track measurements were performed in Brooklyn to investigate signal fading over a local area. Small-scale measurements were taken on a 107 mm (10λ) long linear track, where adjacent track increments were separated by a distance of $\lambda/2 = 5.35$ mm. At each track increment, antenna pointing combinations listed in Table 3.2 were typically performed over 21 adjacent tracks, ranging from Track #1 to Track #21. The following diagram illustrates our linear track.

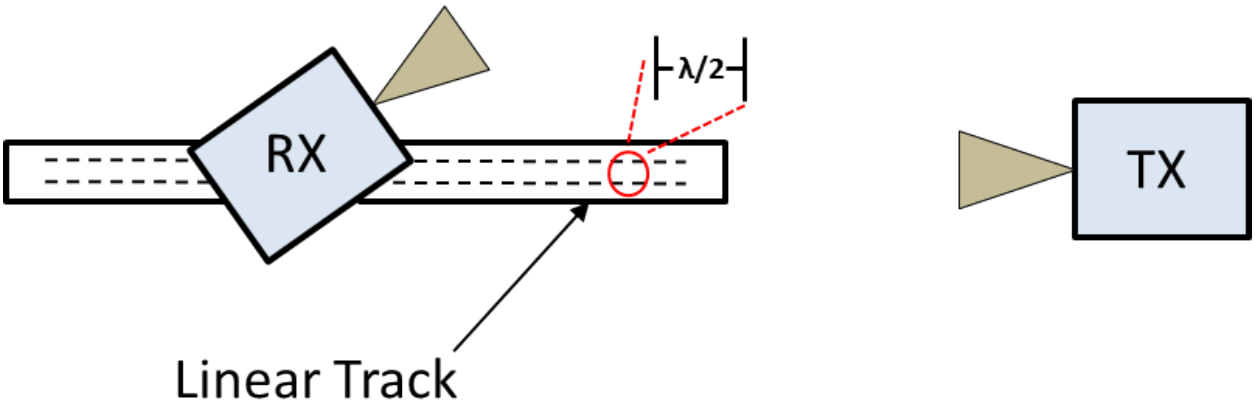

Figure 3.1: Linear track used for small-scale measurements in Brooklyn at 28 GHz.

In total, small-scale measurements were obtained at three RX locations: ROG1 - RX1, ROG1 - RX2 and ROG1 - RX3. Note that small-scale measurements were performed for all available angle pointing combinations at ROG1 - RX1 and ROG1 - RX2. However, due to the extensive amount of time required to capture small-scale track measurements, they were performed only for 8 (out of 12) antenna pointing combinations at ROG1 - RX3. Small scale measurements were not performed thereafter in Brooklyn or Manhattan.

The following graph shows a typical 3-dimensional (3-D) graph juxtaposing power delay profiles collected

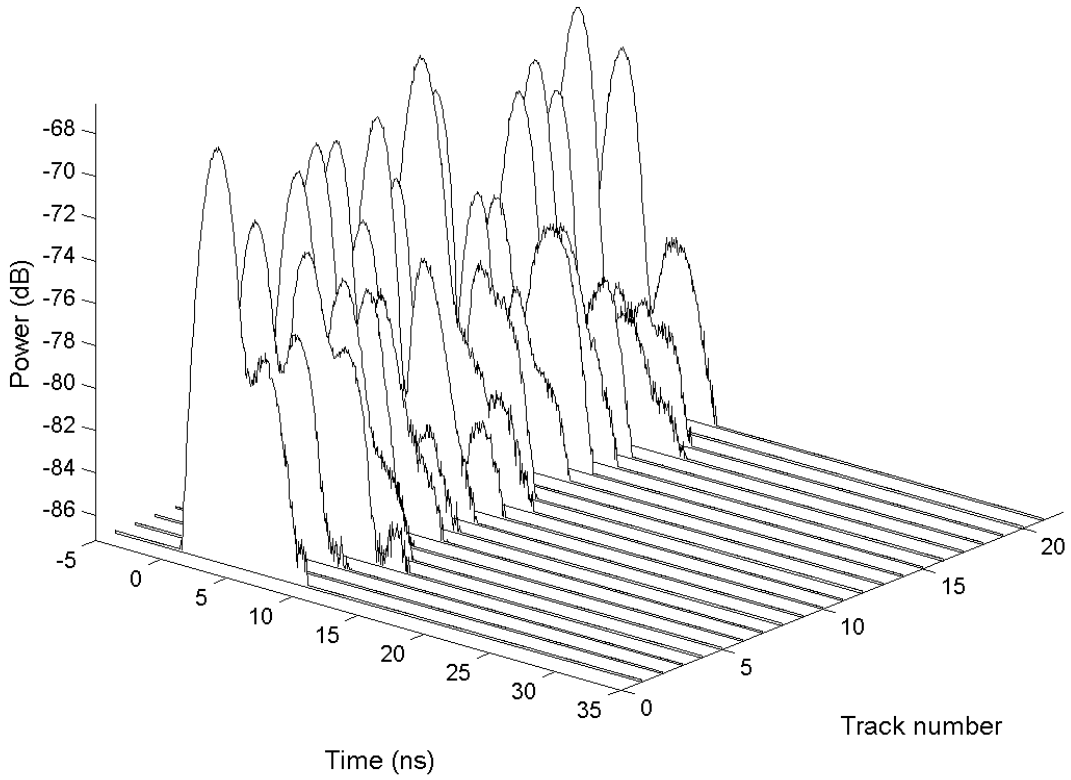

Figure 3.2: Typical 3-D plot showing power delay profiles collected at different track increments along the linear track, obtained at the same RX location for fixed RX AOA.

at different track increments along the linear track at the same RX location for fixed azimuth and elevation

AOA.

3.3.2 RX Locations Map

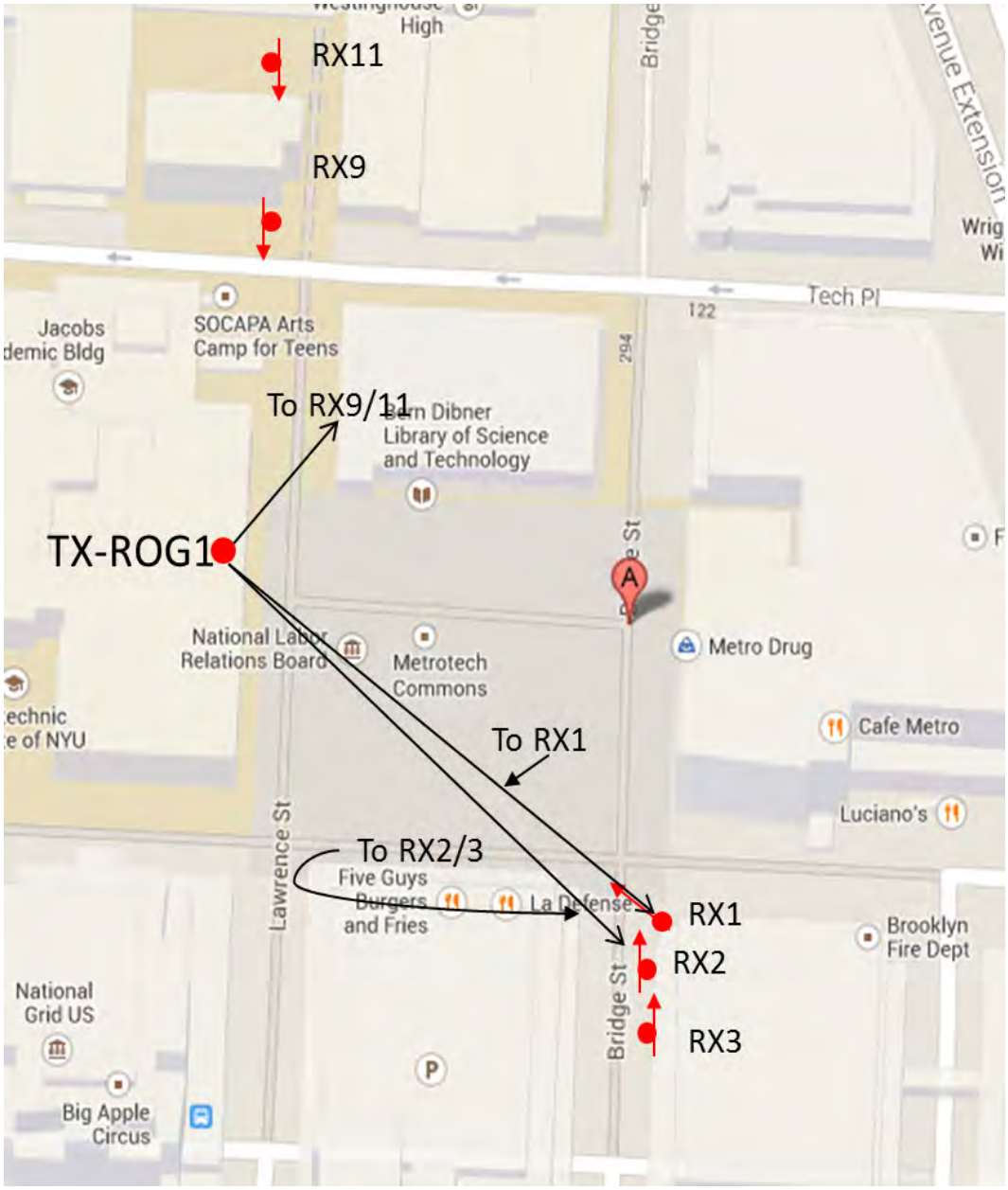

Figure 3.3: ROG1 RX locations where signal was detected and acquired. The black arrows originating from the TX location indicate the TX azimuth 0° for a particular RX location. The arrows at each RX location point in the direction of the RX azimuth 0° direction during the field measurements.

3.3.3 Receiver Locations: Rogers Hall 1 (ROG1)

A description of exact RX locations, and the directions in which the TX 0° and RX 0° azimuth angles were pointed during the field measurements are given below. Note that all angles were re-adjusted to a True North bearing during data post-processing. The maps above visually summarize the contents of this section.

ROG1 - RX1: Partially obstructed. The RX was located at the corner of Bridge St. and Myrtle Ave., on the sidewalk near the ceramic wall of 3 MetroTech center. The TX antenna 0° in the azimuth plane was pointed directly at the intersection of Bridge St. and Myrtle Ave., directly at RX1. See Table 3.1 for the TX antenna downtilt dependent upon the measurement number. The RX antenna 0° in the azimuth plane was pointed straight at the TX.

ROG1 - RX2: Heavily obstructed. The RX was located 1 m to the south of ROG1-RX1, on the side walk. The TX antenna 0° in the azimuth plane was pointed at the north-east building corner of 2 MetroTech center. The RX antenna 0° in the azimuth plane was pointed alongside parallel to Bridge St. pointing to the north.

ROG1 - RX3: Heavily Obstructed. The RX was located 2 m to the south of ROG1-RX3, on the side walk. The TX antenna 0° in the azimuth plane was pointed at the north-east building corner of 2 MetroTech center. The RX antenna 0° in the azimuth plane was pointed north, parallel to Bridge St.

ROG1 - RX9: Partially obstructed. The RX was located 4 m south of the entrance to Othmer Residence Hall at 101 Johnson St. The TX antenna 0° in the azimuth plane was pointed towards the Dibner Library. The RX antenna 0° in the azimuth plane was pointed south, parallel to Lawrence St.

ROG1 - RX11: Heavily obstructed. The RX was located in the courtyard behind Other Residence Hall at 101 Johnson St. The TX antenna 0° in the azimuth plane was pointed towards the Dibner Library. The

RX antenna 0° in the azimuth plane was pointed south, parallel to Lawrence St.

3.4 Manhattan Measurements

The Manhattan sites used 10 antenna pointing angle configurations at each RX location. The antennas were rotated throughout the 360° azimuth plane in 10° increments. Angle configurations #1-9 investigated AOA statistics of the 28 GHz mmWave wireless channel at the RX, while angle configuration #10 investigated AOD statistics at the TX. The TX elevation angle was always set to 10° (i.e. slightly pointed below horizon) for all 10 angle configurations. The TX and RX antennas were always vertically polarized (i.e. the electric field was vertical with respect to the horizon). The TX 0° azimuth angle did not necessarily point to the RX location (only in LOS-B environment situations did the TX 0° azimuth angle point straight at the RX).

The Manhattan measurement procedure began with angle Measurement #10. For Measurement #10, both TX and RX were rotated exhaustively to search for the strongest received power, i.e., the AODs and AOAs (azimuth and elevation) which yielded the strongest link between TX and RX. Once the strongest link was found of all TX azimuth and RX elevation/azimuth pointing angles at the RX location, the TX azimuth angle was noted and the TX was then rotated 360° with angular steps of 10° (while the RX antenna remained stationary) allowing up to 36 power delay profile measurements at the RX location.

Angle configurations #1-9 focused on rotating the RX antenna. The TX azimuth was set to -5°, 0°, and +5° relative to the TX azimuth angle found in Measurement #10 (with the strongest received power). Positively increasing angles corresponded to a counter-clockwise increasing direction. This angle convention was used at both the TX and RX. The RX elevation was set to -20°, 0°, and +20°, thus producing 9 possible TX-RX angle combinations. For each of these 9 angle combinations, the RX was rotated 360° in angular steps of 10°, and a power delay profile was acquired for each measured angle, allowing up to 36 PDP measurements. Hence, one TX-RX location could yield up to 360 PDPs (10 measurements × 36 azimuth angles tested). Table 3.3 summarizes the 10 antenna pointing angle configurations for Manhattan sites. Note that the elevation and azimuth angles are designated in terms of "# of Beamwidths" thus, for example, "-2" in the RX elevation column of Table 3.3 corresponds to 20° below horizon. The TX-RX angle combinations were

pre-determined by the team before actual measurements were performed, and thus do not represent the best angle combinations that yielded the best signal levels at each RX location. However, the search for the best signals was performed in three pre-determined azimuth planes at elevations of -20°, 0°, and +20°. It must be noted that the angle of departure and angle of arrival measurements were designed while keeping in mind that beamforming algorithms will enable the search for the best possible signal levels in azimuth and elevation planes via electrically-steered phased on-chip antennas arrays.

Table 3.3: The different antenna pointing angle combinations used for all outdoor Manhattan measurements at 28 GHz. "Narrow" and "Wide" mean 24.5 dBi horn antenna (with 10.9° beamwidth) and 15 dBi horn antenna (with 28.8° beamwidth), respectively. The Elevation column represents the number of beamwidths above or below horizon. The TX Azimuth column represents the number of beamwidths left or right from boresight where boresight is the angle with the strongest multipath link found during the initial cursory sweep. Positive beamwidths correspond to a counterclockwise increasing direction about the antenna boresight.

Measurement #	**TX Pol.**	**RX Pol.**	**TX Ant. BW**	**RX Ant. BW**	**TX EL. (# of BW)**	**RX EL. (# of BW)**
1	Narrow	-1	-1/2	V-V	Narrow	0
2	Narrow	-1	-1/2	V-V	Narrow	-2
3	Narrow	-1	-1/2	V-V	Narrow	+2
4	Narrow	-1	0	V-V	Narrow	0
5	Narrow	-1	0	V-V	Narrow	-2
6	Narrow	-1	0	V-V	Narrow	+2
7	Narrow	-1	+1/2	V-V	Narrow	0
8	Narrow	-1	+1/2	V-V	Narrow	-2
9	Narrow	-1	+1/2	V-V	Narrow	+2
10	Narrow	-1	360°	V-V	Narrow	Strongest
11	Narrow	-1	0	V-V	Wide	-1/2
12	Narrow	-1	0	V-V	Wide	0
13	Narrow	-1	0	V-V	Wide	+1/2

3.4.1 Manhattan RX Locations and TX AODs

In total, signal was successfully detected and acquired at 28 RX locations in Manhattan for 3 distinct TX locations, Coles 1 (COL1), Coles 2 (COL2) and Kaufman (KAU). The breakdown of the locations, T-R separation distances, type of environments, and angle conventions used are explained in this section. This section also presents maps of the measured New York Downtown area, identifying all RX locations, the 0° RX azimuth angle as well as the TX 0° angle (AODs) used in the field. The RX locations at which a signal

was detected and recorded can be found in Table 3.4.

Table 3.4: Table showing the T-R separation distances and propagation conditions of all Manhattan locations at which a signal was detected and recorded. The T-R separation distances were obtained with Google SketchUp, an environment modeling software. The TX heights for COL1, COL2, and KAU were 7 m, 7 m, and 17 m above ground level, respectively. The propagation conditions are designated according to Section 3.2.

TX ID	**RX ID**	**T-R Separation (m)**	**Propagation Conditions**
COL1	RX1	31	LOS-NB
COL1	RX2	61	NLOS
COL1	RX3	102	LOS-NB
COL1	RX4	118	NLOS
COL1	RX5	114	NLOS
COL1	RX13	133	NLOS
COL1	RX14	162	NLOS
COL1	RX17	82	NLOS
COL2	RX1	51	LOS-NB
COL2	RX2	74	NLOS
COL2	RX3	143	NLOS
COL2	RX4	156	NLOS
COL2	RX5	150	NLOS
COL2	RX13	138	NLOS
COL2	RX14	169	NLOS
COL2	RX17	112	NLOS
KAU	RX10	77	NLOS
KAU	RX11	54	LOS-NB
KAU	RX12	120	NLOS
KAU	RX14	82	NLOS
KAU	RX16	97	NLOS
KAU	RX18	187	NLOS
KAU	RX19	175	NLOS
KAU	RX21	117	NLOS
KAU	RX22	180	NLOS
KAU	RX26	70	O-to-I
KAU	RX30	54	LOS-B
KAU	RX31	33	LOS-B

3.4.2 RX Location Maps

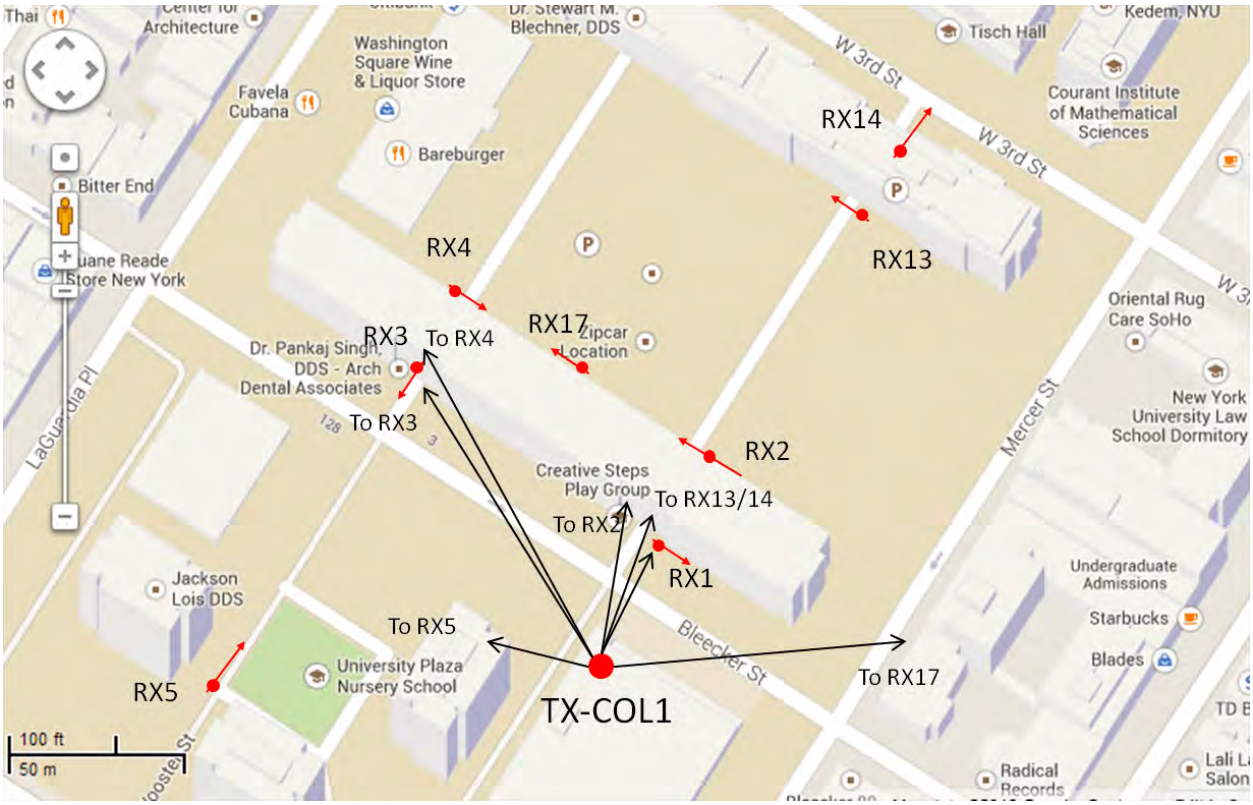

Figure 3.4: RX locations for COL1. The black arrows originating from the TX location indicate the TX azimuth 0° for a particular RX location. The arrows at each RX location point in the direction of the RX azimuth 0° direction during the field measurements. Note that the RX azimuth 0° for COL1 RX1 shown on this map is only valid for Configs. 3-9, see Section 3.3 for the RX azimuth 0° used for Configs. 1 and 2.

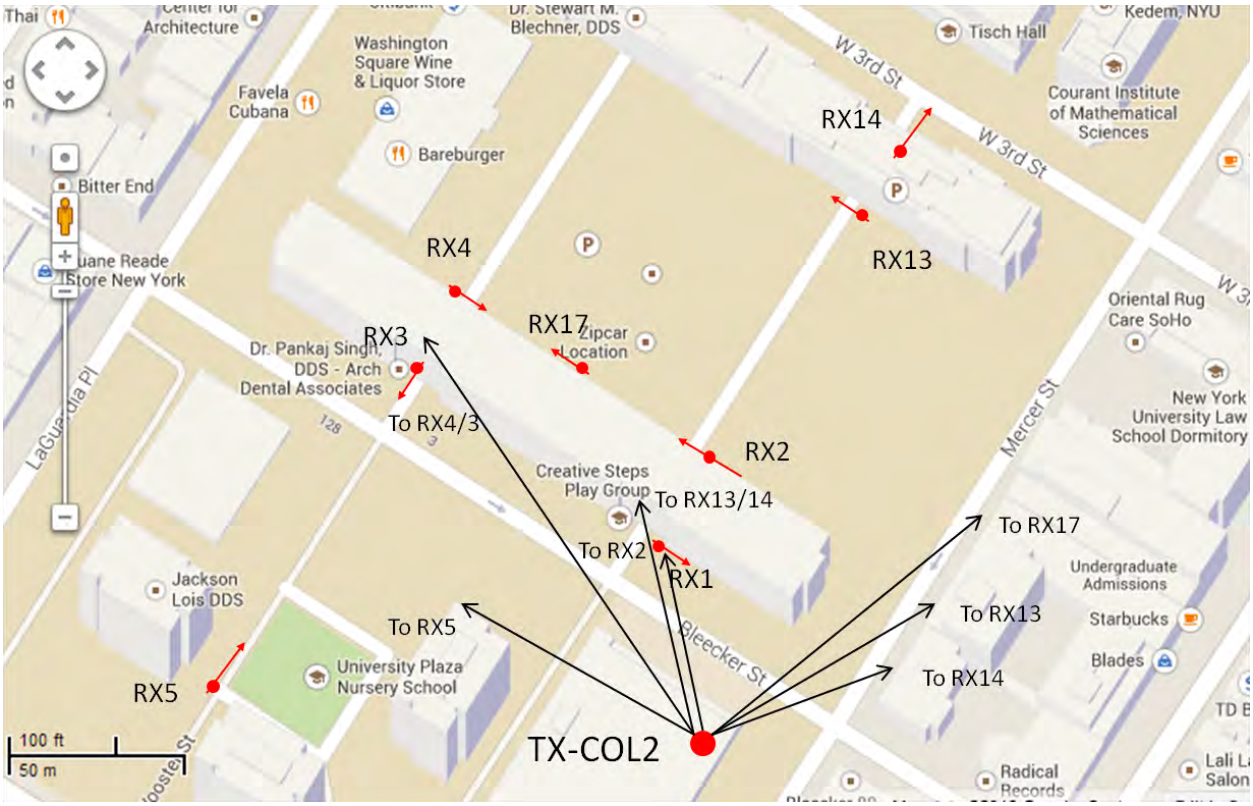

Figure 3.5: RX locations for COL2. The black arrows originating from the TX location indicate the TX azimuth 0° for a particular RX location. The arrows at each RX location point in the direction of the RX azimuth 0° direction during the field measurements.

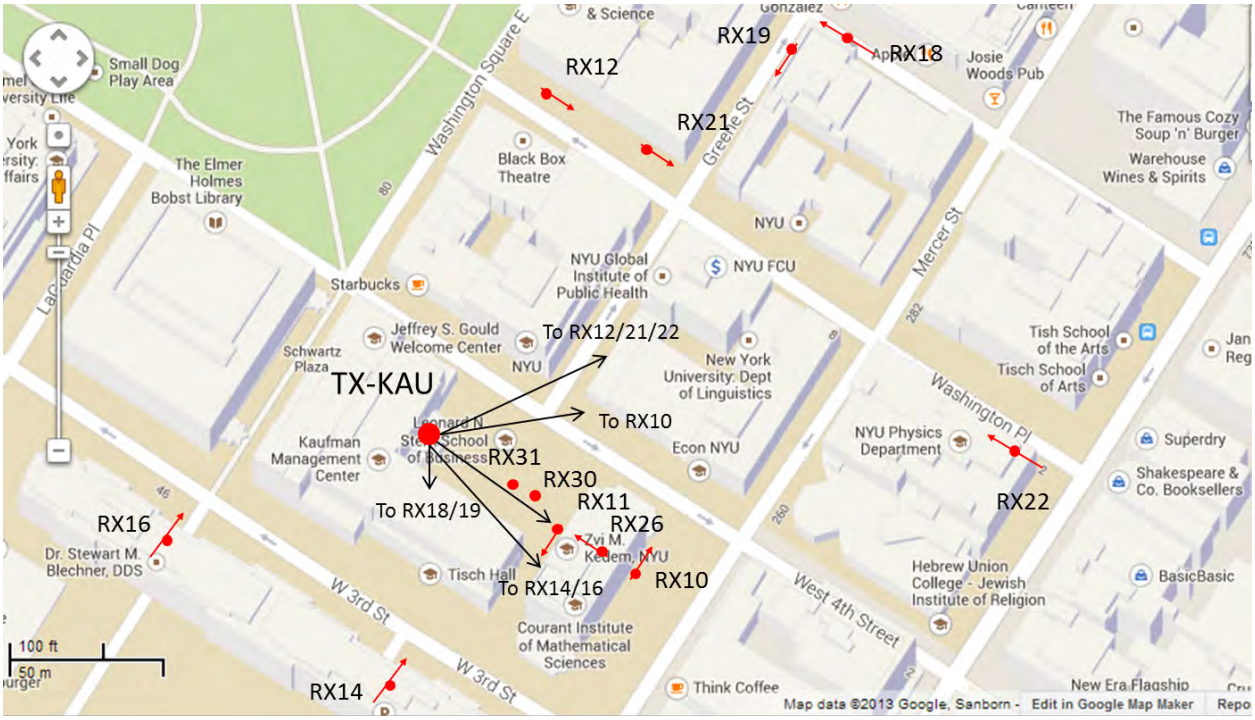

Figure 3.6: RX locations for KAU. The black arrows originating from the TX location indicate the TX azimuth 0° for a particular RX location. The arrows at each RX location point in the direction of the RX azimuth 0° direction during the field measurements. TX AODs for KAU RX30 and 31 are directed straight at RX30 and RX31 (not shown on this map).

A description of exact RX locations, and the directions in which the TX 0° and RX 0° azimuth angles were pointed during the field measurements are given below. The maps above visually summarize the contents of the following section.

3.4.3 Receiver Locations: Coles 1 (COL1)

COL1 - RX1: Line of sight environment. The RX was located on the sidewalk of Bleecker St., to the right of the entrance of 4 Washington Square Village tunnel (observing from TX-COL1). The TX antenna 0° in the azimuth plane was pointed straight at the RX location, with a downtilt of 10°. The RX antenna 0° in the azimuth plane was pointed straight at TX-COL1 for antenna pointing combinations #1 and #2, and then was switched to pointing parallel to Bleecker St. towards Mercer St. for antenna pointing combinations #3-9.

COL1 - RX2: Moderately obstructed environment. The RX was located at the exit of 4 Washington

Square village tunnel, to the right (observing from TX-COL1). The TX antenna 0° in the azimuth plane was pointed to the left of 4 Washington Square Village tunnel, and to the right of the left most pillar (as observing from TX-COL1), with a downtilt of 10°. The RX antenna 0° in the azimuth plane was pointed parallel to Bleecker St., pointing away from Mercer St.

COL1 - RX3: Line of sight environment. The RX was located inside 3 Washington Square Village tunnel, on the side walk closest to Laguardia Place, and closest to Bleecker St. The TX antenna 0° in the azimuth plane was pointed towards RX3, in between the two pillars at the entrance of the tunnel (as observing from TX-COL1), with a downtilt of 10°. The RX antenna 0° in the azimuth plane was pointed towards Bleecker St., perpendicularly to Bleecker St.

COL1 - RX4: Heavily obstructed environment. The RX was located at the exit of 3 Washington Square Village tunnel, to the left (observing from TX-COL1). The TX antenna 0° in the azimuth plane was pointed towards 3 Washington Square Village tunnel, and to the right of the right most pillar (as observing from TX-COL1), with a downtilt of 10°. The RX antenna 0° in the azimuth plane was pointed parallel to Bleecker St., pointing away from Laguardia Place.

COL1 - RX5: Heavily obstructed environment. The RX was located in between the Silver Towers, at the intersection of Wooster and the west-most road encircling the park located in between the towers. The TX antenna 0° in the azimuth plane was pointed at the center of the north-most face of the east-most Silver Tower, with a downtilt of 10°. The RX antenna 0° in the azimuth plane was pointed parallel to Wooster St., pointing towards Mercer St.

COL1 - RX13: Heavily obstructed environment. The RX was located inside Washington Square Park, at the exit of 2 Washington Square Village tunnel, to the right of the tunnel (as observing from TX-COL1). The TX antenna 0° in the azimuth plane was pointed to the center of 4 Washington Square Village tunnel

(as observing from TX-COL1), with a downtilt of 10°. The RX antenna 0° in the azimuth plane was pointed parallel to Bleecker St., pointing away from Mercer St.

COL1 - RX14: Heavily obstructed environment. The RX was located inside 2 Washington Square Village tunnel on the sidewalk closest to Mercer St., and closest to West 3rd St. The TX antenna 0° in the azimuth plane was pointed to the center of 4 Washington Square Village tunnel (as observing from TX-COL1), with a downtilt of 10°. The RX antenna 0° in the azimuth plane was pointed parallel to Mercer St., pointing towards West 3rd St.

COL1 - RX17: Heavily obstructed environment. The RX was located inside Washington Square Park, in the exact middle between 3 Washington Square Village and 4 Washington Square Village, closest to Bleecker St. The TX antenna 0° in the azimuth plane was pointed at the north-west corner of the intersection of Bleecker St. and Mercer St., with a downtilt of 10°. The RX antenna 0° in the azimuth plane was pointed parallel to Bleecker St., pointing away from Mercer St.

3.4.4 Receiver Locations: Coles 2 (COL2)

COL2 - RX1: Line of sight environment. The RX was located on the sidewalk of Bleecker St., to the right of the entrance of 4 Washington Square Village tunnel (observing from TX-COL2). The TX antenna 0° in the azimuth plane was pointed straight at the RX location, with a downtilt of 10°. The RX antenna 0° in the azimuth plane was pointed parallel to Bleecker St., towards Mercer St.

COL2 - RX2: Moderately obstructed environment. The RX was located at the exit of 4 Washington Square village tunnel, to the right of the tunnel (observing from TX-COL1). The TX antenna 0° in the azimuth plane was pointed at the center of the entrance to 4 Washington Square Village tunnel (as observing from TX-COL2), with a downtilt of 10°. The RX antenna 0° in the azimuth plane was pointed parallel to Bleecker St., pointing away from Mercer St.

COL2 - RX3: Line of sight environment. The RX was located inside 3 Washington Square Village tunnel, on the side walk closest to Laguardia Place, and closest to Bleecker Street. The TX antenna 0° in the azimuth plane was pointed towards 3 Washington Square Village tunnel, and to the right of the right most pillar (as observing from TX-COL2), with a downtilt of 10°. The RX antenna 0° in the azimuth plane was pointed towards Bleecker Street, perpendicularly to Bleecker Street.

COL2 - RX4: Heavily obstructed environment. The RX was located at the exit of 3 Washington Square Village tunnel, to the left (observing from TX-COL2). The TX antenna 0° in the azimuth plane was pointed towards 3 Washington Square Village tunnel, and to the right of the right most pillar (as observing from TX-COL2), with a downtilt of 10°. The RX antenna 0° in the azimuth plane was pointed parallel to Bleecker Street, pointing away from Laguardia Place (towards the center of the park).

COL2 - RX5: Heavily obstructed environment. The RX was located in between the Silver Towers, at the intersection of Wooster and the west-most road encircling the park located in between the towers. The TX antenna 0° in the azimuth plane was pointed at the center of the north-most building corner of the east-most Silver Tower, with a 0° elevation angle (the only case for which the TX antenna was not at a 10° downtilt). The RX antenna 0° in the azimuth plane was pointed parallel to Wooster St., pointing towards Mercer St.

COL2 - RX13: Heavily obstructed environment. The RX was located inside Washington Square Park, at the exit of 2 Washington Square Village tunnel, to the right of the tunnel (as observing from TX-COL2). The TX antenna 0° in the azimuth plane was pointed at the center of the intersection of Bleecker St. and Mercer St., with a downtilt of 10°. The RX antenna 0° in the azimuth plane was pointed parallel to Bleecker St., pointing away from Mercer St.

COL2 - RX14: Heavily obstructed environment. The RX was located inside 2 Washington Square Village tunnel on the sidewalk closest to Mercer St., and closest to West 3rd St. The TX antenna 0° in the azimuth plane was pointed at the south-east corner of the intersection of Bleecker St. and Mercer St., with a downtilt of 10°. The RX antenna 0° in the azimuth plane was pointed parallel to Mercer St., pointing towards West 3rd St.

COL2 - RX17: Heavily obstructed environment. The RX was located inside Washington Square Park, in the exact middle between 3 Washington Square Village and 4 Washington Square Village, closest to Bleecker St. The TX antenna 0° in the azimuth plane was pointed at the north-west corner of the intersection of Bleecker St. and Mercer St. with a downtilt of 10°. The RX antenna 0° in the azimuth plane was pointed parallel to Bleecker St., pointing away from Mercer St.

3.4.5 Receiver Locations: Kaufman (KAU)

KAU - RX10: Highly obstructed environment. The RX was located in between the pair of pillars immediately to the left of the Mercer St. entrance to Warren Weaver Hall, 1 meter away from the glass windows. The TX antenna 0° in the azimuth plane was pointed at the intersection of West 4th St. and Greene St., with a downtilt of 10°. The RX antenna 0° in the azimuth plane was pointed parallel to Mercer St., pointing towards West 4th St.

KAU - RX11: Line of sight environment. The RX was located in between the pair of pillars immediately to the right of the back entrance to Warren Weaver Hall, 3 meters away from the glass windows. The TX antenna 0° in the azimuth plane was pointed straight at the RX, with a downtilt of 10°. The RX antenna 0° in the azimuth plane was pointed parallel to Mercer St., pointing towards West 4th St.

KAU - RX12: Heavily obstructed environment. The RX was located on the north sidewalk of Washington Place, in between Greene St. and Washington Square East, two thirds of the block away from the

intersection of Washington Place and Greene St. The TX antenna 0° in the azimuth plane was pointed at the north-west corner of the intersection of West 4th St. and Greene St., with a downtilt of 10°. The RX antenna 0° in the azimuth plane was pointed parallel to Washington Place, pointing towards Greene St.

KAU - RX14: Heavily obstructed environment. The RX was located inside 2 Washington Square Village tunnel on the sidewalk closest to Mercer St., and closest to West 3rd St. The TX antenna 0° in the azimuth plane was pointed towards the alley between Warren Weaver Hall and Stern, to the right of Warren Weaver Hall as seen from TX-KAU, with a downtilt of 10°. The RX antenna 0° in the azimuth plane was pointed parallel to Mercer St., pointing towards West 3rd St.

KAU - RX16: Heavily obstructed environment. The RX was located inside 1 Washington Square Village tunnel, on the sidewalk closest to Laguardia Place and closest to West 3rdSt. The TX antenna 0° in the azimuth plane was pointed towards the alley between Warren Weaver Hall and Stern, to the right of Warren Weaver Hall as seen from TX-KAU, with a downtilt of 10°. The RX antenna 0° in the azimuth plane was pointed parallel to Laguardia Place, pointing towards West 3rd St.

KAU - RX18: Heavily obstructed environment. The RX was located on the south sidewalk of Waverly Place, in between Greene St. and Mercer St., one third of the block away from the intersection of Waverly Place and Greene St.. The TX antenna 0° in the azimuth plane was pointed towards Stern, such that the reflection from Stern enters directly into Greene St., with a downtilt of 10°. The RX antenna 0° in the azimuth plane was pointed parallel to Waverly Place, towards Greene St.

KAU - RX19: Heavily obstructed environment. The RX was located on the west sidewalk of Greene St., in between Washington Place and Waverly Place, one third of the block away from the intersection of Waverly Place and Greene St. The TX antenna 0° in the azimuth plane was pointed towards Stern, such that the reflection from Stern enters directly into Greene St., with a downtilt of 10°. The RX antenna 0° in

the azimuth plane was pointed parallel to Greene St., towards Washington Place.

KAU - RX21: Heavily obstructed environment. The RX was located on Washington Place, in between Greene Street and Washington Square East, one third of the block away from the intersection of Greene St. and Washington Place. The TX antenna 0° in the azimuth plane was pointed at the north-west corner of the intersection of West 4^{th} St. and Greene St., with a downtilt of 10°. The RX antenna 0° in the azimuth plane was pointed parallel to Washington Place, pointing towards Greene St.

KAU - RX22: Heavily obstructed environment. The RX was located on the south sidewalk of Washington Place, in between Mercer St. and Broadway, one third of the block away from the intersection of Washington Square Place and Broadway. The TX antenna 0° in the azimuth plane was pointed at the north-west corner of the intersection of West 4^{th} St. and Greene St., with a downtilt of 10°. The RX antenna 0° in the azimuth plane was pointed parallel to Washington Place, pointing towards Mercer St.

KAU - RX26: Outdoor-to-Indoor. The RX was located inside Warren Weaver Hall, on the ground floor, in the lobby separating the front and back entrances. The TX antenna 0° in the azimuth plane was pointed straight at the back entrance of Warren Weaver Hall straight at the RX, with a downtilt of 10°. The RX antenna 0° in the azimuth plane was pointed straight at the TX location.

KAU - RX30: Optical line of sight measurement. The RX was located in between Warren Weaver Hall, Stern and the Kaufman building. The TX and RX antennas were pointed on boresight to each other.

KAU - RX31: Optical line of sight measurement. The RX was located in between Warren Weaver Hall, Stern and the Kaufman building. The TX and RX antennas were pointed on boresight to each other.

3.5 28 GHz Hardware Equipment

3.5.1 Channel Sounder Operation

A 400 Mcps broadband sliding correlator channel sounder was used to measure the 28 GHz wideband urban channel over a 800 MHz null-to-null RF bandwidth. The transmitter output power was varied between 11 dBm and 30 dBm, depending on the RX location and the RX environment. Two highly directional horn antennas of 24.5 dBi (10.9° and 8.6° half-power beamwidths (HPBW) in the azimuth and elevation planes, respectively) were used at the TX and RX which improved system dynamic range by 49 dB, allowing for a total of 178 dB of measurable path loss (including 42 dB of processing gain [81]) for the Manhattan measurements. The RF signal was obtained by first generating a pseudo-random noise (PN) sequence clocked at 400 MHz, which was mixed with an intermediate frequency (IF) of 5.4 GHz. The IF was then mixed via a Spacek Labs up-converter with a 22.6 GHz local oscillator (LO) allowing for a 800 MHz null-to-null signal centered around the 28 GHz band, which was subsequently fed through the horn antenna and broadcasted into the wireless channel. At the receiver side, the received RF signal was down-converted to IF via a 22.6 GHz LO, and split into its in-phase (I) and quadrature (Q) baseband components. Each component was then sent through a sliding correlator, which performed the correlation between the incoming received signal and an identical PN sequence clocked at a slightly lower frequency of 399.95 MHz. Both I and Q channels were digitized via a National Instruments digitizer at a sampling rate of 2 megasamples/s, and power delay profiles (PDP) were recovered by squaring and adding the I and Q waveforms, i.e., $I^2 + Q^2$. The final recorded data was an averaged PDP, obtained by averaging 20 instantaneous PDPs.

3.5.2 TX-RX Block Diagrams and Channel Sounder Specifications

Fig. 3.7 and Fig. 3.8 show the block diagrams of the TX and RX systems, and Table 3.5 shows the specifications of the 28 GHz sliding correlator channel sounder used during this propagation measurement campaign in New York City.

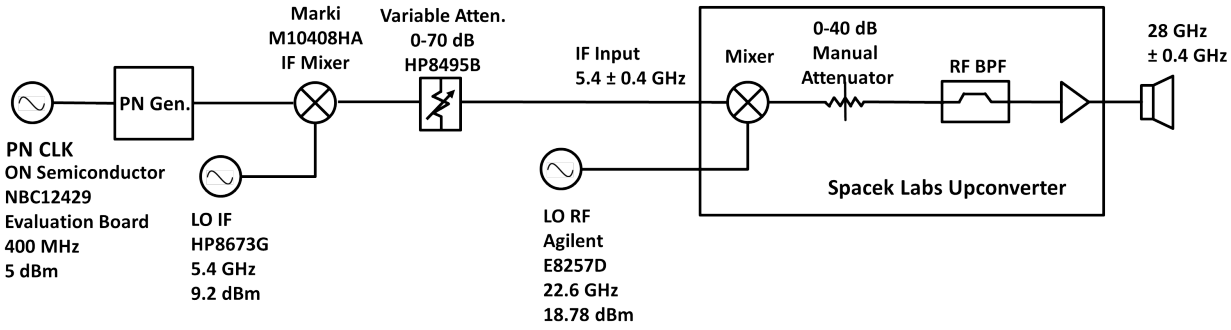

Figure 3.7: 28 GHz transmitter block diagram.

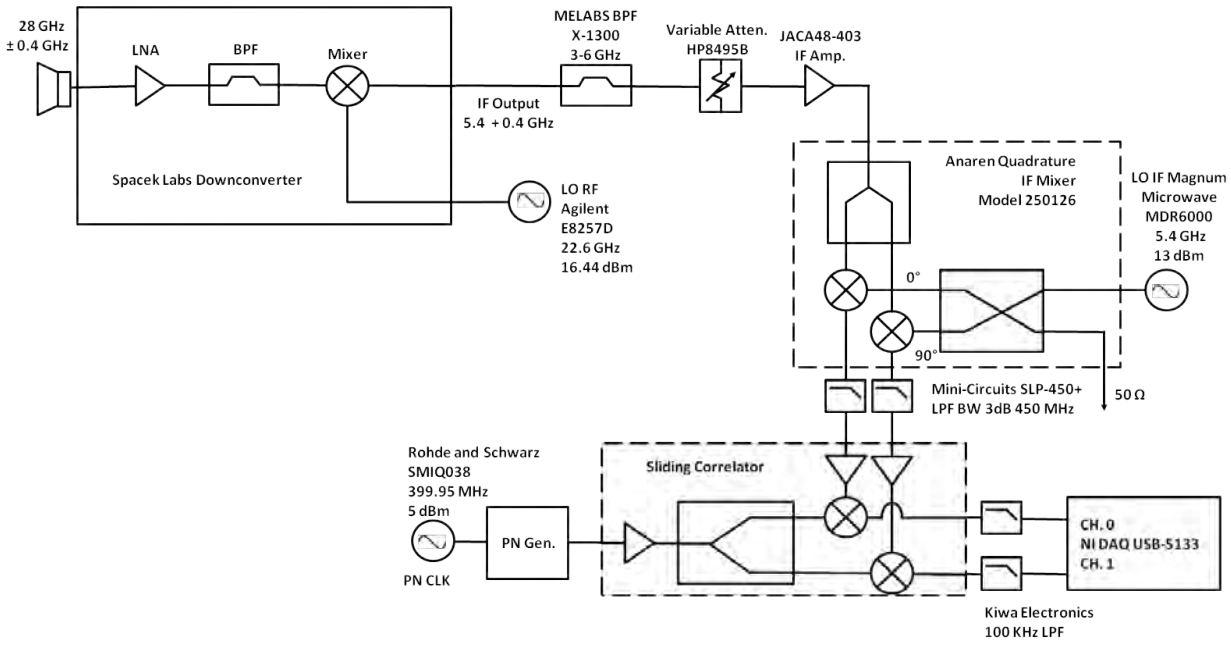

Figure 3.8: 28 GHz receiver block diagram.

Table 3.5: 28 GHz channel sounder specifications.

Description	**Value**
Sequence	11^{th} Order PN Code (Length = 2047)
Transmitted Chip Rate	400 MHz
Receiver Chip Rate	399.95 MHz
RF Bandwidth (Null-to-Null)	800 MHz
Slide Factor	8000
Carrier Frequency	28 GHz
NI Digitizer Sampling Rate	2 MSamples/s
System Measurement Range (5 dB SNR)	178 dB
TX Maximum Output Power	30 dBm
TX-RX Antenna Gains	15 dBi and 24.5 dBi
Multipath Time Resolution	2.5 ns
TX-RX Synchronization	Unsupported

3.5.3 Narrowbeam and Widebeam Antenna Patterns

Two types of directional horn antennas were used for the Brooklyn and Manhattan measurements: a widebeam 15 dBi and a narrowbeam 24.5 dBi gain antennas, both specified to operate in the K_a - Band. The figures below show the measured co- polarization antenna patterns for the 15 dBi and 24.5 dBi antennas.

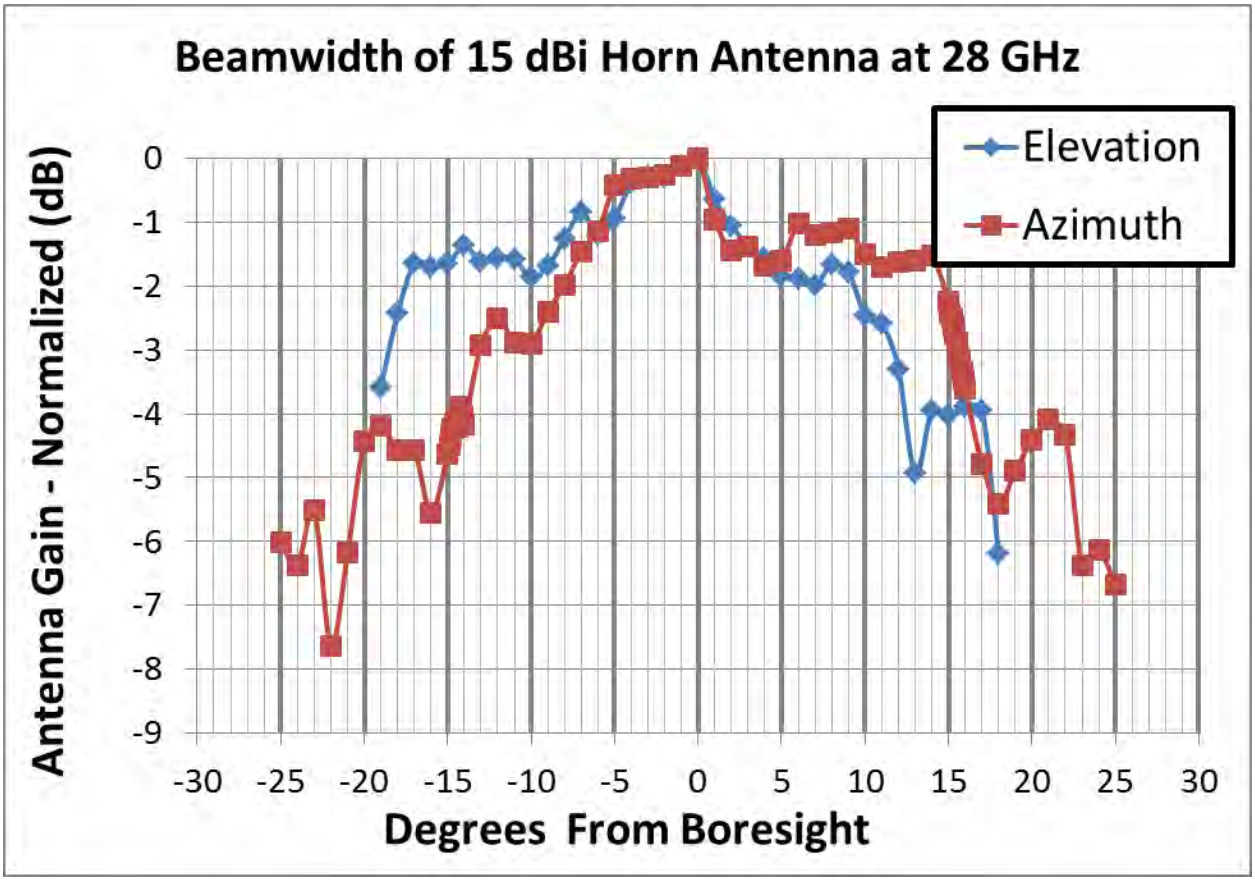

Figure 3.9: At 28 GHz, the 15 dBi horn antenna had a 3 dB beamwidth of 28.8° in azimuth and 30° in elevation planes. The antenna was oriented with vertical polarization (i.e. the received electric field was perpendicular to ground).

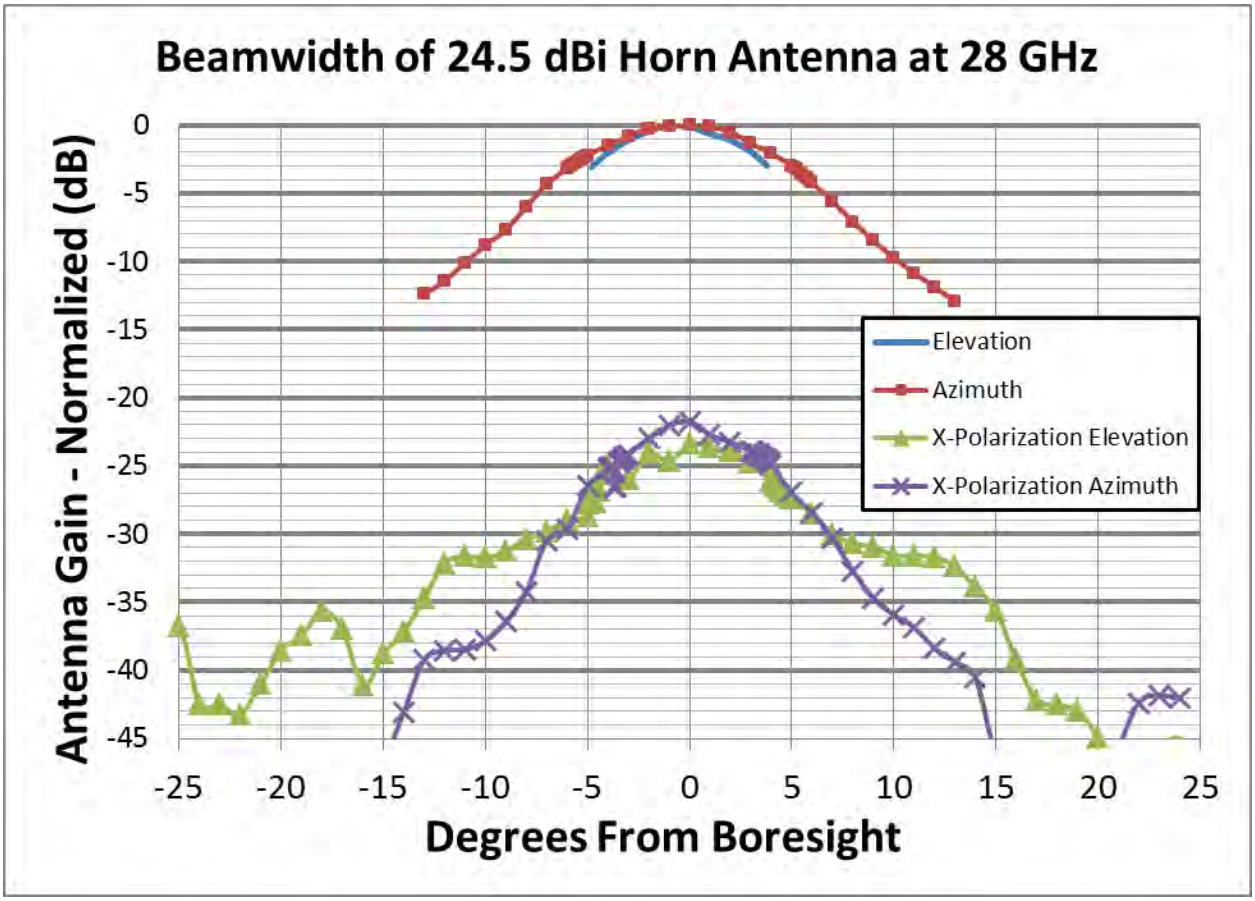

Figure 3.10: At 28 GHz using 3 m separation, the 24.5 dBi horn antenna had an elevation and azimuth 3 dB beamwidth of 8.6° and 10.9°, respectively. The antenna was oriented with vertical polarization (i.e. the received electric field was perpendicular to ground). When excited with a horizontal polarization, the cross-polarized elevation and azimuth 3 dB beamwidths were 7.4° and 8.6°, respectively. Note the cross-polarized gain is -21.74 dB below the co-polarized level.

3.5.4 Derivation of the Slide Factor

The theory of sliding correlation is fairly well understood, and can be obtained from one of the following references [82][83][84][85][86][87]. It seems however that the derivation for the slide factor, a key aspect in understanding sliding correlation, is lacking throughout the sliding correlation literature, and so its derivation is given below as it may provide additional insight into the mechanics of sliding correlation and its properties. In the channel sounding system described above, an incoming PN sequence is correlated with an identical reference PN sequence clocked at a slightly lower frequency at the receiver, producing a maximum peak when the two PN sequences are in-phase, and interference when the two PN sequences are out of phase.

The detection of a peak physically corresponds to the arrival of an incoming multipath component. The slight frequency shift between the two PN sequences produces a 'time dilation', or in other words, actual propagation time of arrivals is stretched out.

In order to understand this phenomenon, let the incoming PN and reference PN sequences, whose frequencies are denoted as f_{tx} and f_{rx} respectively, start out perfectly in-phase and allowed to run. Lets determine the observed time T_{obs} required for the two codes to re-appear in-phase again. In an observed time T_{obs}, the phase difference, or the offset in the number of chips ΔC, between the two codes will be:

$$\Delta C = \frac{T_{obs}}{T_{tx}} - \frac{T_{obs}}{T_{rx}} \tag{3.1}$$

where T_{tx} and T_{rx} are the incoming PN and reference PN sequence chip periods, respectively. Here we implicitly assume that $f_{tx} > f_{rx}$.

We also know that ΔC must equal an integer multiple of the number of chips in one period of the PN sequence in order for the two PN sequences to re-appear in phase. Thus, $\Delta C = nL$, where L is the number of chips in a period of the PN sequence, and n is an integer. We can now solve for the observed time T_{obs} required for the two PN sequences to correlate and produce a spike:

$$\Delta C = \frac{T_{obs}}{T_{tx}} - \frac{T_{obs}}{T_{rx}} = nL \tag{3.2}$$

$$T_{obs}\frac{T_{rx} - T_{rx}}{T_{rx}T_{tx}} = nL \tag{3.3}$$

$$T_{obs} = \frac{nLT_{rx}T_{rx}}{T_{rx} - T_{tx}} \tag{3.4}$$

$$T_{obs} = nT\gamma \tag{3.5}$$

where $LT_{tx} = T$, the period of the incoming PN sequence, and $\frac{T_{rx}}{T_{rx}-T_{tx}} = \gamma$ is the slide factor. We can rewrite the slide factor in terms of the original PN sequence frequencies, which yields:

$$\gamma = \frac{\frac{1}{f_{rx}}}{\frac{1}{f_{rx}} - \frac{1}{f_{tx}}} = \frac{1}{f_{rx}} \times \frac{f_{rx} f_{tx}}{f_{tx} - f_{rx}} = \frac{f_{tx}}{f_{tx} - f_{rx}} \tag{3.6}$$

Substituting for the frequencies used in the 28 GHz channel sounder, we get:

$$\gamma = \frac{400}{400 - 399.95} = 8000 \tag{3.7}$$

Thus, there is a linear mapping between the observed time, also called the 'dilated time', and the actual propagation time, also called 'undilated time', where the constant of proportionality between dilated and undilated time is the slide factor. The observed time for the two PN sequences to slide past each other, or produce a correlation spike, is:

$$T_{obs} = LT_{tx}\gamma \tag{3.8}$$

The digitizer provides the time array $t_{obs} = kT_{dig}$, where T_{dig} is the sampling period, and k is an integer. In order to recover actual propagation time of arrival (i.e., undilated time), one must divide the sampled time array by the slide factor. Thus,

$$t_{undilated} = \frac{t_{obs}}{\gamma} = \frac{kT_{dig}}{\gamma} \tag{3.9}$$

3.6 28 GHz Path Loss Results

3.6.1 Brooklyn and Manhattan Path Loss Exponent Plots

Fig. 3.11 shows all 28 GHz Manhattan path loss values measured with 24.5 dBi TX and RX antennas, obtained at each measured RX azimuth and elevation angle combinations using the nine RX antenna pointing combinations, and the 10^{th} TX antenna pointing combination at each T-R separation, for NLOS and LOS environments. Since each antenna pointing combination consisted in rotating the RX antenna in 10° step increments, a maximum of 36 possible measurements could be performed for each antenna pointing combination, with up to 360 measured channel impulses when considering all 10 antenna pointing combina-

tions for a given RX location. These results were published in [88] and [89] for a 5 m free space reference, and are now shown here for a 1 m free space reference. The NLOS path loss exponent and shadowing factor with respect to a 1 m free space reference distance were found to be 4.4 and 10.0 dB over all NLOS measurements, respectively. Here, "NLOS" refers to LOS NB and NLOS environments. However, when considering the strongest TX-RX unique pointing angle with the lowest path loss at each T-R separation, the best path loss exponent and shadowing factor were reduced to 3.7 and 9.2 dB respectively, indicating the advantage of employing beamforming and beam combining at the receiver to significantly improve link margin [90]. It must be emphasized that beamforming and beam combining technologies using electrically-phased on chip antennas will combine received energy from multiple incoming directions to improve signal quality, as demonstrated in [90][91][92].

The models shown in Fig. 3.11 are directional models, in the sense that they allow one to estimate the path loss observed at an arbitrary azimuth and elevation combination. Directional models are in direct contrast with omnidirectional models, which allow one to estimate the path loss as if measured using an omnidirectional antenna, capable of receiving energy uniformly throughout the azimuth and elevation planes. These omnidirectional models are recovered and discussed in Chapter 5. These directional path loss models shown in Fig. 3.11, while not in use today in standards work, are applicable for estimating the received power at a unique RX azimuth and elevation angle combination for a fixed TX azimuth with -10° downtilt for any TX height ranging from 7 m to 17 m, and are invaluable in designing mmWave radio systems which will incorporate beamforming and beam combining algorithms.

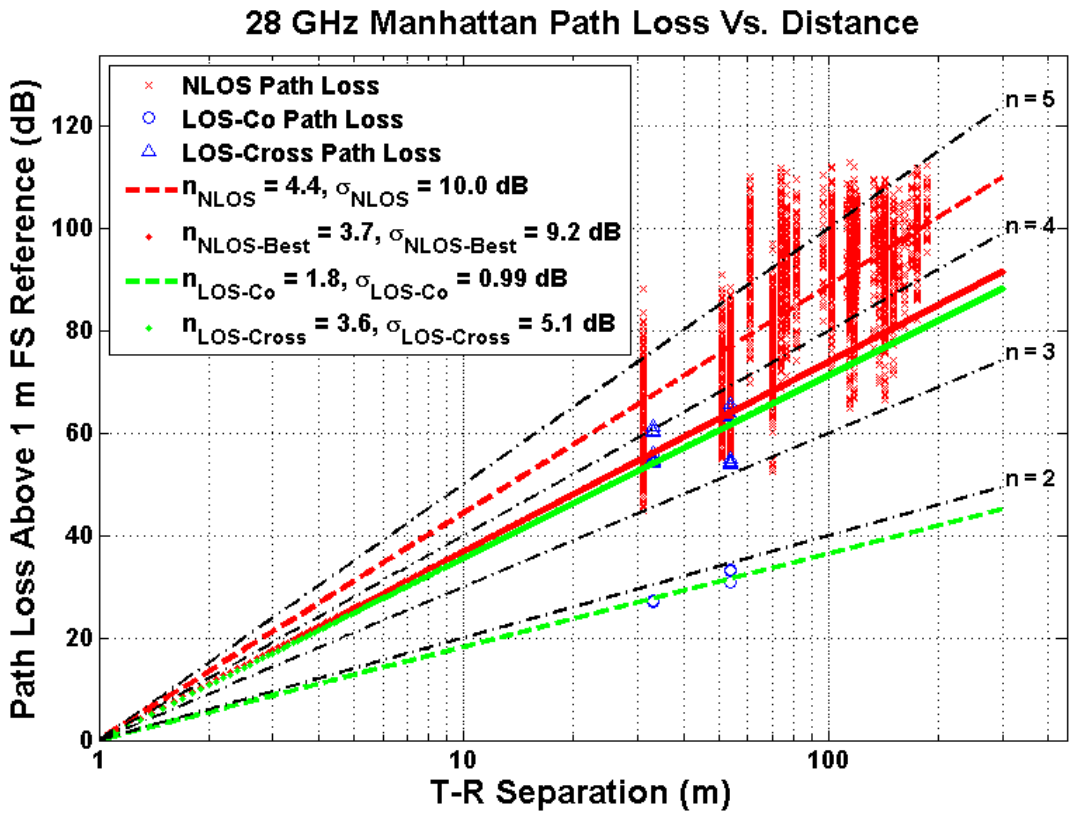

Figure 3.11: 28 GHz Manhattan single beam path losses as a function of T-R separation using 24.5 dBi (10.9° HPBW) antennas at both the TX and RX, and 15 dBi (28.8° HPBW) horn antennas at both the TX and RX. NLOS path losses include LOS NB and truly NLOS measurements. Co-polarized and cross-polarized LOS measured path losses are also shown. The corresponding close-in reference equation lines with respect to a 1 m free space reference distance are shown.

Fig. 3.12 shows the 28 GHz path loss values measured at each of the measured RX azimuth and elevation angle combiniations using the 11 antenna pointing combinations at each of the five NLOS RX locations in Brooklyn at which signal was detected and acquired. The path loss exponent and shadowing factor with respect to a 1 m free space reference distance for co-polarized measurements (VV and HH) were found to be 4.5 and 8.1 dB respectively, while the best path loss exponent and shadowing factor were obtained from the strongest TX-RX angular links, and were found to be 3.6 and 4.1 dB respectively. Cross-polarized measurements (VH) yielded a path loss exponent and shadowing factor of 4.8 and 5.2 dB. Measurements with a widebeam TX antenna and narrowbeam RX antenna yielded a path loss exponent and shadowing factor of 4.1 and 7.1 dB. Finally, measurements performed with narrowbeam antennas at both the TX and

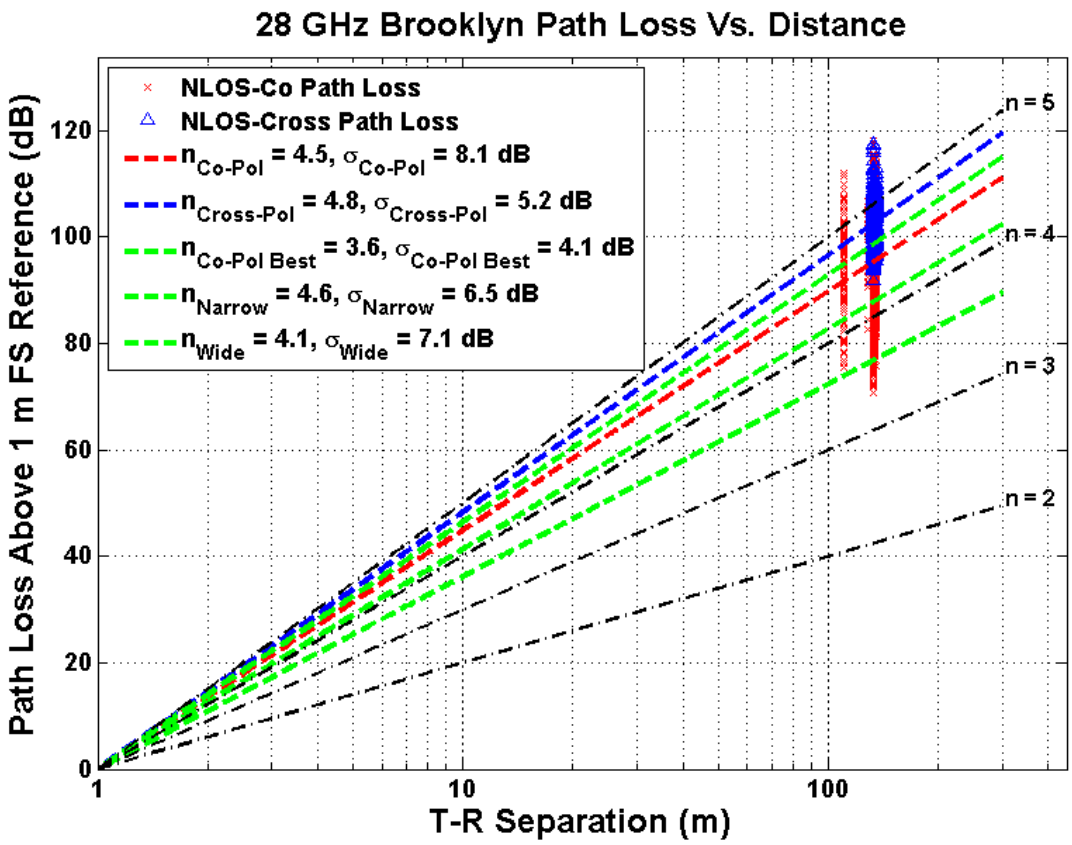

Figure 3.12: 28 GHz Brooklyn single beam path losses as a function of T-R separation using a narrowbeam 24.5 dBi (28.8° HPBW) horn antenna at the RX, and either a widebeam 15 dBi or narrowbeam 24.5 dBi (10.9° HPBW) antenna at the TX (depending on the antenna pointing combination). In the legend, "co-Pol" refers to co-polarized measurements (VV and HH), "cross-Pol" refers to cross-polarized measurements (VH), "Narrow" corresponds to measurements obtained with a 24.5 dBi horn antennas at both the TX and RX, while "wide" refers to measurements obtained with a 15 dBi horn antenna at the TX, and a 24.5 dBi horn antenna at the RX.

RX yielded a path loss exponent and shadowing factor of 4.6 and 6.5 dB.

3.7 Conclusion

This section presented the details and logistics of the 28 GHz measurements in Brooklyn and Manhattan obtained in the summer of 2012, and preliminary path loss results for unique TX-RX pointing angle combinations. The post-processing procedures applied to the collected measurements are presented in Chapter 4.

Chapter 4

Post-Processing Procedures for the 28 GHz Collected Measurements

4.1 Recovering RF Received Power from the Collected Measurements

4.1.1 Theoretical Considerations

An ideal multipath component is commonly represented as a delta spike, with an amplitude equal to its total received power. In practice, however, it is not feasible to observe and record the power envelope of an ideal multipath component as this would require infinite sampling resolution. Instead, we define the total power in a multipath component as the sum (in linear units) of the individual sample powers making up the digitized multipath component arising from the cross-correlation of the incoming TX PN sequence and the reference RX PN sequence, denoted as P_{field} in Eq. 4.1.

$$P_{field} = 10 \times \log_{10} \left(\sum_{m=0}^{M-1} P_{field}(\tau_m) \right) \tag{4.1}$$

where $P_{field}(\tau_m)$ is the instantaneous observed power level of a measurement sample in mW at the excess time delay τ_m, and M is the number of sample points making up *a multipath component*.

The RX system is a composition of amplifiers (downconverter, low noise amplifiers and sliding correlator gains) and attenuators (mixers and lossy cables), and can be regarded as an amplifier with a net gain $G^{Avg}_{RX,NL}$ (See Chapter 3). Outside factors such as temperature and pressure will also affect the net gain. This amplifying system will operate on all input powers in the same manner provided they are within a certain range, and will saturate if the input power level is either too little or too great. The gain of this net RX system is therefore highly non-linear with respect to RF input power, in the sense that the gain associated with an input RF power lying in between $P_{RF,min}$ and $P_{RF,max}$ will be constant, while the gain associated with an input power lower than $P_{RF,min}$ or greater than $P_{RF,max}$ will be less due to amplifier saturation. When the RF input power lies in between $P_{RF,min}$ and $P_{RF,max}$, this RF input power is said to lie in the linear range of the RX system. Since the net gain of the RX system will vary with respect to RF power, the RX system gain must be characterized for all incoming power levels to obtain a complete description of its behavior.

The total RF power in a multipath component is then related to the total observed power as in Eq. 4.2,

$$P_{RF,true} + G^{Avg}_{RX,NL} = P_{field} \tag{4.2}$$

where $G^{Avg}_{RX,NL}$ stands for the non-linear (NL) average RX system gain in dB, $P_{RF,true}$ is the total RF power in the incoming multipath component in dBm, and P_{field} is the total multipath power in dBm measured at baseband.

In theory, it is possible to completely characterize $G^{Avg}_{RX,NL}$ for all ranges of RF input powers using a calibration routine, however in practice, it is sufficient to characterize $G^{Avg}_{RX,NL}$ in the linear range of the RX system, which we shall call $G^{Avg}_{RX,L}$.

4.1.1.1 RF Calibration Routine

The purpose of a calibration routine is to provide a day-to-day characterization of the RX system, that is, provide a one-to-one mapping between RF input multipath power and observed multipath power at baseband from a field measurement.

A RF calibration measurement should ideally be performed in a controlled multipath environment, where the T-R separation distances and TX output powers are chosen appropriately, so as to map the power in the LOS RF incoming multipath to that same multipath power observed from a baseband measurement, the ratio in powers representing the net gain of the RX system. This can be done for several known T-R separation distances, for instance, d_0 = 5 m, 10 m, 15 m, 20 m, etc. Using the Friis free space path loss formula, it is possible to compute the theoretical RF input power of an ideal delta spike multipath, and thus relate it to the observed baseband multipath power. A one-to-one mapping can then be produced between RF input power and measured power, which completely characterizes the RX system, i.e., the gain of the RX system as a function of RF input power.

However, it is very tedious and time-consuming to separate the TX from the RX for several T-R distances in a real calibration measurement. In order to increase the speed of the calibration procedure, a constant T-R separation distance is chosen, and a variable RX attenuator is added to the RX system at the IF stage and stepped in 10 dB increments to simulate an increase in path loss, effectively simulating an increase in T-R separation distance. Note that in this scheme, the RF input power is constant, since the T-R distance does not change, while the RX power level input into the sliding correlator is attenuated in steps of 10 dB.

The multipath power in the LOS component can then be computed and plotted as a function of the RX attenuation setting, as in Fig. 4.1. Note that if multipath components other than the strongest LOS component appear on the calibration power delay profiles, they should be disregarded. Only the LOS component should be treated, since the mapping between RF input power and the measurement can only be done for the LOS component using the Friis transmission formula.

The following graph is a typical calibration graph characterizing the RX system, where the y-axis is the

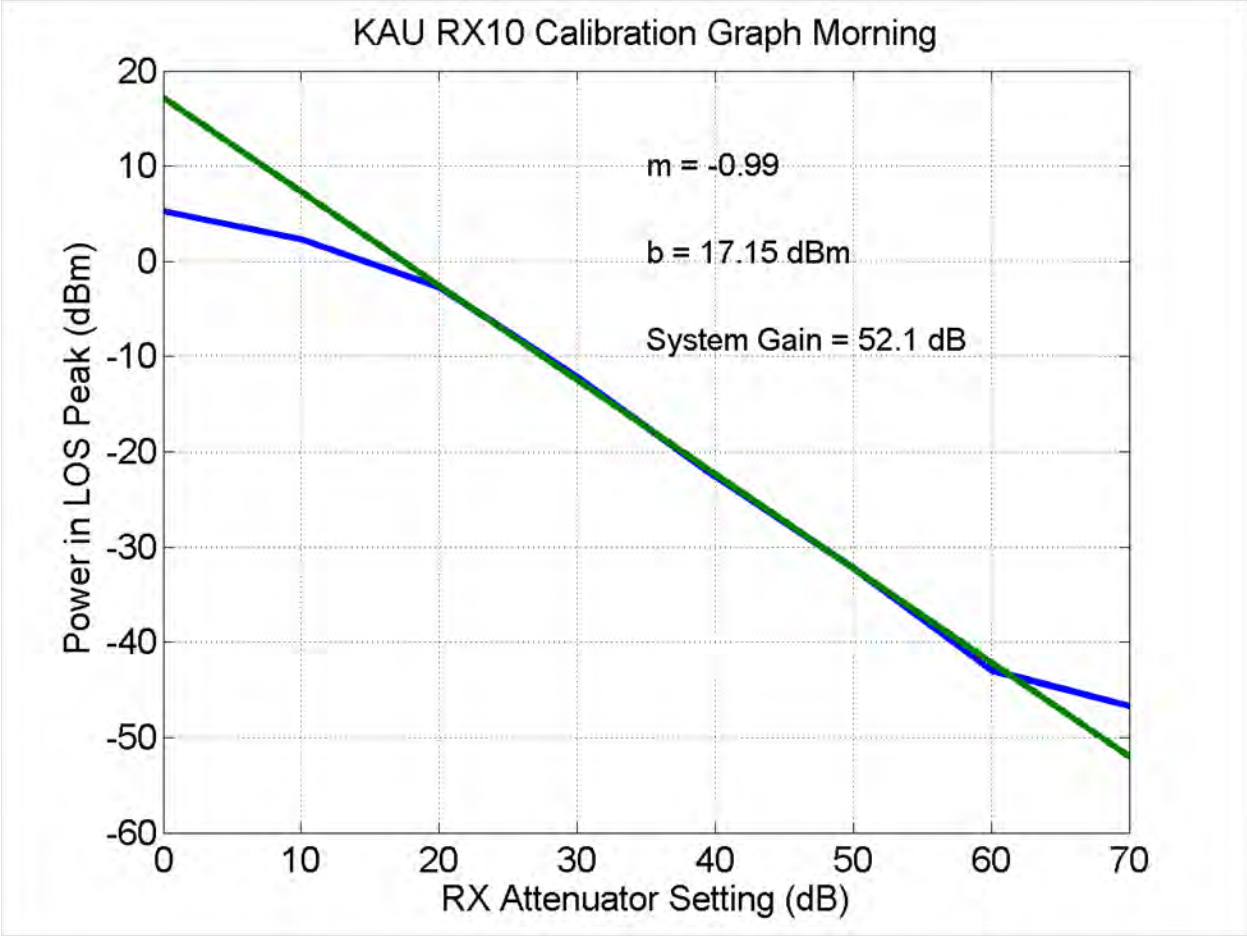

Figure 4.1: A typical calibration graph obtained from a RF calibration routine at 28 GHz at a free space calibration distance of 5 m. The linear range of the RX system is found to be for measured power levels between -3 dBm and -33 dBm. The RX system gain was found to have a near-ideal response (slope $m = -0.99$) with a gain of 52.1 dB. $b = 17.15$ dBm is the intercept of the green line.

total power P_{cal} (dBm) in the LOS component observed as computed from Eq. 4.1 during the calibration routine, and the x-axis is the setting of the variable RX attenuator $RX_{atten,cal}$ (dB) during the calibration routine. The blue curve represents the measured power levels for RX variable attenuator settings of 0 dB to 70 dB at each 10 dB increment, while the green line approximates the measured power levels lying in the linear range of the RX system.

The linear range of the RX system is the range of input powers for which a 1 dB increase in the RX variable attenuator results in a constant 1 dB decrease in the observed power $P_{field,cal}$. Here in Fig. 4.1, the linear range of observed powers can be visually identified to lie between -3 dBm and -33 dBm, or equivalently,

for the RX variable attenuator setting lying in between 20 dB and 50 dB. The average gain of the RX system is recovered from the calibration graph. The relationship shown in Eq. 4.3 holds true during the calibration routine for all values of RF input power levels.

$$P_{RF,cal} + G_{RX,NL}^{Avg} - RX_{atten,cal} = P_{field,cal} \tag{4.3}$$

The relationship shown in Eq. 4.4 *only* holds true during the calibration routine when the measured power level lies in the linear range of the RX system.

$$P_{cal}(RX_{atten,cal}) = m \times RX_{atten,cal} + b \tag{4.4}$$

where m and b are the slope and intercept, respectively, of the linear fit approximating the RX system power levels at baseband from the calibration routine, i.e.: 20 dB $< RX_{atten,cal} <$ 50 dB. The slope m represents the average decrease in power level for a 1 dB increase in the variable attenuator setting in the linear range. In this case, the received power level decreases by 0.99 dB for every 1 dB increase in RX variable attenuator setting. The intercept b represents the received power level for a RX variable attenuator setting of 0 dB assuming this setting belongs to the linear range. This particular calibration graph demonstrates a near-ideal RX system average response in the linear range of input powers since a 1 dB increase in the RX variable attenuator setting results in a decrease of nearly 1 dB (actually, it is 0.99 dB) in the received power level. Putting Eq. 4.3 and Eq. 4.4 together yields the following:

$$P_{RF,cal} + G_{RX,NL}^{Avg} - RX_{atten,cal} = P_{field,cal} = m \times RX_{atten,cal} + b \tag{4.5}$$

$$P_{RF,cal} + G_{RX,NL}^{Avg} - RX_{atten,cal} = m \times RX_{atten,cal} + b \tag{4.6}$$

Solving for the average gain $G_{Rx,L}^{Avg}$ yields the following:

$$G_{RX,L}^{Avg} = (m+1) \times RX_{atten,cal} + b - P_{RF,cal} \tag{4.7}$$

$$G_{RX,L}^{Avg} = \frac{m+1}{m} \times (P_{cal} - b) + b - P_{RF,cal} \tag{4.8}$$

where Eq. 4.4 was used in going from Eq. 4.7 to Eq. 4.8.

In general, the average gain of the RX system in the linear range will depend on the slope m, the intercept b, but also on the observed power level of a multipath component. Thus the gain of the system is different for two multipath components with different received power levels. We can generalize the gain dependence as follows:

$$G_{RX,L}^{Avg} = f(m, b, P_{field}) \tag{4.9}$$

Once the average gain $G_{RX,L}^{Avg}$ for a particular multipath component is known, the true RF power of that multipath component is recovered using Eq. 4.2 and Eq. 4.8.

$$P_{RF,true} = P_{field} - \frac{m+1}{m} \times (P_{field} - b) + b - P_{RF,cal} \tag{4.10}$$

where P_{cal} from Eq. 4.8 was substituted for P_{field}.

Special cases:

- m = -1

  When m is equal to -1, the average net gain becomes independent of observed power, as can be seen from Eq. 4.7. The average net gain becomes a constant, that is, the RX system gain applied to every incoming multipath component is the same irrespective of its power, provided its total power lies in the linear range of input powers. In this case, a 1 dB increase in the RX variable attenuator setting results in a decrease of exactly 1 dB in received power levels.

- $m \neq$ -1

  When m is not equal to -1, the average net gain becomes dependent on the observed power level P_{field}, indirectly dependent on input RF power, as can be seen from Eq. 4.10. This case is typically seen in a real calibration procedure. In this case, a 1 dB increase in the RX variable attenuator setting can result in either more or less than a 1 dB decrease in received power levels.

4.1.1.2 New Channel Sounder Parameter Definition

From Eq. 4.8, we see that the average RX system gain is weighted by a factor of $\frac{m+1}{m}$, which represents the amount by which the gain depends on the dBm value of the observed power P_{field}. We can therefore take this fraction to characterize the response of the RX system. As this fraction tends to 0 (m tends to -1), the RX response becomes independent of input power level and tends to an ideal response, that is, a 1 dB increase in attenuation results in exactly a 1 dB decrease in received power. Similarly, as this fraction gets farther away from 0 (m tends to 0 or infinity), the RX response becomes increasingly dependent upon input power levels, i.e., a 1 dB increase in attenuation results in less or more than 1 dB decrease in received power. For simplicity, lets define this fraction to be a new channel sounder parameter $\beta = \frac{m+1}{m}$, which describes the response of the channel sounder for a particular calibration routine.

4.1.1.3 The RX System Response Approximation

In practice, the slope m on the calibration graph is rarely equal to the theoretical value of -1. Its value usually lies very close to -1 (observed from the 28 GHz calibration data). Accounting for this deviation away from the theoretical value of -1 is possible when recovering true RF received power, but in practice results in insignificant improvements in received power levels. It is therefore chosen in this work to approximate the RX system behavior as ideal in order to simplify the general understanding of post-processing and to reduce computation complexity. Under this approximation, the slope m becomes an irrelevant parameter since we choose to treat the RX system as ideal (i.e., $m = -1$) and thus does not yield useful information. The only critical parameter that must be considered is the intercept b. From the intercept b (dBm) and theoretical calibration RF input power $P_{RF,cal}(d_0)$ (dBm), the average RX system gain (dB) for input power levels belonging to the linear range is recovered as follows:

$$G_{RX,L}^{Avg} = b - P_{RF,cal} \tag{4.11}$$

4.1.1.4 Recovering Total Received RF Power and Path Loss

Each multipath component should be weighted by the RX system gain as described above so as to recreate the true RF power delay profile. The RF power delay profile can be expressed as in Eq. 4.12.

$$P_{RF,true}(\tau) = P_{BB}(\tau) - G_{RX,L}^{Avg} + RX_{atten,field} \tag{4.12}$$

where $RX_{atten,field}$ is the RX variable attenuator setting during the field measurement, and $P_{BB}(\tau)$ represents the collected power delay profile at baseband.

The total RF power received is the integral sum (in linear units) of the RF power delay profile:

$$P_{RF,total,true} = 10 \times \log_{10}\left(\sum_{i=0}^{N-1} P_{RF,true}(\tau_i)\right) \tag{4.13}$$

where N is the total number of samples in the power delay profile, and $P_{RF,true}(\tau_i)$ is in units of mW/sample. The total path loss is computed from the Friis free space transmission formula (shown here in log scale), as follows:

$$PL\ [dB] = P_{TX} + G_t + G_r - P_{RF,total,true} \tag{4.14}$$

where P_{TX}, G_t and G_r are the transmit power (dBm), transmitter and receiver antenna directive gains (dBi), respectively. An important assumption that must be noted when recovering the total path loss as in Eq. 4.14 is that the directive gains G_t and G_r, which are generally a function of θ and ϕ, are assumed to be *relatively* constant over the 3 dB HPBW angular window.

4.1.1.5 Motivation for Rescaling PDPs in Units of mW/ns

The process of sampling, or digitizing, an analog signal introduces an extraneous and inconvenient dependence upon the sampling frequency of the recorded waveform. In other words, an analog signal that is digitized at a sampling frequency F1 will actually look different than the corresponding analog signal digitized at a different frequency F2. By "look different", it is meant that the recorded values will have

different numerical values in each sampled waveform. The overall "shape" of the waveforms will however remain independent of sampling frequency.

To understand this phenomenon, one may model a digitizer as a door that can be in two different states: open or closed. When the door is open, the power is let through (hence recorded and digitized) and when the door is closed, the power is not let through (and not recorded). Now assume the door is opening and closing at a rate of 10 times per second (corresponding to a digitizer with sampling frequency of 10 Hz). Each time the door opens, power is let through for 0.1 seconds. The total (sum) power that has flowed through the door during that 0.1 s will represent the numerical value for that sample point. Now assume the door is opening and closing twice as fast, that is, at a rate of 20 times per second. Clearly, the amount of power that flows through the door for 0.05 second is twice as small as the amount of power that flows through the door for just 0.1 seconds. Thus, the sample value corresponding to the second situation will be twice as small in magnitude, but there will be twice as many sample points as in the first case to make up for each magnitude being twice as small. Regardless of the sampling rate, the total integrated power over a given duration of time should be the same in both situations.

The example above illustrates the dependence of a digitized waveform upon the operating sampling frequency. It is quite inconvenient to look at a digitized waveform in units of mW/sample, because the numerical values of each sample are a function of the operating frequency. It is thus important to remove the dependence on sampling frequency, that is, to normalize a sampled waveform so that the numerical values are independent of sampling frequency.

A convenient way to normalize a sampled waveform is to map the power in a sample to the power that would have been obtained during a unit of time, say 1 second or 1 ns, had the power in that sample been delivered at a constant rate during that unit of time. For instance, if a recorded sample has a power value of 0.5 mW and the sample was obtained with a sampling frequency of 2 kHz (i.e., 0.5 ms per sample) then the corresponding power that would have been obtained during a unit of time of 1 second would have been 1000 mW (0.5×2000), or equivalently, 1 mW in 1 ms, or 1 μW in 1 μs. All three values are correct as long as the chosen unit of time remains consistent throughout the renormalization procedure.

Fig. 4.2 shows a RF sampled waveform, with operating sampling frequency of 2 MSamples/s, in addition to a slide factor of 8000 (See Chapter 3), yielding a net (undilated) digitization rate of 16 samples/ns. The corresponding normalized waveform is obtained by multiplying every sample point by 16 in the linear scale, which corresponds to a gain of $10 \times \log_{10}(16) \approx 12$ dB greater than the sampled waveform.

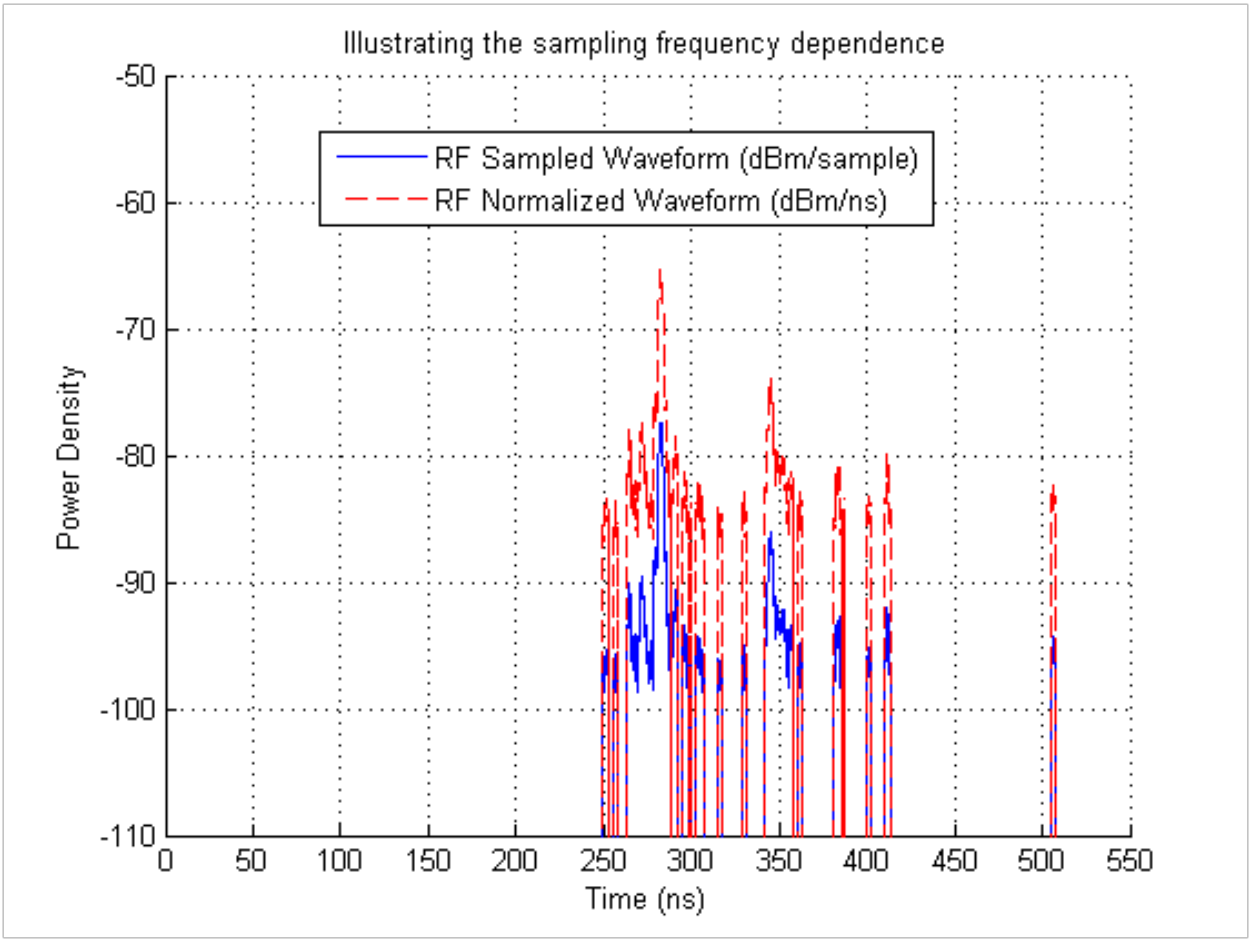

Figure 4.2: Digitized waveform in units of dBm/sample with its corresponding normalized waveform in units of dBm/ns.

Below are two simple rules to keep in mind when manipulating PDPs with units of mW/sample or mW/ns:

a. If the y-axis units of the PDP are in mW/sample, then the total power in the PDP is the sum of the sample point values.

b. If the y-axis units of the PDP are in mW/ns, then the total power in the PDP is the Riemann sum of the waveform, i.e., the sum of sample points weighted by the time duration between two adjacent samples.

In a., the waveform is not truly a power density function, it is merely a collection of power points and so the total power is just the sum of the power samples. In b., the waveform is truly a power density function since it has units of power per unit time, and so we must take the discrete time integral to find the total power in the PDP. The conversion between a. and b. is achieved by multiplying the units of mW/samples by the number of samples/ns.

4.1.1.6 Multipath Time Resolution

The multipath time resolution is a key parameter of any RF equipment capable of measuring channel impulse responses, describing the shortest detectable multipath component in time. This parameter depends on the signal bandwidth. There is no official definition of the multipath time resolution, and so, a number of definitions can be used to describe this parameter. However, in practice, some definitions are more useful than others, as described in this section.

The simple and most intuitive definition of the multipath time resolution is the undilated width duration at the base of a single pulse, obtained from the cross-correlation of the incoming TX signal and reference RX signal. However, it is readily seen that the base duration of a single pulse depends on the SNR of that pulse. In fact, the base duration is in theory linearly proportional to the SNR of the multipath component. For instance, a signal pulse with large SNR will tend to last longer above the system noise floor than a single pulse with SNR close to 0 dB. This is illustrated in Fig. 4.3, where the first arriving multipath component has approximately a 16 dB SNR and a base duration of 5 ns (above noise floor), and the third multipath component has a SNR of 1 dB and base duration of 1.9 ns (above noise floor). Clearly, the multipath time duration is heavily affected by the SNR level, and is an inconvenient way to define the multipath time resolution of a RF measurement system.

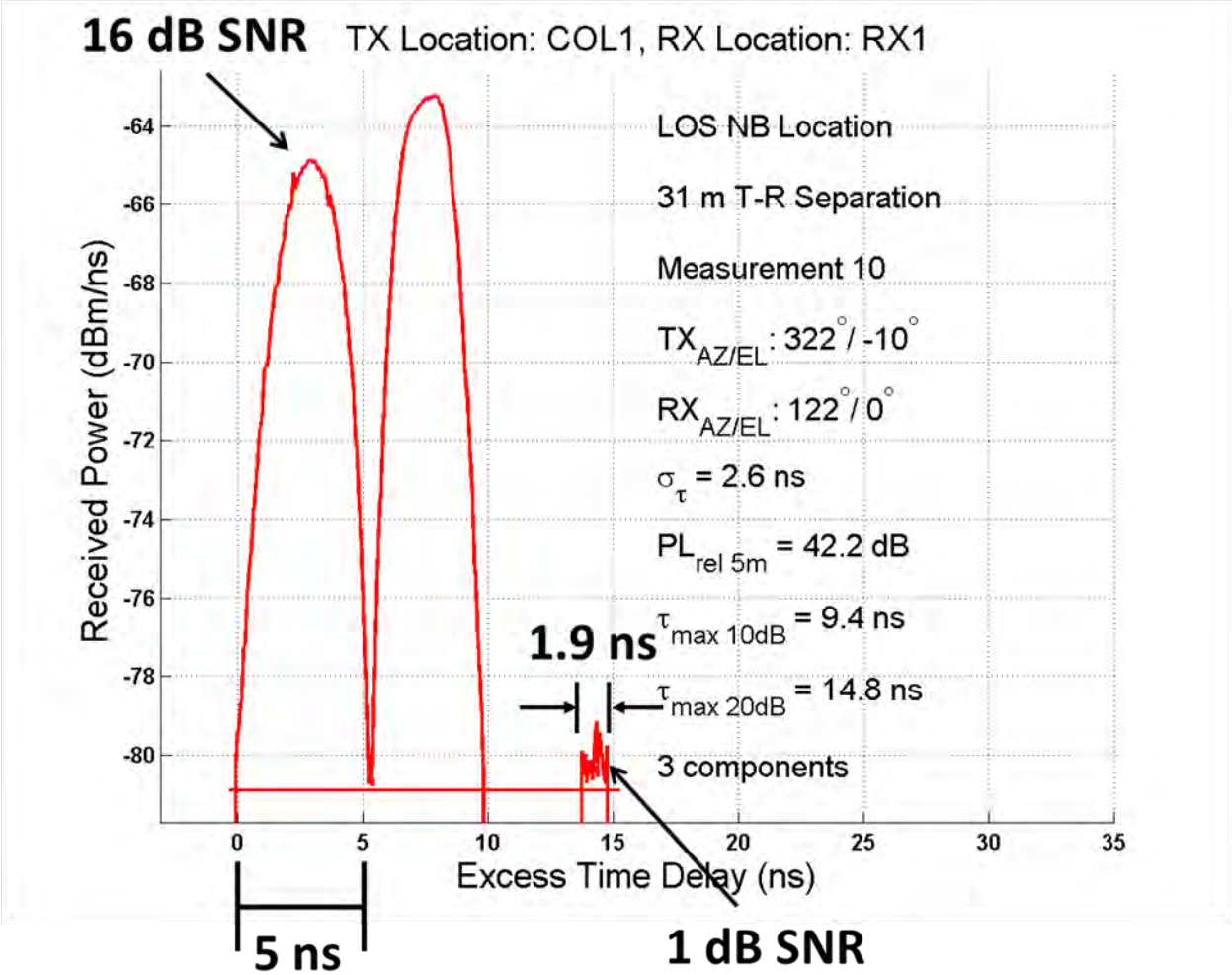

Figure 4.3: Typical power delay profile obtained at 28 GHz in Manhattan, showing three multipath components with various pulse durations. The first multipath component has a base duration of 5 ns and a SNR of 16 dB, while the third multipath component has a base duration of 1.9 ns and a SNR of 1 dB, illustrating the idea that multipath pulse duration heavily depends on SNR.

A more useful and convenient way of defining multipath time resolution is using the RMS delay spread of a single pulse. Since the RMS delay spread quantity is independent of SNR, this quantity is more suited to describe a fundamental parameter of our equipment hardware. Below is the derivation for obtaining the RMS delay spread of a single pulse.

$$\sigma_{pulse} = \sqrt{\overline{\tau^2} - \overline{\tau}^2} \tag{4.15}$$

where,

$$\overline{\tau} = \frac{\int t f(t)\, dt}{\int f(t)\, dt} \tag{4.16}$$

$$\overline{\tau^2} = \frac{\int t^2 f(t)\, dt}{\int f(t)\, dt} \tag{4.17}$$

where,

$$f(t) = \begin{cases} a \times (t - t_0) + b, & -\frac{T}{2} + t_0 < t < t_0 \\ -a \times (t - t_0) + b, & +t_0 < t < t_0 + \frac{T}{2} \\ 0, & |t - t_0| > \frac{T}{2} \end{cases}$$

where $a = \frac{2b}{T}$, and $b > 0$, $T = \frac{2}{f_{TX}}$, and $f_{TX} = 400$ MHz is the chip rate of the TX PN sequence at baseband (See Chapter 3).

The power distribution of a multipath component is easily obtained by considering the convolution of two chips in the time domain, which results in a triangular pulse, as is mathematically described by $f(t)$. Solving for Eq. 4.16 and Eq. 4.17 yields the solution to Eq. 4.15:

$$\overline{\tau} = t_0 \tag{4.18}$$

$$\overline{\tau^2} = \frac{T^2}{28} + t_0^2 \tag{4.19}$$

$$\sigma_{pulse} = \frac{T}{2\sqrt{7}} = \frac{5}{2\sqrt{7}} = 0.945 \text{ ns} \tag{4.20}$$

where we substitute $T = 5$ ns, following the hardware parameters used during the 28 GHz measurement campaign.

Thus, we obtain the RMS delay spread of a single ideal theoretical pulse to be 0.945 ns. A consistent measure of the multipath time resolution is therefore equal to $2\sigma = 1.89$ ns ≈ 2 ns.

4.1.2 MATLAB Post-Processing: Functionalities

Assuming a perfect noiseless receiver, the RF PDP would be easily obtained by subtracting the RX system gain from the measured PDP at baseband. However, since the recorded waveform contains noise, a number of additional processing steps must be performed to remove as many noise samples as possible before subtracting the RX system gain from the measured PDP to recover the RF PDP.

4.1.2.1 Multipath Thresholding Procedure

The 28 GHz Manhattan and Brooklyn measurements were processed using a multipath thresholding algorithm with a 5 dB SNR above mean noise floor. All sample points lying above this threshold were kept as received multipath signals, while all points below were given a value of -200 dBm (e.g. effectively set to zero). The plots below show a measured PDP as recorded from the NI USB-5133 Digitizer and containing noise samples, with its corresponding thresholded version using the thresholding algorithm described above.

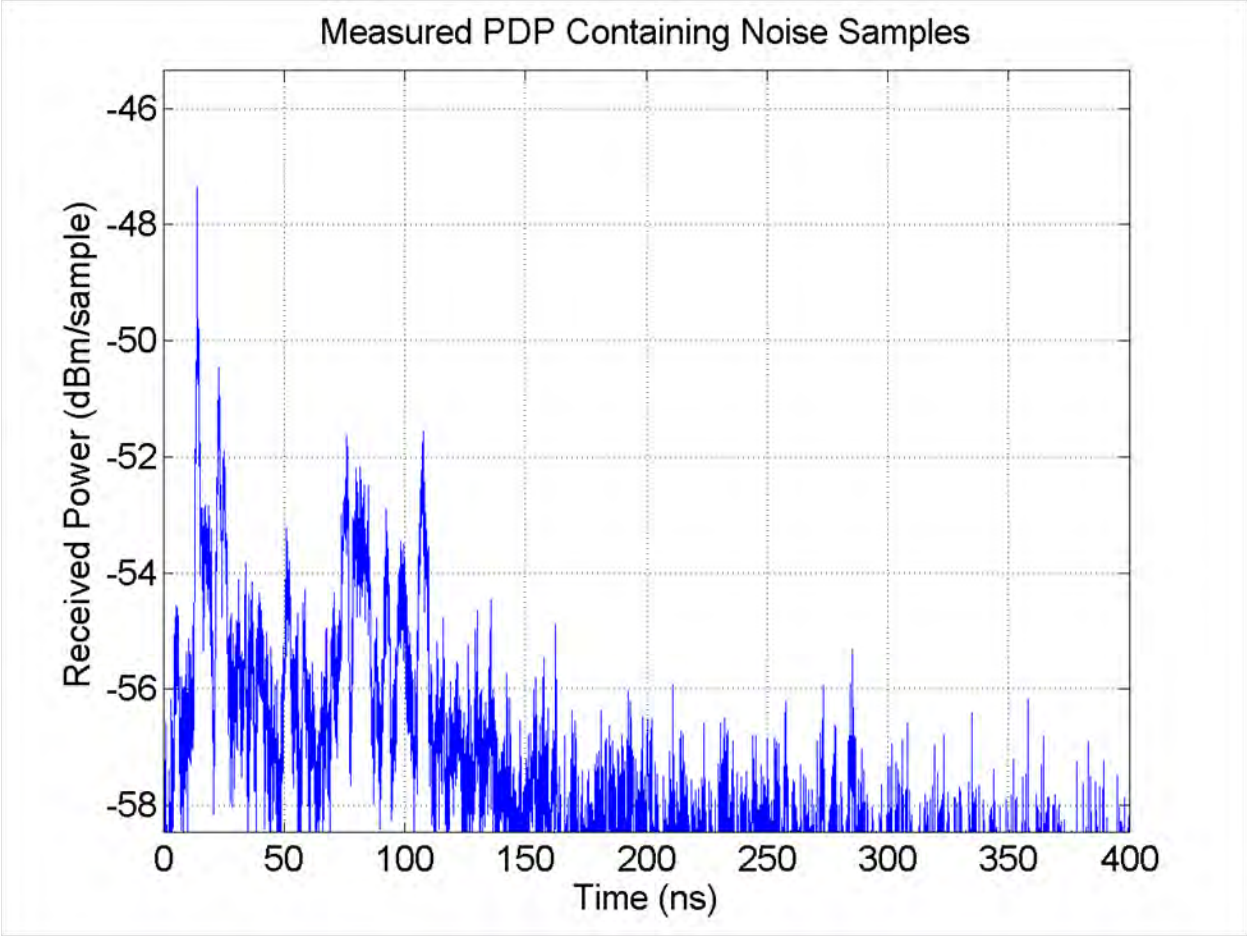

Figure 4.4: A sample recorded PDP at baseband containing noise samples from the 28 GHz measurement campaign.

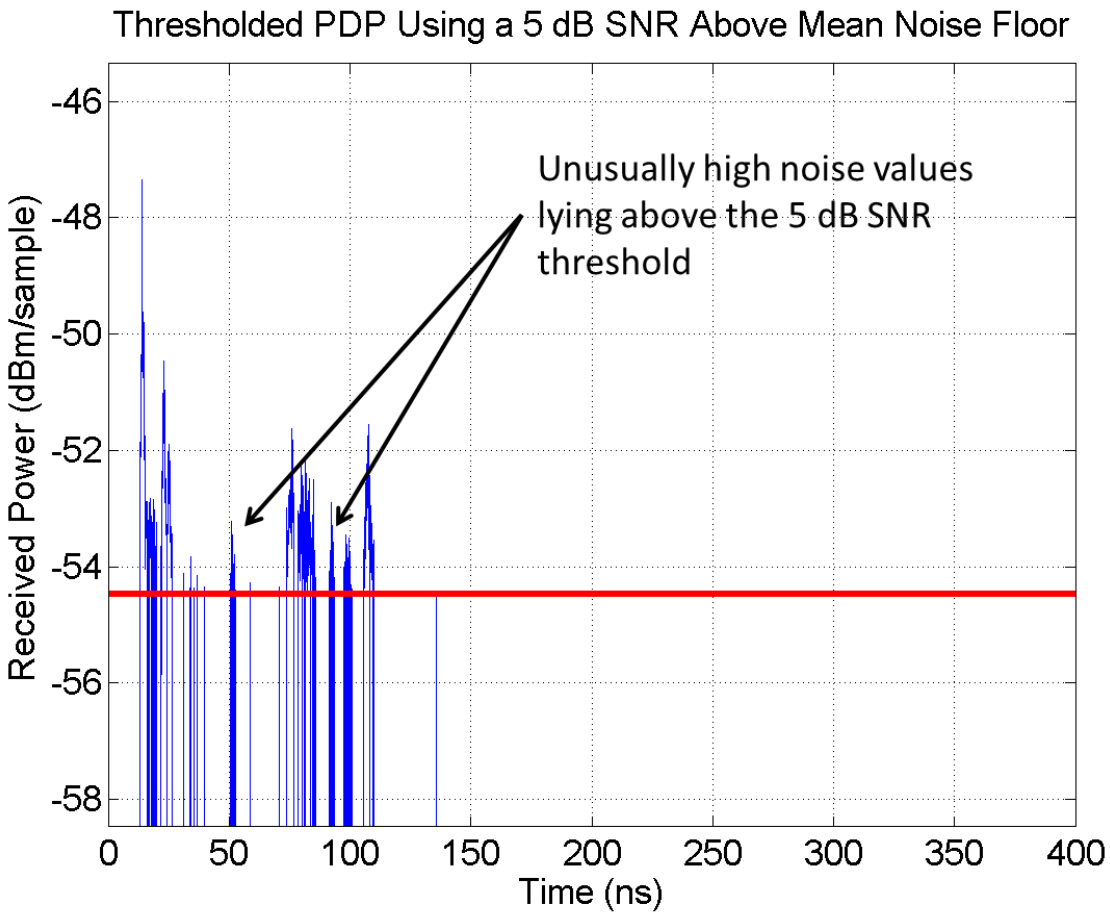

Figure 4.5: A sample PDP upon which a 5 dB SNR above mean noise floor threshold (the red line) has been applied. All points above this threshold are kept as valid multipath signals, while all points lying below this threshold are given a value of -200 dBm (effectively setting them to 0). This PDP still contains unusually high noise values above this threshold which can be removed with additional processing.

4.1.2.2 Further Improvements in Thresholding Procedure

Assuming a Gaussian PDF envelope for the noise sample values, there is still some small probability of finding unusually high noise samples lying above the 5 dB SNR threshold in the thresholded PDP above. It is possible to remove those high noise samples by considering the multipath time resolution specifications. Since the RMS delay of a single pulse was calculated to be approximately 2 ns, any consecutive samples lasting less than 2 ns cannot represent a multipath component, but rather, unusually high consecutive noise samples. Additional code may be written to remove those unusually noise samples, as illustrated in the following figure.

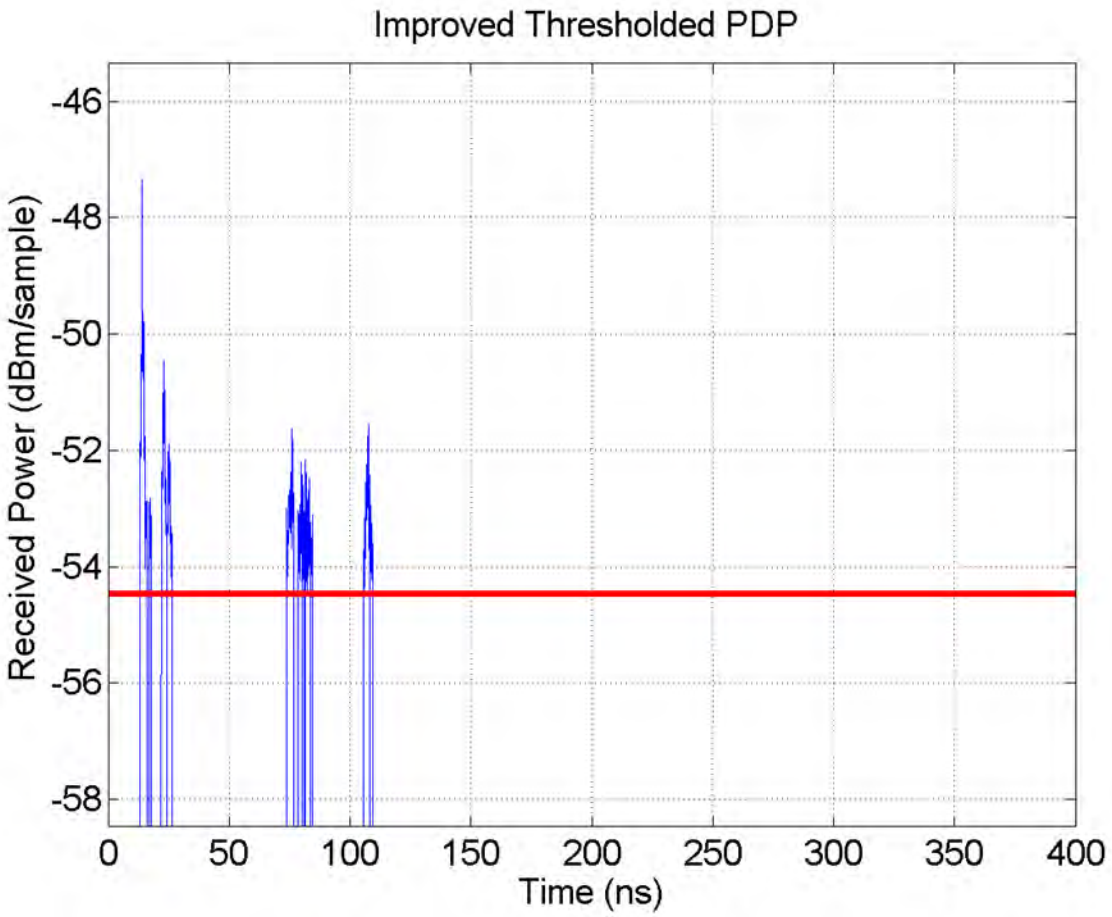

Figure 4.6: A sample thresholded PDP. All noise samples have been removed.

4.2 Recovering Absolute Timing Information Using 3-D Ray-Tracing Techniques

4.2.1 Motivation for Ray-Tracing

Independent frequency sources used in the 28 GHz channel sounder that provided the PN clocks, the IF and the LO signals at both TX and RX were not slaved to a common 10 MHz reference signal during the measurement campaign, causing jitter, nor were they GPS synchronized using absolute time stamping. The observed jitter was removed with additional LabVIEW software designed to provide real-time trigger alignment algorithm of the I and Q waveforms, in which contiguous PDPs at one measured angle were

aligned to the time of arrival of the strongest received multipath component before averaging. The power delay profiles collected therefore did not represent absolute time delay channel impulse responses, but rather, excess time delay channel impulse responses. As illustrated in Fig. 4.7a, two typical measured excess time delay power delay profiles are shown as measured at two distinct azimuth angles at a receiver location. Since the TX and RX were not GPS-locked, our measurement system was unable to measure absolute propagation time delay, as the strongest arriving multipath component was used to trigger and establish the relative $t = 0$ ns time marker for all recorded PDPs. This limitation is illustrated in Case 1 of Fig. 4.7b, where both PDPs are shown to start at $t = 0$ ns, thus not capturing actual arrival time of power. Case 2 illustrates the desired result, showing the two PDPs measured along an absolute propagation time axis, where $t = 0$ ns corresponds to electromagnetic radiation emerging from the TX antenna. In Case 2, the recorded excess time delay power delay profiles have been shifted in time appropriately, accounting for the distance travelled of the first arriving multipath in each PDP, enabling complete and accurate characterization of received power in time at the RX. Polar plots in conjunctions with absolute time delay power delay profiles provide an accurate means of recovering angular and temporal statistics of the wireless channel that may be used for any type of antenna or beamforming/MIMO analysis for omnidirectional channel models. Future measurements using cesium clock standards and time synchronization will ensure true propagation times for all recorded PDPs. In order to achieve the desired result shown in Case 2 of Fig. 4.7b, complementary 3-D ray-tracing software was developed to recreate absolute time of multipath arrivals from TX to RX.

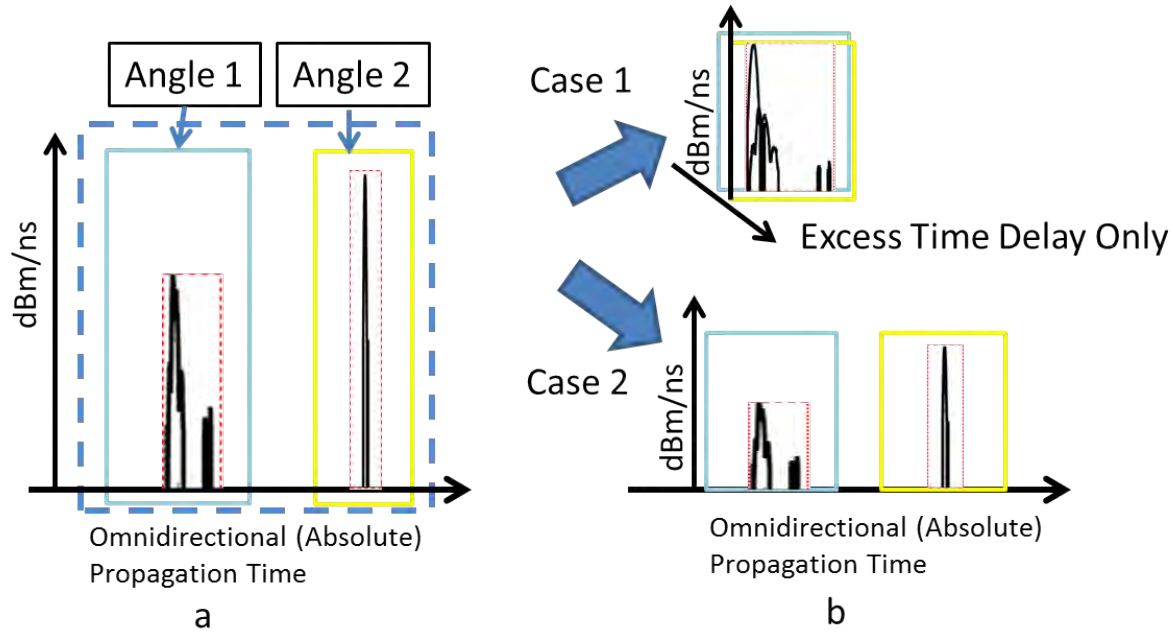

Figure 4.7: a) Superimposed PDP of two individual received PDPs, where each PDP comes from a different AOA at the same RX location. The multipath signals from Angle 1 arrived before those of Angle 2 (i.e. multipath arriving at different times from two distinct lobes). The absolute propagation times were found using manual ray-tracing, thus allowing alignment with absolute timing of multipath signals at the RX, independent of AOAs. b) Case 1 illustrates a situation where the receiver is not able to recover absolute propagation times of arrival, resulting in all PDPs aligned to the same point (first arriving multipath) in time. Case 2 illustrates a situation where the receiver is able to distinguish absolute propagation times across azimuth, thus keeping track of the absolute temporal distribution of received power.

4.2.2 MATLAB-Based 3-D Ray-Tracer: Functionalities

Ray-tracing methods provide invaluable insight into communication channel characteristics such as impulse response power delay profiles (PDP), RMS delay spreads, coherence bandwidth, angle of departure (AOD) and angle of arrival (AOA) information, and signal coverage by simulating electromagnetic propagation in a finite numerical description of the environment. Several ray-tracing techniques have been developed to accurately emulate electromagnetic radiation from a point source and address inherent issues of ray-tracing such as ray divergence and double ray counting at the receiver. The well-known reception sphere model is used to account for diverging propagating rays by varying the radius of the reception sphere as a function of angular ray spacing and distance travelled by the ray [93][94][95][96]. Geodesic ray launching is performed to retain large-scale and small-scale uniformity of diverging rays such that all emitted rays illuminate space

equally and the angular spacing in between adjacent rays remains uniform throughout the simulation [97][98]. The double ray counting problem is solved with a distributed wavefront weighting function which weighs power contributions of received rays based on the arc-length distance between arriving rays and the reception point [97]. The method of images is another common ray-tracing approach, in which artificial sources are placed appropriately in the discretized environment so as to simulate reflections from flat smooth surfaces [99][100]. The above ray-tracing techniques have been shown to accurately predict path loss and RMS delay spreads of low frequency (below 6 GHz) indoor and outdoor communication channels.

The MATLAB-based 3-D ray-tracer used in recovering absolute timing information of the 28 GHz measurements currently implements the law of reflection, a diffraction model, and a simple radar cross section (RCS) scattering model. It has been shown to successfully recreate the strongest angle of departures and of arrivals on outdoor Manhattan measured locations. In total, 17 of 24 angle of departure locations and 20 of 24 angle of arrival locations were successfully ray-traced. The remaining 7 AOD locations and 4 AOA locations did not yield ray-tracing information, and can be explained because of the imprecision of the database that could not predict rays that would propagate from the TX to the RX.

4.2.2.1 Theoretical Considerations

A 3-D ray-tracing software package was developed in MATLAB to emulate electromagnetic propagation in any type of environment and for arbitrary antenna pattern. The ray-tracer currently implements the law of reflection, which states that the direction of of an impinging ray upon a smooth flat surface is equal to that of the outgoing ray, a simple empirical diffraction model and a RCS scattering model. Each emitted ray from a point source carries a sphere at each position along the ray trajectory, whose radius increases as the ray propagates forward. In this ray-tracing approach, the reception sphere radius is constant for all incoming rays, and an incoming ray is detected if any point on its spherical surrounding surface intersects the reception sphere.

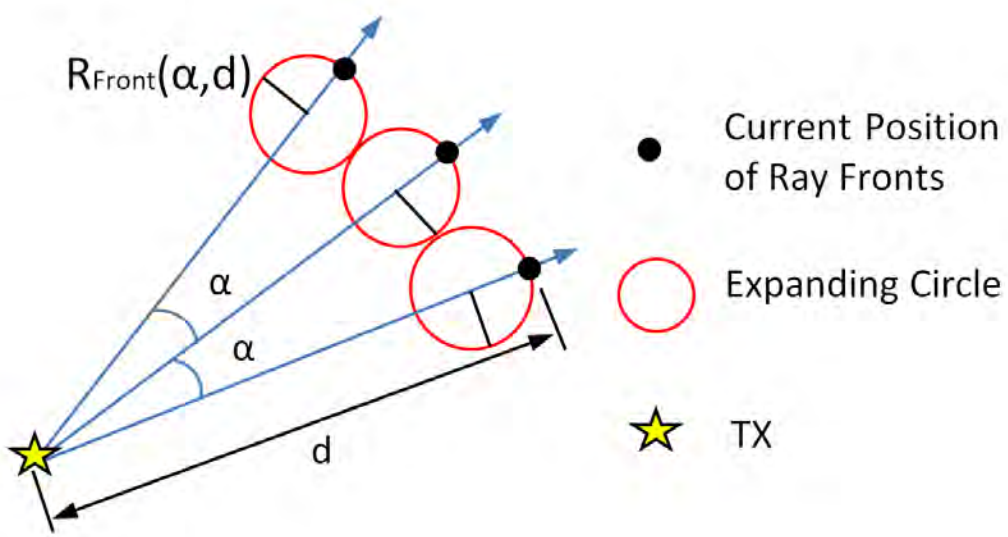

Figure 4.8: Diagram of three adjacent propagating rays, whose current positions correspond to the edges of expanding circles. The radius of the circle depends on the angular spacing α between adjacent rays and the total current distance travelled d of the ray. The circles never intersect each other, thus providing each ray with its own propagating space. This model represents the propagation of an electromagnetic field throughout the work presented.

Fig. 4.9 illustrates a two-dimensional (2-D) view of three adjacent propagating rays separated by angle α, each carrying a circle (sphere in 3-D) of radius R_{Front} at the current position of the ray front. Note that the circle (or sphere) is not centered at the current position of the ray front, but slightly before the current position, such that the front of the circle (or sphere) coincides with the current position. In 3-D, the expanding sphere models the current position of the ray, and centering the sphere at the current position would result in looking ahead into the future of the current position point. As illustrated in Fig 4.8, the circle must fit inside an isosceles triangle such that the circle is tangent to the triangle sides.

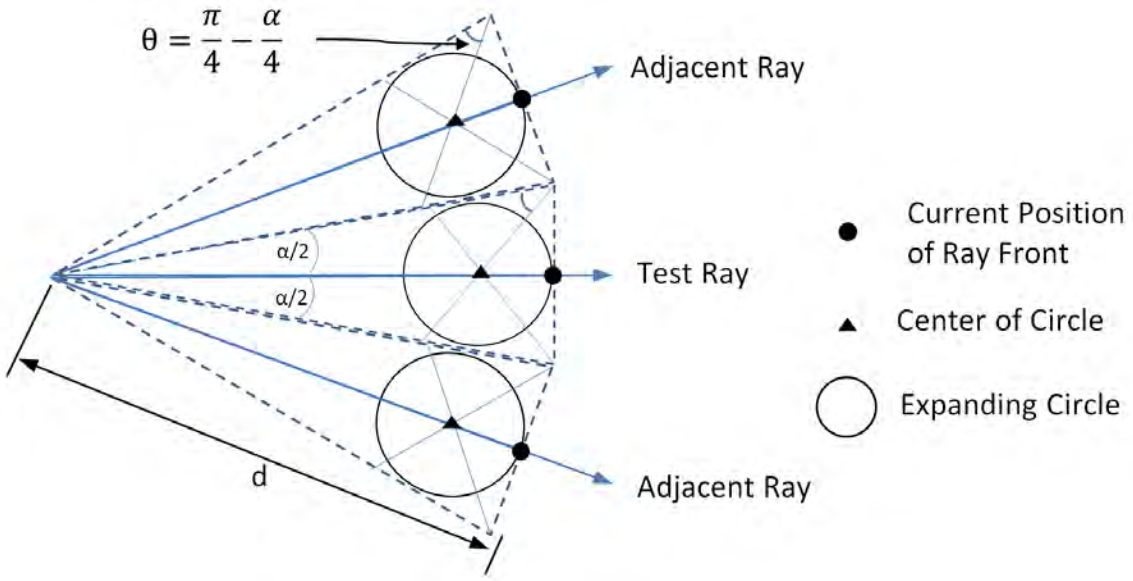

Figure 4.9: The circle representing the current position of the ray fits inside an isosceles triangle. The center of the circle is the intersection of the three triangle bisectrices. The radius of the circle is a function of angle spacing α and distance d.

The radius of the circle is recovered by noting that its center coincides with the intersection of the three bisectrices of the triangle. Using trigonometry, the radius is given by Eq. 4.21:

$$R_{Front}(\alpha, d) = d \times \left(\frac{\pi}{4} - \frac{\alpha}{4}\right) \times \left(\frac{\alpha}{2}\right) \tag{4.21}$$

where α (rad) is the angular spacing between two adjacent rays, and d is the total distance travelled by the ray. Fig. 4.8 and Fig. 4.9 illustrate that adjacent circles will never overlap. In 3-D, each ray will thus travel along the center line of a cone as the radius of the expanding sphere increases with increasing travelled distance, as shown in Fig. 4.10.

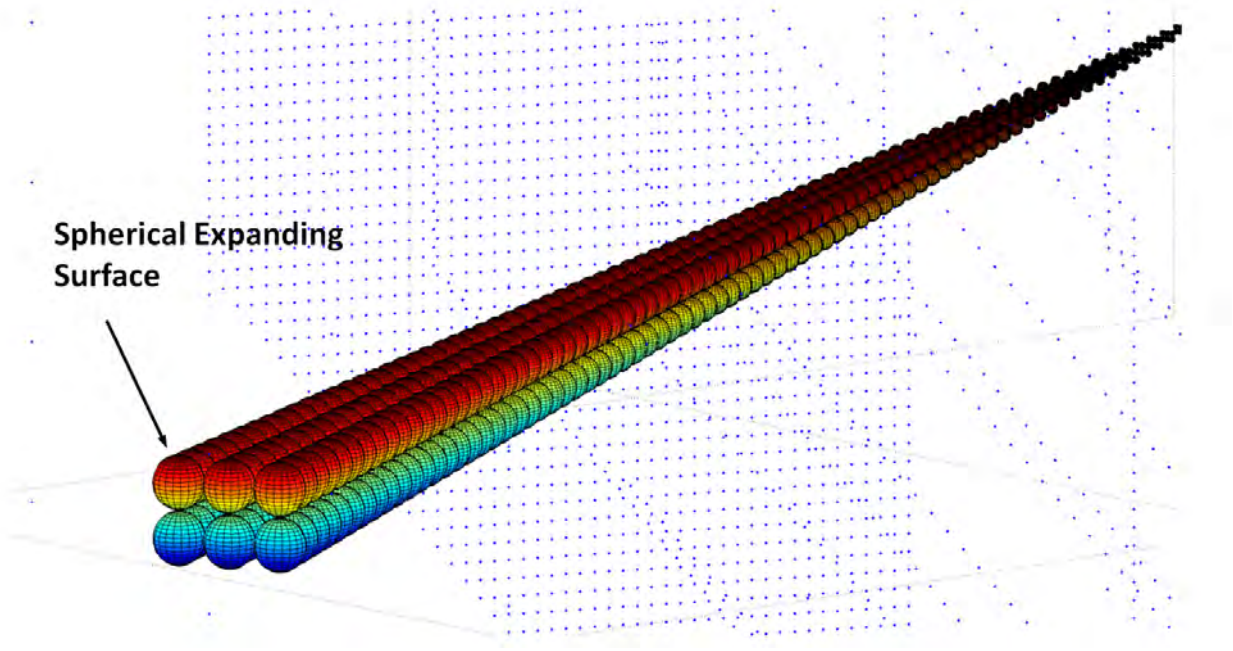

Figure 4.10: A 3-dimensional view of six adjacent propagating ray paths generated in MATLAB. The radius of the propagating spheres is a function of the angular spacing α between adjacent rays and total distance travelled d.

Before a ray-tracing simulation is started, a 'ray-tracing calibration' must be performed to determine the best angular spacing between adjacent rays. This is achieved by considering an ideal optical LOS situation between a transmit and a receive antenna. In this fictitious scenario, both antennas are facing each other on boresight, and one LOS multipath component can be measured at the RX. Geometrically speaking, this means that only one ray must be detected by the reception sphere. This condition yields a unique angular spacing α_{Best} which can be determined with the T-R separation distance d_{LOS}, the user input reception sphere radius R_{Sphere} and the user input $R_{Front}(\alpha_{Best}, d_{LOS})$, the radius that the sphere must assume at the reception sphere. A reasonable value for $R_{Front}(\alpha_{Best}, d_{LOS})$ is R_{Sphere} such that the sphere radius exactly equals the radius of the reception sphere at the reception sphere itself in an optical LOS situation, but a smaller fraction of R_{Sphere} can be chosen. α_{Best} must be determined such that Eq. 4.22 holds true:

$$\left(\frac{\pi}{4} - \frac{\alpha_{Best}}{4}\right) \times \left(\frac{\alpha_{Best}}{2}\right) = \frac{R_{Front}(\alpha_{Best}, d_{LOS})}{d_{LOS}} \tag{4.22}$$

Once the best angular spacing is found, the number of rays to be launched for a given azimuth and

elevation angle combination must be determined based on the antenna patterns used. For the 28 GHz propagation measurement campaign, two 24.5 dBi horn antennas were used, whose 3 dB, 9 dB and 15 dB power attenuations occur at angles of 5°, 10° and 15° away from antenna boresight in the azimuth plane, respectively, and whose 3 dB and 10 dB directive gain attenuations occur at angles of 4° and 8° away from antenna boresight in the elevation plane, respectively. Thus, an angle spread $\Delta\theta$ of $\pm 15°$, or 30°, was chosen over which to launch rays in both the azimuth and elevation planes. The number of rays that must be sent out from the TX over azimuth and elevation must be equal, and can be found using Eq. 4.23:

$$\#\text{ of Rays} = \left(\frac{\Delta\theta}{\alpha_{Best}}\right)^2 \tag{4.23}$$

where $\Delta\theta$ and α_{Best} must have the same units (rad or °).

4.2.2.2 Building the Database

The Downtown Manhattan environment was modelled in Google SketchUp which allowed fast and easy 3-D site-specific modelling using simple geometrical shapes such as cubes. The 3-D information was then exported in XML format, and subsequently extracted to numerically reconstruct and discretize the environment in MATLAB.

Fig. 4.11 and Fig. 4.12 below show the top views of the Coles Sports Center (COL) and Kaufman (KAU) environments recreated in MATLAB with the corresponding Google Maps view for quick comparison.

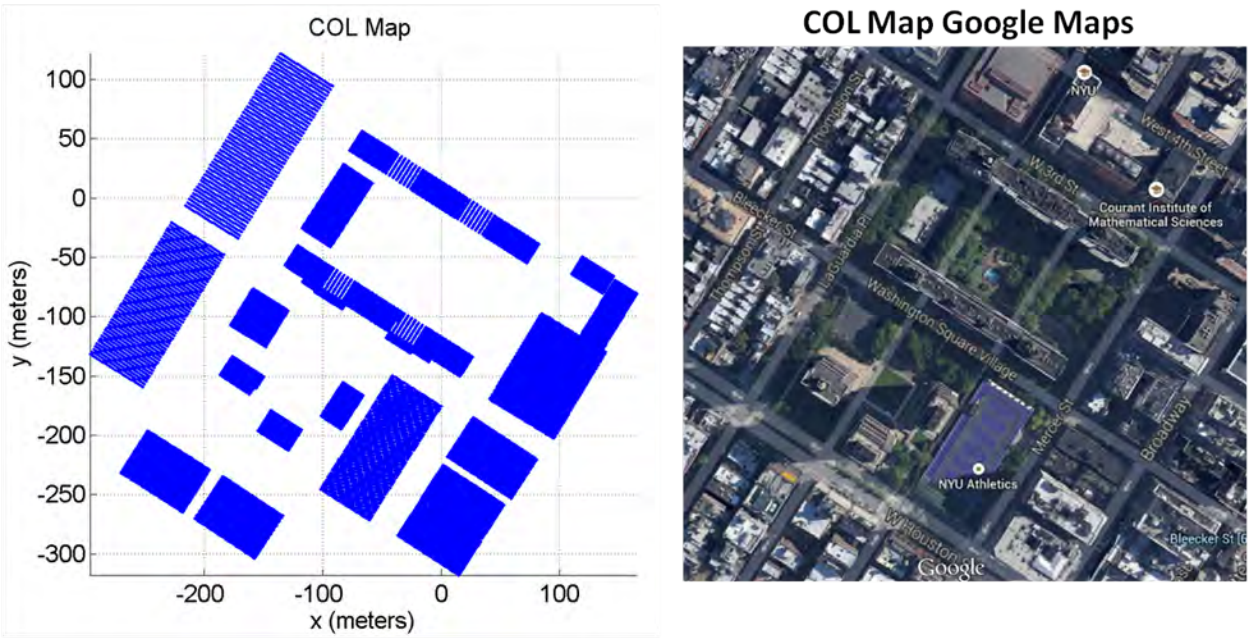

Figure 4.11: Top view of the Coles Sports Center environment taken from Google Maps (right), and corresponding environment (top view) reproduced in MATLAB (left). Buildings were modeled as 3-D cubes with infinitely smooth and flat surfaces, and other objects such as trees, cars, benches, etc. were not modelled. The third dimension (z-dimension) is not shown here.

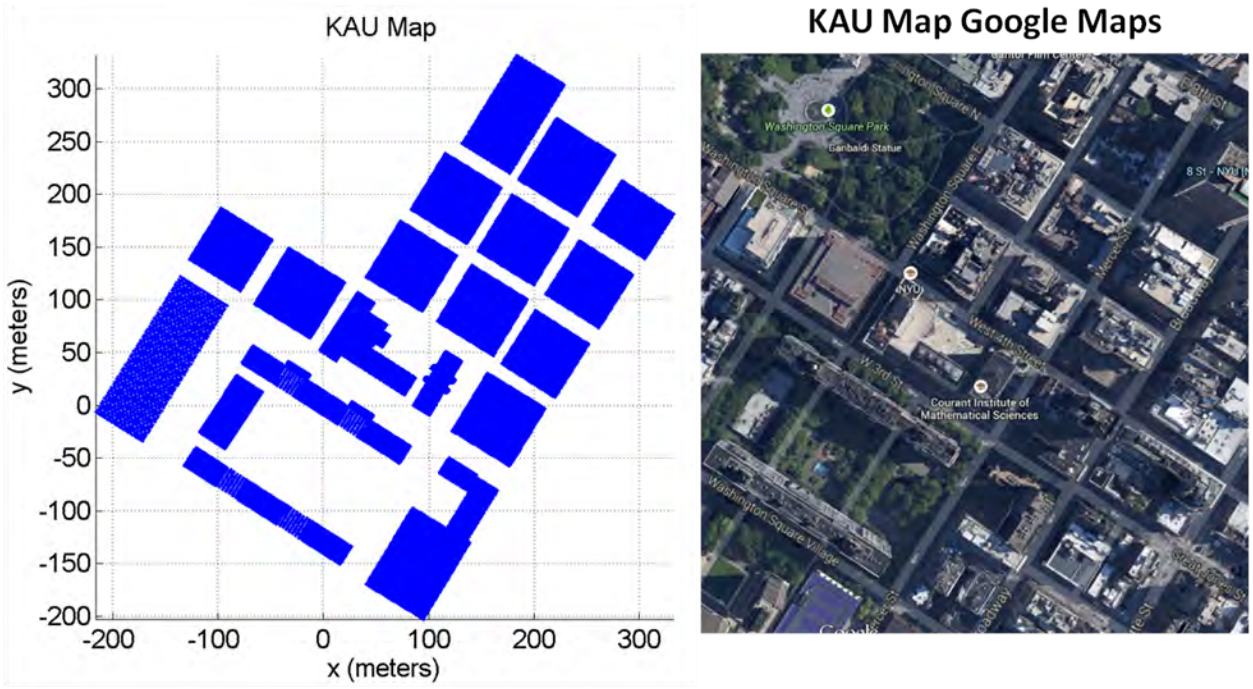

Figure 4.12: Top view of the Kaufman Center environment taken from Google Maps (right), and corresponding environment (top view) reproduced in MATLAB (left). Buildings were modeled as 3-D cubes with infinitely smooth and flat surfaces, and other objects such as trees, cars, benches, etc. were not modelled. The third dimension (z-dimension) is not shown here.

4.2.3 Ray-Tracer Outputs and Omnidirectional PDPs: Example

Fig. 4.13 shows a map of the measured Manhattan environment, identifying the TX and RX locations. The transmitter was located on the north-west corner of the second floor rooftop of the Coles Sports Center 7 m above ground level and well below surrounding rooftops while the receive antenna was located 113 m away at a height of 1.5 m on Wooster Street. The RX location was placed in a highly obstructed environment, where heavy foliage and high-rise building obstructions induced multipath propagation. The TX and RX antennas were 24.5 dBi (10.9° and 8.6° HPBW in azimuth and elevation, respectively) high-gain directional horn antennas. The TX antenna boresight was pointed at the north-most face of the east-most Silver Tower, at a downtilt of 10° with respect to the horizon. The receiver elevation angle was parallel to the horizon (i.e., 0° elevation), and was swept in 10° increments in the azimuth plane. At each azimuth angle, a power delay profile was acquired (for signal strength above noise floor of -100 dBm) by averaging 20 consecutive

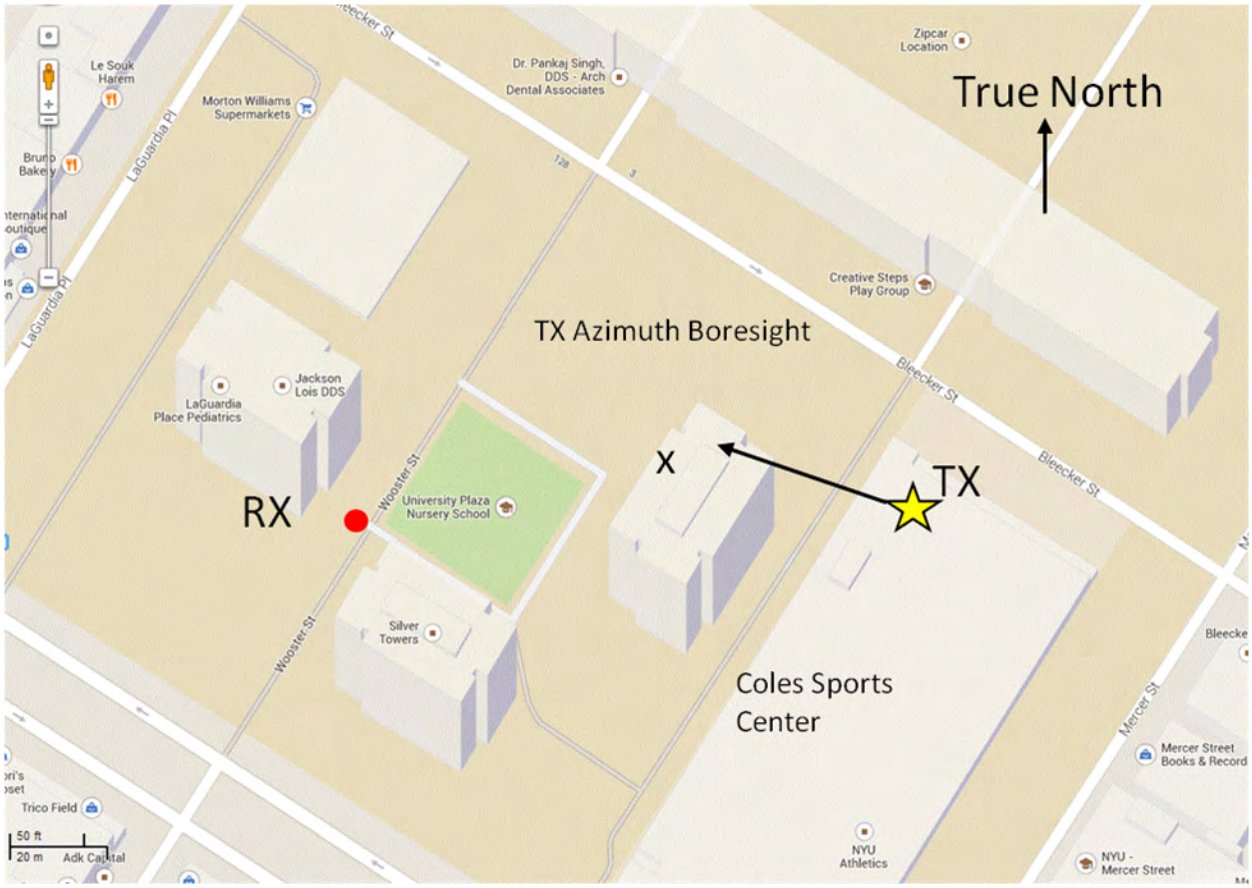

Figure 4.13: Map of Downtown Manhattan showing the TX and RX locations considered in this example. The TX is located on the second floor rooftop of the Coles Sports Center 7 m above ground level, and the RX is located 113 m away from the TX, 1.5 m above ground level. The black arrow denotes the pointing direction of the boresight of the TX antenna. The east-most Silver Tower is marked by an 'X'.

instantaneous channel impulse responses.

Fig. 4.14 is the fully ray-traced RX location map showing each ray that leaves the TX and successfully arrives at the RX, and Fig. 4.15 is a comparison between predicted and measured AOAs at the RX location. The ray-tracer was found to predict the strongest AOA angles to within an accuracy of 20° (i.e., two antenna beamwidths). Thus, the strongest AOA may in reality be found by searching ±20° about the predicted AOA. Each ray detected at the reception sphere carries a set of distinct parameters, which are displayed in Table 4.1.

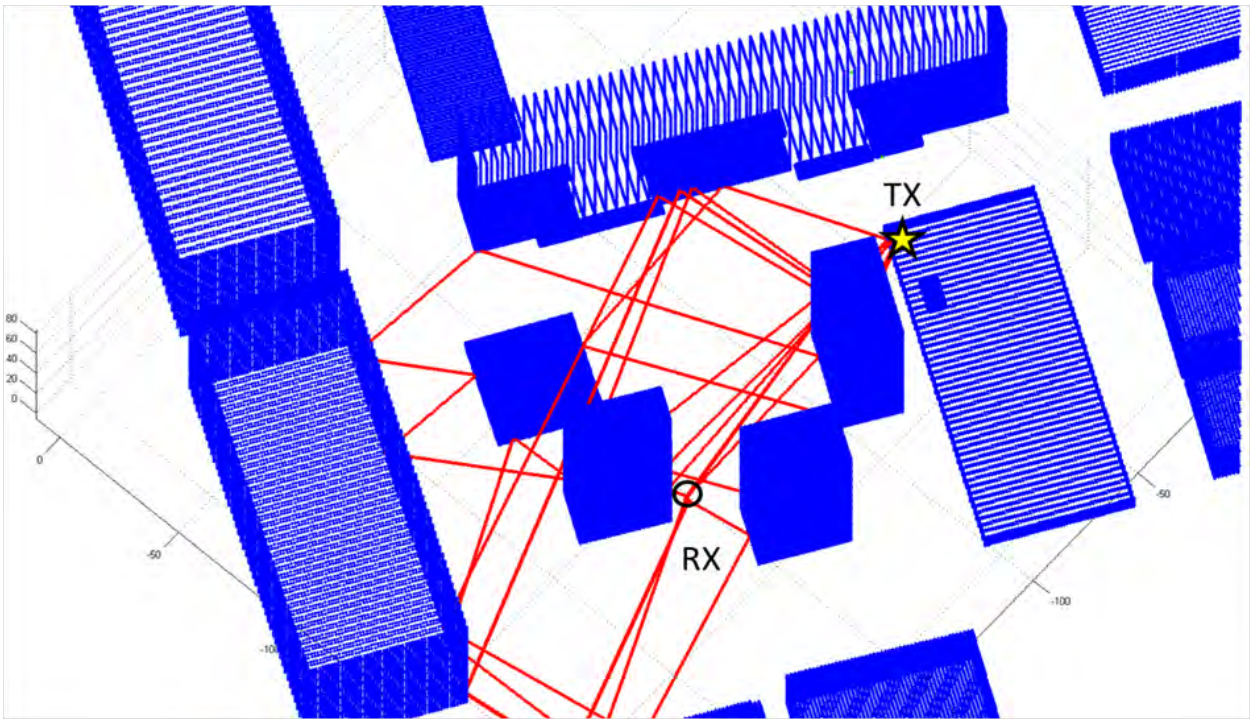

Figure 4.14: A 3-dimensional view of the Manhattan Downtown area recreated using a MATLAB-based ray-tracer. The rays which leave the TX and successfully arrive at the RX are shown in red, and represent multipath signal trajectories in a dense urban microcell. The TX was located on the rooftop of the Coles Sports Center 7 m above ground (yellow star), and the RX was located 113 m away, 1.5 m above ground (black circle).

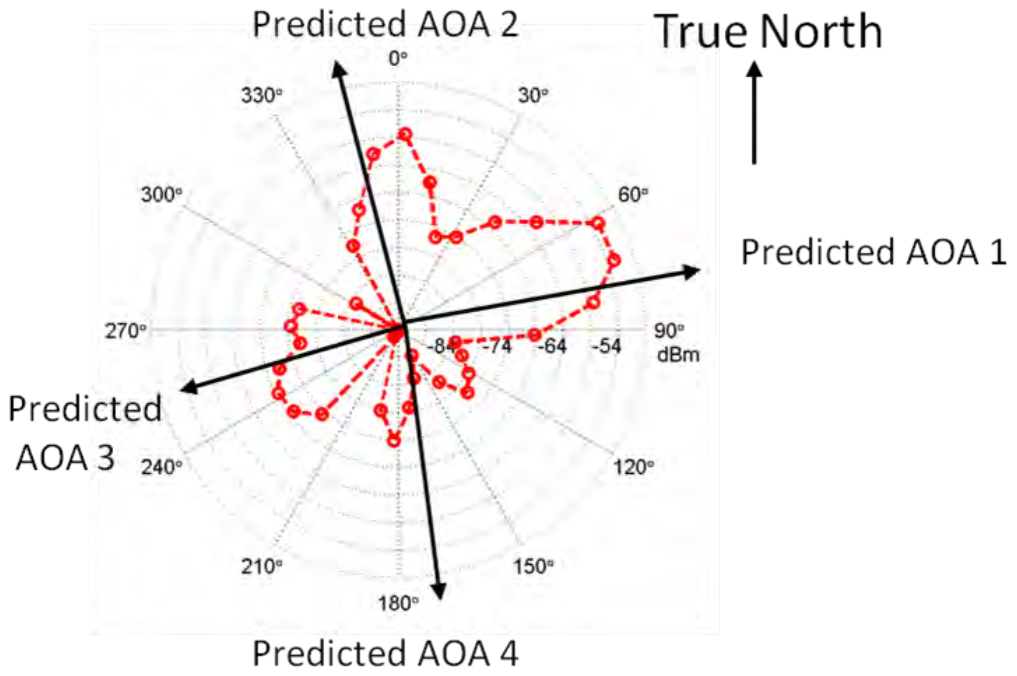

Figure 4.15: Azimuthal distribution of total received power (dBm units), also referred to as polar plot, showing the predicted AOAs using 3-D ray-tracing at the Manhattan RX location on Wooster Street. The center of the plot corresponds to the RX location. The RX and TX antennas were both 24.5 dBi with 10.9° (in azimuth) and 8.6° (in elevation) 3 dB beamwidths, and the RX azimuth 0° mark points to the True Noth bearing direction. The TX antenna boresight was pointed at the north-most face of the east-most Silver Tower, at a downtilt of 10° with respect to the horizon.

Table 4.1: Parameters describing each ray detected at the reception sphere in Fig. 4.14. These parameters are the direct output of the MATLAB-based ray-tracer. All azimuth angles denoted as θ are with respect to a True North bearing where the clockwise direction corresponds to positively increasing azimuth angles, and all elevation angles denoted as ϕ are with respect to the horizon.

Ray #	$\theta_{AOD}(°)$	$\phi_{AOD}(°)$	**Distance Travelled (m)**	**# of Reflections**	$\theta_{AOA}(°)$	$\phi_{AOA}(°)$
1	270.2	-3.7	114.3	0	82.9	3.7
2	269.9	-3.4	114.6	0	82.6	3.4
3	269.9	-5.0	122.6	2	339.4	-5.0
4	251.2	-1.0	429.8	4	251.1	1.0
5	251.2	-1.3	430.5	5	251.0	-1.3
6	254.3	-1.0	450.3	5	170.9	1.0
7	249.4	-1.3	465.4	7	246.2	-1.3
8	248.0	-1.3	513.2	7	88.7	-1.3
9	271.1	-1.3	516.1	8	339.5	-1.3

Figs. 4.16 - 4.19 show four excess delay PDPs corresponding to the four strongest measured AOAs, and

are found by searching ±20° about the predicted AOAs.

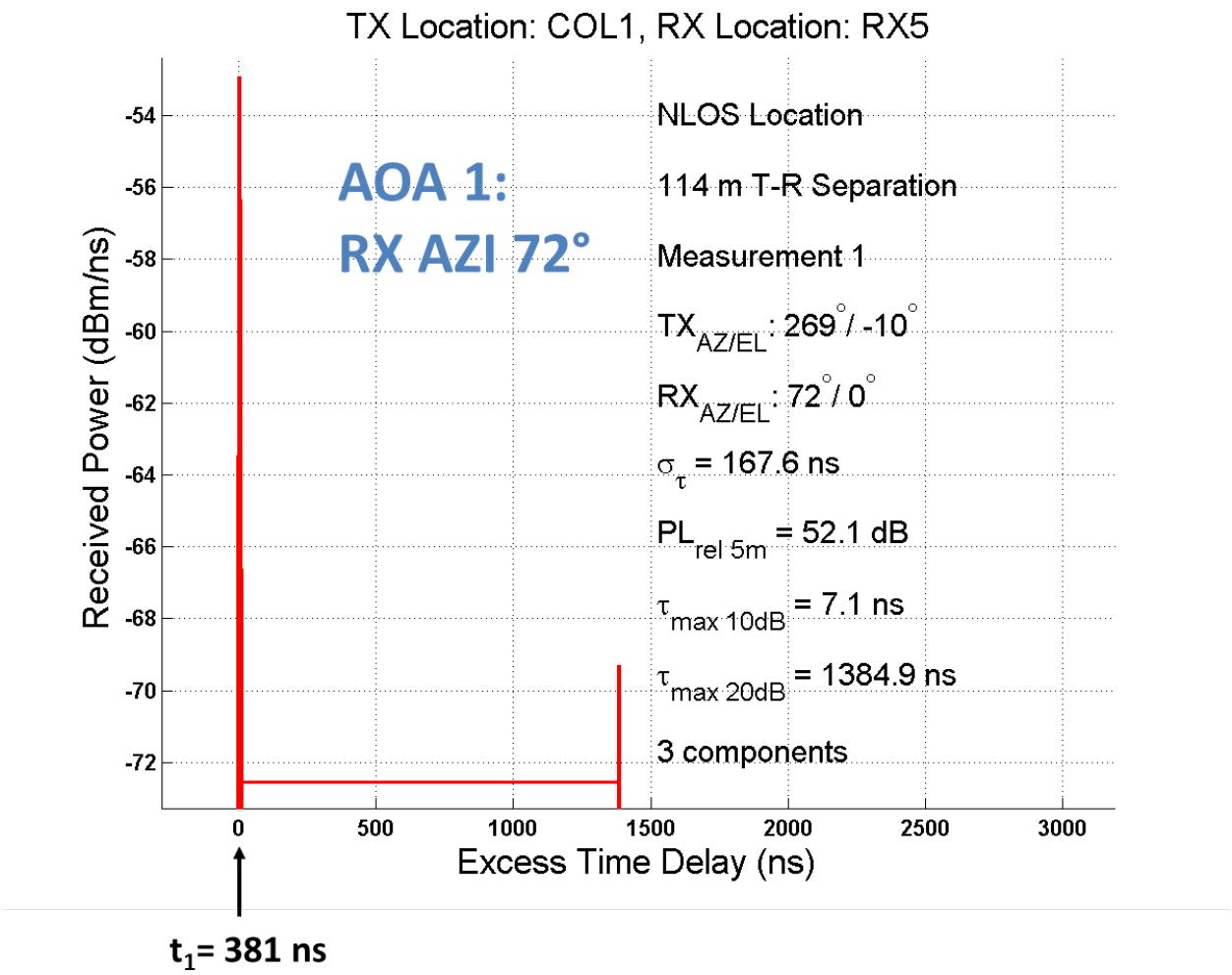

Figure 4.16: PDP collected at RX azimuth/elevation of 72°/0° and TX azimuth/elevation of 269°/-10°. The 3-D ray-tracer predicted that energy was received at this angle combination. Azimuth angles are with respect to a True North 0° angle.

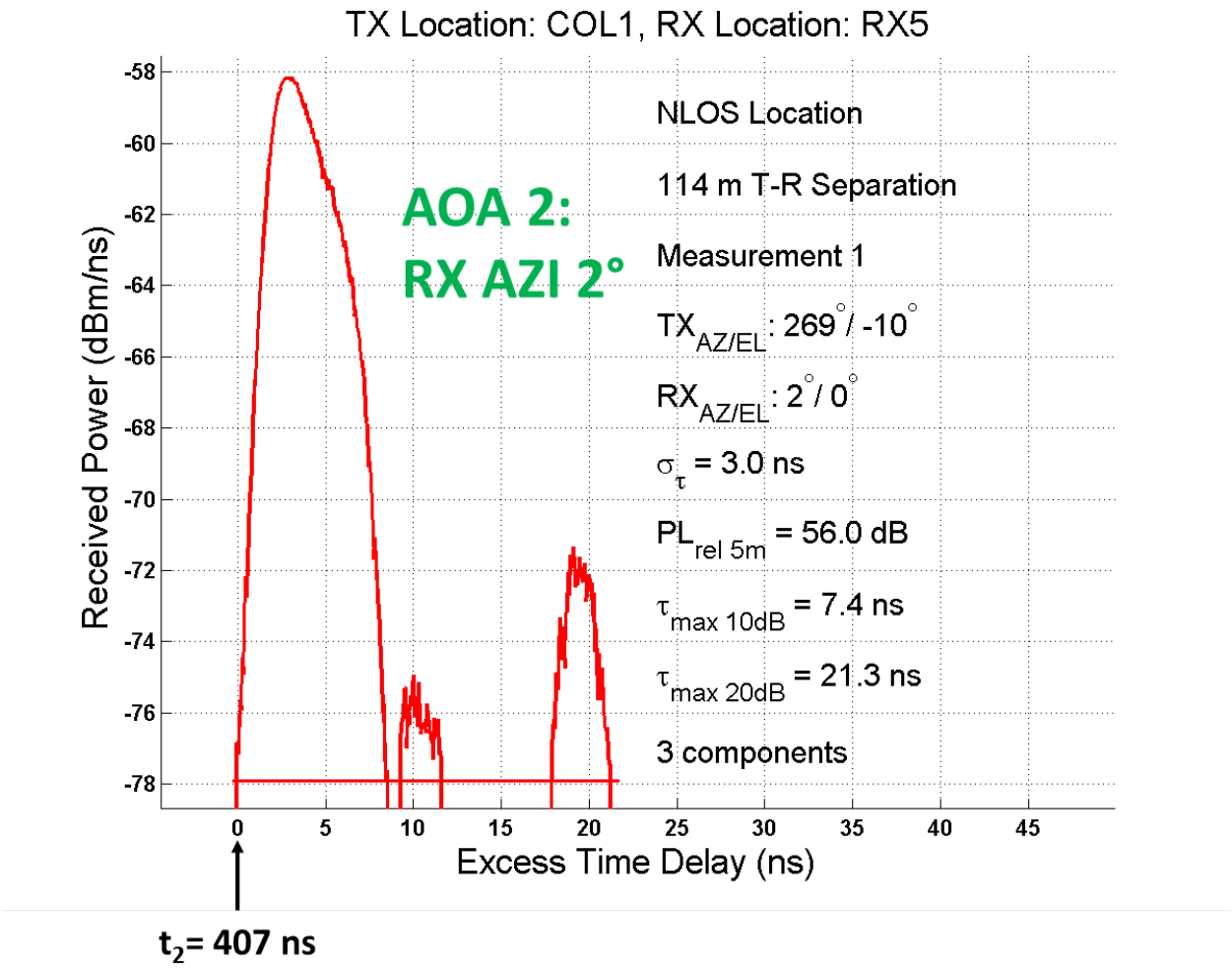

Figure 4.17: PDP collected at RX azimuth/elevation of 2°/0° and TX azimuth/elevation of 269°/-10°.The 3-D ray-tracer predicted that energy was received at this angle combination. Azimuth angles are with respect to a True North 0° angle.

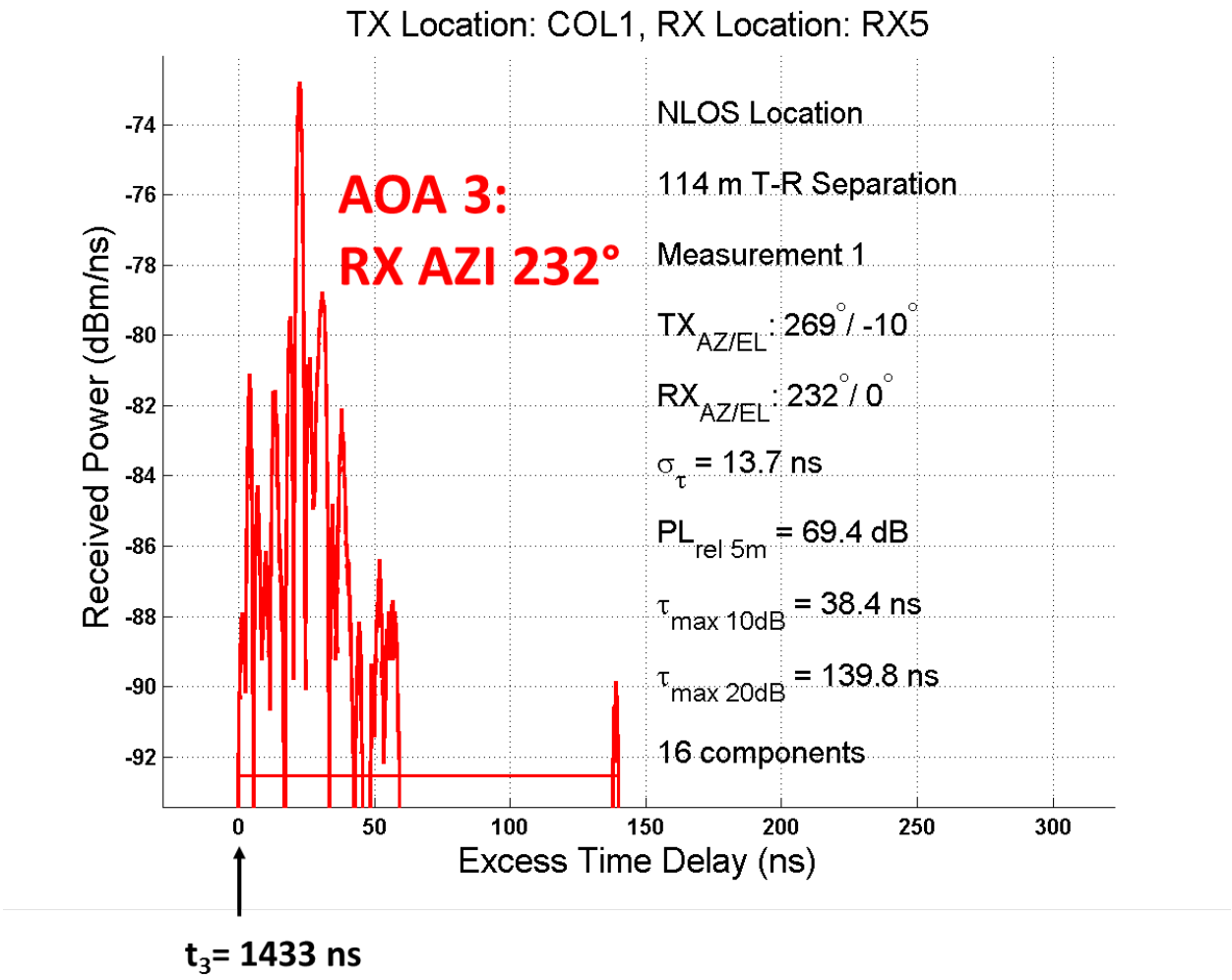

Figure 4.18: PDP collected at RX azimuth/elevation of 232°/0° and TX azimuth/elevation of 269°/-10°. The 3-D ray-tracer predicted that energy was received at this angle combination. Azimuth angles are with respect to a True North 0° angle.

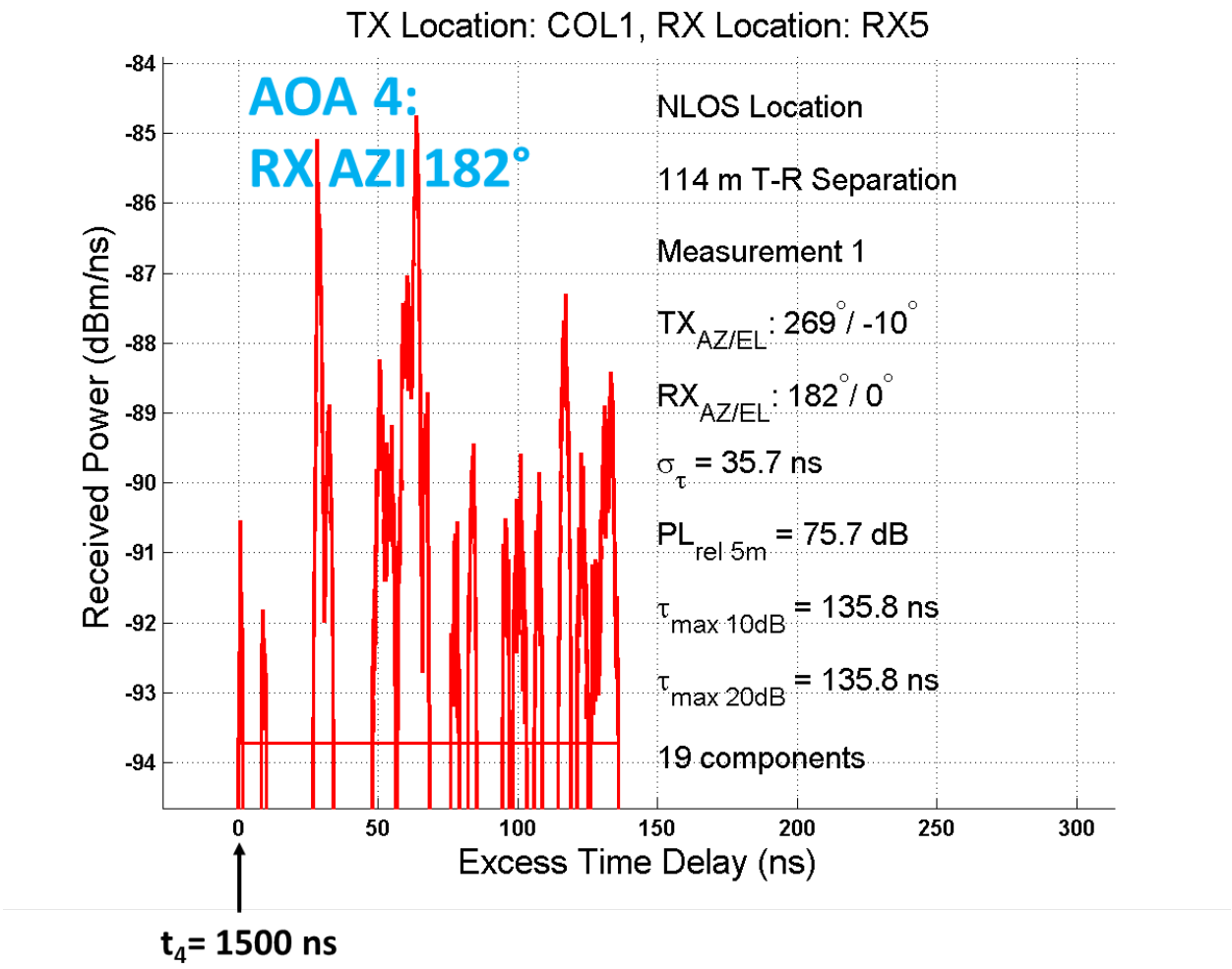

Figure 4.19: PDP collected at RX azimuth/elevation of 182°/0° and TX azimuth/elevation of 269°/-10°. The 3-D ray-tracer predicted that energy was received at this angle combination. Azimuth angles are with respect to a True North 0° angle.

Fig. 4.20 shows the omnidirectional PDP generated from the above four excess delay PDPs. The excess delay PDPs were appropriately shifted using the absolute propagation time (obtained from the ray-tracer by dividing the propagation distance by the speed of light in free space) of the first arriving peak at the corresponding RX azimuth angle. The absolute propagation times of the first arriving peak for AOA 1, 2, 3 and 4 were 381 ns, 407 ns, 1433 ns and 1500 ns, respectively. Since the four angles are independent (i.e., not adjacent to each other), the four excess delays PDPs were shifted and summed in the linear scale to recreate the omnidirectional PDP.

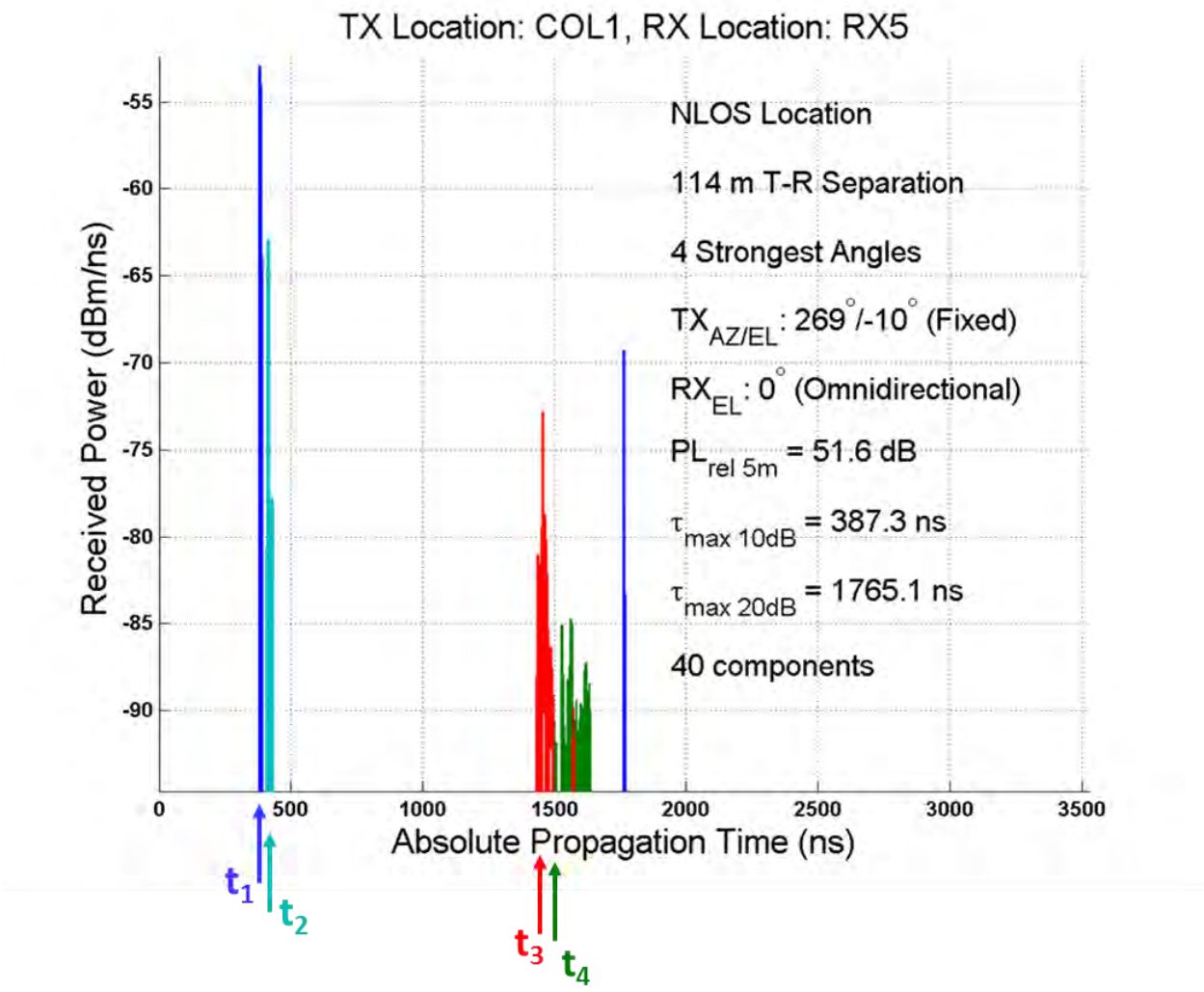

Figure 4.20: Omnidirectional PDP in the azimuth plane specified at a RX elevation of 0° synthesized using the 3-D ray-tracing absolute time of arrivals and the four excess delay PDPs shown above for the RX location on Wooster Street.

This procedure was repeated for all measured RX locations at which signal was obtained so as to synthesize many omnidirectional PDPs, which were further processed to recover channel temporal statistics needed for an omnidirectional channel model, as described in the next chapter.

4.3 Conclusion

This section discussed the fundamental processing techniques used throughout this work in recovering processed power delay profiles using a 5 dB above mean noise floor SNR, and absolute propagation times of arrival in 3 dimensions using a MATLAB-based ray-tracing package. These two aspects have allowed us to recover omnidirectional power delay profiles, using the processed excess delay PDPs measured at the different strongest TX and RX angles, in conjunction with the absolute times of arrival using the ray-tracer. The omnidirectional PDPs can now be used to extract fundamental channel statistics, which are needed to model channel parameters such as temporal cluster delays and powers. These extracted statistics will allow us to build a statistical simulator capable of recreating the statistics of the measured channels. Chapter 5 provides a comprehensive framework against which to study temporal and spatial channel parameters, presents extracted statistics from the synthesized omnidirectional power delay profiles, and outlines a step procedure for generating channel coefficients and corresponding departure and arrival power azimuth spectra.

Chapter 5

28 GHz Wideband Channel Models and Statistical Simulator for Dense Urban Environments

This section presents newly generated omnidirectional channel models based on the 28 GHz narrowbeam LOS and NLOS measurements obtained in Manhattan using absolute timing as synthesized from 3-D ray-tracing. In total, 20 of 24 angles of arrival locations and 17 of 24 angles of departure locations were successfully ray-traced. The remaining AOA and AOD locations did not yield usable ray-tracing information, and can be explained because of the imprecision of the database that could not predict rays propagating from the TX to the RX. A total of 114 LOS lobes and 377 NLOS lobes were obtained from the Manhattan measurements to synthesize spatial channel models. In order to understand both temporal and spatial channel models, definitions and diagrams are provided to illustrate the channel parameters.

5.1 Cluster and Lobe Definitions

The two principal units of propagation considered in this work are a time cluster and a spatial lobe, which represent the two major parts of the SSCM, namely, the temporal (i.e., omnidirectional) and spatial components of the ultimate statistical channel model.

A time cluster is defined as a group of cluster subpaths (i.e., multipath components) traveling close in time and space. A time cluster is further represented by nine principal cluster parameters: the absolute time of arrival at the receiver, the azimuth/elevation angles of departure, the azimuth/elevation spreads of departure, the azimuth/elevation angles of arrival, and the azimuth/elevation spreads of arrival.

A spatial lobe is defined as a departing or incoming direction of contiguous energy over the azimuth and/or elevation planes. A spatial lobe is identified by eight principal lobe parameters: the azimuth/elevation angles of departure, the azimuth/elevation spreads at the transmitter, the azimuth/elevation angles of arrival, and the azimuth/elevation spreads at the receiver. The diagrams below illustrate time cluster and spatial lobe terminologies.

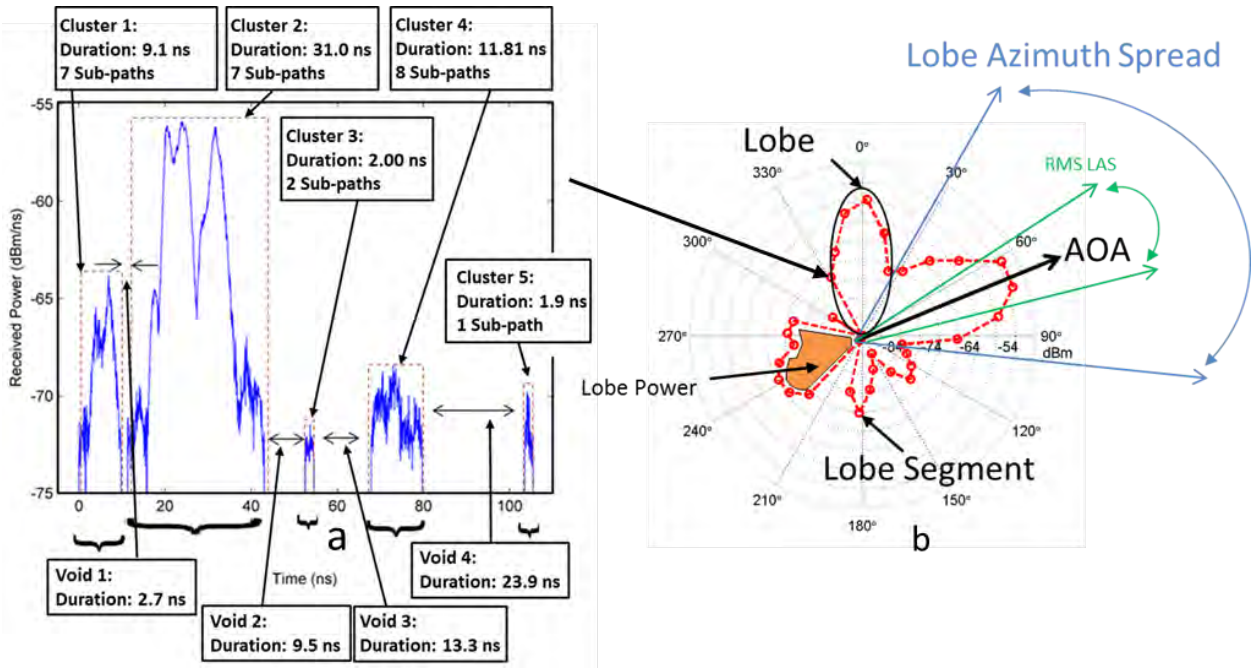

Figure 5.1: a. Diagram showing typical power delay profile measured in Manhattan at 28 GHz with energy arriving from a particular AOA, obtained with directional 24.5 dBi gain antennas (10.9° HPBW), where cluster terminology is illustrated. Four time clusters may be seen with time durations ranging from 2 ns to 31 ns. b. Diagram showing a polar plot measured in Manhattan at 28 GHz, where lobe terminology is illustrated. Five distinct lobes may be seen with various lobe azimuth spreads and AOAs. Each 'dot' is a lobe angular segment, and represents the total integrated received power over a 10° angle.

Fig. 5.2 illustrates the combined spatial and temporal definitions described above. Initially, two clusters are transmitted from the TX at Position 1. Each cluster arrives at the receive antenna via different propagation paths to Position 2. The first (yellow) arriving time cluster comes from one reflected propagation path and breaks up into two microscopic subpaths, and the second (red) arriving time cluster is composed of three cluster subpaths. It is important to recognize that, although both clusters arrive at the same receive angle, they each have different propagation delays. A cluster can be identified by nine parameters: the absolute time of arrival at the receiver, the azimuth and elevation angles of departure, the azimuth and elevation spreads of departure, the azimuth and elevation angles of arrival, and the azimuth and elevation spreads of arrival.

Thus, in the diagram below, both time clusters are denoted by the same azimuth/elevation AOD at the transmit antenna and the same azimuth/elevation AOA at the receive antenna, but have two different propagation delays, and different AOD and AOA azimuth/elevation spreads. They constitute two unique

time clusters. It is physically impossible to determine the true azimuth/elevation AOD and azimuth/elevation AOA. We can only resolve and specify the AOD and AOAs up to one antenna beamwidth.

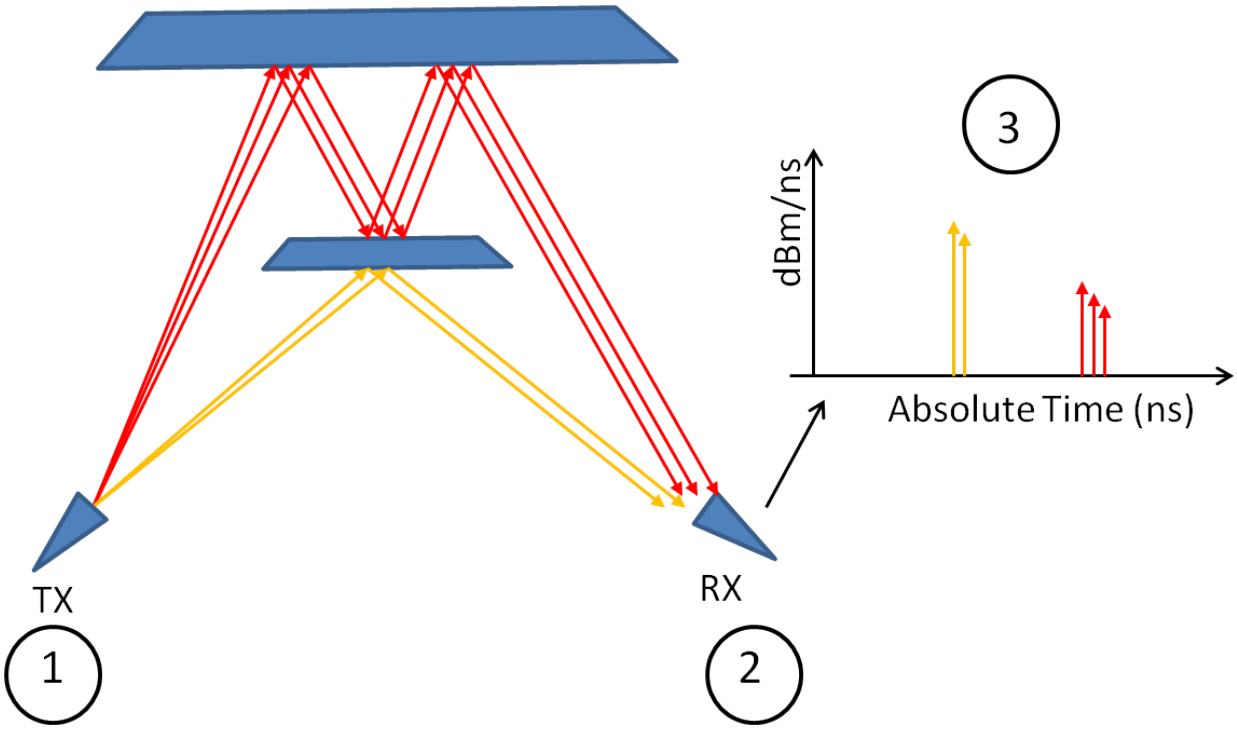

Figure 5.2: Diagram illustrating two traveling time clusters leaving the same narrowbeam transmit antenna and arriving at the same narrowbeam receive antenna (i.e., same AOA). Each time cluster is described using nine parameters: the absolute time of arrival at the receiver, the azimuth and elevation angles of departure, the azimuth and elevation spreads of departure, the azimuth and elevation angles of arrival, and the azimuth and elevation spreads of arrival. Both clusters shown in this diagram are distinct clusters even though they arrive at the same AOA.

The parameters representing time clusters and spatial lobes are identified and defined below.

5.1.1 Time Cluster Terminology

5.1.1.1 Number of Time Clusters in an Omnidirectional Power Delay Profile

The number of time clusters in an omnidirectional power delay profile corresponds to the number of discrete propagation paths along which electromagnetic radiation travels from the transmitter to the receiver.

Time clusters are typically composed of several multipath components, which arise from electromagnetic reflections (penetrations) upon (through) obstructions such as buildings, pillars, trees, etc...Physical

obstructions typically exhibit macroscopic roughness, and upon impact of such obstructions, the radiation will tend to break up into microscopic subpath components.

5.1.1.2 Number of Subpaths in a Time Cluster

The number of subpaths in each time cluster corresponds to the number of subpath components contained within one time cluster. Each cluster subpath physically corresponds to a microscopic propagation path from transmitter to receiver that composes the macroscopic propagation path.

The subpath components typically come about from reflections upon impact from physical obstructions, but nevertheless remain close in time and space to each other within the macroscopic propagation path.

5.1.1.3 Cluster Excess Time Delays

The cluster excess time delay corresponds to the time of arrival of the first subpath component composing a time cluster, relative to the time of arrival of the first arriving cluster. By definition, the first cluster in an omnidirectional power delay profile has an excess time delay of 0 ns, and all other subsequent clusters have excess time delays of $\tau_n = t_n - t_1$, where t_1 corresponds to the absolute propagation time of arrival of the first arriving cluster.

5.1.1.4 Cluster Subpath Excess Time Delays

The cluster subpath excess time delay, or intra-cluster time delay, corresponds to the time of arrival of a subpath component within a time cluster, relative to the first arriving subpath component in the same cluster. By definition, the first subpath component in the time cluster has an intra-cluster time delay of 0 ns, and all other subsequent subpath components inside the same time cluster have intra-cluster time delays of $\rho_{m,n} = \tau_{m,n} - \tau_{1,n}$, where $\tau_{1,n}$ corresponds to the excess time delay of the first subpath component composing the time cluster.

5.1.1.5 Relative Cluster Power Levels with respect to the Total Integrated Received Power in the Omnidirectional Profile

The relative cluster power levels correspond to the fraction of power contained in a cluster with respect to the total power contained in the omnidirectional PDP. The cluster powers were studied by considering the ratio between the total cluster power (in linear units) and the total power in the omnidirectional profile (in linear units). Each cluster power ratio thus lies between a value of 0 and 1. A cluster power ratio value close to 0 indicates that the cluster carries a very small amount of power, while a cluster power ratio value close to 1 indicates that the cluster carries most of the power found in the omnidirectional PDP. The cluster power ratios $R_{Cluster}$ are obtained as follows:

$$R_{Cluster} = \frac{\sum_n P(\tau_n)}{\sum_i P(\tau_i)} \tag{5.1}$$

where the sub-index n is taken over all points forming the cluster, and the sub-index i is taken over all points forming the entire omnidirectional PDP.

5.1.1.6 Relative Cluster Subpath Power Levels with respect to the Total Integrated Received Power in the Time Cluster

The relative cluster subpath power levels correspond to the fraction of power contained in a subpath component with respect to the total power contained in the same time cluster. The cluster subpath powers were studied by considering the ratio between the subpath component power (in linear units) and the total power in the same time cluster (in linear units). Each cluster subpath power ratio thus lies between a value of 0 and 1. A cluster subpath power ratio value close to 0 indicates that the subpath component carries a very small amount of power compared to other components in the same time cluster, while a cluster subpath power ratio value close to 1 indicates that the subpath component carries most of the power found in the

time cluster. The cluster subpath power ratios $R_{Subpath}$ are obtained as follows:

$$R_{Subpath} = \frac{\sum P(\tau_k)}{\sum P(\tau_n)} \tag{5.2}$$

where the sub-index k is taken over all points making the cluster subpath, and the sub-index n is taken over all points making the time cluster.

5.1.1.7 RMS Delay Spread of an Omnidirectional Profile

The RMS delay spread σ_τ of an omnidirectional PDP is the second moment of the omnidirectional PDP, and is obtained from the following equations:

$$\sigma_\tau = \sqrt{\overline{\tau^2} - \overline{\tau}^2} \tag{5.3}$$

where,

$$\overline{\tau} = \frac{\sum \tau_i P(\tau_i)}{\sum P(\tau_i)}, i = 1, 2, ...N \tag{5.4}$$

$$\overline{\tau^2} = \frac{\sum \tau_i^2 P(\tau_i)}{\sum P(\tau_i)}, i = 1, 2, ...N \tag{5.5}$$

where $P(\tau_i)$ is the power level at time delay τ_i, and N is the total number of samples making up the omnidirectional PDP. The RMS delay spread of the omnidirectional profile offers a time scale over which most of the power is collected at the receiver.

5.1.1.8 RMS Delay Spread of a Time Cluster

The RMS delay spread s_τ of a time cluster is the second moment of the time cluster, and is obtained from the following equations:

$$s_\tau = \sqrt{\overline{\tau^2} - \overline{\tau}^2} \tag{5.6}$$

where,

$$\overline{\tau} = \frac{\sum \tau_n P(\tau_n)}{\sum P(\tau_n)}, n = 1, 2, ...K \tag{5.7}$$

$$\overline{\tau^2} = \frac{\sum \tau_n^2 P(\tau_n)}{\sum P(\tau_n)}, n = 1, 2, ...K \tag{5.8}$$

where $P(\tau_n)$ is the power level at time delay τ_n, and K is the total number of samples making up the time cluster. The RMS delay spread of a time cluster offers a time scale over which most of the power is contained within the cluster.

5.1.1.9 Time Duration of a Time Cluster

The time duration of a cluster is the time duration over which the cluster power is collected at the receiver. The time duration Δt_C of a cluster is obtained as follows:

$$\Delta t_C = \tau_K - \tau_1 \tag{5.9}$$

where τ_1 and τ_K are the time delays of the first and last samples forming the time cluster, respectively.

5.1.1.10 Void Duration between Two Consecutive Time Clusters

The void duration between two consecutive time clusters is the duration of time separating two consecutive clusters. The void duration Δt_V between two consecutive clusters is obtained as follows:

$$\Delta t_V = \tau_{1,n+1} - \tau_{K,n} \tag{5.10}$$

where $\tau_{1,n+1}$ and $\tau_{K,n}$ are the time delay of the first power sample in the $(n+1)^{\text{st}}$ cluster, and the time delay of the last power sample in the n^{th} cluster, respectively.

5.1.2 Spatial Lobe Terminology

5.1.2.1 Number of Lobes in a Polar Plot

The number of lobes in a polar plot corresponds to the number of outgoing (AOD) or incoming (AOA) energy directions at the transmitter or receiver, respectively.

5.1.2.2 Azimuth and Elevation Spreads of a Lobe

The azimuth $\Delta\theta$ and elevation $\Delta\phi$ spreads of a lobe are defined as the azimuth and elevation angle spans over which the lobe exists, and are obtained from the following equations:

$$\Delta\theta = |\theta_K - \theta_1| + \Theta_{3dB} \tag{5.11}$$

$$\Delta\phi = |\phi_K - \phi_1| + \Phi_{3dB} \tag{5.12}$$

where (θ_1, ϕ_1) and (θ_K, ϕ_K) are the first and last azimuth and elevation angles composing the lobe respectively. $\Theta_{3dB} = 10^\circ$ is the azimuth HPBW of the horn antennas used during measurements, and is also the azimuthal step increment between two adjacent measurements.

5.1.2.3 Angle of Departure/Arrival of a Lobe

The AOD/AOA of a lobe is defined as the power weighted mean angle of the lobe power azimuth spectrum, as is shown below:

$$\overline{\theta} = \frac{\sum_k \theta_k P(\theta_k)}{\sum_k P(\theta_k)} \tag{5.13}$$

where $P(\theta_k)$ is the total received power (i.e., area underneath measured PDP) in linear units at azimuth angle θ_k. The sub-index k runs through all angles belonging to the same lobe.

5.1.2.4 Relative Power Levels of Lobe Angular Segments with respect to the Maximum Lobe Peak Power Level

The lobe segment power ratios correspond to the fractional amount of power in each lobe segment with respect to the maximum power segment in the lobe. The ratios are obtained as follows:

$$R(\Delta\theta = |\theta_k - \theta_{max}|) = \frac{P(\theta_k)}{P(\theta_{max})}, k = 1, 2, ...K \tag{5.14}$$

$$\theta_{max} = \underset{k}{\operatorname{argmax}}\, P(\theta_k) \tag{5.15}$$

where $P(\theta_k)$ is the total received power at angle θ_k, $P(\theta_{max})$ is the maximum total received power at angle θ_{max}, and K is the total number of angular segments contained in the lobe. All power levels are in linear units.

5.1.2.5 RMS Azimuth and Elevation Spreads of a Lobe

The lobe RMS azimuth and elevation spreads σ_θ and σ_ϕ are the second moment of the lobe power azimuth and elevation spectra, respectively, and are computed as follows:

$$\sigma_\theta = \sqrt{\overline{\theta^2} - \overline{\theta}^2} \tag{5.16}$$

$$\sigma_\phi = \sqrt{\overline{\phi^2} - \overline{\phi}^2} \tag{5.17}$$

where,

$$\overline{\theta} = \frac{\sum_i \theta_i P(\theta_i, \phi_j)}{\sum_i P(\theta_i, \phi_j)}, \qquad \overline{\phi} = \frac{\sum_j \phi_j P(\theta_i, \phi_j)}{\sum_j P(\theta_i, \phi_j)} \tag{5.18}$$

$$\overline{\theta^2} = \frac{\sum_i \theta_i^2 P(\theta_i, \phi_j)}{\sum_i P(\theta_i, \phi_j)}, \qquad \overline{\phi^2} = \frac{\sum_j \phi_j^2 P(\theta_i, \phi_j)}{\sum_j P(\theta_i, \phi_j)} \tag{5.19}$$

where $P(\theta_i, \phi_j)$ is the total integrated received power (in linear units) at azimuth and elevation angle combination (θ_i, ϕ_j), and the sub-indices i and j run over all angles belonging to a lobe. The lobe azimuth RMS spread indicates the azimuth and elevation ranges over which most of the power is contained in the lobe. These quantities will be important when designing future electrically-steered phased antenna arrays, in which on-chip antennas will be able to steer their antenna pattern towards the strongest directions of arrival to improve received signal levels. It is important to estimate the azimuth and elevation ranges over which to spread the antenna pattern in order to match the antenna to the incoming energy spread at the receiver.

5.2 Primary and Secondary Statistics

The ultimate goal of the work presented herein is to produce omnidirectional power delay profiles and corresponding power azimuth spectra which recreate the measured statistics of the 28 GHz wideband dense urban wireless channel. The measured statistics refer to all the extracted models from the synthesized omnidirectional power delay profiles, which were recreated using 3-D ray-tracing techniques in conjunction with measured excess delay power delay profiles obtained at different angular channel windows, and measured power azimuth spectra.

It is thus important to identify the statistics required to generate a power delay profile and corresponding power azimuth spectrum in order to develop a statistical simulator. Indeed, many statistics may be extracted which can describe a wealth of channel parameters, some of which will bear no impact on the generated profiles. For example, finding the statistical distribution that models the RMS delay spread of omnidirectional power delay profiles does not help in actually generating a PDP, since the RMS delay spread itself depends on more fundamental channel quantities, namely, the power levels and time of arrivals of individual multipath components in the profile.

A complete understanding of the required statistics that bear a direct impact on the power delay profiles is crucial, while the statistics bearing indirect impact are of secondary importance. This is not intended to suggest that statistics that bear indirect impact are not useful. They indeed provide additional sanity checks and overall validity of a statistical simulator as a faithful and accurate tool that can recreate omnidirectional profiles of the wireless channel.

We classify here all possible extracted channel statistics, depending on whether or not they bear any effect on the generated power delay profiles, into two categories: primary and secondary statistics.

A primary statistic models a channel parameter which has a direct effect on the generated power delay profiles. Examples of primary statistics are the cluster excess time delays and cluster subpath excess time delays.

A secondary statistic models a channel parameter which has an indirect effect on the generated power delay profiles, that is, which does not influence the shape of the power delay profile. Secondary statistics

provide a means of testing the validity and accuracy of a statistical simulator, but are not used in generating power delay profiles. An example of a secondary statistic is the RMS delay spread of an omnidirectional PDP.

The temporal primary statistics needed to generate power delay profiles are listed below:

1. The number of time clusters in an omnidirectional power delay profile
2. The number of subpath in each time cluster
3. The cluster excess time delays
4. The cluster subpath excess time delays
5. The relative cluster power levels with respect to the total integrated received power in the omnidirectional profile
6. The relative cluster subpath power levels with respect to the total integrated received power in the time cluster

The spatial primary statistics needed to generate power azimuth spectra, in conjunction with temporal primary statistics, are listed below:

1. The number of lobes in a polar plot
2. The azimuth spread of a lobe
3. The angle of departure/angle of arrival of a lobe
4. The relative power levels of lobe angular segments with respect to the maximum lobe segment power level

The secondary statistics which will allow to test the validity and overall accuracy of the statistical simulator are listed below:

1. The RMS delay spread of the omnidirectional profile
2. The RMS delay spread of a time cluster
3. The time duration of a cluster
4. The void duration between two consecutive time clusters
5. The RMS azimuth spread of a lobe

A statistical simulator is considered to be validated once it is capable of reproducing the mean and standard deviation, as well as distribution type, of both primary and secondary statistics within a reasonable error margin.

5.3 Cluster Partitioning

It is important to recognize that all primary statistics (some more than others) are dependent upon the clustering algorithm used in determining the time cluster partitioning within an omnidirectional power delay profile. To illustrate this concept, lets imagine two very different cluster partitioning algorithms. In Algorithm A, suppose a simple cluster algorithm is chosen for which the inter-cluster void duration is 0 ns: a time cluster is composed of continuous received signal, and two consecutive clusters are separated by an absence of signal. In Algorithm B, suppose we use a K-means clustering algorithm in which the time cluster centroids are optimized by minimizing the within-cluster variance. In Algorithm B, a time cluster may be composed of continuous received signal as well as small inter-cluster void intervals. Computing the temporal statistics under these two algorithms will clearly yield significant differences, especially for the number of clusters and the number of cluster subpaths found in an omnidirectional power delay profile. By extension, the other temporal primary statistics (cluster excess delays, cluster subpath excess delays, and relative power levels) will also yield different statistics under these two hypothetical algorithms.

Through numerous attempts involving several different clustering algorithm schemes, it has been recognized that the method yielding the 'best' clustering partitioning scheme requires an optimization method based on the χ^2 criterion, as opposed to a K-means clustering algorithm [101], or a linkage or hierarchical algorithm [102]. Here, 'best' refers to the most convenient clustering of the data, which yields statistical distributions for the primary statistics that are most easily reproducible using standard and well-known distributions, such as the Poisson distribution, the Exponential distribution, and the normal Gaussian distribution.

After extensive attempts at fitting the channel parameters corresponding to primary statistics into known statistical distributions obtained from several different clustering algorithms, it has been observed

that of the six presented temporal primary statistics, the ones that fluctuate the most from one clustering algorithm to the next are the number of time clusters in an omnidirectional PDP (channel parameter 1) and the number of subpaths per cluster (channel parameter 2), while the remaining temporal primary statistics (channel parameters 3-6) tend to come out with the same distribution type regardless of the clustering algorithm used.

This observation has led to the recognition that the cluster partitioning scheme used does not alter the type of distribution corresponding to channel parameters 3-6, while significantly impacts the statistics of channel parameters 1 and 2. In other words, the channel modeler can directly influence the outcome of the distributions corresponding to channel parameters 1 and 2, while channel parameters 3-6 tend to follow distributions which tend to behave relatively independently from channel parameters 1 and 2.

The cluster partitioning optimization must be performed on channel parameters 1 and 2 in such a way as to conveniently reproduce their measured distributions using standard and well-known distributions. The modeler may then choose the 'best' cluster partitioning scheme, so that channel parameters 1 and 2 fit conveniently into pre-determined simple distributions. In order to find the 'best' cluster partitioning scheme, one must extract channel parameters 1 and 2 by varying the minimum inter-cluster void duration over a wide range of values on the entire NLOS omnidirectional power delay profile ensemble, and find the 'optimum' inter-cluster void duration that simultaneously minimizes the χ^2 criterion between the expected (pre-determined) distributions and the computed statistics [103], presented in the following equation:

$$\chi^2 = \sum_{i=1}^{k} \frac{(n_i - E_i)^2}{E_i} \tag{5.20}$$

where n_i is the number of observations and E_i is the expected number of observations for the i^{th} class.

The number of clusters in an omnidirectional PDP is negatively correlated with the number of cluster subpaths. Indeed, as the minimum inter-cluster void duration increases, the number of clusters in an omnidirectional PDP must decrease, and therefore the number of subpaths per cluster must increase. Conversely, as the minimum inter-cluster void duration decreases, the number of clusters must increase, and the number of subpaths per cluster must decrease. The general skewness of these two distributions will tend to be op-

posite. A natural first attempt at modeling the number of clusters and the number of subpaths per cluster is to choose a Poisson and Exponential distribution, which exhibit opposite skewness, as is indicated by the intuitive explanation provided above.

In this thesis, the number of clusters in an omnidirectional PDP and the number of cluster subpaths were fit as the composite of a Poisson and Discrete Uniform distributions, and to a Discrete Exponential distribution, respectively, by numerically minimizing the χ^2 criterion. Both of these distributions are easily obtained from a simple random number generator.

The optimization was performed numerically by computing the statistics of temporal channel parameters 1 and 2 by varying the inter-cluster void interval over the ensemble of NLOS omnidirectional PDPs. This optimization procedure yielded the 'best' optimum inter-cluster void interval, which was then used to produce the entire set of temporal primary statistics. In this work, the optimum inter-cluster void interval was determined to be 2.7 ns. This 2.7 ns void interval between two consecutive time clusters accounts for the theoretical pulse width of the multipath components. After deconvolving each multipath component into a delta-spike with infinitely short time duration (and thus removing the effects of the sliding correlation at the receiver), the inter-cluster void interval becomes 2.7 ns+ 2.5×2 ns = 7.7 ns.

Once the cluster partitioning scheme was determined so that channel parameters 1 and 2 fit closely to the Poisson distribution and Exponential distributions respectively, the statistics of channel parameters 3-6 were fit to theoretical distributions. A χ^2 goodness of fit test with significance level of 5% was consistently performed on the primary statistics to ensure that the measured distributions fit the theoretical distributions very closely.

5.4 Measured Channel Statistics

This section presents 28 GHz wideband measured channel statistics, namely the omnidirectional path loss models, temporal cluster and spatial lobe statistics in both LOS and NLOS environments based on the collected measurements in Manhattan. The statistics presented here were obtained from measurements performed at 4 LOS locations, and 21 NLOS locations and so additional measurements must be performed

to enhance and complement the channel models presented here.

While quite extensive, the 28 GHz field measurements were not truly omnidirectional, in that highly directional horn antennas were used to obtain sufficient link margin, and only one elevation angle and three azimuthal pointing angles were used at the transmitter while the RX was swept in azimuth. Furthermore, when the RX azimuth sweeps were made, there were only three different elevation angles used at the RX. For the case where the TX was rotated over all azimuth directions at a single down tilt angle, a single RX pointing angle was used. However, this procedure was crafted to assure that most of the energy (e.g. reasonably close to a true omnidirectional situation) would be measured. For the RX sweeps, it had been shown earlier (and was further verified in the 28 GHz measurements) that most of the energy arriving at the RX comes from a relatively small azimuthal range of TX antenna orientations. Since the 24.5 dBi TX antennas had 10° beamwidths, the powers summed at the RX's contained some overlapping energy from each of the three TX orientations, since the TX azimuth angles used in the RX sweep measurements were spaced 5° (a half- beamwidth) apart from each other.

From these synthesized omnidirectional PDPs, the omnidirectional path losses were extracted by finding the received power (area under the omnidirectional PDPs) at each RX location, and removing antenna gains from the received power (double counting received powers at the same TX-RX angle combination from different TX sweeps was carefully removed). The corresponding large scale omnidirectional path loss model was then found from the resulting received power levels at each RX location. Both the synthesized and measured omnidirectional path loss models in LOS and NLOS environments are presented here.

5.4.1 LOS Wideband Channels

5.4.1.1 LOS Omnidirectional Path Loss Model

Fig. 5.3 shows the omnidirectional 28 GHz LOS large scale path loss with respect to a 1 m free space reference, where the omnidirectional path loss is obtained from all of the measured powers from all PDPs measured over all angles at both the TX and RX, with antenna gains deducted from each measured PDP. The measured data yields an omnidirectional measured path loss exponent and shadowing factor (with respect

to a 1 m free space reference) of $\overline{n}_{All} = 2.1$ and $\sigma_{All} = 3.6$ dB, respectively, yielding the large scale path loss model shown below,

$$PL[dB](d) = 61.4 + 21 \times \log_{10}(d) + \chi_{\sigma} \tag{5.21}$$

where χ_{σ} is the typical 0 dB mean lognormal random variable with standard deviation σ_{All}.

Note that when using just the few strongest measured PDPs at each RX location, with synthesized absolute propagation time included providing an omnidirectional PDP, the synthesized timing approach yields a path loss exponent of $\overline{n}_{Syn} = 2.6$ and shadowing factor $\sigma_{Syn} = 2.4$ dB, thus agreeing reasonably well (variation of only 5 dB per decade of distance) with the omnidirectional path loss model developed from all of the measured PDPs over all angles. This clearly illustrates how just a few key AOAs and AODs and provide most of the energy in an urban mmWave channel. However, the SSCM in Section 5.5.1 uses a path loss exponent of $n = 2$ for LOS channels which is expected from electromagnetic propagation in free space. The directional horn antennas used during the measurement campaign were not aligned on boresight in LOS measurements, which explains the higher path loss exponent of $\overline{n} = 2.1$.

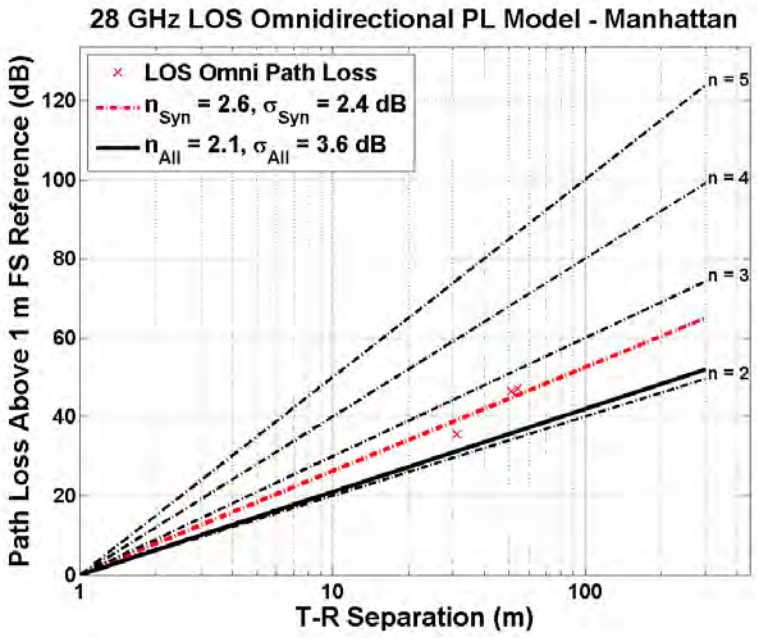

Figure 5.3: The omnidirectional path loss model for the LOS environment is shown here, obtained from the wideband measurements in Manhattan. The omnidirectional power at each LOS RX location was obtained from all PDPs for all RX and TX pointing angles (but double counts were eliminated), and antenna gains were removed from each PDP. The path loss exponent and shadowing factor obtained when summing all received powers at all azimuth and elevation angles are 2.1 and 3.6 dB, respectively, using a 1 m free space reference distance. The synthesized omnidirectional PDPs using only up to four measured PDPs (the most prominent AODs) yield a path loss exponent and shadowing factor (with respect to a 1 m free space reference) of 2.6 and 2.4 dB (red line), showing good agreement to field measurements.

5.4.1.2 Cluster (Temporal) Statistics for LOS Environments

This section presents histograms and cumulative distribution curves of extracted and generated 28 GHz NLOS wideband channel models for temporal statistics. The statistical generation of all channel parameters is explained in Section 5.5.1. In all cases, a χ^2 goodness of fit test with significance level of 5% was performed to ensure a close fit between the measured and corresponding theoretical distributions. All presented temporal statistics are given based on a 2.7 ns minimum inter-cluster void interval.

5.4.1.2.1 Number of Clusters in an Omnidirectional PDP

The mean and standard deviation of the number of time clusters in an omnidirectional PDP were found to be 4.1 and 2.3 respectively.

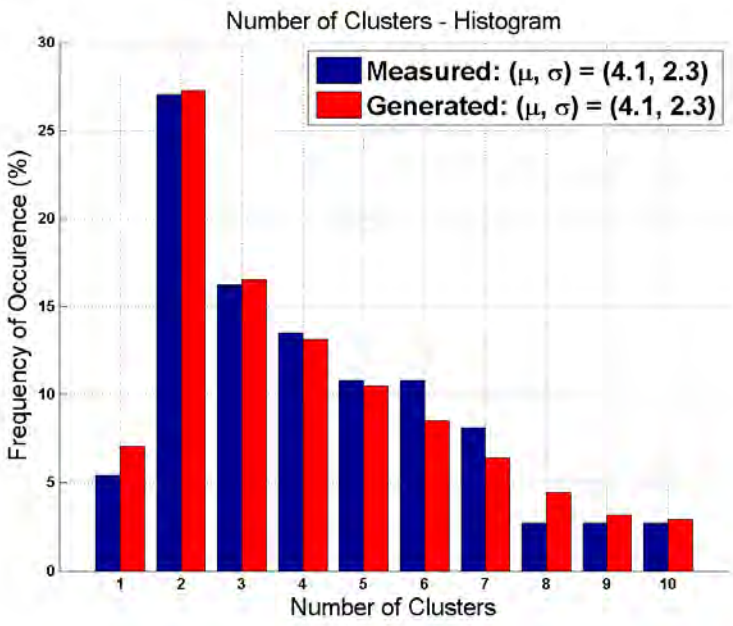

Figure 5.4: The histogram of the number of time clusters in a LOS omnidirectional power delay profile. The blue bars correspond to the measured frequency of occurrence. The red bars, which approximate the data (blue bars), were generated based on the procedure outlined in Section 5.5.1, Step 3.

5.4.1.2.2 Number of Cluster Subpaths

The mean and standard deviation of the number of cluster subpaths, that is, the number of subpath components found in each time cluster, were found to be 2.0 and 1.7 respectively.

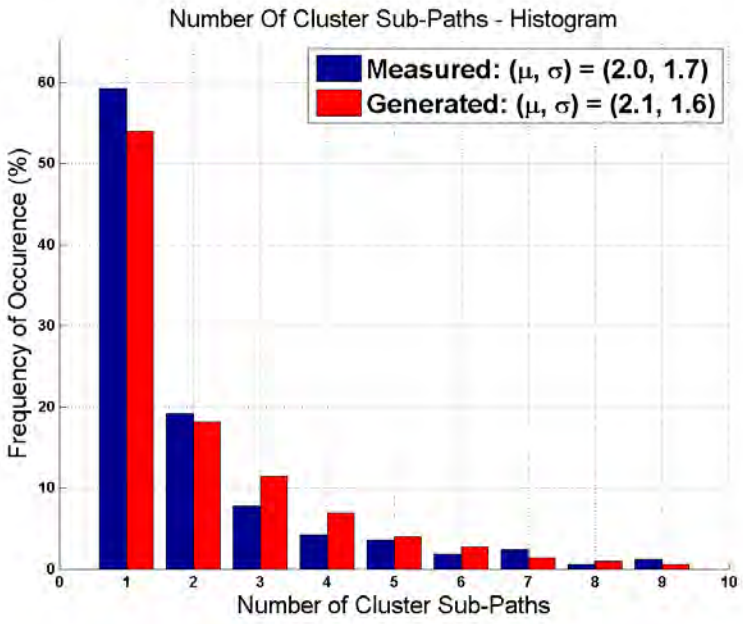

Figure 5.5: The histogram of the number of subpaths in a time cluster in a LOS omnidirectional power delay profile. The blue bars correspond to the measured frequency of occurrence. The red bars were generated based on the procedure outlined in Section 5.5.1, Step 4.

5.4.1.2.3 Cluster Excess Time Delays

The cluster excess time delays were found to have an average of 161.8 ns and a standard deviation of 189.1 ns, and were fit to an exponential distribution with a mean of 162 ns. The histogram and cumulative distribution curve are shown below. The mathematical procedure for generating the exponential distribution is explained in Section 5.5.1. The theoretical exponential distribution with mean 162 ns is plotted in red on the CDF plot for comparison.

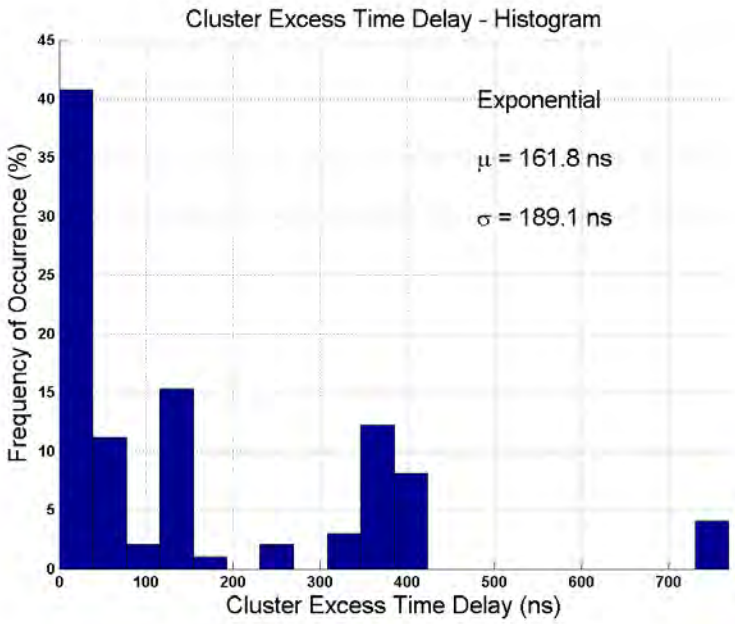

Figure 5.6: Histogram of the cluster excess time delays for LOS environments. The mean and standard deviation of the cluster excess time delays are 161.8 ns and 189.1 ns respectively.

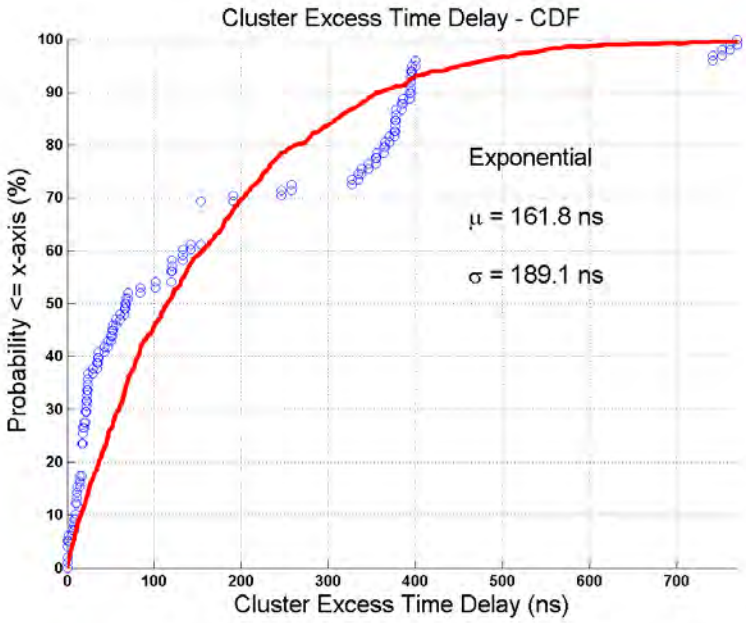

Figure 5.7: Cumulative distribution curve of the cluster excess time delays for LOS environments. The mean and standard deviation of the cluster excess time delays are 161.8 ns and 189.1 ns respectively. The red cumulative distribution curve approximating the cluster excess time delay CDF is generated with an exponential random variable as described in Section 5.5.1.

5.4.1.2.4 Cluster Powers as a function of Cluster Excess Time Delays

The cluster power ratios were plotted as a function of the cluster excess time delays, and exhibit a deterministic trend. As the cluster excess time delays increase, the cluster power ratios have a tendency to decrease. The best fit exponential curve is plotted in Fig. 5.8. In order to introduce random variations about the mean fit curve, we plot the histogram and cumulative distribution curve of the difference in power levels in dB-scale in Fig. 5.10 and Fig. 5.11, which are shown to follow a lognormal distribution with a mean of 0 dB and a standard deviation of 9.5 dB. These random fluctuations may be thought of as per-cluster shadowing, which serves the same functionality as the shadowing term in the traditional close-in reference path loss model. Finally, we show the generated cluster powers with the per-cluster shadowing in Fig. 5.9, which appears to fit quite well to the data.

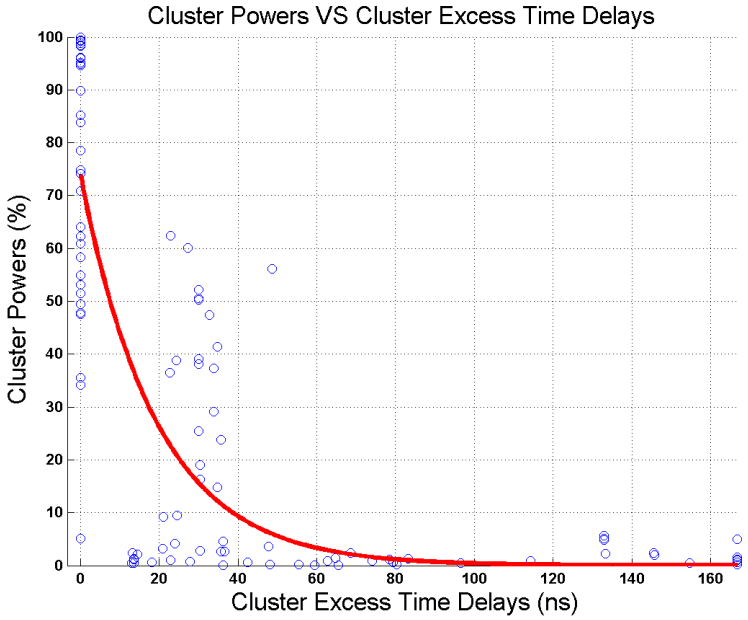

Figure 5.8: The cluster power ratios plotted against cluster excess time delays in LOS environments. A deterministic trend is observed: as the cluster excess time delays increase, the cluster power ratios tend to decrease. The red curve is an exponential best line fit of the form $y = \alpha e^{-\frac{\tau}{\beta}}$, where $\alpha = 0.738$ and $\beta = 19.3$ ns.

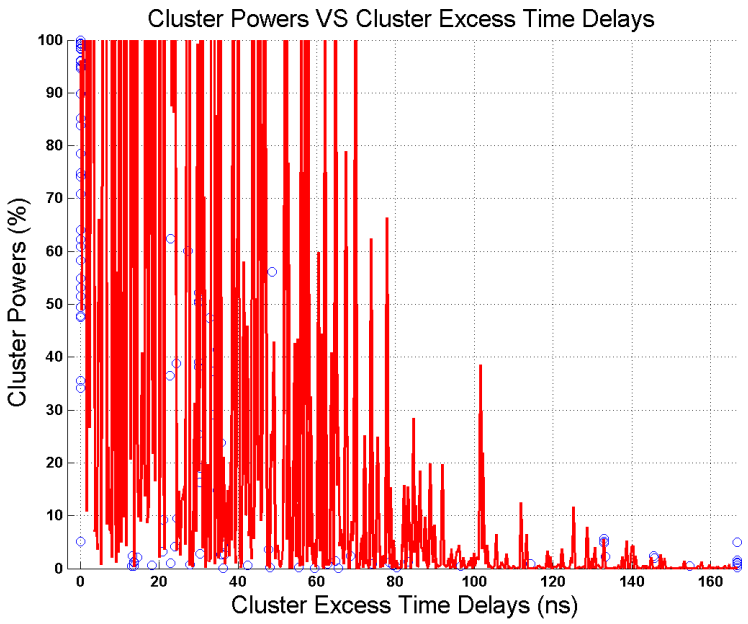

Figure 5.9: The cluster power ratios plotted against cluster excess time delays in LOS environments. The red curve approximating the data points is generated with an exponential function (shown on Fig. 5.8) multiplied by a lognormal per-cluster shadowing random variable with a mean of 0 dB and a standard deviation of 9.5 dB.

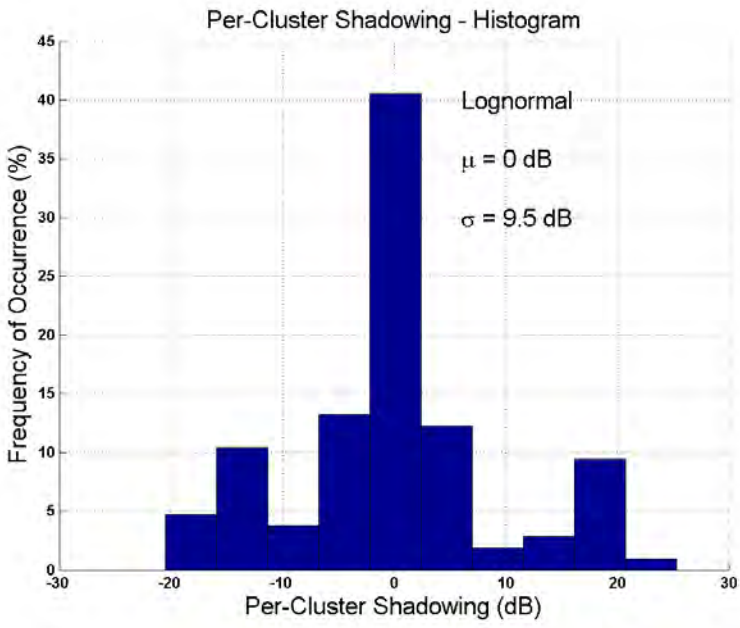

Figure 5.10: The histogram of the difference between the exponential best line fit (dB) and the cluster power ratios (dB) follows lognormal random variations with a mean of 0 dB and a standard deviation of 9.5 dB, for LOS environments. This is the per-cluster shadowing.

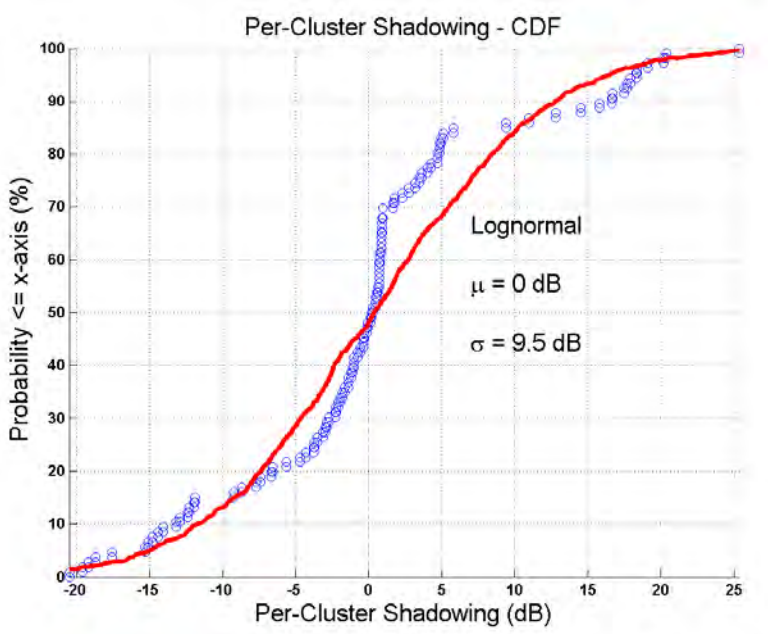

Figure 5.11: The cumulative distribution curve of the difference between the exponential best line fit (dB) and the cluster power ratios (dB) for LOS environments. The red curve is generated with a lognormal random variable with a mean of 0 dB and a standard deviation of 9.5 dB.

5.4.1.2.5 Cluster Subpath Excess Time Delays

The cluster subpath excess time delays were found to have an average of 8 ns and a standard deviation of 8.3 ns, and were fit to an exponential distribution with a mean of 8 ns. The histogram and cumulative distribution curve are shown below. The theoretical exponential distribution with mean 8 ns is plotted in red on the CDF plot for comparison.

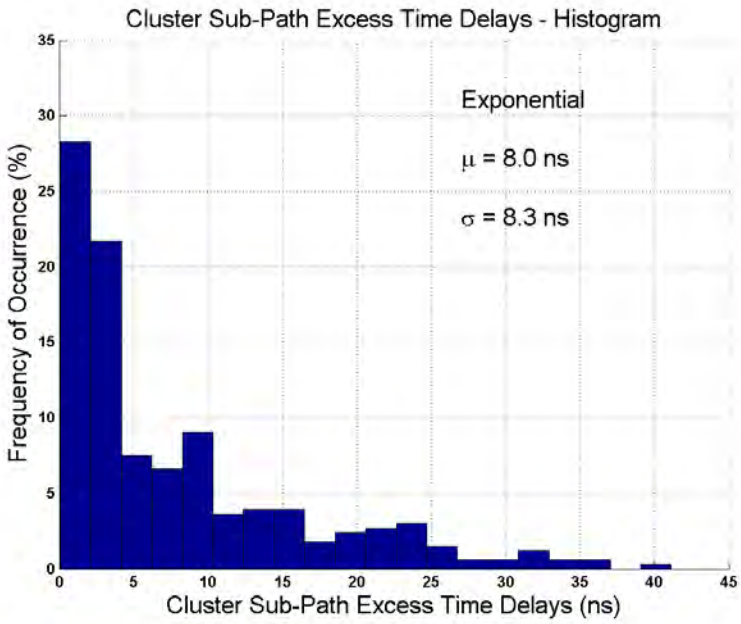

Figure 5.12: Histogram of the cluster subpath excess time delays in LOS environments. The mean and standard deviation of the cluster excess time delays are 8.0 ns and 8.3 ns respectively.

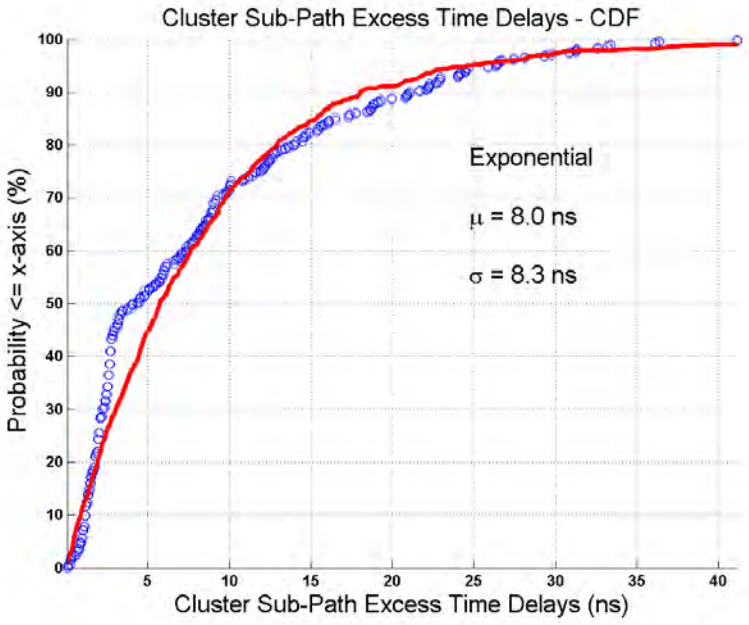

Figure 5.13: Cumulative distribution curve of the cluster excess time delays in LOS environments. The mean and standard deviation of the cluster excess time delays are 8.0 ns and 8.3 ns respectively. The red cumulative distribution curve approximating the cluster excess time delay CDF is generated with an exponential random variable with a mean of 8.0 ns.

5.4.1.2.6 Cluster Subpath Powers as a function of Cluster Subpath Time Delays

The cluster subpath power ratios were plotted as a function of the cluster subpath excess time delays, and exhibit a deterministic trend. As the cluster subpath excess time delays increase, the cluster subpath power ratios have a tendency to decrease. The best fit exponential curve is plotted in Fig. 5.14. In order to introduce random variations about the mean fit curve, we plot the histogram and cumulative distribution curve of the difference in power levels in dB-scale, which are shown to follow a lognormal distribution with a mean of 0 dB and a standard deviation of 5.1 dB, with slight deviations from the measured distribution. These random fluctuations may be thought of as per-cluster subpath shadowing, which serves the same functionality as the shadowing term in the traditional close-in reference path loss model. Finally, we show the generated cluster powers with the per-cluster subpath shadowing in Fig. 5.15, which appears to fit the data fit quite well.

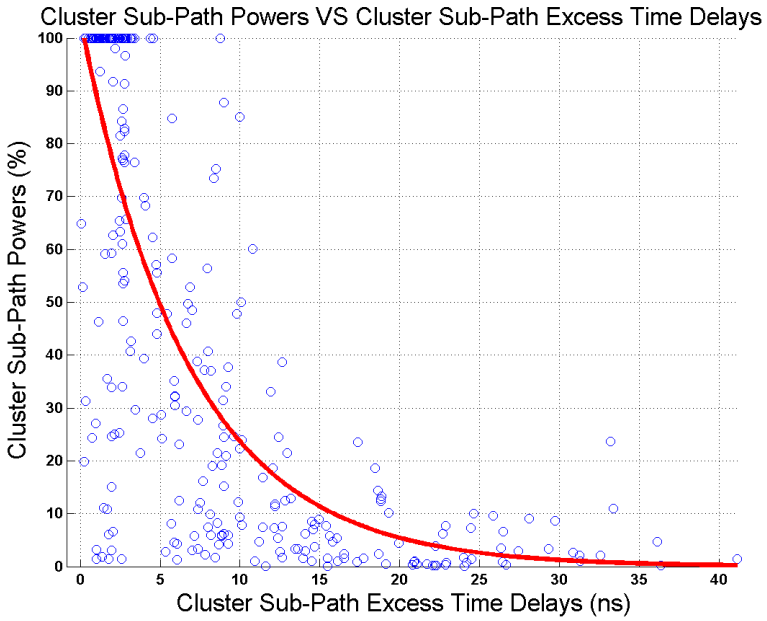

Figure 5.14: The cluster subpath power ratios plotted against cluster subpath excess time delays in LOS environments. A deterministic trend is observed: as the cluster subpath excess time delays increase, the cluster subpath power ratios tend to decrease. The red curve is an exponential best line fit of the form $y = \alpha e^{-\frac{\rho}{\beta}}$, where $\alpha = 1$ and $\beta = 6.78$ ns.

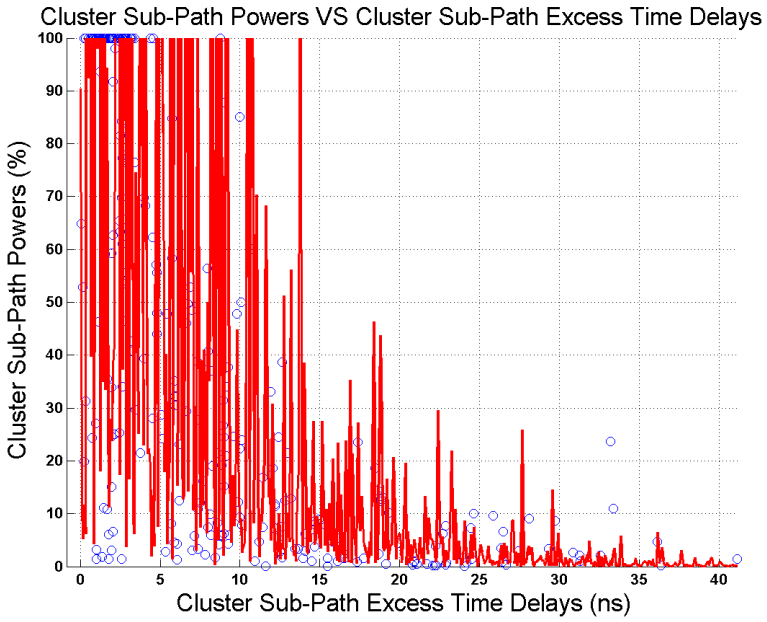

Figure 5.15: The cluster subpath power ratios plotted against cluster subpath excess time delays in LOS environments. The red curve approximating the data points is generated with an exponential function (shown on Fig. 5.14) multiplied by a lognormal per-cluster shadowing random variable with a mean of 0 dB and a standard deviation of 5.1 dB.

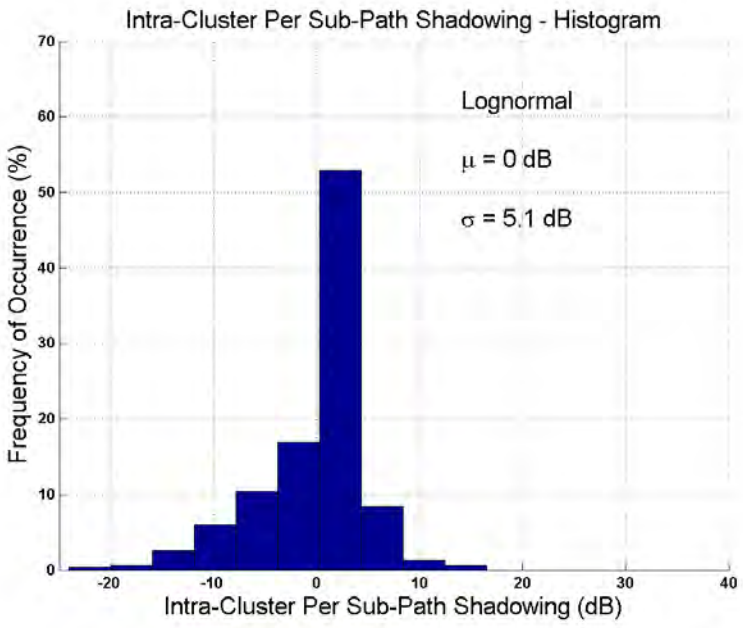

Figure 5.16: The histogram of the difference between the exponential best line fit (dB) and the cluster subpath power ratios (dB) follows lognormal random variations with a mean of 0 dB and a standard deviation of 5.1 dB, for LOS environments. This is the per-cluster subpath shadowing.

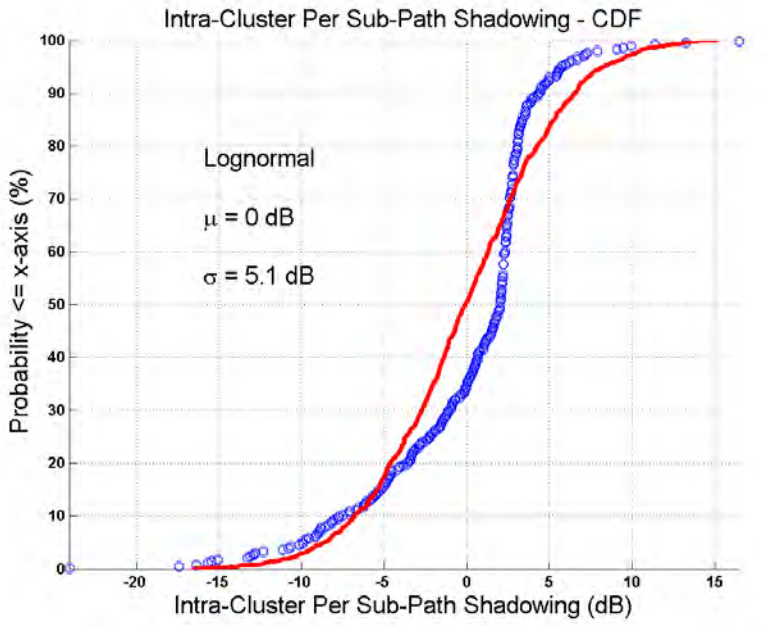

Figure 5.17: The cumulative distribution curve of the difference between the exponential best line fit (dB) and the cluster subpath power ratios (dB), for LOS environments. The red curve is generated with a lognormal random variable with a mean of 0 dB and a standard deviation of 5.1 dB.

5.4.1.2.7 Omnidirectional PDP RMS Delay Spread

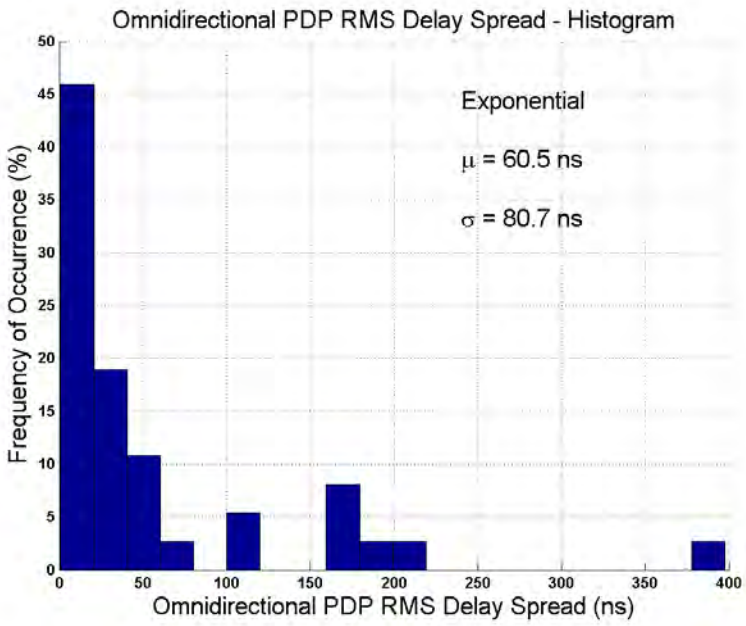

Figure 5.18: The histogram of the RMS delay spreads of the omnidirectional power delay profiles synthesized using 3-D ray-tracing techniques, in LOS environments. The mean and standard deviations are 60.5 ns and 80.7 ns, respectively.

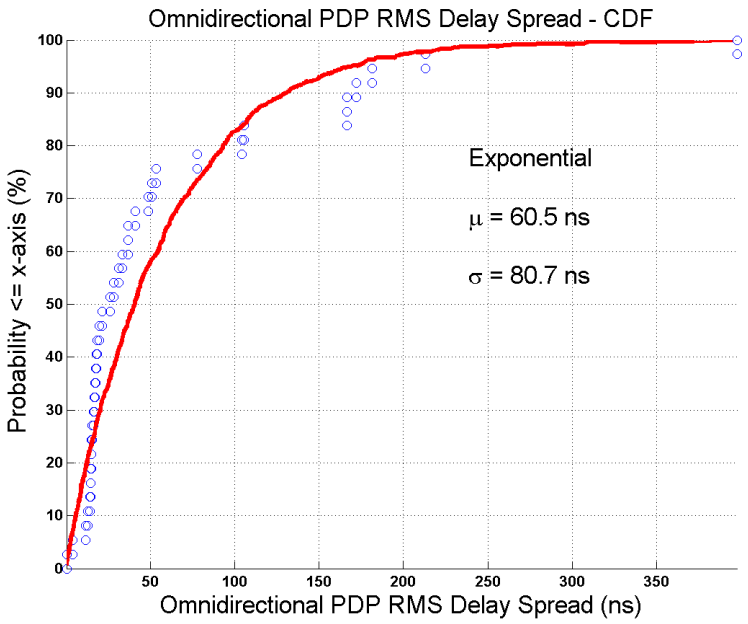

Figure 5.19: The cumulative distribution curve of the RMS delay spreads of the omnidirectional power delay profiles synthesized using 3-D ray-tracing techniques, in LOS environments. The mean and standard deviations are 60.5 ns and 80.7 ns, respectively. The red curve approximating the data was generated with an exponential random variable with mean 60.5 ns.

5.4.1.2.8 Cluster RMS Delay Spread

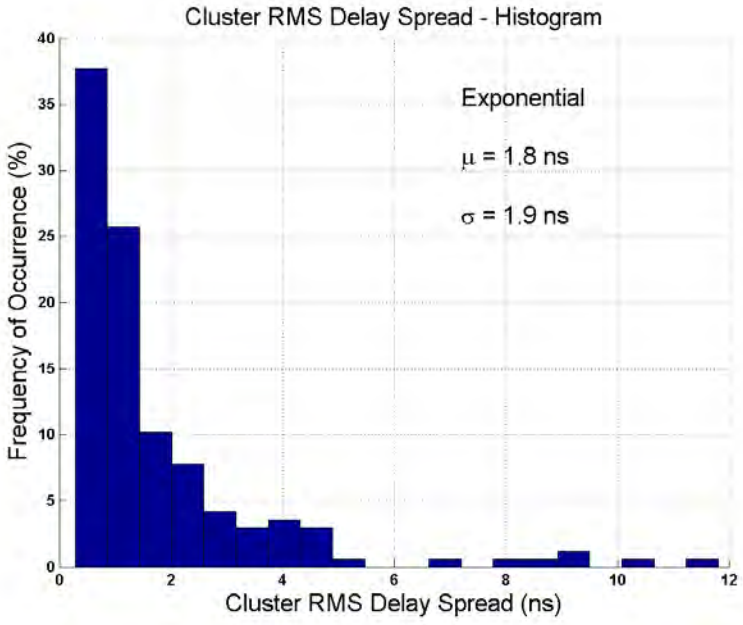

Figure 5.20: The histogram of cluster RMS delay spreads in an omnidirectional PDP in LOS environments. The mean and standard deviations are 1.8 ns and 1.9 ns, respectively.

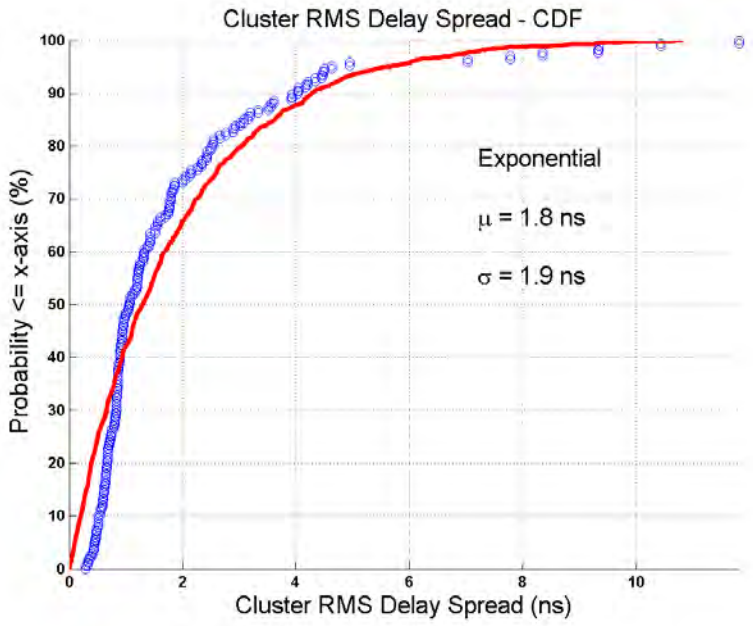

Figure 5.21: The cumulative distribution curve of cluster RMS delay spreads in an omnidirectional PDP in LOS environments. The mean and standard deviations are 1.8 ns and 1.9 ns, respectively. The red curve approximating the data was generated with an exponential random variable with mean 1.8 ns.

5.4.1.2.9 Cluster Duration

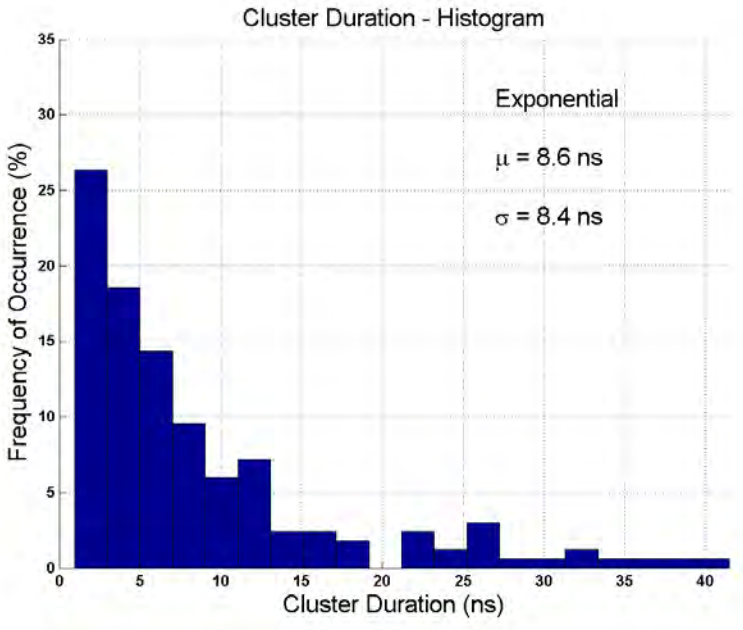

Figure 5.22: The histogram of the cluster durations in LOS environments. The mean and standard deviations are 8.6 ns and 8.4 ns respectively.

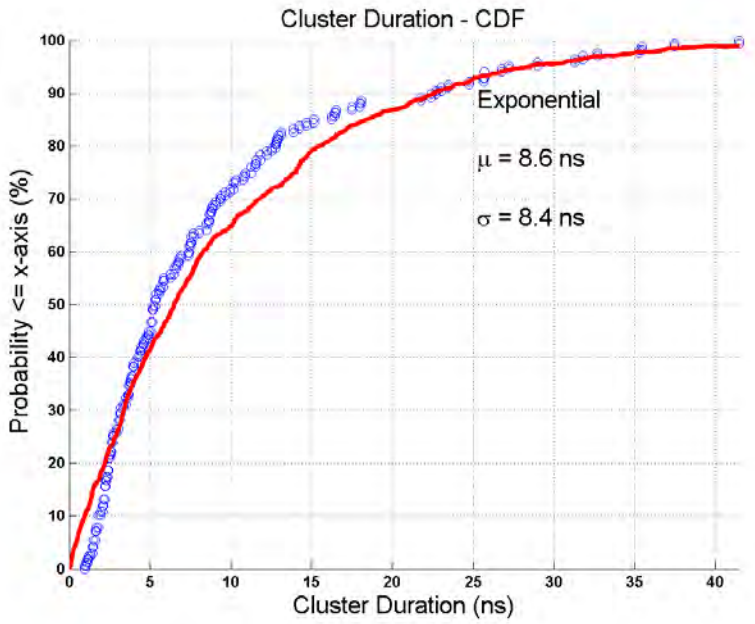

Figure 5.23: The cumulative distribution curve of the cluster durations in LOS environments. The mean and standard deviations are 8.6 ns and 8.4 ns respectively. The red curve approximating the data was generated with an exponential random variable with mean 8.6 ns.

5.4.1.2.10 Inter-Cluster Void Duration

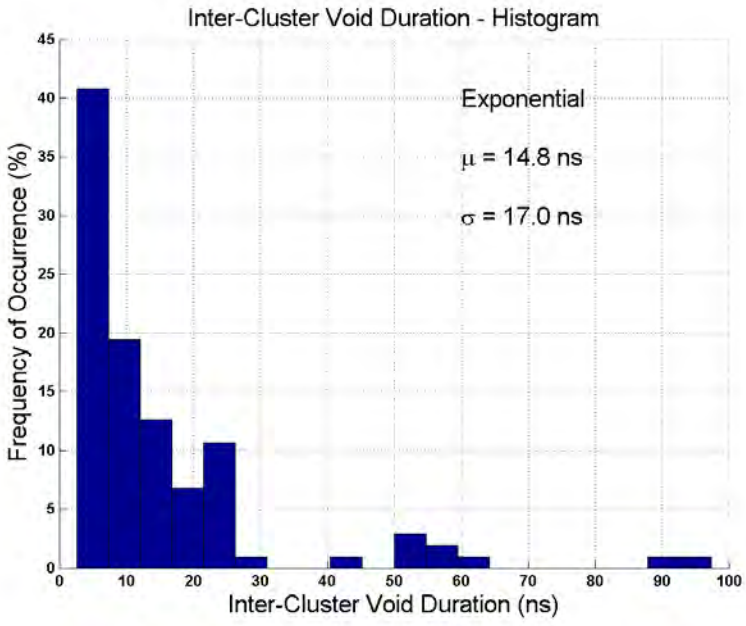

Figure 5.24: The histogram of the inter-cluster void durations in an omnidirectional PDP in LOS environments. The mean and standard deviations are 14.8 ns and 17.0 ns respectively.

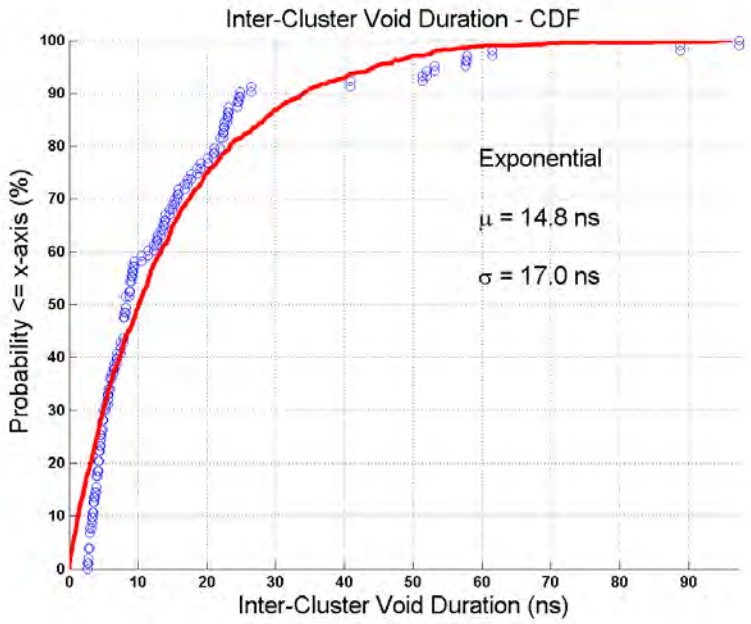

Figure 5.25: The cumulative distribution curve of the inter-cluster void durations in an omnidirectional PDP in LOS environments. The mean and standard deviations are 14.8 ns and 17.0 ns respectively. The red curve approximating the data was generated with an exponential random variable with mean 14.8 ns.

5.4.1.3 AOD Lobe (Spatial) Statistics for LOS Environments

This section presents 28 GHz LOS wideband channel models for AOD spatial statistics. The statistical generation of all channel parameters is explained in Section 5.5.1.

5.4.1.3.1 Number of Lobes at a LOS RX Location

The number of lobes at each TX for measured LOS RX locations was obtained by applying a thresholding procedure on the measured power azimuth spectra, that is, total received power as a function of RX azimuth angle. The thresholding algorithm consisted in finding the maximum total received power in the azimuth spectrum and applying a 10 dB below maximum power threshold over the whole azimuth spectrum. All presented spatial statistics are therefore valid for a 10 dB thresholding value.

Fig. 5.26 shows the histogram for the number of AOD lobes measured in Manhattan, with a superimposed histogram fitting (shown in red). A total of 11 AOD lobes were identified over all measured LOS Manhattan TX locations. The mean and standard deviation of the number of lobes measured was found to

be $\mu_{Lobe} = 2.8$ and $\sigma_{Lobe} = 1.3$, respectively.

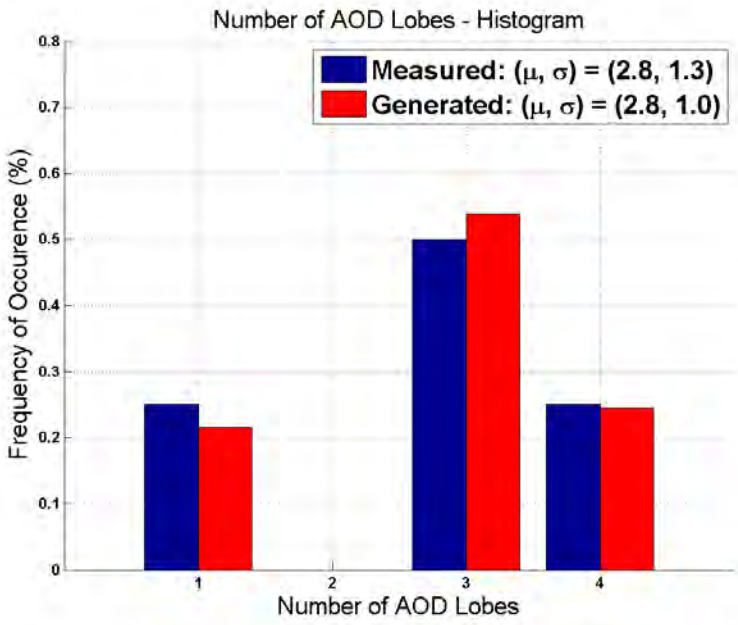

Figure 5.26: The histogram of the number of AOD lobes measured at all TX locations for all LOS RX locations from the 28 GHz wideband collected measurements in Manhattan. The mean and standard deviation of the number of AOD lobes were 2.8 and 1.3 respectively.

5.4.1.3.2 Mean Angle of Departures (AODs)

The lobe AODs were found to differ from a uniformly distributed random variable in the azimuth plane. The plot below shows the cumulative distribution curve for the lobe AODs, with a superimposed theoretical distribution curve of a uniformly distributed random variable between 0° and 360°. It must be noted however that more measurements will be collected to enhance AODs in LOS environments, and so we assume for the purposes of channel modeling that the lobe AODs are uniformly distributed between 0° and 360°.

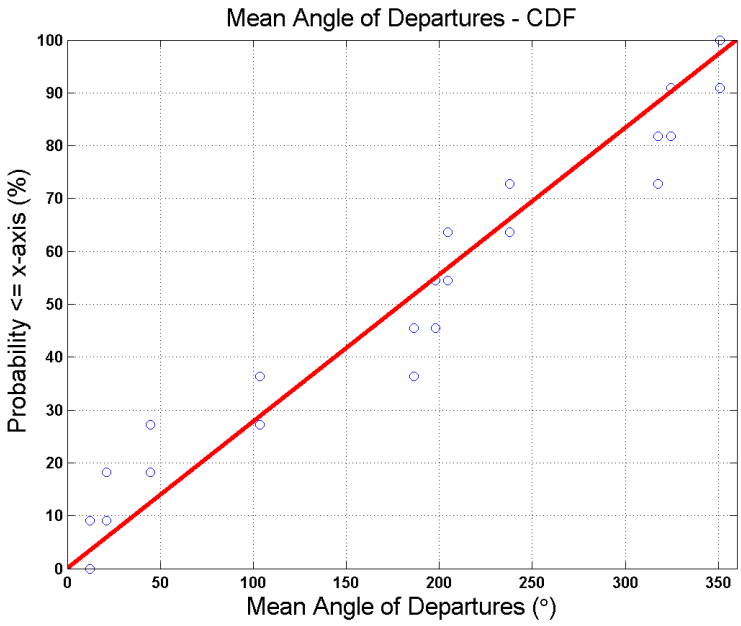

Figure 5.27: Cumulative distribution curve of the lobe AODs for all LOS RX locations from the 28 GHz wideband collected measurements in Manhattan. The lobe AOD is assumed to follow a random variable uniformly distributed between 0° and 360° for the purposes of channel modeling.

5.4.1.3.3 AOD Lobe Azimuth Spread

The mean and standard deviation of the AOD lobe azimuth spreads were 27.3° and 13.5° respectively.

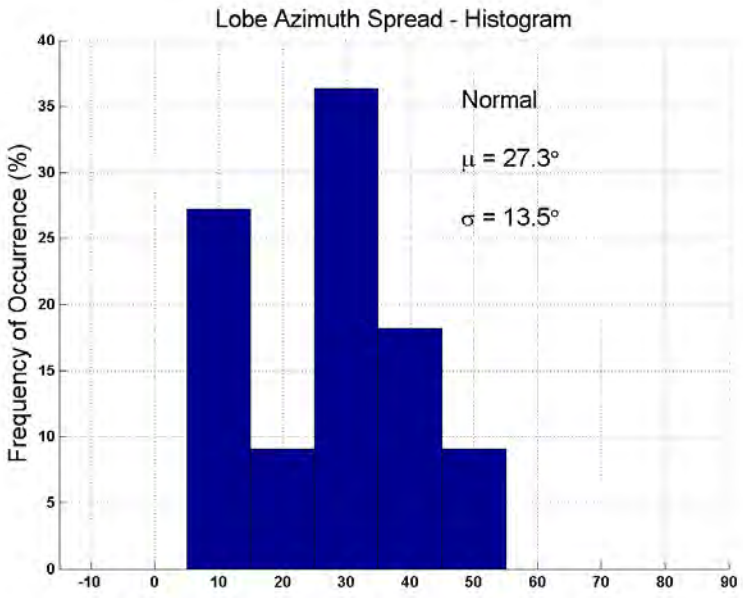

Figure 5.28: The histogram of the AOD lobe azimuth spreads from the 28 GHz wideband collected measurements in Manhattan, in LOS environments. The mean and standard deviations are 27.3° and 13.5° respectively.

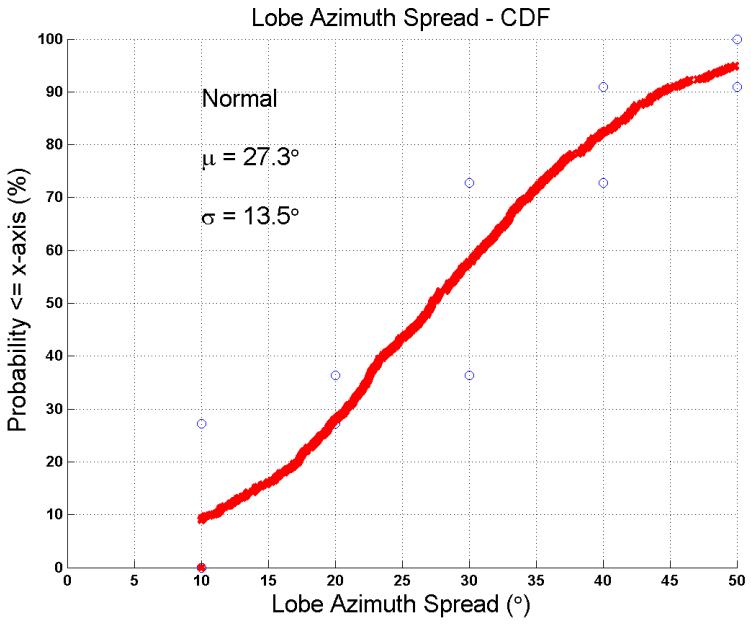

Figure 5.29: The cumulative distribution of the AOD lobe azimuth spreads from the 28 GHz wideband collected measurements in Manhattan, in LOS environments. The mean and standard deviations are 27.3° and 13.5° respectively.

5.4.1.3.4 Lobe Segment Angular Power Levels as a function of Angular Separation from Lobe Angle with Maximum Received Power

The lobe segment angular power ratios (with respect to a maximum lobe segment power) are plotted against angular deviation away from the strongest angle (e.g., the lobe angle that received the most power). A deterministic trend may be observed whereby the lobe segment power tends to decrease as the angular deviation away from strongest angle increases. The lobe segment angular ratios are estimated with a Gaussian function (shown in red on the graphs below).

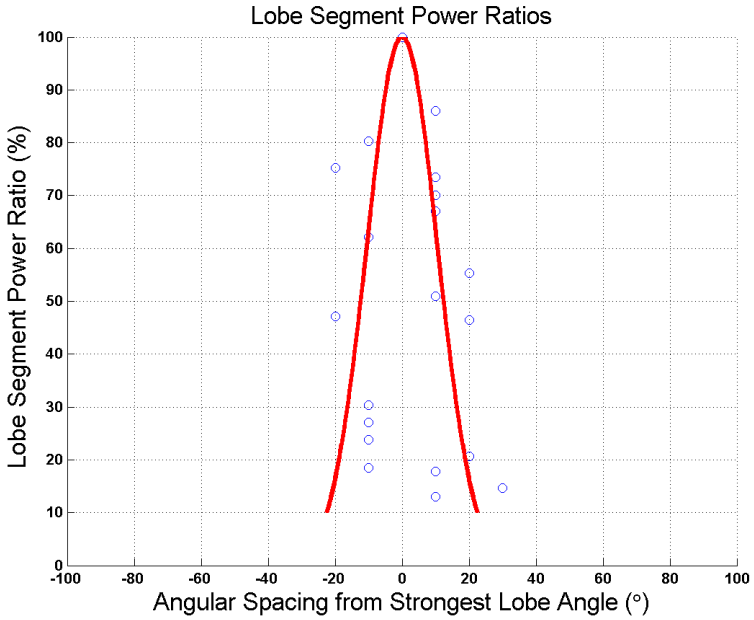

Figure 5.30: AOD lobe segment power ratios (% of maximum lobe power) as a function of angular spacing from strongest angle (e.g., angle with strongest received power in the lobe), in LOS environments. The red curve approximating the data is of the form $y = e^{-\frac{(\Delta\theta)^2}{2\sigma^2}}$, where $\sigma = 10.5°$.

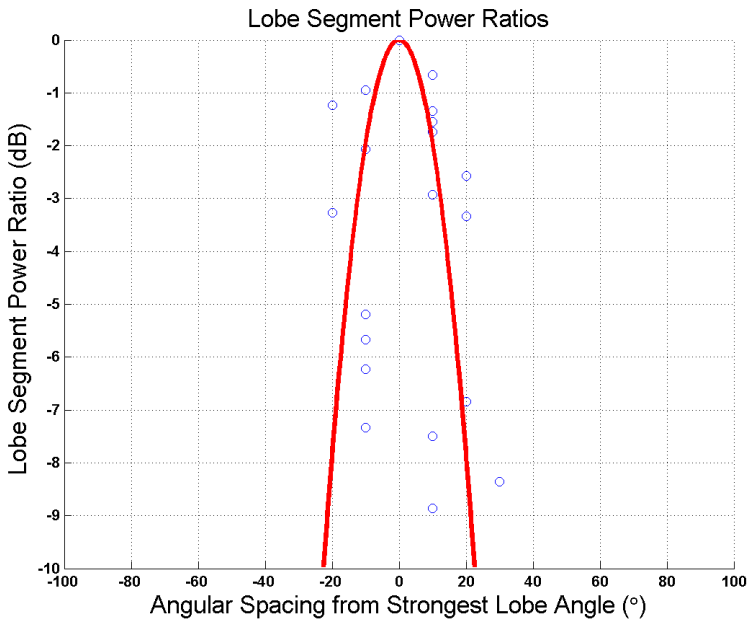

Figure 5.31: AOD lobe segment power ratios (% of maximum lobe power) as a function of angular spacing from strongest angle (e.g., angle with strongest received power in the lobe), in LOS environments. The red curve approximating the data is of the form $y = e^{-\frac{(\Delta\theta)^2}{2\sigma^2}}$, where $\sigma = 10.5°$. This plot is the same as Fig. 5.30, plotted on a dB-scale.

5.4.1.3.5 AOD RMS Lobe Azimuth Spreads

The AOD RMS lobe azimuth spreads were found to have an average of 5.5° and a standard deviation of 3.9°, and were fit to a Gaussian distribution.

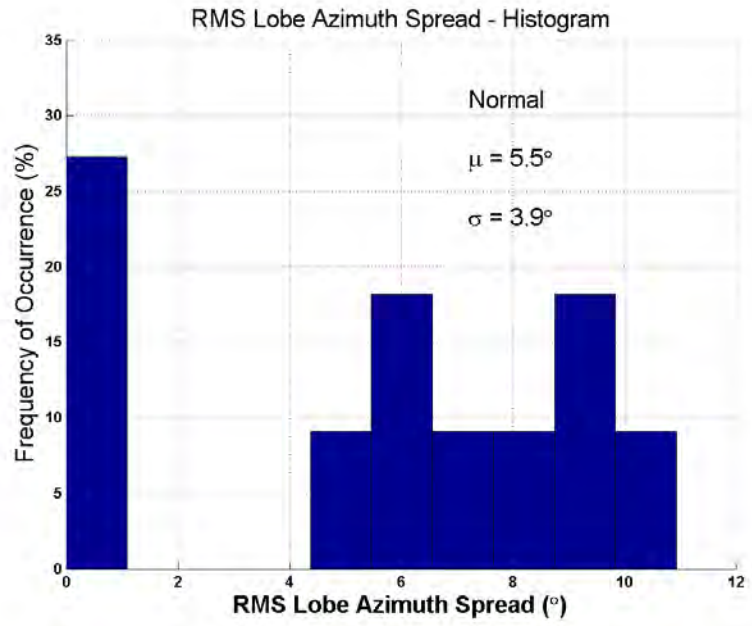

Figure 5.32: The histogram of the AOD RMS lobe azimuth spreads, in LOS environments. The mean and standard deviations are 5.5° and 3.9° respectively.

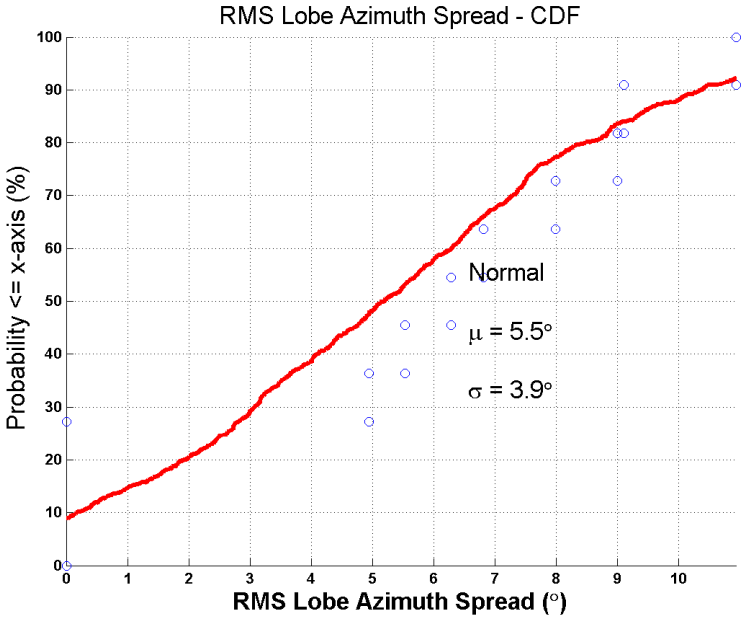

Figure 5.33: The cumulative distribution curve of the AOD RMS lobe azimuth spreads, in LOS environments. The mean and standard deviations are 5.5° and 3.9° respectively. The red curve approximating the data was generated with a normal distribution.

5.4.1.4 AOA Lobe (Spatial) Statistics for LOS Environments

This section presents 28 GHz LOS wideband channel models for AOA spatial statistics. The statistical generation of all channel parameters is explained in Section 5.5.1.

5.4.1.4.1 Number of AOA Lobes at a LOS RX Location

The number of lobes at each measured LOS RX location was obtained by applying a thresholding procedure on the measured power azimuth spectra, that is, total received power as a function of RX azimuth angle. The thresholding algorithm consisted in finding the maximum total received power in the azimuth spectrum and applying a 10 dB below maximum power threshold over the whole azimuth spectrum. All presented spatial statistics are therefore for valid a 10 dB thresholding value.

Fig. 5.34 shows the histogram for the number of AOA lobes measured in Manhattan, with a superimposed histogram fitting (shown in red). A total of 103 AOA lobes were identified over all measured LOS Manhattan TX locations. The mean and standard deviation of the number of lobes measured was found to be $\mu_{Lobe} = 2.9$ and $\sigma_{Lobe} = 1.5$, respectively.

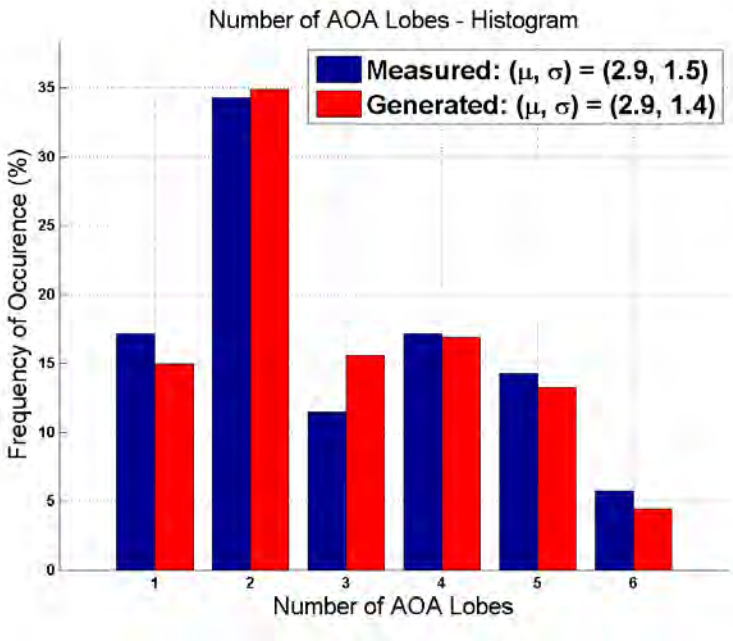

Figure 5.34: The histogram of the number of AOA lobes measured at all LOS RX locations from the 28 GHz wideband collected measurements in Manhattan. The mean and standard deviation of the number of AOA lobes were 2.9 and 1.5 respectively.

5.4.1.4.2 Mean Angle of Arrival (AOAs)

The lobe AOAs were found to be uniformly distributed in the azimuth plane. The plot below shows the cumulative distribution curve for the lobe AOAs, with a superimposed theoretical distribution curve of a uniformly distributed random variable between 0° and 360°.

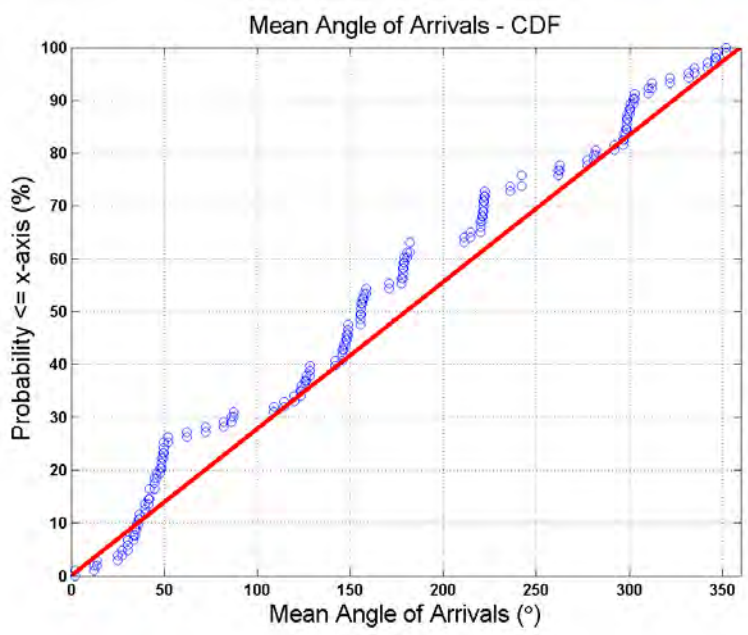

Figure 5.35: Cumulative distribution curve of the lobe AOAs from the 28 GHz wideband collected measurements in Manhattan, in LOS environments. The lobe AOA follows a random variable uniformly distributed between 0° and 360°.

5.4.1.4.3 AOA Lobe Azimuth Spread

The mean and standard deviation of the AOA lobe azimuth spreads were 39.9° and 31.4° respectively, and were fit to a normal Gaussian distribution. The histogram and the cumulative distribution curve are shown below.

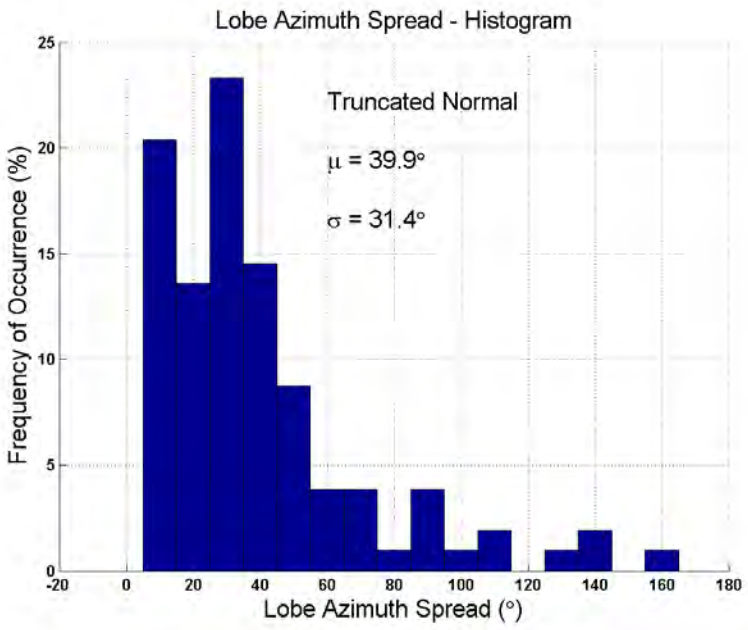

Figure 5.36: The histogram of the AOA lobe azimuth spreads from the 28 GHz wideband collected measurements in Manhattan, in LOS environments. The mean and standard deviations are 39.9° and 31.4° respectively.

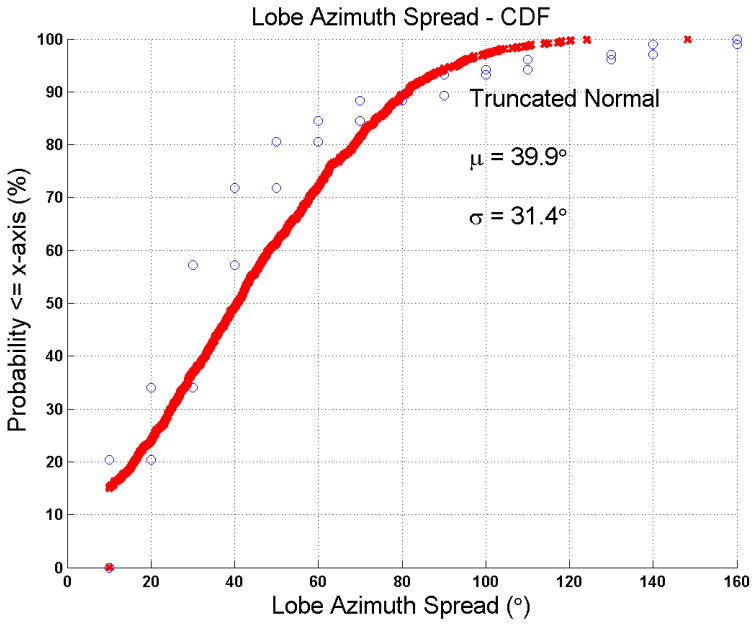

Figure 5.37: The cumulative distribution curve of the AOA lobe azimuth spreads from the 28 GHz wideband collected measurements in Manhattan, in LOS environments. The red crosses approximating the data were generated with an exponential random variable with a mean of 40°.

5.4.1.4.4 Lobe Segment Angular Power Levels as a function of Angular Separation from Lobe Angle with Maximum Received Power

The lobe segment angular power ratios (with respect to a maximum lobe segment power) are plotted against angular deviation away from the strongest angle (e.g., the lobe angle that received the most power), in LOS environments. A deterministic trend may be observed whereby the lobe segment power tends to decrease as the angular deviation away from strongest angle increases. The lobe segment angular ratios are estimated with a Gaussian function (shown in red on the graphs below).

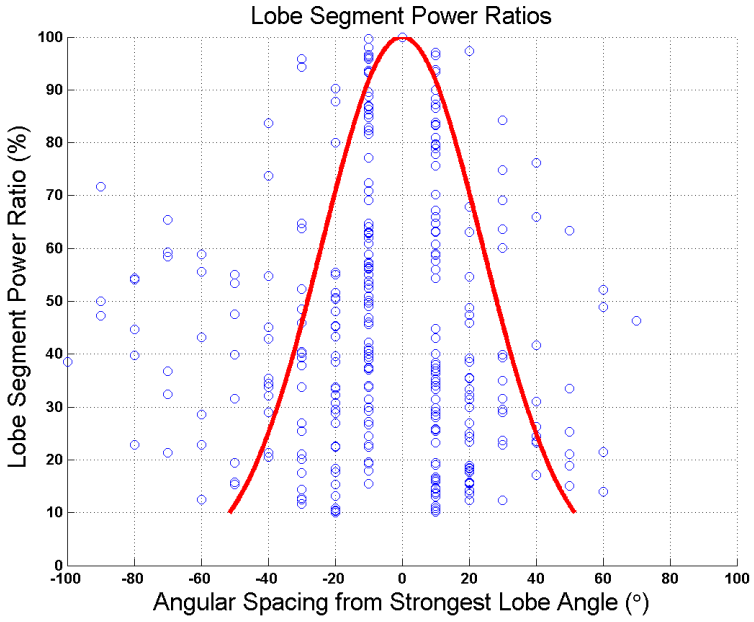

Figure 5.38: AOA lobe segment power ratios (% of maximum lobe power) as a function of angular spacing from strongest angle (e.g., angle with strongest received power in the lobe), in LOS environments. The red curve approximating the data is of the form $y = e^{-\frac{(\Delta\theta)^2}{2\sigma^2}}$, where $\sigma = 24°$.

Figure 5.39: AOA lobe segment power ratios (% of maximum lobe power) as a function of angular spacing from strongest angle (e.g., angle with strongest received power in the lobe). The red curve approximating the data is of the form $y = e^{-\frac{(\Delta\theta)^2}{2\sigma^2}}$, where $\sigma = 24°$. This plot is the same as Fig. 5.38, plotted on a dB-scale.

5.4.1.4.5 The AOA RMS Lobe Azimuth Spread

The RMS lobe azimuth spreads were found to have an average of 8.9° and a standard deviation of 8.7°, and were fit to an exponential distribution with mean 8.8°.

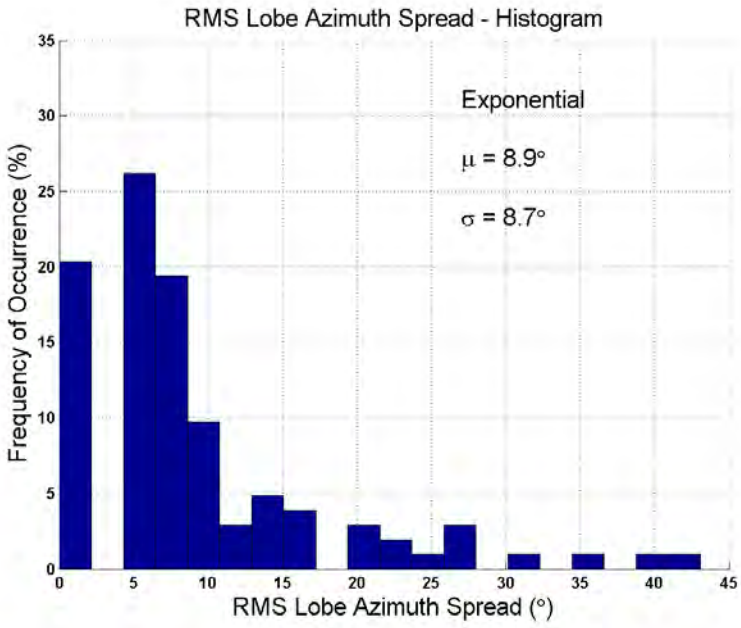

Figure 5.40: The histogram of the AOA RMS lobe azimuth spreads in LOS environments. The mean and standard deviations are 8.9° and 8.7° respectively.

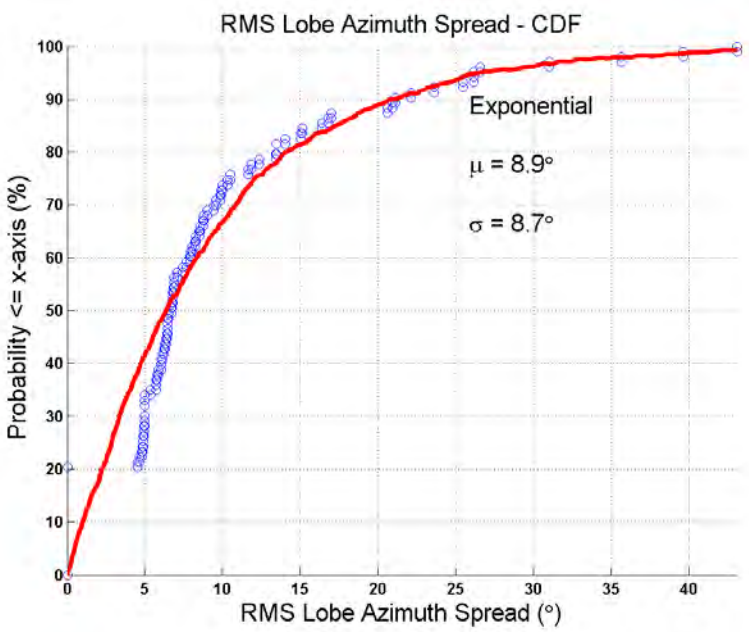

Figure 5.41: The cumulative distribution curve of the AOA RMS lobe azimuth spreads in LOS environments. The mean and standard deviations are 8.9° and 8.7° respectively. The red curve approximating the data was generated from an exponential random variable with mean 8.8°.

5.4.2 NLOS Wideband Channels

5.4.2.1 NLOS Omnidirectional Path Loss Model

Fig. 5.42 shows the omnidirectional 28 GHz NLOS large scale path loss with respect to a 1 m free space reference, where the omnidirectional path loss is obtained from all of the measured powers from all PDPs measured over all angles at both the TX and RX, with antenna gains deducted from each measured PDP. The measured data yields an omnidirectional measured path loss exponent and shadowing factor (with respect to a 1 m free space reference) of $\overline{n}_{All} = 3.4$ and $\sigma_{All} = 9.7$ dB, respectively, yielding the large scale path loss model shown below,

$$PL[dB](d) = 61.4 + 34 \times \log_{10}(d) + \chi_{\sigma} \tag{5.22}$$

where χ_{σ} is the typical 0 dB mean lognormal random variable with standard deviation σ_{All}.

Note that when using just the few strongest measured PDPs at each RX location, with synthesized absolute propagation time included providing an omnidirectional PDP, the synthesized timing approach yields a path loss exponent of $\overline{n}_{Syn} = 3.7$ and shadowing factor $\sigma_{Syn} = 12.3$ dB, thus agreeing reasonably well (variation of only 3 dB per decade of distance) with the omnidirectional path loss model developed from all of the measured PDPs over all angles (note: the SSCM presented here uses the field measured path loss exponent and shadowing values). This clearly illustrates how just a few key AOAs and AODs and provide most of the energy in an urban mmWave channel. For completeness, a floating intercept path loss model from 30 to 200 m determined from all of the measured data illustrating the similarity of these various models.

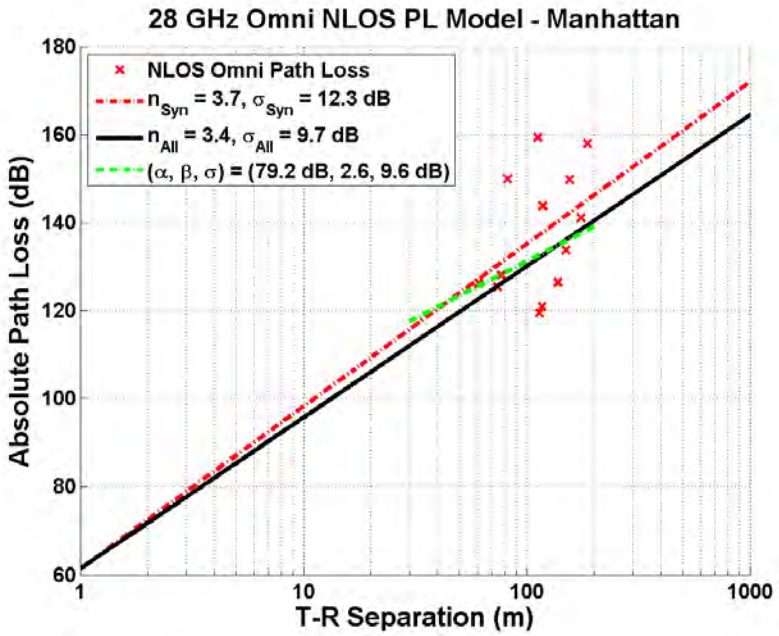

Figure 5.42: The omnidirectional path loss model for the NLOS environment is shown here, obtained from the wideband measurements in Manhattan. The omnidirectional power at each NLOS RX location was obtained from all PDPs for all RX and TX pointing angles (but double counts were eliminated), and antenna gains were removed from each PDP. The path loss exponent and shadowing factor obtained when summing all received powers at all azimuth and elevation angles are 3.4 and 9.7 dB, respectively, using a 1 m free space reference distance. The floating-intercept type model for 28 GHz, (similar to the form used in 3GPP) is shown in green between 30-200 m. The synthesized omnidirectional PDPs using only up to four measured PDPs (the most prominent AOAs) yield a path loss exponent and shadowing factor (with respect to a 1 m free space reference) of 3.7 and 12.3 dB (red line), showing good agreement to field measurements.

5.4.2.2 Cluster (Temporal) Statistics for NLOS Environments

This section presents histograms and cumulative distribution curves of extracted and generated 28 GHz NLOS wideband channel models for temporal statistics. The statistical generation of all channel parameters is explained in Section 5.5.1. In all cases, a χ^2 goodness of fit test with significance level of 5% was performed to ensure a close fit between the measured and corresponding theoretical distributions. All presented temporal statistics are given based on a 2.7 ns minimum inter-cluster void interval.

5.4.2.2.1 Number of Clusters in a NLOS Omnidirectional PDP

The mean and standard deviation of the number of time clusters in an omnidirectional PDP were found to be 3.4 and 2.1 respectively.

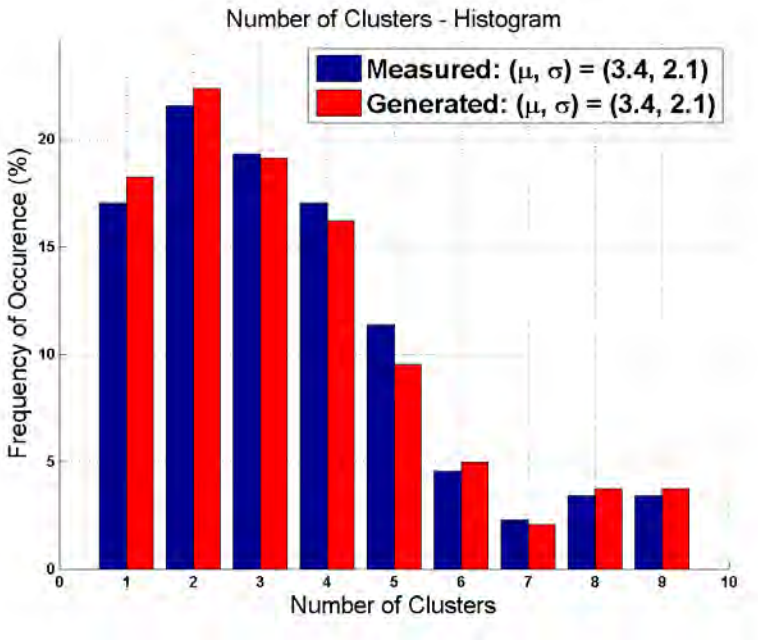

Figure 5.43: The histogram of the number of time clusters in a NLOS omnidirectional power delay profile. The blue bars correspond to the measured frequency of occurrence. The red bars, which approximate the data (blue bars), were generated based on the procedure outlined in Section 5.5.1, Step 3.

5.4.2.2.2 Number of Cluster Subpaths

The mean and standard deviation of the number of cluster subpaths, that is, the number of subpath components found in each time cluster, were found to be 2.1 and 1.6 respectively.

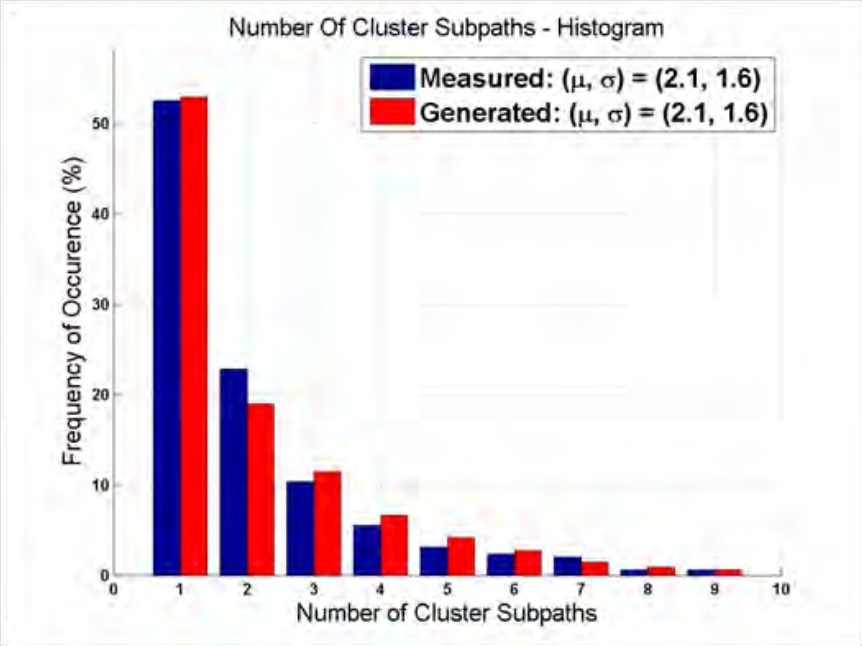

Figure 5.44: The histogram of the number of subpaths in a time cluster in a NLOS omnidirectional power delay profile. The blue bars correspond to the measured frequency of occurrence. The red bars were generated based on the procedure outlined in Section 5.5.1, Step 4.

5.4.2.2.3 Cluster Excess Time Delays

The cluster excess time delays were found to have an average of 66.3 ns and a standard deviation of 68 ns, and were fit to an exponential distribution with a mean of 67 ns. The histogram and cumulative distribution curve are shown below. The theoretical exponential distribution with mean 67 ns is plotted in red on the CDF plot for comparison.

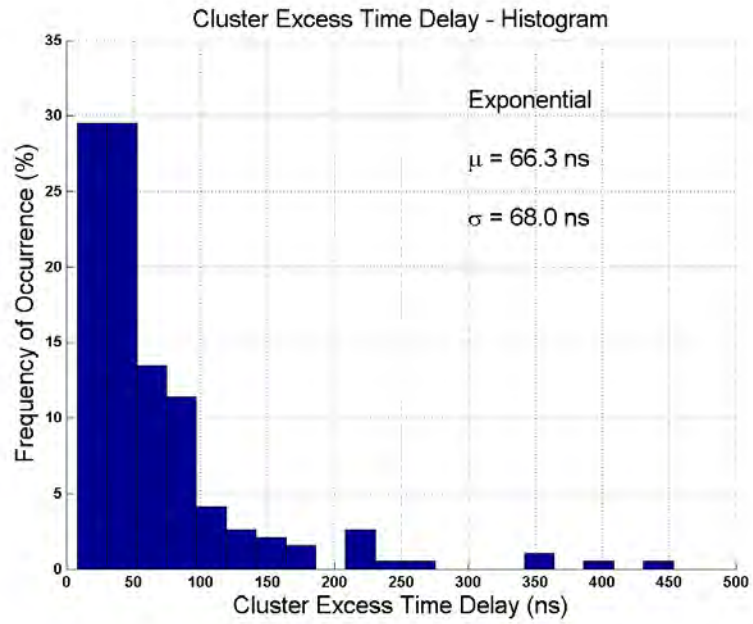

Figure 5.45: Histogram of the cluster excess time delays for NLOS environments. The mean and standard deviation of the cluster excess time delays are 66.3 ns and 68 ns respectively.

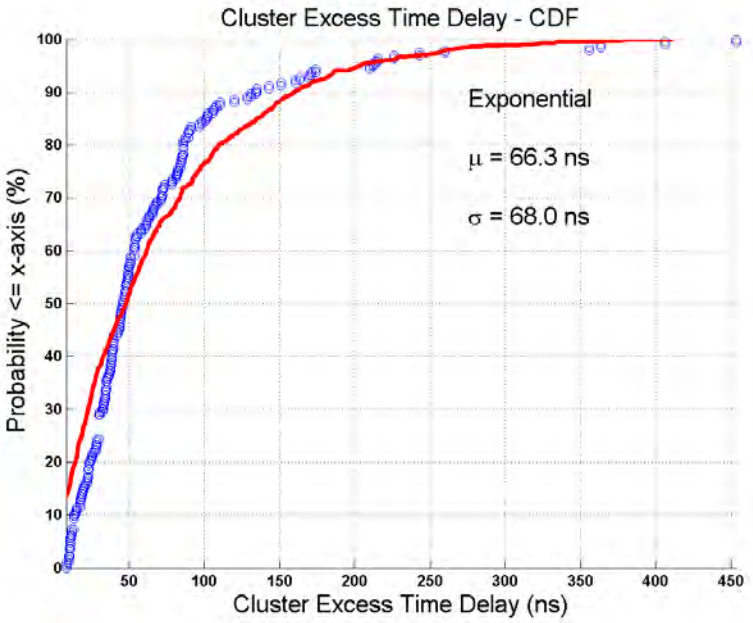

Figure 5.46: Cumulative distribution curve of the cluster excess time delays for NLOS environments. The mean and standard deviation of the cluster excess time delays are 66.3 ns and 68 ns respectively. The red cumulative distribution curve approximating the cluster excess time delay CDF is generated with an exponential random variable as described in Section 5.5.1.

5.4.2.2.4 Cluster Powers as a function of Cluster Excess Time Delays

The cluster power ratios were plotted as a function of the cluster excess time delays, and exhibit a deterministic trend. As the cluster excess time delays increase, the cluster power ratios have a tendency to decrease. The best fit exponential curve is plotted in Fig. 5.47. In order to introduce random variations about the mean fit curve, we plot the histogram and cumulative distribution curve of the difference in power levels in dB-scale in Fig. 5.49 and Fig. 5.50, which are shown to follow a lognormal distribution with a mean of 0 dB and a standard deviation of 9.4 dB. These random fluctuations may be thought of as per-cluster shadowing, which serves the same functionality as the shadowing term in the traditional close-in reference path loss model. Finally, we show the generated cluster powers with the per-cluster shadowing in Fig. 5.48, which appears to fit quite well to the data.

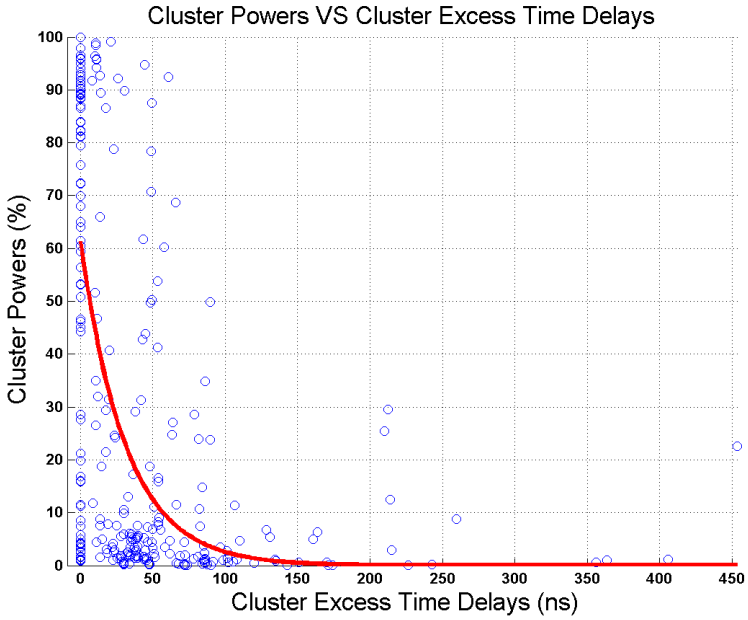

Figure 5.47: The cluster power ratios plotted against cluster excess time delays in NLOS environments. A deterministic trend is observed: as the cluster excess time delays increase, the cluster power ratios tend to decrease. The red curve is an exponential best line fit of the form $y = \alpha e^{-\frac{\tau}{\beta}}$, where $\alpha = 0.631$ and $\beta = 31.4$ ns.

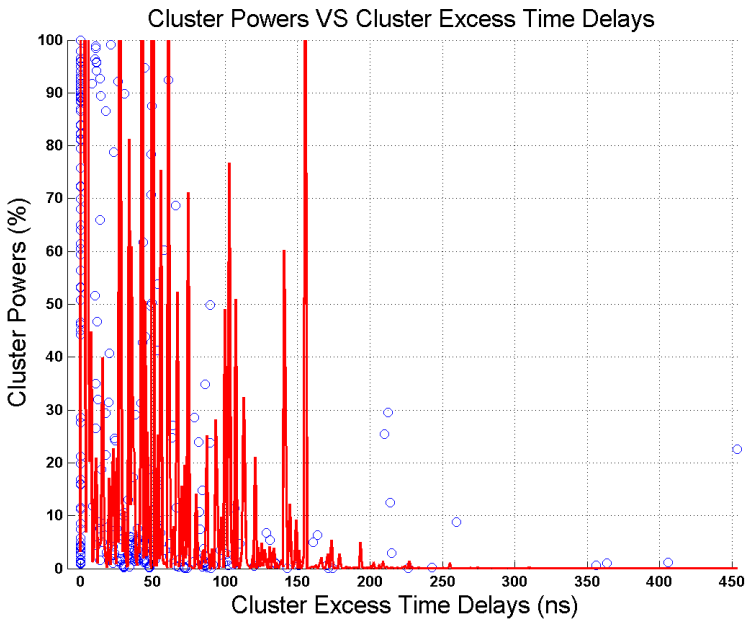

Figure 5.48: The cluster power ratios plotted against cluster excess time delays in NLOS environments. The red curve approximating the data points is generated with an exponential function (shown on Fig. 5.47) multiplied by a lognormal per-cluster shadowing random variable with a mean of 0 dB and a standard deviation of 9.4 dB.

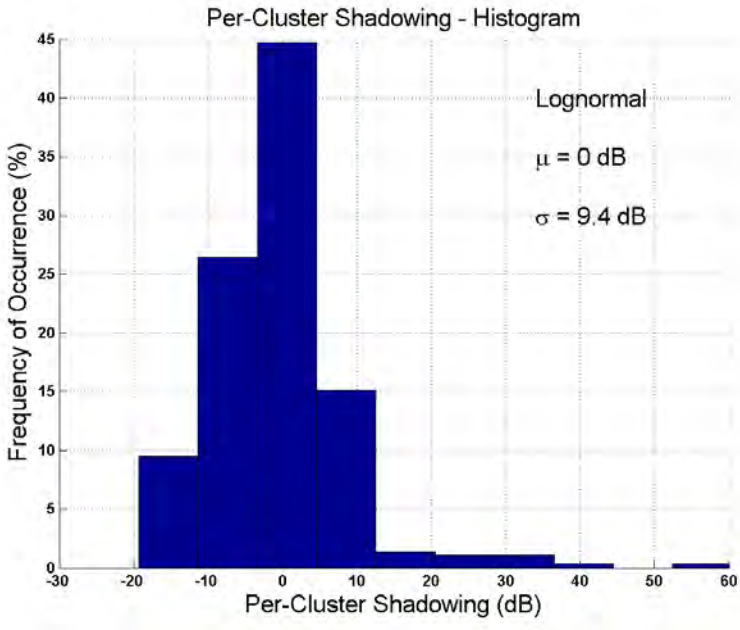

Figure 5.49: The histogram of the difference between the exponential best line fit (dB) and the cluster power ratios (dB) follows lognormal random variations with a mean of 0 dB and a standard deviation of 9.4 dB, for NLOS environments. This is the per-cluster shadowing.

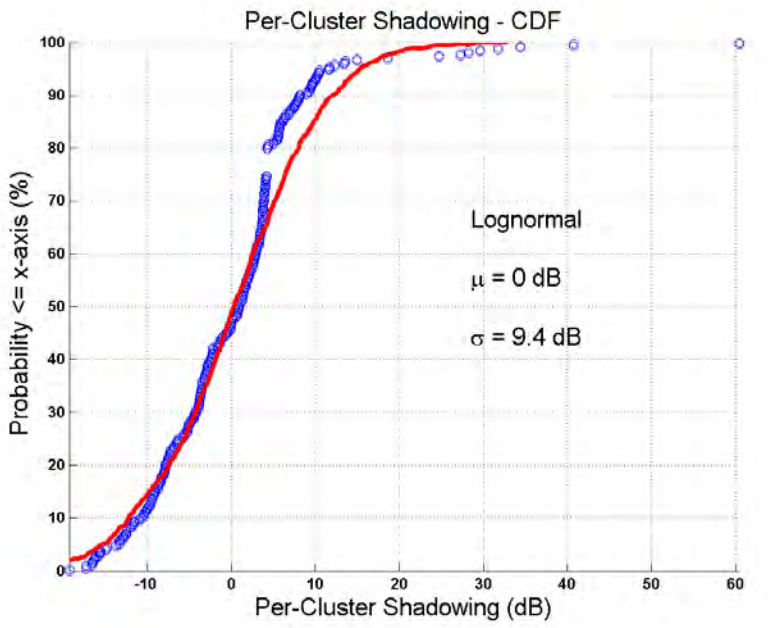

Figure 5.50: The cumulative distribution curve of the difference between the exponential best line fit (dB) and the cluster power ratios (dB). The red curve is generated with a lognormal random variable with a mean of 0 dB and a standard deviation of 9.4 dB, for NLOS environments.

5.4.2.2.5 Cluster Subpath Excess Time Delays

The cluster subpath excess time delays were found to have an average of 8.1 ns and a standard deviation of 8.8 ns, and were fit to an exponential distribution with a mean of 8 ns. The histogram and cumulative distribution curve are shown below. The theoretical exponential distribution with mean 8.4 ns is plotted in red on the CDF plot for comparison.

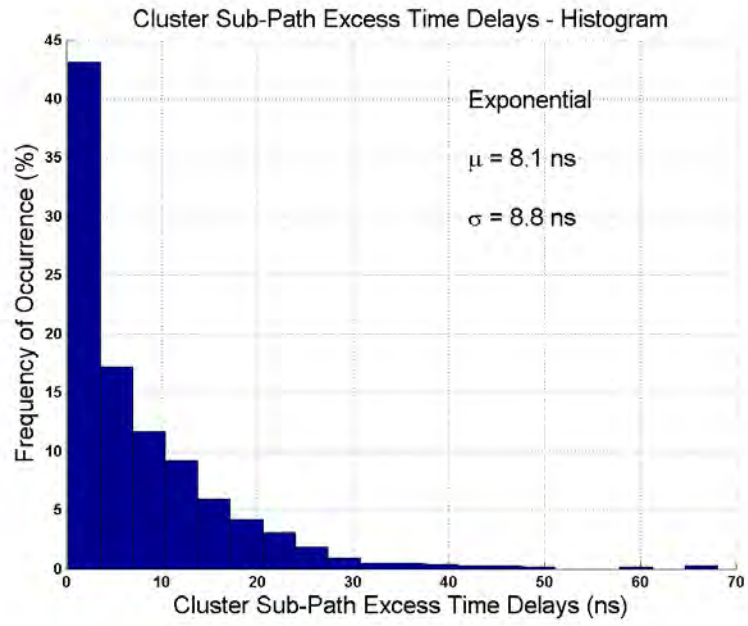

Figure 5.51: Histogram of the cluster subpath excess time delays, in NLOS environments. The mean and standard deviation of the cluster excess time delays are 8.1 ns and 8.8 ns respectively.

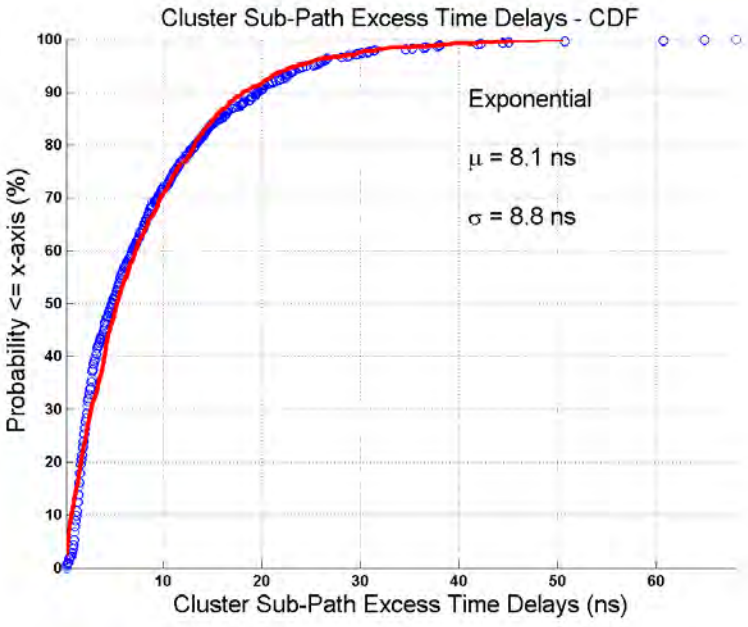

Figure 5.52: Cumulative distribution curve of the cluster excess time delays, in NLOS environments. The mean and standard deviation of the cluster excess time delays are 8.1 ns and 8.8 ns respectively. The red cumulative distribution curve approximating the cluster excess time delay CDF is generated with an exponential random variable with a mean of 8.4 ns.

5.4.2.2.6 Cluster Subpath Powers as a function of Cluster Subpath Time Delays

The cluster subpath power ratios were plotted as a function of the cluster subpath excess time delays, and exhibit a deterministic trend. As the cluster subpath excess time delays increase, the cluster subpath power ratios have a tendency to decrease. The best fit exponential curve is plotted in Fig. 5.53. In order to introduce random variations about the mean fit curve, we plot the histogram and cumulative distribution curve of the difference in power levels in dB-scale, which are shown to follow a lognormal distribution with a mean of 0 dB and a standard deviation of 5.1 dB, with slight deviations from the measured distribution. These random fluctuations may be thought of as per-cluster subpath shadowing, which serves the same functionality as the shadowing term in the traditional close-in reference path loss model. Finally, we show the generated cluster powers with the per-cluster subpath shadowing in Fig. 5.54, which appears to fit the data fit quite well.

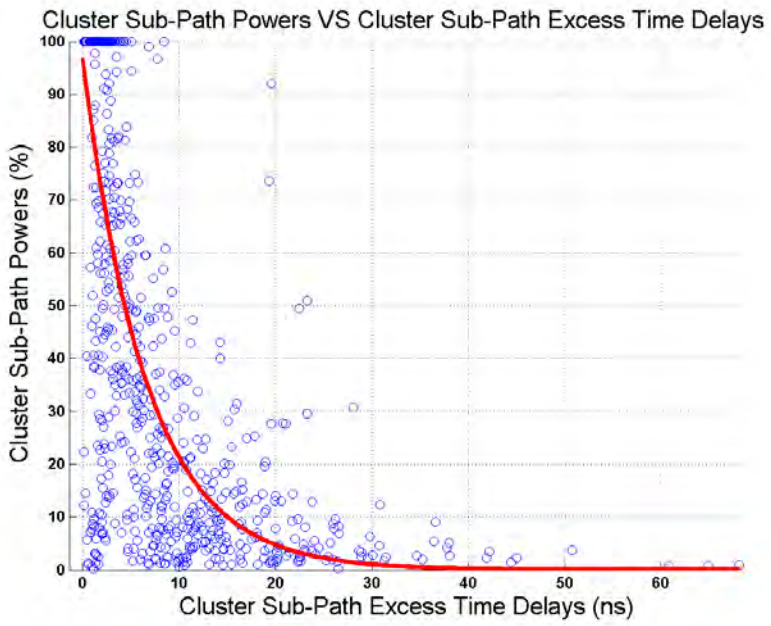

Figure 5.53: The cluster subpath power ratios plotted against cluster subpath excess time delays, in NLOS environments. A deterministic trend is observed: as the cluster subpath excess time delays increase, the cluster subpath power ratios tend to decrease. The red curve is an exponential best line fit of the form $y = \alpha e^{-\frac{\rho}{\beta}}$, where $\alpha = 0.966$ and $\beta = 6.63$ ns.

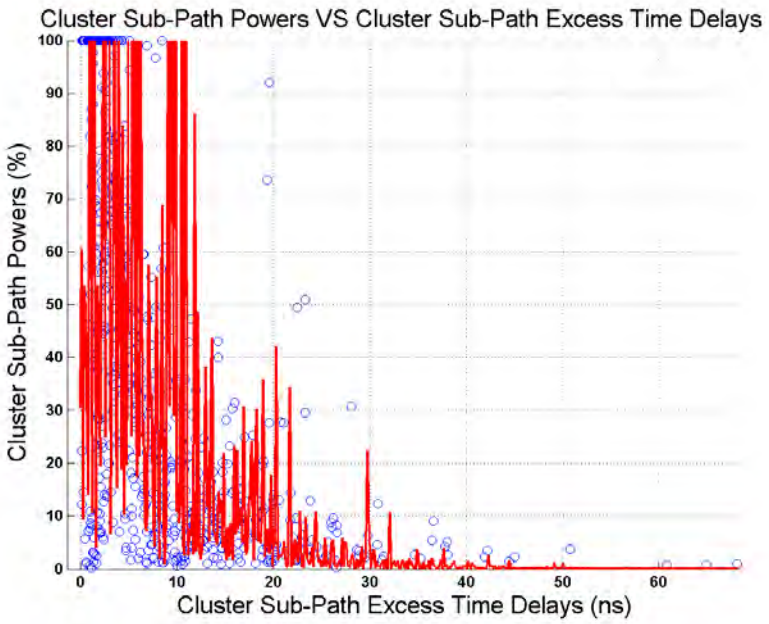

Figure 5.54: The cluster subpath power ratios plotted against cluster subpath excess time delays, in NLOS environments. The red curve approximating the data points is generated with an exponential function (shown on Fig. 5.53) multiplied by a lognormal per-cluster shadowing random variable with a mean of 0 dB and a standard deviation of 5.1 dB.

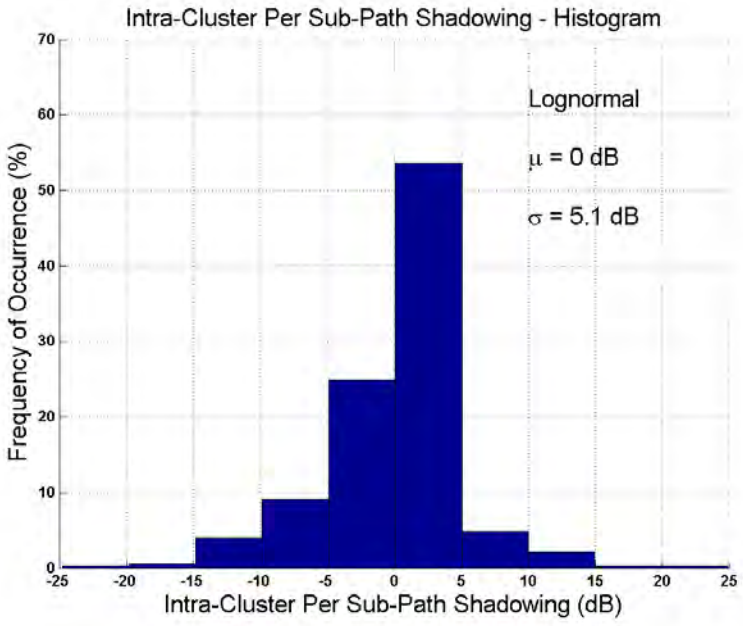

Figure 5.55: The histogram of the difference between the exponential best line fit (dB) and the cluster subpath power ratios (dB) follows lognormal random variations with a mean of 0 dB and a standard deviation of 5.1 dB, in NLOS environments. This is the per-cluster subpath shadowing.

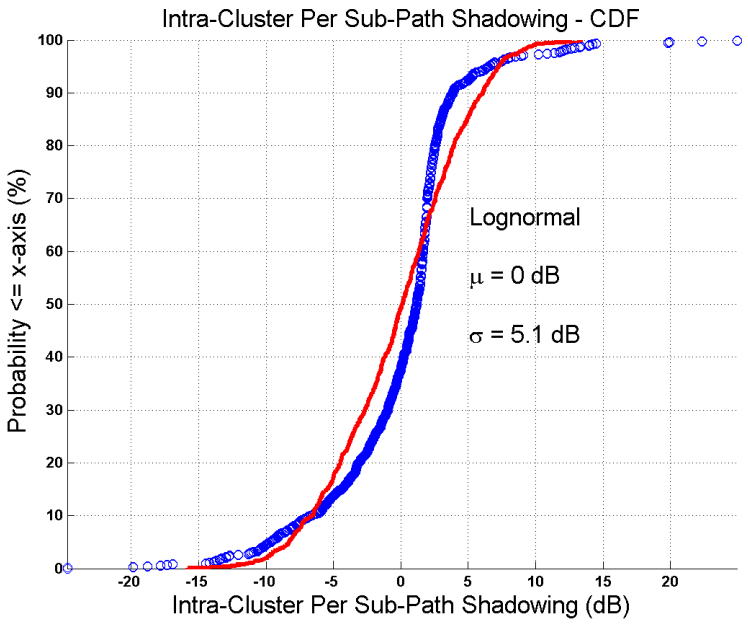

Figure 5.56: The cumulative distribution curve of the difference between the exponential best line fit (dB) and the cluster subpath power ratios (dB). The red curve is generated with a lognormal random variable with a mean of 0 dB and a standard deviation of 5.1 dB, in NLOS environments.

5.4.2.2.7 Omnidirectional PDP RMS Delay Spread

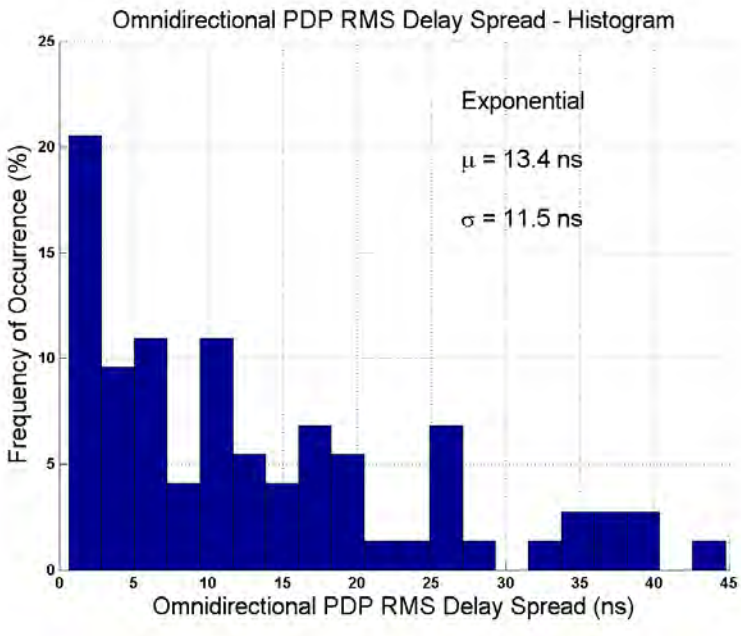

Figure 5.57: The histogram of the RMS delay spreads of the omnidirectional power delay profiles synthesized using 3-D ray-tracing techniques, in NLOS environments. The mean and standard deviations are 13.4 ns and 11.5 ns, respectively.

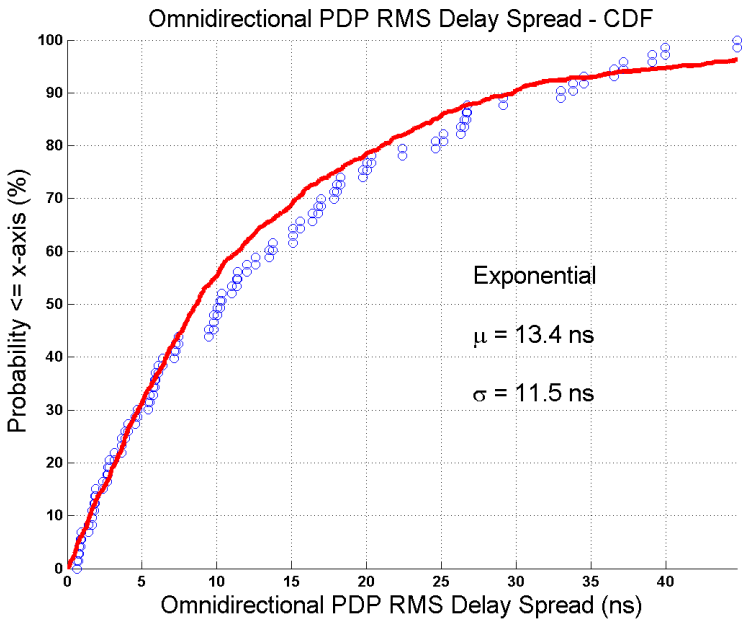

Figure 5.58: The cumulative distribution curve of the RMS delay spreads of the omnidirectional power delay profiles synthesized using 3-D ray-tracing techniques, in NLOS environments. The mean and standard deviations are 13.4 ns and 11.5 ns, respectively. The red curve approximating the data was generated with an exponential random variable with mean 13.4 ns.

5.4.2.2.8 Cluster RMS Delay Spread

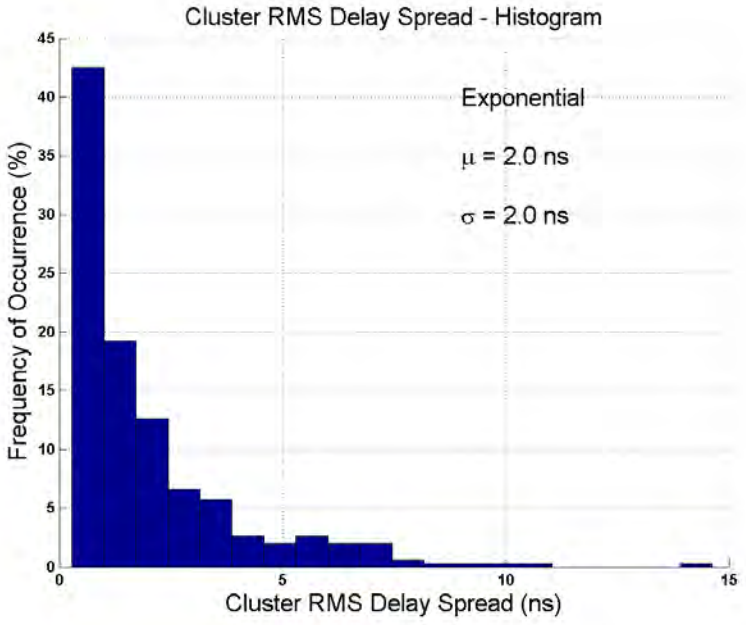

Figure 5.59: The histogram of cluster RMS delay spreads in an omnidirectional PDP in NLOS environments. The mean and standard deviations are both 2 ns.

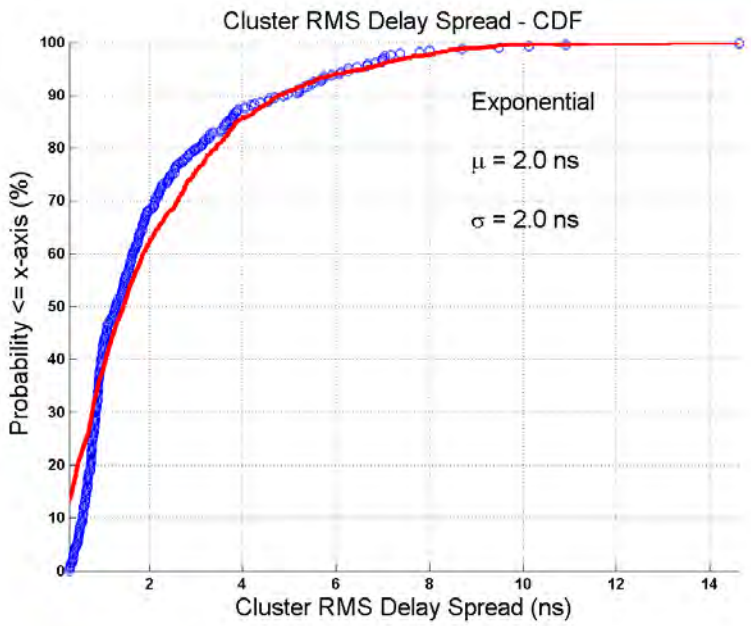

Figure 5.60: The cumulative distribution curve of cluster RMS delay spreads in an omnidirectional PDP in NLOS environments. The mean and standard deviations are both 2 ns. The red curve approximating the data was generated with an exponential random variable with mean 2 ns.

5.4.2.2.9 Cluster Duration

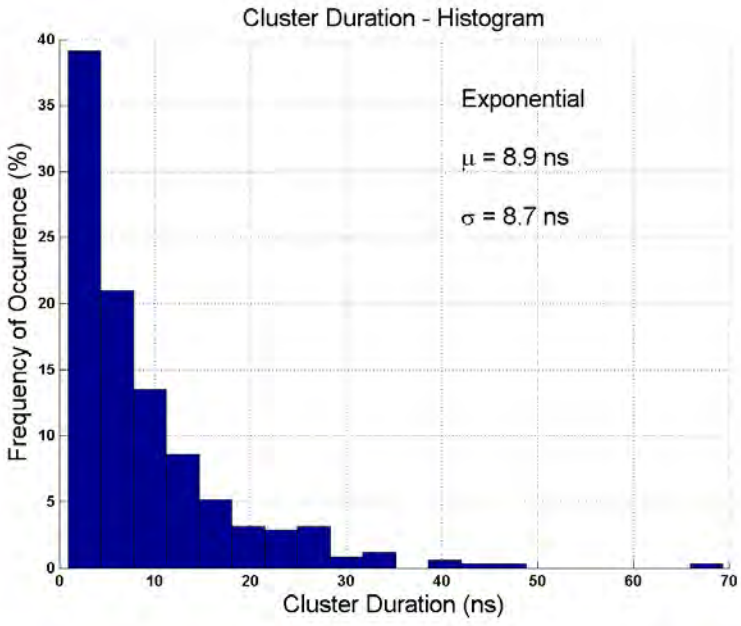

Figure 5.61: The histogram of the cluster durations in NLOS environments. The mean and standard deviations are 8.9 ns and 8.7 ns respectively.

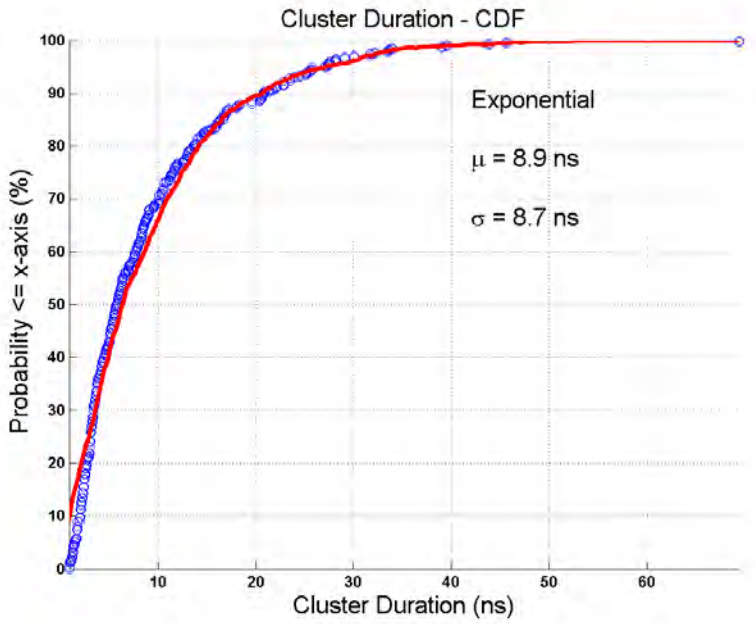

Figure 5.62: The cumulative distribution curve of the cluster durations in NLOS environments. The mean and standard deviations are 8.9 ns and 8.7 ns respectively. The red curve approximating the data was generated with an exponential random variable with mean 8.7 ns.

5.4.2.2.10 Inter-Cluster Void Duration

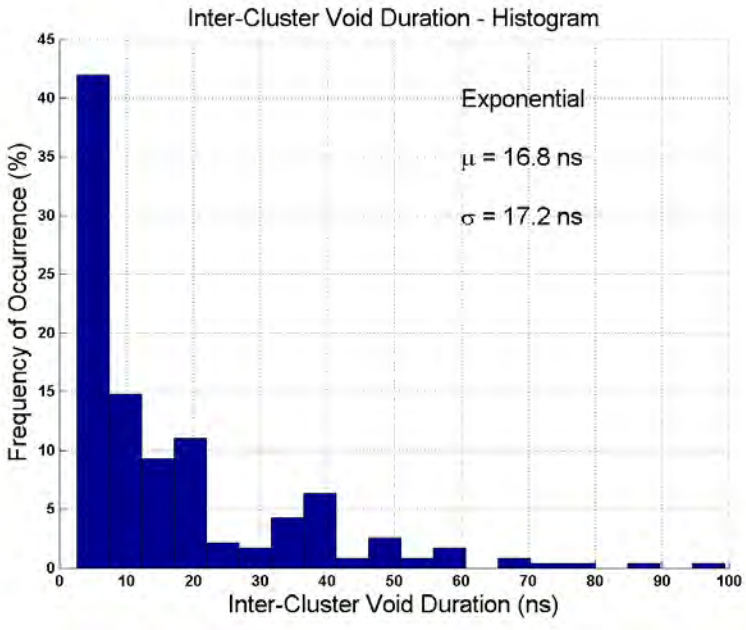

Figure 5.63: The histogram of the inter-cluster void durations in an omnidirectional PDP, in NLOS environments. The mean and standard deviations are 16.8 ns and 17.2 ns respectively.

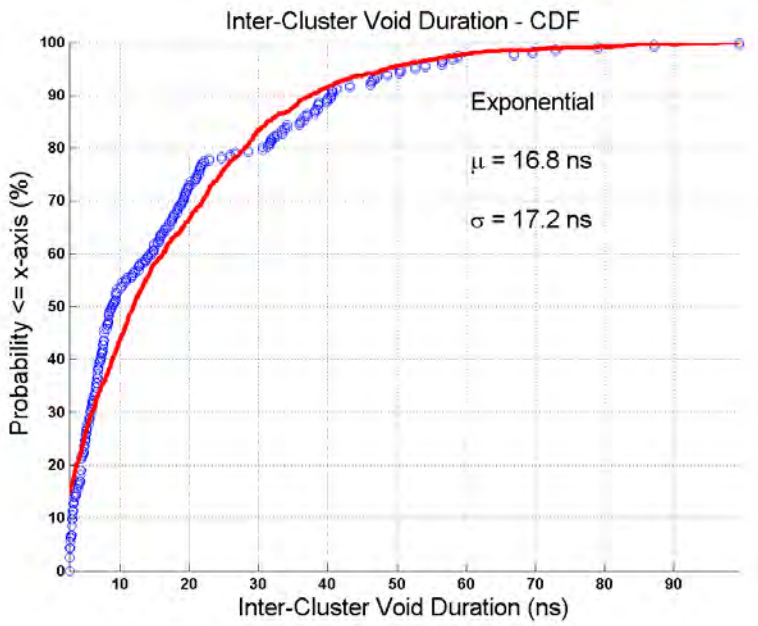

Figure 5.64: The cumulative distribution curve of the inter-cluster void durations in an omnidirectional PDP, in NLOS environments. The mean and standard deviations are 16.8 ns and 17.2 ns respectively. The red curve approximating the data was generated with an exponential random variable with mean 17 ns.

5.4.2.3 AOD Lobe (Spatial) Statistics for NLOS Environments

This section presents 28 GHz NLOS wideband channel models for AOD spatial statistics. The statistical generation of all channel parameters is explained in Section 5.5.1.

5.4.2.3.1 Number of Lobes at a NLOS RX Location

The number of lobes at each TX for measured NLOS RX locations was obtained by applying a thresholding procedure on the measured power azimuth spectra, that is, total received power as a function of RX azimuth angle. The thresholding algorithm consisted in finding the maximum total received power in the azimuth spectrum and applying a 20 dB below maximum power threshold over the whole azimuth spectrum. All presented spatial statistics are therefore for valid a 20 dB thresholding value.

Fig. 5.65 shows the histogram for the number of AOD lobes measured in Manhattan, with a superimposed histogram fitting (shown in red). A total of 40 AOD lobes were identified over all measured NLOS Manhattan TX locations. The mean and standard deviation of the number of lobes measured was found to

be $\mu_{Lobe} = 2.0$ and $\sigma_{Lobe} = 1.3$, respectively

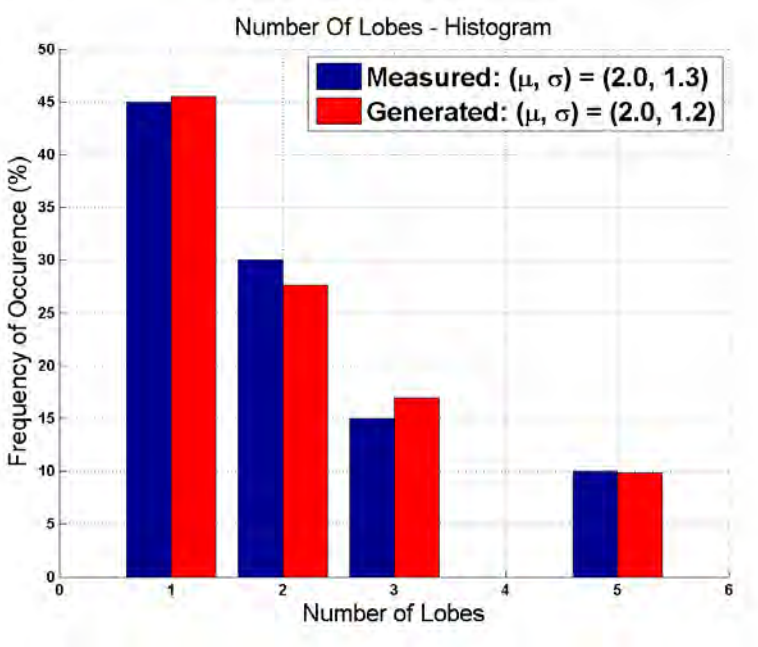

Figure 5.65: The histogram of the number of AOD lobes measured at a all TX locations for all NLOS RX locations from the 28 GHz wideband collected measurements in Manhattan. The mean and standard deviation of the number of AOD lobes were 2.0 and 1.3 respectively.

5.4.2.3.2 Mean Angle of Departures (AODs)

The lobe AODs were found to be relatively uniformly distributed in the azimuth plane. The plot below shows the cumulative distribution curve for the lobe AODs, with a superimposed theoretical distribution curve of a uniformly distributed random variable between 0° and 360°.

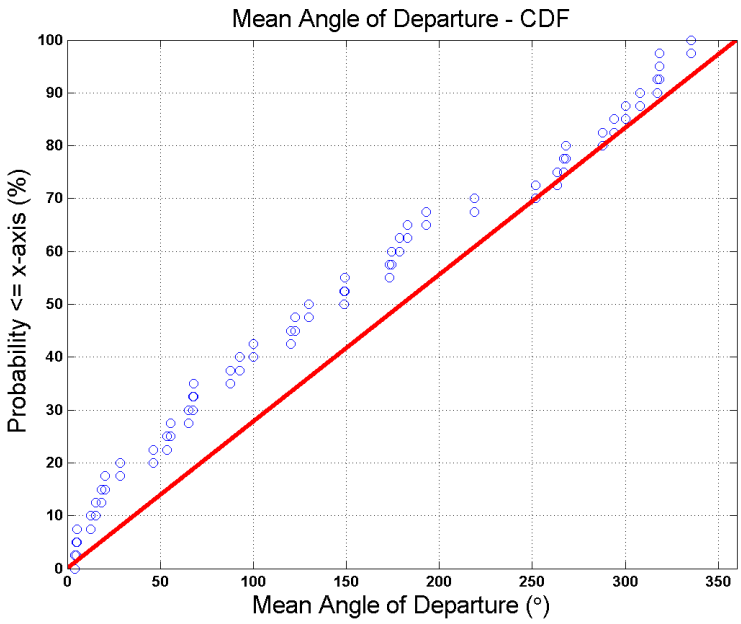

Figure 5.66: Cumulative distribution curve of the lobe AODs for all NLOS RX locations from the 28 GHz wideband collected measurements in Manhattan. The lobe AOD follows a random variable uniformly distributed between 0° and 360°.

5.4.2.3.3 AOD Lobe Azimuth Spread

The mean and standard deviation of the AOD lobe azimuth spreads were 42.5° and 25.2° respectively, and were fit to a Gaussian distribution. The histogram and the cumulative distribution curve are shown below.

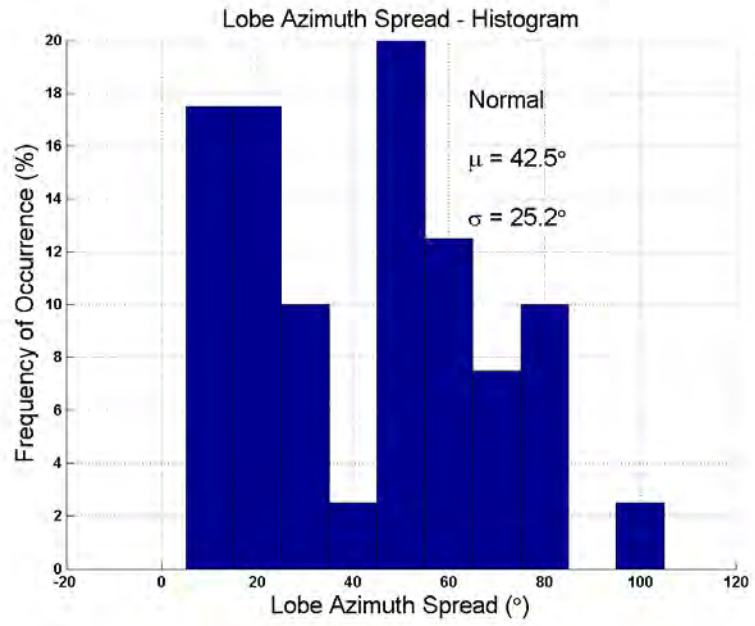

Figure 5.67: The histogram of the AOD lobe azimuth spreads in NLOS environments. The mean and standard deviations are 42.5° and 25.2° respectively.

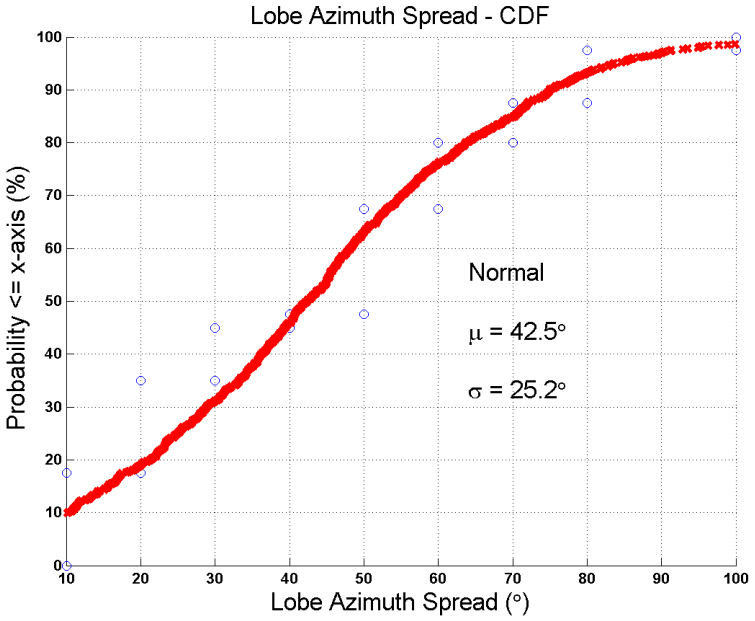

Figure 5.68: The histogram of the AOD lobe azimuth spreads in NLOS environments. The mean and standard deviations are 42.5° and 25.2° respectively. The red curve approximating the data was generated using a Gaussian random variable with a mean of 42.5° and standard deviation of 25.2°.

5.4.2.3.4 Lobe Segment Angular Power Levels as a function of Angular Separation from Lobe Angle with Maximum Received Power

The lobe segment angular power ratios (with respect to a maximum lobe segment power) are plotted against angular deviation away from the strongest angle (e.g., the lobe angle that received the most power). A deterministic trend may be observed whereby the lobe segment power tends to decrease as the angular deviation away from strongest angle increases. The lobe segment angular ratios are estimated with a Gaussian function (shown in red on the graphs below).

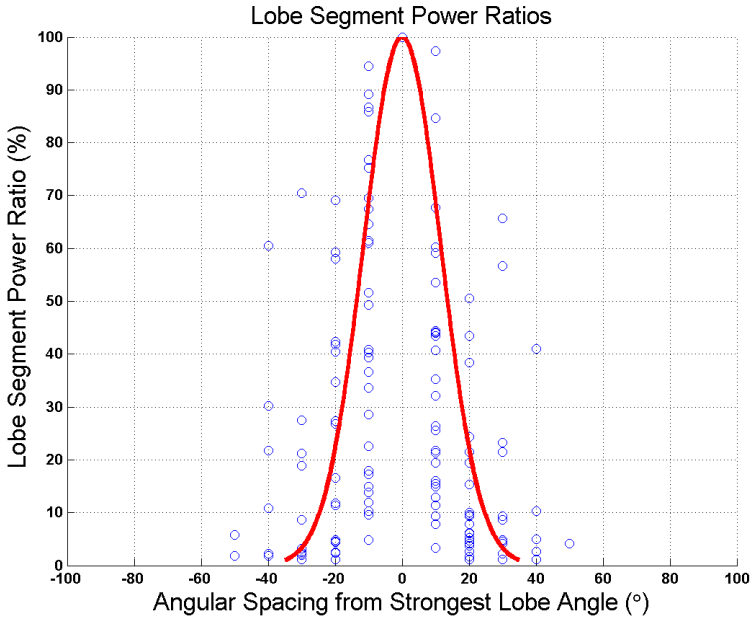

Figure 5.69: AOD lobe segment power ratios (% of maximum lobe power) as a function of angular spacing from strongest angle (e.g., angle with strongest received power in the lobe), in NLOS environments. The red curve approximating the data is of the form $y = e^{-\frac{(\Delta\theta)^2}{2\sigma^2}}$, where $\sigma = 11.5°$.

Figure 5.70: AOD lobe segment power ratios (% of maximum lobe power) as a function of angular spacing from strongest angle (e.g., angle with strongest received power in the lobe), in NLOS environments. The red curve approximating the data is of the form $y = e^{-\frac{(\Delta\theta)^2}{2\sigma^2}}$, where $\sigma = 11.5°$. This plot is the same as Fig. 5.69, plotted on a dB-scale.

5.4.2.3.5 AOD RMS Lobe Azimuth Spreads

The AOD RMS lobe azimuth spreads were found to have an average of 7.7° and a standard deviation of 5.3°, and were fit to a Gaussian distribution.

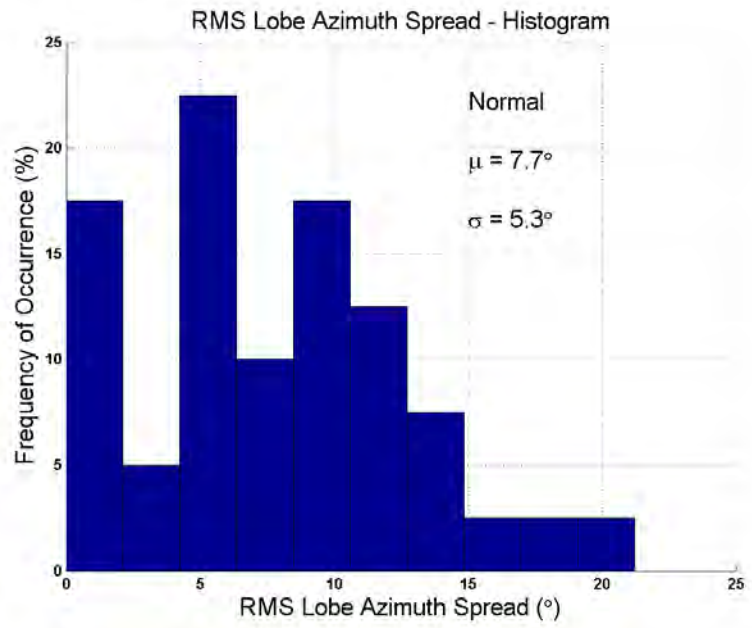

Figure 5.71: The histogram of the AOD RMS lobe azimuth spreads in NLOS environments. The mean and standard deviations are 7.7° and 5.3° respectively.

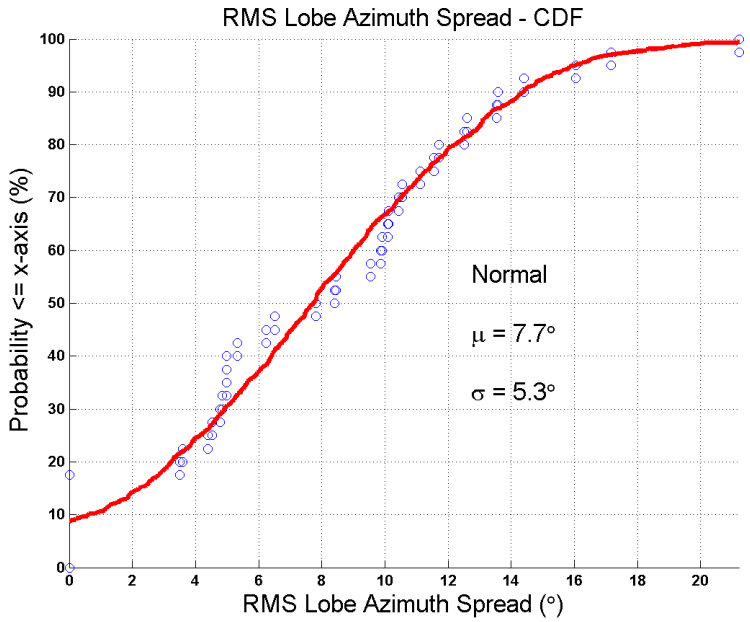

Figure 5.72: The cumulative distribution curve of the AOD RMS lobe azimuth spreads in NLOS environments. The mean and standard deviations are 7.7° and 5.3° respectively. The red curve approximating the data was generated with a normal distribution.

5.4.2.4 AOA Lobe (Spatial) Statistics for NLOS Environments

This section presents 28 GHz NLOS wideband channel models for AOA spatial statistics. The statistical generation of all channel parameters is explained in Section 5.5.1.

5.4.2.4.1 Number of AOA Lobes at a NLOS RX Location

The number of lobes at each measured NLOS RX location was obtained by applying a thresholding procedure on the measured power azimuth spectra, that is, total received power as a function of RX azimuth angle. The thresholding algorithm consisted in finding the maximum total received power in the azimuth spectrum and applying a 20 dB below maximum power threshold over the whole azimuth spectrum. All presented spatial statistics are therefore for valid a 20 dB thresholding value.

Fig. 5.73 shows the histogram for the number of AOA lobes measured in Manhattan, with a superimposed histogram fitting (shown in red). A total of 337 AOA lobes were identified over all measured NLOS Manhattan RX locations. The mean and standard deviation of the number of lobes measured was found to be $\mu_{Lobe} = 2.4$ and $\sigma_{Lobe} = 1.3$, respectively

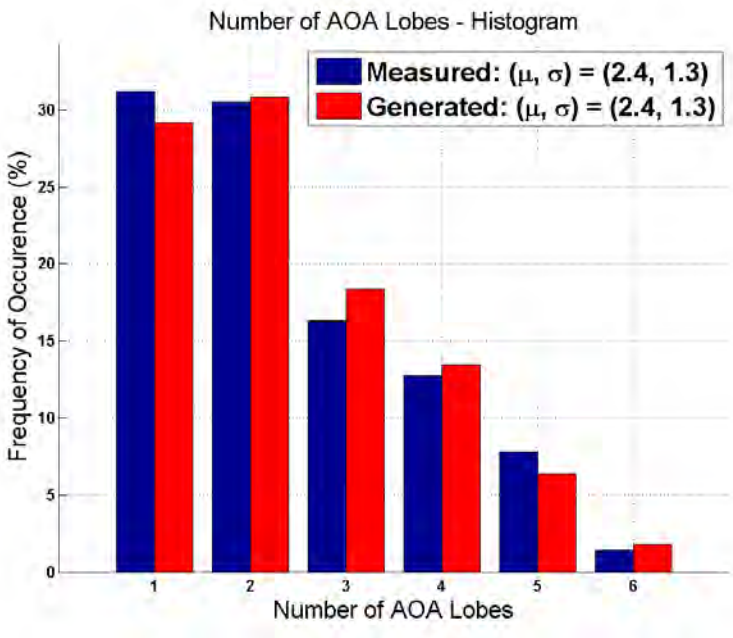

Figure 5.73: The histogram of the number of AOA lobes measured at all NLOS RX locations from the 28 GHz wideband collected measurements in Manhattan. The mean and standard deviation of the number of AOA lobes were 2.4 and 1.3 respectively.

5.4.2.4.2 Mean Angle of Arrival (AOAs)

The lobe AOAs in NLOS were found to be uniformly distributed in the azimuth plane. The plot below shows the cumulative distribution curve for the lobe AOAs, with a superimposed theoretical distribution curve of a uniformly distributed random variable between 0° and 360°.

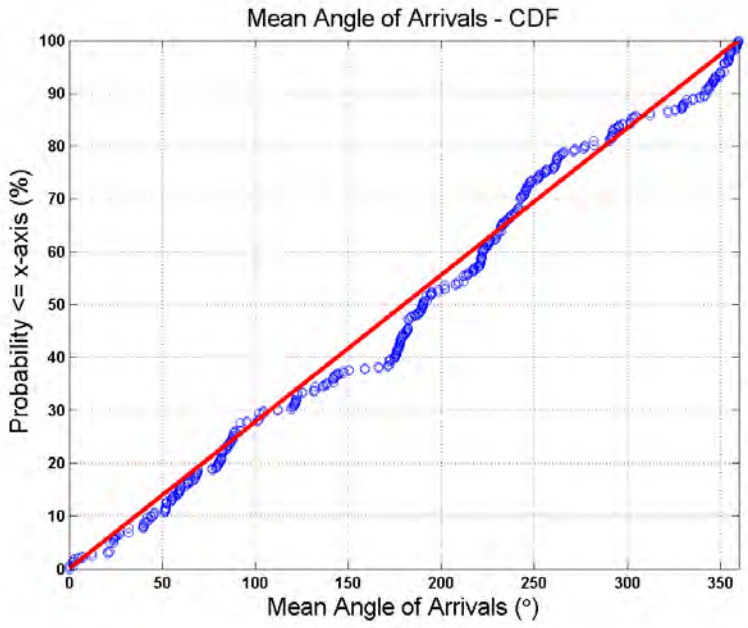

Figure 5.74: Cumulative distribution curve of the lobe AOAs from the 28 GHz wideband collected measurements in Manhattan, in NLOS environments. The lobe AOA follows a random variable uniformly distributed between 0° and 360°.

5.4.2.4.3 AOA Lobe Azimuth Spread

The mean and standard deviation of the AOA lobe azimuth spreads were 35.8° and 28.8° respectively. However, one AOA LAS outlier of 240° slightly skewed the distribution, and so was removed from the displayed histograph and cumulative distribution function. Upon removal of this outlier, the mean and standard deviation were found to be 34.8° and 25.7° respectively, and were fit to a truncated normal Gaussian distribution above 10°. The histogram and the cumulative distribution curve are shown below.

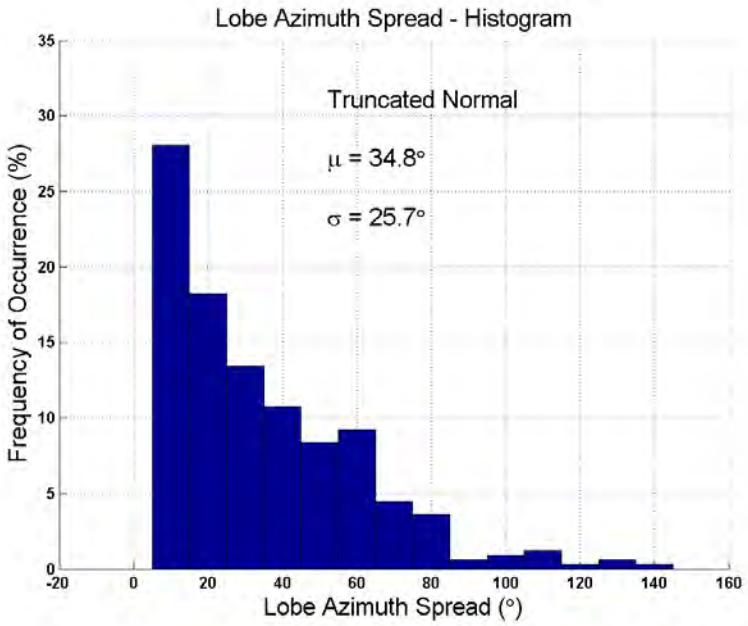

Figure 5.75: The histogram of the AOA lobe azimuth spreads from the 28 GHz wideband collected measurements in Manhattan, in NLOS environments. The mean and standard deviations are 34.8° and 25.7° respectively.

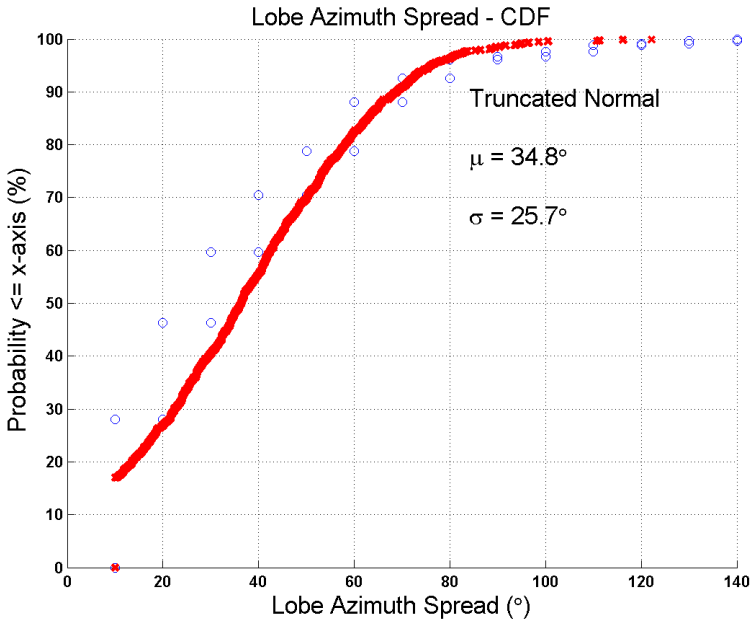

Figure 5.76: The cumulative distribution curve of the AOA lobe azimuth spreads from the 28 GHz wideband collected measurements in Manhattan, in NLOS environments. The red crosses approximating the data were generated with a truncated normal Gaussian distribution above 10°.

5.4.2.4.4 Lobe Segment Angular Power Levels as a function of Angular Separation from Lobe Angle with Maximum Received Power

The lobe segment angular power ratios (with respect to a maximum lobe segment power) are plotted against angular deviation away from the strongest angle (e.g., the lobe angle that received the most power). A deterministic trend may be observed whereby the lobe segment power tends to decrease as the angular deviation away from strongest angle increases. The lobe segment angular ratios are estimated with a Gaussian function (shown in red on the graphs below).

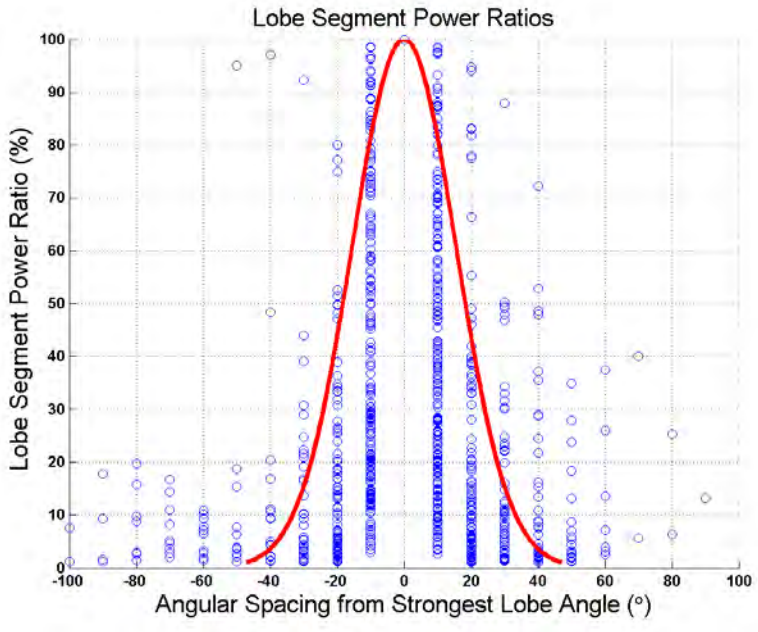

Figure 5.77: AOA lobe segment power ratios (% of maximum lobe power) as a function of angular spacing from strongest angle (e.g., angle with strongest received power in the lobe), in NLOS environments. The red curve approximating the data is of the form $y = e^{-\frac{(\Delta\theta)^2}{2\sigma^2}}$, where $\sigma = 15.5°$.

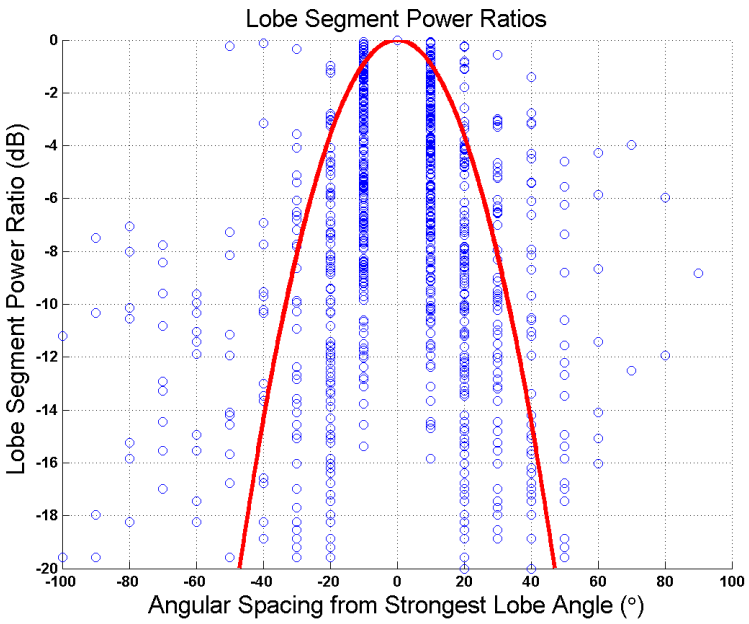

Figure 5.78: AOA lobe segment power ratios (% of maximum lobe power) as a function of angular spacing from strongest angle (e.g., angle with strongest received power in the lobe), in NLOS environments. The red curve approximating the data is of the form $y = e^{-\frac{(\Delta\theta)^2}{2\sigma^2}}$, where $\sigma = 15.5°$. This plot is the same as Fig. 5.77, plotted on a dB-scale.

5.4.2.4.5 The AOA RMS Lobe Azimuth Spread

The mean and standard deviation of the AOA RMS lobe azimuth spreads were 6.3° and 6.7° respectively. However, one AOA RMS LAS outlier of 70° slightly skewed the distribution, and so was removed from the displayed histograph and cumulative distribution function. Upon removal of this outlier, the mean and standard deviation were found to be 6.1° and 5.8° respectively, and were fit to an exponential distribution with mean 6.1°.

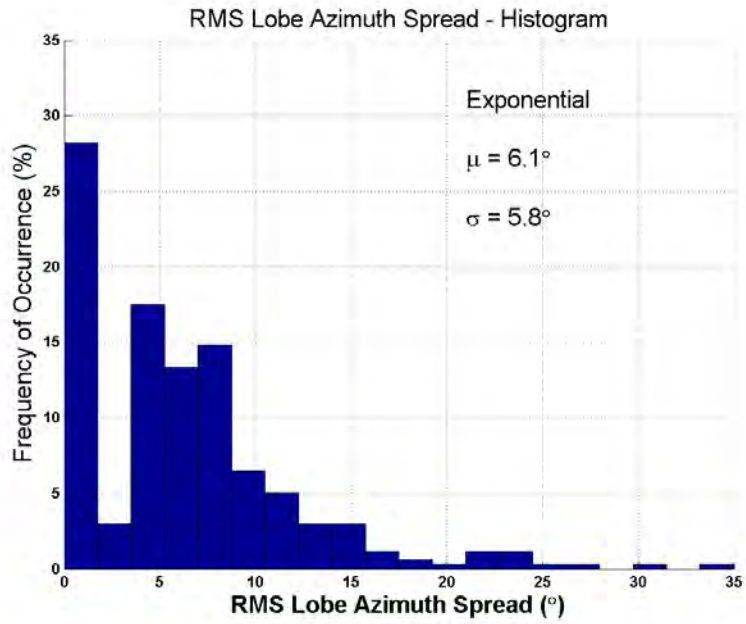

Figure 5.79: The histogram of the AOA RMS lobe azimuth spreads in NLOS environments. The mean and standard deviations are 6.1° and 5.8° respectively.

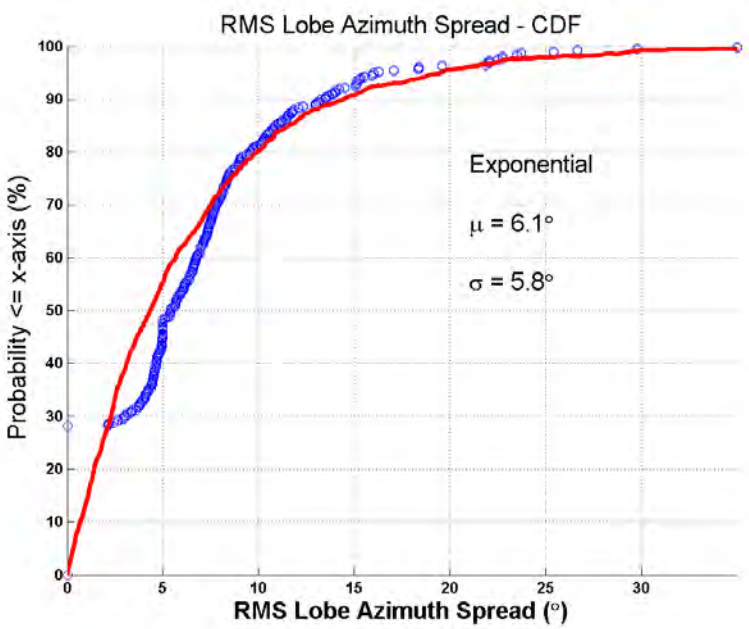

Figure 5.80: The cumulative distribution curve of the AOA RMS lobe azimuth spreads in NLOS environments. The mean and standard deviations are 6.1° and 5.8° respectively. The red curve approximating the data was generated with an exponential random variable with mean 6.1°.

5.4.3 LOS and NLOS Probabilities at COL1, COL2 and KAU TX Locations

The LOS probability corresponds to the probability that the radiation emerging from the transmitter will travel along a viable straight and unobstructed propagation path (i.e., zero reflections) to reach the receiver. Similarly, the NLOS probability corresponds to the probability that the radiation will travel along an obstructed path to reach the receiver (i.e., one or more reflections) These two probabilities heavily depend upon the environment in which the TX and RX are located, and must be provided for a complete SSCM, and to estimate channel capacities.

Using the numerical database built and described in Chapter 4, the LOS probability was obtained numerically over T-R separation distances ranging from 20 m to 200 m, for the 3 TX locations measured and for a RX height of 1.5 m. Only large buildings were modelled and smaller obstructions such as trees, lampposts and vehicular traffic were not taken into account.

In order to estimate the LOS probability at some T-R separation distance R, a circle or radius R was discretized around the TX location, and for each position along the circle, an optical line was traced to the TX. If that optical line penetrated through one building, the corresponding position on the circle was denoted as a NLOS position. If that optical line to the TX was unobstructed, that position counted as a LOS position. This was repeated for all positions along the circle, and the ratio of the number of LOS positions to the number of positions along the circle provided the LOS probability. This was performed over radii ranging from 20 m to 200 m, for all three TX locations.

The LOS probabilities for COL1, COL2 and KAU are shown below, along with the 3GPP and WINNER II LOS probabilities for microcellular environments (see Chapter 2 for the LOS probability formulas of WINNER II and 3GPP).

The WINNER II LOS probability agrees remarkably well with the computed LOS probability for COL1 and COL2 for T-R separations above 40 m, while it overestimates the LOS probability at KAU. The LOS probabilities at 200 m for COL1, COL2 and KAU are 3%, 10% and 0%, respectively.

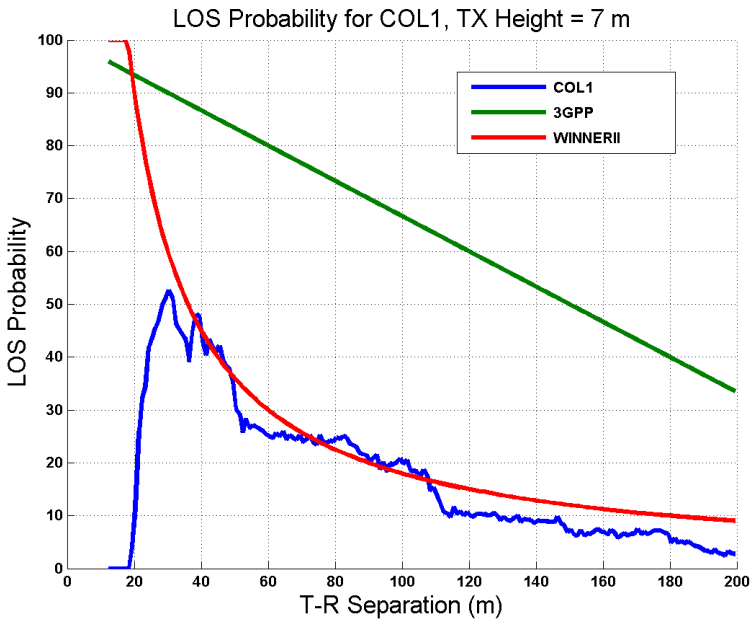

Figure 5.81: LOS probability for the transmitter location at Coles 1 (COL1) located 7 m above ground level for T-R separations ranging from 20 m to 200 m. The WINNER II LOS probability agrees fairly well with the COL1 LOS probability for T-R separation distances above 40 m. The 3GPP overestimates the LOS probability at COL1.

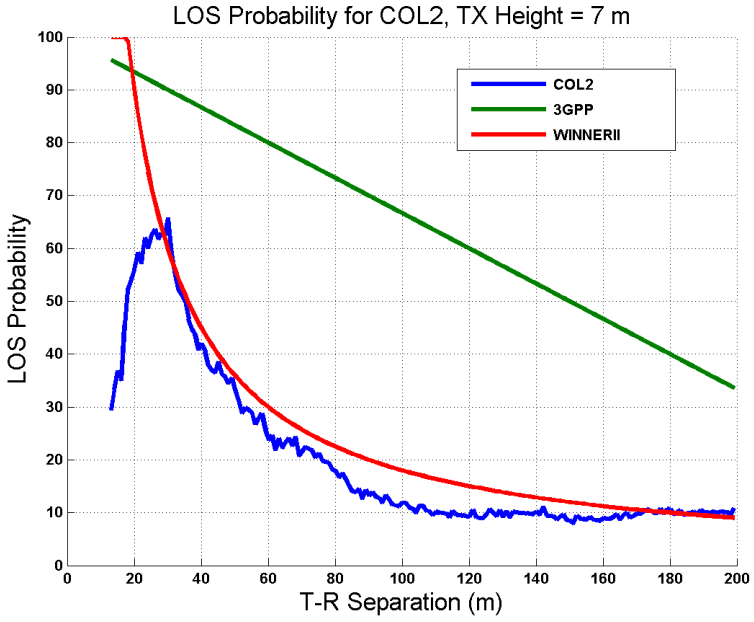

Figure 5.82: LOS probability for the transmitter location at Coles 2 (COL2) located 7 m above ground level for T-R separations ranging from 20 m to 200 m. The WINNER II LOS probability agrees fairly well with the COL2 LOS probability for T-R separation distances above 40 m. The 3GPP overestimates the LOS probability at COL2.

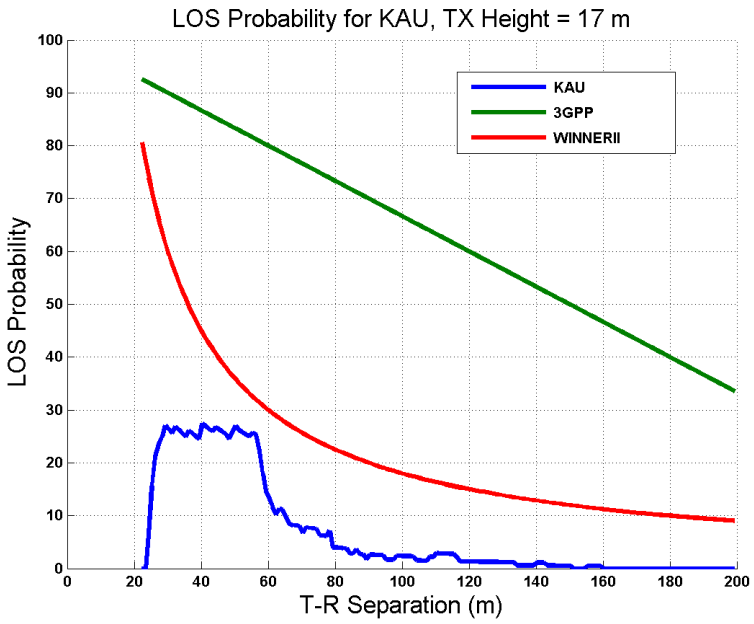

Figure 5.83: LOS probability for the transmitter location at the Kaufman Center (KAU) located 17 m above ground level for T-R separations ranging from 20 m to 200 m. The WINNER II LOS probability overestimates the LOS probability.

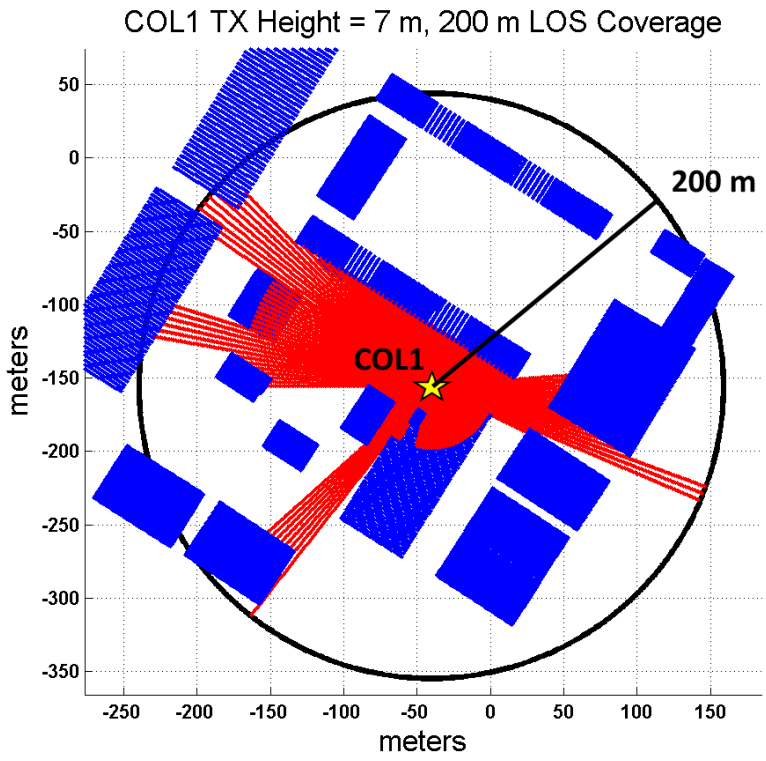

Figure 5.84: 200 m coverage around TX COL1 (yellow star) obtained in MATLAB. The red lines indicate an optical LOS path as seen from the TX at a RX mobile height of 1.5 m. The LOS probability at 200 m away from TX COL1 is 3%.

The 200 m coverage around COL1 is shown in Fig. 5.84.

For all intents and purposes, the LOS and NLOS probabilities can be estimated using the WINNER II equation for distances ranging from 30 m to 200 m (see Chapter 2).

5.5 Statistical Simulator for 28 GHz Millimeter-Wave Wideband Dense Urban Channels

An accurate omnidirectional channel statistical simulator should be able to generate a collection of PDPs and PAS which, when viewed as a statistical ensemble, recreate the statistics of the measured channels [104]. The extracted channel parameters given here generate key primary statistics that properly generate omnidirectional PDPs, AOD and AOA PAS that are identical (in a statistical sense) to actual field

measurements in 28 GHz wideband dense urban channels.

To validate the channel models, a MATLAB-based statistical simulator was created, based upon the following step-by-step procedure for generating channel coefficients. The models are valid for the types of channels measured in [89],[88], and assume a carrier frequency of 28 GHz, an RF channel bandwidth up to 800 MHz in a dense urban NLOS environment, with obstructions between the TX and RX. The step procedure for generating temporal and spatial profiles is provided below. We note that Step 11 bridges the temporal and spatial components of the SSCM by associating temporal cluster powers to the directions of strongest arriving power; a similar feature was used in previous 3GPP or WINNER models, but we keep the PAS.

5.5.1 Generating Channel Coefficients based on Millimeter-Wave Statistical Omnidirectional and Spatial Wideband Channel Models

A statistical simulator may be built based upon a well-defined step-by-step procedure for generating channel coefficients. This step-by-step procedure is outlined in this section. The assumptions under which the validity of these channel models and statistical simulator is maintained are outlined below:

- 28 GHz 800 MHz RF (null-to-null) bandwidth transmit signal
- Dense urban LOS and NLOS environments as defined in this thesis (See Chapter 3)
- T-R Separation ranging from 30-200 m based on the measured locations
- Generated PDPs are for the strongest measured angles at the RX location (based on ray-tracing results, see Chapter 4)
- Receiver sensitivity close to -100 dBm (over 800 MHz bandwidth) in hardware system used for collecting measurements
- Lobe segments in power azimuth spectra correspond to narrowband powers. It is impossible at this time to generate the wideband power delay profiles at weak scattered angles because omnidirectional profiles containing energy from scattered angles could not be synthesized via 3-D ray-tracing techniques[1].

[1]3-D ray-tracing techniques were unable to predict angles where diffuse scattering was received. At the time of writing, diffuse scattering statistics are unobtainable from the lack of GPS synchronization at the TX and RX in our summer 2012 measurements. Our current data must be enhanced with additional 28 GHz measurements obtained with GPS synchronization

These will be determined at a later time, when GPS synchronization between TX and RX has been integrated into the existing channel sounding system and we are able to synthesize omnidirectional profiles at strong and weak angles, which will enhance the summer 2012 measurements.

It will be noticed that Step 11 bridges the temporal and spatial aspects of the channel model by assigning temporal cluster powers to spatial lobe AODs and AOAs angles.

fully integrated into our channel sounding system, which will then allow us to recover omnidirectional PDPs using all available measured angles, and extract diffuse scattering statistics.

Step 1: Generate the T-R separation distance d ranging from 30-100 m in LOS, and 60-200 m in NLOS (based on our field measurements, and could be modified with further measurements):

$$d \sim Uniform(d_{min}, d_{max}) \tag{5.23}$$

where
$$\begin{cases} d_{min} = 30 \text{ m}, d_{max} = 100 \text{ m}, & LOS \\ d_{min} = 60 \text{ m}, d_{max} = 200 \text{ m}, & NLOS \end{cases}$$

Note: To validate our simulation, we used the above distance ranges, but for standards work any distance less any distance less than 200 m is valid.

Step 1 bis: If the environment type is left unspecified, generate the T-R separation distance and the WINNER II LOS probability, and determine the environment type:

$$d \sim Uniform(d_{min}, d_{max}) \tag{5.24}$$

where $d_{min} = 30$ m, and $d_{max} = 200$ m.

$$P_{LOS}(d) = \min(\frac{18}{d}, 1)(1 - e^{-\frac{d}{36}} + e^{-\frac{d}{36}}) \tag{5.25}$$

$$X \sim Uniform(0, 1) \tag{5.26}$$

$$\text{Environment Type} = \begin{cases} LOS, & X \leq P_{LOS} \\ NLOS, & X > P_{LOS} \end{cases}$$

Step 2: Generate the total received omnidirectional power Pr (dBm) at the RX location according to the environment type:

$$P_r[dBm] = P_t + G_t + G_r - PL[dB] \tag{5.27}$$

$$PL[dB] = PL(d_0) + 10\overline{n}\log_{10}(\frac{4\pi d}{\lambda}) + \chi_\sigma \tag{5.28}$$

$$PL(d_0) = 20 \times \log_{10}\left(\frac{4\pi d_0}{\lambda}\right) = 61.4 \text{ dB} \tag{5.29}$$

$$\begin{cases} n = 2, \sigma = 3.6 \text{ dB}, & LOS \\ \overline{n} = 3.4, \sigma = 9.7 \text{ dB}, & NLOS \end{cases}$$

P_t is the transmit power in dBm, G_t and G_r are the TX and RX antenna gains respectively, $d_0 = 1$ m, $\lambda = 0.0107$ m, and $\overline{n}$ is the path loss exponent for omnidirectional TX and RX antennas. χ_σ is the lognormal random variable with 0 dB mean and corresponding standard deviation depending on the environment type. Note that the measured path loss exponent in LOS environments was $\overline{n} = 2.1$, but we use here $n = 2$ which is expected from free space propagation.

Step 3: Generate the number of time clusters N and the number of spatial AOD and AOA lobes (L_{AOD}, L_{AOA}) *at the RX location according to the environment type (See Appendix, MATLAB Code):*

For LOS:

$$N = \max(1, A_1)$$

$$L_{AOA,LOS} = \begin{cases} \max(1, B_1), & B_1 \leq N \\ N, & B_1 > N \end{cases}$$

$$L_{AOD,LOS} = \begin{cases} \max(1, C_1), & C_1 \leq N \\ N, & C_1 > N \end{cases}$$

where,

$$A_1 = \begin{cases} A_2, & A_{Temp} = 1 \\ A_{Temp}, & 2 \leq A_{Temp} \leq 10 \\ A_3, & A_{Temp} \geq 11 \end{cases} \quad B_1 = \begin{cases} B_2, & B_{Temp} = 1 \\ 2, & B_{Temp} \geq 7 \\ B_{Temp}, & otherwise \end{cases} \quad C_1 = \begin{cases} C_2, & C_{Temp} \geq 5 \\ C_{Temp}, & otherwise \end{cases}$$

$$A_{Temp} \sim [\text{Exp}(\mu = \mu_N)] + 1 \qquad B_{Temp} \sim [\text{Exp}(\mu = \mu_{L,AOA} + 3)] \qquad C_{Temp} \sim Poisson(\mu = \mu_{L,AOD} + 2)$$

$$A_2 = \begin{cases} 1, & X > 0.5 \\ DU(6,7) & X \leq 0.5 \end{cases} \qquad B_2 = \begin{cases} 4, & X < 0.33 \\ 5 & X \geq 0.67 \end{cases} \qquad C_2 = \begin{cases} 1, & X < 0.5 \\ 4 & X \geq 0.5 \end{cases}$$

$$A_3 = \begin{cases} 1, & Y > 0.75 \\ 2 & Y \leq 0.25 \end{cases}$$

$(X,Y) \sim Uniform(0,1) \qquad X \sim Uniform(0,1) \qquad X \sim Uniform(0,1)$

where $\mu_N = 4.1$, $\mu_{L,AOA} = 2.9$, and $\mu_{L,AOD} = 2.8$, the average number of time clusters in an omnidirectional PDP, and average number of AOA lobes and AOD lobes observed at all LOS RX locations, respectively.

For NLOS:

$$N = \max(1, A_1)$$

$$L_{AOA,NLOS} = \begin{cases} \max(1, B_1), & B_1 \leq N \\ N, & B_1 > N \end{cases}$$

$$L_{AOD,NLOS} = \begin{cases} \max(1, C_1), & C_1 \leq N \\ N, & C_1 > N \end{cases}$$

where,

$$A_1 = \begin{cases} A_2, & A_{Temp} = 1 \\ A_3, & A_{Temp} = 3 \\ 7, & A_{Temp} \geq 10 \\ A_{Temp}, & otherwise \end{cases} \qquad B_1 = \begin{cases} B_2, & B_{Temp} = 3 \\ 5, & B_{Temp} \geq 7 \\ 1, & B_{Temp} = 5 \\ B_{Temp}, & otherwise \end{cases} \qquad C_1 = \begin{cases} C_2, & C_{Temp} = 3 \\ 1, & C_{Temp} = 4 \\ 5, & C_{Temp} \geq 6 \\ C_{Temp}, & otherwise \end{cases}$$

$A_{Temp} \sim Poisson(\mu = \mu_N - 0.5) \quad B_{Temp} \sim Poisson(\mu = \mu_{L,AOA} + 1.5) \quad C_{Temp} \sim Poisson(\mu = \mu_{L,AOD} + 2)$

$$A_2 = \begin{cases} 1, & X > 0.8 \\ 8 & X \leq 0.2 \end{cases} \qquad B_2 = \begin{cases} 1, & X < 0.2 \\ 3 & X \geq 0.8 \end{cases} \qquad C_2 = \begin{cases} 1, & X < 0.25 \\ 3 & X \geq 0.75 \end{cases}$$

$$A_3 = \begin{cases} 3, & Y > 0.85 \\ 9 & Y \leq 0.15 \end{cases}$$

$(X, Y) \sim Uniform(0, 1) \qquad X \sim Uniform(0, 1) \qquad X \sim Uniform(0, 1)$

where $\mu_N = 3.4$, $\mu_{L,AOA} = 2.4$, and $\mu_{L,AOD} = 2$, the average number of time clusters in an omnidirectional PDP, and average number of AOA lobes and AOD lobes observed at a NLOS RX location, respectively.

Step 4: Generate the number of cluster subpaths (SP) M_n in each time cluster: LOS and NLOS:

$$M_n = \begin{cases} \max(1, A), & 1 \leq A \leq 9 \\ 1, & A \geq 10 \end{cases}$$

where,

$$A \sim [\text{Exp}(\mu = \mu_{SP})]$$

where $\mu_{SP,LOS} = 2.0$ and $\mu_{SP,NLOS} = 2.1$, the observed average number of cluster subpaths in a LOS and NLOS omnidirectional PDP, respectively.

Step 5: Generate the intra-cluster subpath excess delays $\rho_{m,n}$ (ns):

$$\rho_{m,n} = 5 \times (m - 1), \qquad m = 1, 2, ...M_n, n = 1, 2, ...N$$

Step 6: Generate the cluster delays τ_n (ns) using the intra-cluster subpath delays generated in Step 5:

For LOS:

$$\tau_n' \sim \text{Exp}(\mu = r_{\tau,LOS}\mu_{\tau,LOS})$$

$$\tau_n'' = \min(\tau_n' - \min(\tau_n'), 800)$$

$$\tau_n = \rho_{M_n,n-1} + \tau_n'' + 10$$

where $\mu_{\tau,LOS} = 162$ ns, $r_{\tau,LOS} = 0.41$ are the observed average cluster excess time delay in a LOS omnidirectional PDP, and the delay proportionality constant, respectively.

For NLOS:

$$\tau_n' \sim \text{Exp}(\mu = r_{\tau,NLOS}\mu_{\tau,NLOS})$$

$$\tau_n'' = \tau_n' - \min(\tau_n')$$

$$\tau_n = \rho_{M_n,n-1} + \tau_n'' + 10$$

where $\mu_{\tau,NLOS} = 67$ ns, $r_{\tau,NLOS} = 0.25$ are the observed average cluster excess time delay in a NLOS omnidirectional PDP, and the delay proportionality constant, respectively.

This step assures no temporal cluster overlap with a 10 ns inter-cluster void interval. The optimum inter-cluster void interval was determined to be 2.7 ns when accounting for pulse widths, and 7.7 ns when removing pulse widths, and so an inter-cluster void interval of 10 ns provides an extra margin of $10-7.7 = 2.3$ ns between two consecutive clusters.

Step 7: Generate the time cluster powers P_n (mW):

$$P_n' = 10^{\frac{Z}{10}} e^{-\frac{\tau_n}{\beta}}$$

Per-cluster shadowing: $Z \sim N(\mu, \sigma)$

$$P_n = \frac{P_n'}{\sum_{k=1}^{k=N} P_k'} \times P_r[mW]$$

where,

$$\begin{cases} \alpha = 0.738, \beta = 2.5 * 19.3 \text{ ns}, \mu = 0 \text{ dB}, \sigma = 9.5 \text{ dB}, & LOS \\ \alpha = 0.631, \beta = 31.4 \text{ ns}, \mu = 0 \text{ dB}, \sigma = 9.4 \text{ dB}, & NLOS \end{cases}$$

Step 8: Generate the cluster subpath powers $\Pi_{m,n}$ *(mW)* :

$$\Pi'_{m,n} = 10^{\frac{U}{10}} e^{-\frac{\rho_n}{\beta}}$$

$$\text{Per-cluster shadowing: } U \sim N(\mu, \sigma)$$

$$\Pi_{m,n} = \frac{\Pi'_{m,n}}{\sum_{k=1}^{k=N} \Pi'_{k,n}} \times P_n[mW]$$

where,

$$\begin{cases} \alpha = 1, \beta = 6.78 \text{ ns}, \mu = 0 \text{ dB}, \sigma = 5.1 \text{ dB}, & LOS \\ \alpha = 0.966, \beta = 6.63 \text{ ns}, \mu = 0 \text{ dB}, \sigma = 5.1 \text{ dB}, & NLOS \end{cases}$$

Note: our measurements have much greater temporal and spatial resolution than previous models. Intra-cluster power levels were observed to fall off exponentially over intra-cluster time delay.

Step 9: Recover absolute time delays $t_{m,n}$*(ns) of cluster subpaths using the T-R Separation distance:*

$$t_{m,n} = t_0 + \tau_n + \rho_{m,n}, \qquad m = 1, 2, ...M_n, n = 1, 2, ...N$$

$$t_0 = \frac{d}{c}$$

where $c = 3 \times 10^8 m/s$ is the speed of light in free space.

Step 10: Generate the mean AOA and AOD angles $\theta_i(^\circ)$ *of the spatial lobes to avoid overlap of lobe angles (per definition)*: For LOS and NLOS:

$$\theta_{i,AOA} = U(\theta_{min}, \theta_{max}), \qquad i = 1, 2, ...L_{AOA}$$

$$\theta_{min} = \frac{360(i-1)}{L_{AOA}} \text{ and } \theta_{max} = \frac{360i}{L_{AOA}}$$

For LOS and NLOS:

$$\theta_{i,AOD} = U(\theta_{min}, \theta_{max}), \qquad i = 1, 2, ...L_{AOD}$$

$$\theta_{min} = \frac{360(i-1)}{L_{AOD}} \text{ and } \theta_{max} = \frac{360i}{L_{AOD}}$$

Step 11: Assign cluster powers P_n successively to the different lobe angles θ_i based on Step 7 for both LOS and NLOS environments. This step distributes temporal powers into the spatial domain to match our measured data:

$$\begin{gathered} P(\theta_{1,AOA}) = \max(P_1, P_2, ..., P_N) \\ P(\theta_{2,AOA}) = \max(P_1, P_2, ..., P_{N-1}) \\ \vdots \\ P(\theta_{L,AOA}) = \max(P_1, P_2, ..., P_{N-L_{AOA}}) \end{gathered}$$

Add the remaining $J_{AOA} = N - L_{AOA} - 1$ temporal cluster powers to the L_{AOA} lobes in a uniformly random fashion.

$$\begin{gathered} P(\theta_{1,AOD}) = \max(P_1, P_2, ..., P_N) \\ P(\theta_{2,AOD}) = \max(P_1, P_2, ..., P_{N-1}) \\ \vdots \\ P(\theta_{L,AOD}) = \max(P_1, P_2, ..., P_{N-L_{AOD}}) \end{gathered}$$

Add the remaining $J_{AOD} = N - L_{AOD} - 1$ temporal cluster powers to the L_{AOD} lobes in a uniformly random fashion. This fit the data well.

Step 12: Generate the number of AOA and AOD lobe angular segments K_i to find the angular spread (for azimuth, but will be extended also for elevation):

For LOS:

$$K_i' \sim N(\mu_{AS}, \sigma_{AS})$$

$$K_i'' = \max(K_i', 10)$$

$$K_i = \frac{[K_i'']}{10}$$

$$\begin{cases} (\mu_{AS}, \sigma_{AS}) = (\mu_{AS,AOD} + 6, \sigma_{AS,AOD}) \\ (\mu_{AS}, \sigma_{AS}) = (\mu_{AS,AOA} + 1, \sigma_{AS,AOA}) \end{cases}$$

where $(\mu_{AS,AOD}, \sigma_{AS,AOD}) = (27.3°, 13.5°)$, and $(\mu_{AS,AOA}, \sigma_{AS,AOA}) = (39.9°, 31.4°)$, the mean and standard deviation of the measured AOD and AOA lobe azimuth spread in LOS environments, respectively.

For NLOS:

$$K_i' \sim N(\mu_{AS}, \sigma_{AS})$$

$$K_i'' = \max(K_i', 0)$$

$$K_i = \frac{[K_i'']}{10}$$

$$\begin{cases} (\mu_{AS}, \sigma_{AS}) = (\mu_{AS,AOD} + 7.5, \sigma_{AS,AOD} - 5.2) \\ (\mu_{AS}, \sigma_{AS}) = (\mu_{AS,AOA} + 5, \sigma_{AS,AOA}) \end{cases}$$

where $(\mu_{AS,AOD}, \sigma_{AS,AOD}) = (42.5°, 25.2°)$, and $(\mu_{AS,AOA}, \sigma_{AS,AOA}) = (34.8°, 25.7°)$, the mean and standard deviation of the measured AOD and AOA lobe azimuth spread in NLOS environments, respectively.

Step 13: Generate the discretized lobe segment azimuth angles $\theta_{i,j}(°)$ for each lobe for LOS and NLOS environments:

For LOS and NLOS, and for AOD and AOA's:

$$\theta_{i,j} = \theta_i + 10k, \qquad j = 1, 2, ...K_i, i = 1, 2, ...L$$

where,

$$\begin{cases} k = -\frac{K_i - 1}{2}, ..., -2, -1, 0, 1, 2, ..., \frac{K_i - 1}{2}, & K_i \text{ odd} \\ k = -\frac{K_i}{2} + Y, ..., -2, -1, 0, 1, 2, ..., \frac{K_i}{2} - X, & K_i \text{ odd} \end{cases}$$

$$X \sim \textit{Discrete Uniform}(0,1), \text{ and } Y = 1 - X$$

Step 14: Generate the lobe angular segment powers $P(\theta_{i,j})(mW)$:

$$P(\theta_{i,j}) = \begin{cases} P(\theta_i), & \Delta\theta_{i,j} = 0 \\ R(\Delta\theta_{i,j})P(\theta_i)10^{\frac{Z}{10}}, & \Delta\theta_{i,j} \neq 0 \end{cases}$$

$$j = 1, 2, ..., K_i, i = 1, 2, ..., L$$

$$R(\Delta\theta_{i,j}) = e^{-\frac{(\Delta\theta_{i,j})^2}{2\sigma^2}}$$

$$Z \sim N(0 \text{ dB}, 6 \text{ dB})$$

where,

$$\sigma = \begin{cases} 0.55\sigma_{AOA}, & LOS \\ 0.7\sigma_{AOA}, & NLOS \end{cases} \qquad \sigma = \begin{cases} 0.1\sigma_{AOD}, & LOS \\ 0.3\sigma_{AOD}, & NLOS \end{cases}$$

where,

$$\sigma_{AOA} = \begin{cases} 22.5°, & LOS \\ 15.5°, & NLOS \end{cases} \qquad \sigma_{AOD} = \begin{cases} 10.5°, & LOS \\ 11.5°, & NLOS \end{cases}$$

5.5.2 Recreating the Statistics of the 28 GHz Wideband Dense Urban Measured Channels using a MATLAB-Based Statistical Simulator

An ensemble (10,000) of omnidirectional PDPs and PAS (polar plots) were generated, and the primary and secondary statistics were extracted using the same cluster partitioning algorithm described in Section 5.3, and 10 dB and 20 dB PAS (for LOS and NLOS, respectively) thresholding procedure to compare with the measured statistics. Fig. 5.85 shows the comparison between measured and simulated omnidirectional RMS delay spreads from measured 28 GHz NLOS data. We also show the CDF of the NLOS RMS delay spreads obtained from measured PDPs using directional antennas over 10° angle increments for comparison. The following tables present and compare the generated statistics from the simulator with the actual measured statistics. The simulated omnidirectional path loss model provides good agreement with the measured omnidirectional path loss model. The means of simulated temporal and spatial primary statistics are all within 10% of the measured means, and the simulated distributions remained identical to the measured distributions. The reproduced simulated statistics indicate that the statistical simulator presented can accurately reproduce the statistics of the 28 GHz dense urban LOS and NLOS measured channels.

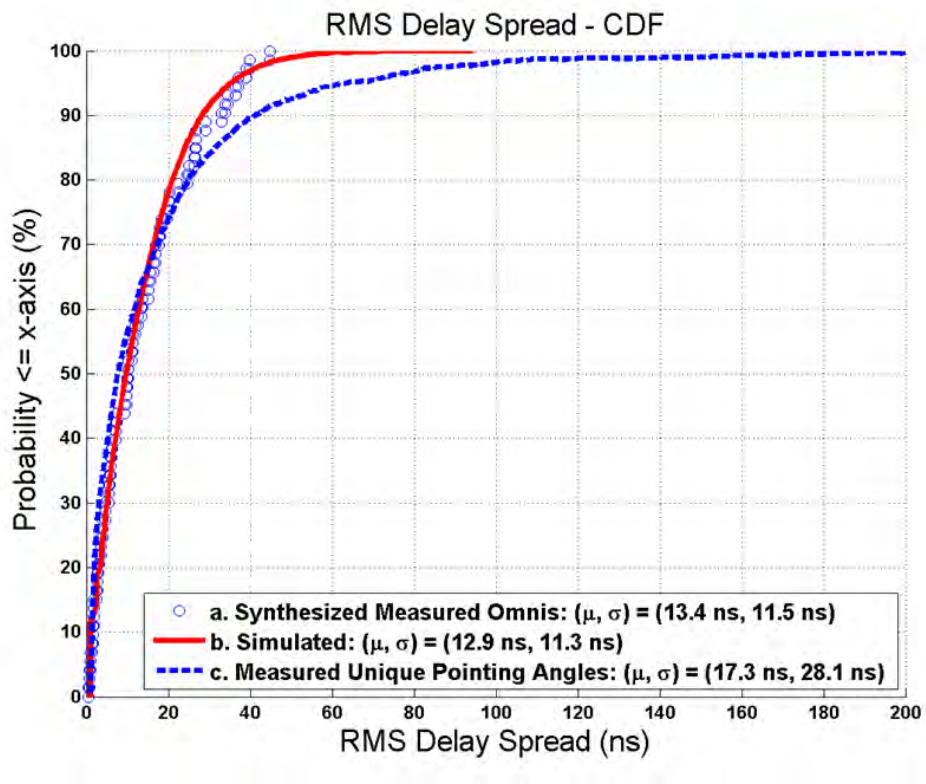

Figure 5.85: Cumulative distribution of RMS delay spread for a) simulated NLOS omnidirectional PDPs using the procedure in Section 5.5.1; b) the measured NLOS omnidirectional PDPs based on synthesized propagation time, and c) the entire NLOS measurement database using rotating horn antennas in [88][89]. The three curves are in close agreement, with higher delay spreads occurring with directional antennas.

5.5.2.1 Omnidirectional Path Loss Models

The measured and simulated statistics based on the step procedure outlined in Section 5.5.1 corresponding to the omnidirectional path loss models for LOS and NLOS environments are shown in Table 5.1.

Table 5.1: Summary of measured and simulated omnidirectional path loss models with respect to a 1 m free space reference distance using 10,000 simulated PDPs. (P) stands for primary statistic.

Path Loss Model	**Environment**	**Measured($\overline{n}, \sigma$)**	**Simulated($\overline{n}, \sigma$)**	**Error (%)**
Omnidirectional (P)	LOS	(2.0, 3.6 dB)	(2.0, 3.5 dB)	(0, 2.8)
Omnidirectional (P)	NLOS	(3.4, 9.7 dB)	(3.4, 9.8 dB)	(0, 1.0)

5.5.2.2 Cluster (Temporal) Statistics

The measured and simulated statistics based on the step procedure outlined in Section 5.5.1 corresponding to the LOS temporal cluster statistics are shown in Table 5.2.

Table 5.2: Summary of the measured statistics obtained from 28 GHz omnidirectional PDPs, and the simulated statistics generated from 10,000 PDPs obtained from the statistical simulator implementing the step procedure presented in 5.5.1 for the LOS environment. (P) and (S) stand for primary and secondary, respectively.

Type of Statistic	**Quantity**	**Measured(μ, σ)**	**Simulated(μ, σ)**	**Error (%)**
Temporal (LOS)	Number of Clusters (P)	Poisson (4.1, 2.3)	(4.0, 2.4)	(2.1, 1.7)
	Number of Cluster Subpaths (P)	Exponential (2.0, 1.7)	(2.1, 1.6)	(5.0, 5.9)
	Cluster Excess Time Delay (ns) (P)	Exponential (161.8, 189.1)	(172.9, 170.7)	(6.7, 9.6)
	Cluster Subpath Excess Time Delay (ns) (P)	Exponential (8.0, 8.3)	(8.3, 7.8)	(3.8, 6.0)
	RMS Delay Spread (ns) (S)	Exponential (60.5, 80.7)	(25.0, 20.3)	(58.7, 74.6)
	Cluster RMS Delay Spread (ns) (S)	Exponential (1.8, 1.9)	(2.3, 1.6)	(27.8, 11.0)
	Cluster Duration (ns) (S)	Exponential (8.6, 8.4)	(10.2, 8.1)	(18.6, 3.6)
	Inter-cluster Void Duration (ns) (S)	Exponential (14.8, 17.0)	(41.6, 26.0)	(180, 53)

Table 5.3: Summary of measured and simulated cluster and cluster subpath power ratios generated from 10,000 PDPs. α and β are defined in Step 7 and 8 of Section 5.5.1. (P) stands for primary.

Type of Statistic	**Quantity**	**Measured($\alpha, \beta[ns]$)**	**Simulated($\alpha, \beta[ns]$)**	**Error (%)**
Temporal (LOS)	Cluster Power Ratio (P)	(0.738, 19.3)	(0.538, 71.6)	(27.1, 271)
	Cluster Subpath Power Ratio (P)	(1, 6.78)	(0.863, 5.15)	(14, 24)

The measured and simulated statistics based on the step procedure outlined in Section 5.5.1 corresponding to the NLOS temporal cluster statistics are shown in Table 5.4.

Table 5.4: Summary of the measured statistics obtained from 28 GHz omnidirectional PDPs, and the simulated statistics generated from 10,000 PDPs obtained from the statistical simulator implementing the step procedure presented in 5.5.1 for the NLOS environment. (P) and (S) stand for primary and secondary, respectively.

Type of Statistic	**Quantity**	**Measured(μ, σ)**	**Simulatedμ, σ)**	**Error (%)**
Temporal (NLOS)	Number of Clusters (P)	Poisson (3.4, 2.1)	(3.2, 2.1)	(5.9, 0)
	Number of Cluster Subpaths (P)	Exponential (2.1, 1.6)	(2.2, 1.7)	(4.7, 6.3)
	Cluster Excess Time Delay (ns) (P)	Exponential (66.3, 68.0)	(71.8, 62.1)	(8.3, 8.7)
	Cluster Subpath Excess Time Delay (ns) (P)	Exponential (8.1, 8.8)	(8.6, 8.0)	(6.2, 9.1)
	RMS Delay Spread (ns) (S)	Exponential (13.4, 11.5)	(12.9, 11.3)	(3.7, 1.7)
	Cluster RMS Delay Spread (ns) (S)	Exponential (2.0, 2.0)	(2.4, 1.7)	(20.0, 15.0)
	Cluster Duration (ns) (S)	Exponential (8.9, 8.7)	(10.7, 8.4)	(20.2, 3.5)
	Inter-cluster Void Duration (ns) (S)	Exponential (16.8, 17.2)	(21.5, 15.9)	(28.0, 7.5)

Table 5.5: Summary of measured and simulated cluster and cluster subpath power ratios generated from 10,000 PDPs. α and β are defined in Step 7 and 8 of Section 5.5.1. (P) stands for primary.

Type of Statistic	**Quantity**	**Measured($\alpha, \beta[ns]$)**	**Simulated($\alpha, \beta[ns]$)**	**Error (%)**
Temporal (NLOS)	Cluster Power Ratio (P)	(0.613, 31.4)	(0.584, 41.3)	(4.7, 35.7)
	Cluster Subpath Power Ratio (P)	(0.966, 6.63)	(0.859, 5.02)	(11.1, 24.3)

5.5.2.3 Spatial AOD and AOA Statistics

The measured and simulated statistics based on the step procedure outlined in Section 5.5.1 corresponding to the LOS spatial lobe statistics are shown in Table 5.6.

Table 5.6: Summary of the measured statistics obtained from 28 GHz power azimuth spectra, and the simulated statistics generated from 10,000 power azimuth spectra obtained from the statistical simulator implementing the step procedure presented in 5.5.1 for the LOS environment. (P) and (S) stand for primary and secondary, respectively.

Type of Statistic	**Quantity**	**AOA/AOD**	**Measured(μ, σ)**	**Simulated(μ, σ)**	**Error (%)**
Spatial (LOS)	Number of Lobes (P)	AOA	Exponential (2.9, 1.5)	(3.1, 1.3)	(7.0, 13.3)
		AOD	Poisson (2.8, 1.3)	(2.8, 1.0)	(0, 23.3)
	Mean Pointing Angle (°) (P)	AOA	Uniform(0, 360)	Uniform(0, 360)	0
		AOD	Uniform(0, 360)	Uniform(0, 360)	0
	Lobe Azimuth Spread (°) (P)	AOA	Normal (39.9, 31.4)	(39.5, 30.5)	(1.0, 2.9)
		AOD	Normal (27.3, 13.5)	(25.3, 13.9)	(7.3, 3.0)
	RMS Lobe Azimuth Spread (°) (S)	AOA	Exponential (8.9, 8.7)	(9.0, 8.3)	(1.3, 4.6)
		AOD	Normal (5.5, 3.9)	(7.0, 4.1)	(27.3, 5.1)

The measured and simulated statistics based on the step procedure outlined in Section 5.5.1 corresponding to the NLOS spatial lobe statistics are shown in Table 5.7.

Table 5.7: Summary of the measured statistics obtained from 28 GHz power azimuth spectra, and the simulated statistics generated from 10,000 power azimuth spectra obtained from the statistical simulator implementing the step procedure presented in 5.5.1 for the NLOS environment. (P) and (S) stand for primary and secondary, respectively.

Type of Statistic	**Quantity**	**AOA/AOD**	**Measured(μ, σ)**	**Simulated(μ, σ)**	**Error (%)**
Spatial (NLOS)	Number of Lobes (P)	AOA	Poisson (2.4, 1.3)	(2.3, 1.1)	(4.2, 15.4)
		AOD	Poisson (2.0, 1.3)	(1.8, 0.9)	(10.0, 30.0)
	Mean Pointing Angle (°) (P)	AOA	Uniform(0, 360)	Uniform(0, 360)	0
		AOD	Uniform(0, 360)	Uniform(0, 360)	0
	Lobe Azimuth Spread (°) (P)	AOA	Normal (34.8, 25.7)	(34.6, 27.8)	(0.2, 9.0)
		AOD	Normal (42.5, 25.2)	(43.6, 26.1)	(2.6, 3.6)
	RMS Lobe Azimuth Spread (°) (S)	AOA	Exponential (6.1, 5.8)	(8.3, 6.8)	(36.0, 17.0)
		AOD	Normal (7.7, 5.3)	(8.0, 7.0)	(4.0, 32.0)

Chapter 6

Conclusion and Future Work

This thesis began by introducing previous mmWave propagation measurements and results obtained above 6 GHz, presenting past knowledge of indoor and outdoor propagation characteristics and material properties at mmWave frequencies. While mmWave propagation has been extensively conducted over the past three decades for many types of applications, Chapter 1 identified the need to understand mmWave propagation in dense urban environments for broadband mobile cellular, knowledge which is lacking up-to-date.

Chapter 2 described current 3GPP and WINNER II channel models in use today for estimating channel coefficients stochastically based on previous measurements conducted below 6 GHz for RF bandwidths spanning 5 MHz to 100 MHz. The statistical channel models developed are an appropriate alternative against solving Maxwell's set of differential equations, and illustrate the ultimate purpose of propagation measurements, that is, providing a basis for extracting channel parameter statistics and ultimately serving as a tool for evaluating system capacities, as well as help in designing appropriate radio-systems for the measured channels. Chapter 2 provided a necessary channel modeling framework to begin the 28 GHz channel modeling based on the wideband measurements collected in Manhattan.

Chapter 3 provided details and logistics of the 28 GHz wideband propagation measurement campaign conducted in Brooklyn and Manhattan in the summer of 2012, as well as the equipment hardware specifi-

cations used. Initial path loss results for unique pointing angles are shown. A significant system limitation of the equipment came from the lack of GPS synchronization between TX and RX, which led us to recreate absolute timing using 3-D ray-tracing.

Chapter 4 discussed fundamental processing procedures followed for recovering received power levels from the collected data in Brooklyn and Manhattan, and presented the methodology for synthesizing absolute time stamping using 3-D ray-tracing techniques.

Finally, Chapter 5 presented a channel modeling framework by distinguishing temporal and spatial components of the omnidirectional SSCM, and showed extracted channel statistics for both LOS and NLOS dense urban wideband channels. A detailed step procedure for generating new mmWave channel coefficients for dense urban environments was given, which provide joint temporal and spatial channel coefficients, that is, an angle of departure azimuth spectrum, an omnidirectional channel impulse reponse, and the corresponding angle of arrival azimuth spectrum that recreate the statistics of measured channels in both LOS and NLOS environments. When viewed as a statistical ensemble, the means of NLOS primary generated parameter statistics were reproduced to within 10% of the corresponding measured parameter statistics. It is noted here that additional measurement data is needed to enhance and complete the presented models here, especially for the LOS models which were extracted from only four measurement locations.

As mentioned throughout this thesis, the lack of GPS synchronization between TX and RX induced us to synthesize absolute timing using 3-D ray-tracing, which was shown to predict the strongest angle of departures and angle of arrivals at the measured RX locations, while weaker angles (angles with weak received power) could not be reproduced. The measurements collected at weaker angles could not be used in recovering omnidirectional PDPs, and these weaker angles represented a significant portion of the collected data. It is important to include the statistics of weakly received energy (attributed mainly to diffuse scattering phenomena) to accurately reflect mmWave channels. In the future, GPS synchronization using cesium standards will be implemented so as to measure absolute timing PDPs, from which omnidirectional PDPs will be recovered using all available measurements. Most notably, diffuse scattering statistics will be recovered, which will enhance the models presented here. The summer 2012 measurements investigated a sub-set of

elevation planes, $\pm 20^\circ$ about the horizon, and 0° (parallel to the horizon), and so elevation of departure and arrival statistics could not be extracted. Future measurements will investigate elevation angles in step increments of 10° (one antenna HPBW) so as to accurately model the elevation parameter. Additionally, polarization measurements were lacking and will be studied in future measurements.

Finally, the channel sounding hardware will be upgraded by removing all baseband analog components and replacing them with National Instruments FPGA-based hardware and software, so as to implement the PN sequence on the FPGA platform, allowing us to measure greater RF bandwidths, reducing the size and weight of the equipment, and allowing easier and swifter measurement acquisition in the future.

Appendices

Appendix A

Statistical Simulator MATLAB Code

```
%%%%%%%%%%%%%%%%%%%%%%%%%%%%%%%%%%%%%%%%%%%%%%%%%%%%%%%%%%%%%%%%%%%%%%%%%%%%%%%
%%%%%%%%%%%%%%%%% START WIDEBAND STATISTICAL SIMULATOR %%%%%%%%%%%%%%%%%%%%%%%%
%%%%%%%%%%%%%%%%%%%%%%%%%%%%%%%%%%%%%%%%%%%%%%%%%%%%%%%%%%%%%%%%%%%%%%%%%%%%%%%


%%% Step 1: Generate T-R Separation distance (m) ranging from 30 - 200 m
%%% depending on the environment type. Also, if environment type is not
%%% specified, generate a T-R Separation distance between 30 and 200 m, and
%%% then use the LOS/NLOS probabilities to determine the environment type.
if strcmp(envType,'LOS')
    dmin = 30; dmax = 100;
elseif strcmp(envType,'NLOS')
    dmin = 60; dmax = 200;
else
end
TRDistance = getTRSep(dmin,dmax);

%%% Step 1 bis: use LOS/NLOS probabilities based on WINNER II LOS probability to
%%% determine LOS or NLOS environment based on T-R Separation
```

```
% dmin = 30;dmax = 200;
% [TRDistance envType] = getTRSep_envType(dmin,dmax);


%%% Step 2: Generate the total received omnidirectional power (mW) using
%%% path loss exponent n, and shadowing factor (SF) sigma in dB
if strcmp(envType,'LOS')
    n = 2.0; SF = 3.6;
elseif strcmp(envType,'NLOS')
    n = 3.4; SF = 9.7;
else
end
TXpower = 30; %% dBm
d0 = 1; %% free space reference distance
Pr_Lin = getRXPower(TRDistance,n,SF,TXpower,d0);

%%% Step 3: Generate the number of time clusters N, and number of AOD and
%%% AOA spatial lobes
if strcmp(envType,'LOS')
    meanClusters = 4.1;
    meanAOALobes = 2.9;
    meanAODLobes = 2.8;
    [numberOfClusters,numberOfAOALobes,numberOfAODLobes] = ...
        getClusters_AOA_AOD_LOS(meanClusters,meanAOALobes,meanAODLobes);
elseif strcmp(envType,'NLOS')
    meanClusters = 3.4;
    meanAOALobes = 2.4;
    meanAODLobes = 2;
    [numberOfClusters,numberOfAOALobes,numberOfAODLobes] = ...
        getClusters_AOA_AOD_NLOS(meanClusters,meanAOALobes,meanAODLobes);
else
end
```

```
53
54 %%% Step 4: Generate the number of cluster subpaths M_n in each time
55 %%% cluster
56 if strcmp(envType,'LOS')
57     meanNumberOfClusterSubPaths = 2;
58 elseif strcmp(envType,'NLOS')
59     meanNumberOfClusterSubPaths = 2.1;
60 else
61 end
62 numberOfClusterSubPaths = getNumberOfClusterSubPaths(...
63     meanNumberOfClusterSubPaths,numberOfClusters);
64
65 %%% Step 5: Generate the number of intra-cluster subpath delays rho_mn (ns)
66 rho_mn = getIntraClusterDelays(numberOfClusterSubPaths);
67
68 %%% Step 6: Generate the cluster excess time delays tau_n (ns)
69 if strcmp(envType,'LOS')
70     meanClusterExcessTimeDelay = 162;
71 elseif strcmp(envType,'NLOS')
72     meanClusterExcessTimeDelay = 67;
73 else
74 end
75 tau_n = getClusterExcessTimeDelays(meanClusterExcessTimeDelay,...
76     numberOfClusters,rho_mn,envType);
77
78 %%% Step 7: Generate temporal cluster powers (mW)
79 if strcmp(envType,'LOS')
80     alphaCluster = 0.738; betaCluster = 19.3; muCluster = 0.4; sigmaCluster = 9.5;
81 elseif strcmp(envType,'NLOS')
82     alphaCluster = 0.613; betaCluster = 31.4; muCluster = -2.1; sigmaCluster = 9.4;
83 else
84 end
```

```
85  clusterPowers_Lin = getClusterPowers(tau_n,Pr_Lin,alphaCluster,betaCluster,muCluster,...
        sigmaCluster,envType);
86
87  %%% Step 8: Generate the cluster subpath powers (mW)
88  if strcmp(envType,'LOS')
89      alphaSubPath = 1; betaSubPath = 6.78; muSubPath = 0.8; sigmaSubPath = 5.1;
90  elseif strcmp(envType,'NLOS')
91      alphaSubPath = 0.966; betaSubPath = 6.63; muSubPath = -0.8; sigmaSubPath = 5.1;
92  else
93  end
94  subPathPowers_Lin = getSubPathPowers(rho_mn,clusterPowers_Lin,alphaSubPath,betaSubPath,...
        muSubPath,sigmaSubPath);
95
96  %%% Step 9: Recover absolute propagation times t_mn (ns) of each subpath
97  %%% component
98  t_mn = getAbsolutePropTimes(TRDistance,tau_n,rho_mn);
99
100 %%% Step 10: Generate the AOA and AOD mean lobe angles
101 lobeAOA = getLobeMeanPointingAngles(numberOfAOALobes);
102 lobeAOD = getLobeMeanPointingAngles(numberOfAODLobes);
103
104 %%% Step 11: Assign maximum temporal cluster powers to AOA and AOD lobe
105 %%% angles
106 AOAlobeMaxPower_Lin = getLobeMaxPowers(lobeAOA,clusterPowers_Lin,envType);
107 AODlobeMaxPower_Lin = getLobeMaxPowers(lobeAOD,clusterPowers_Lin,envType);
108
109 %%% Step 12: Generate the number of lobe angular segments
110 if strcmp(envType,'LOS')
111     meanAOAAngularSpread = 39.9+1;sigmaAOAAngularSpread = 31.4;
112     meanAODAngularSpread = 27.3+6; sigmaAODAngularSpread = 13.5;
113 elseif strcmp(envType,'NLOS')
114     meanAOAAngularSpread = 34.8+5; sigmaAOAAngularSpread = 25.7;
115     meanAODAngularSpread = 42.5+7.5; sigmaAODAngularSpread = 25.2-5.2;
```

```
116 else
117 end
118 %%% for AOA lobe
119 numberOfAOAAngularSegments = getNumberOfAngularSegments_AOA(...
120     meanAOAAngularSpread,sigmaAOAAngularSpread,numberOfAOALobes,envType);
121
122 %%% for AOD lobe
123 numberOfAODAngularSegments = getNumberOfAngularSegments_AOD(...
124     meanAODAngularSpread,sigmaAODAngularSpread,numberOfAODLobes,envType);
125
126 %%% Step 13: Generate the lobe segment azimuth angles for the AOA and AOD
127 %%% lobes
128 AOAlobeAngles = getLobeAngles(numberOfAOAAngularSegments,lobeAOA);
129 AODlobeAngles = getLobeAngles(numberOfAODAngularSegments,lobeAOD);
130
131 %%% Step 14: Generate the AOA and AOD lobe angular segment powers (mW)
132 if strcmp(envType,'LOS')
133     sigmaAOA = 22.5*.55;
134     sigmaAOD = 10.5*.1;
135     margin = 10;
136 elseif strcmp(envType,'NLOS')
137     sigmaAOA = 15.5*.7;
138     sigmaAOD = 11.5*.3;
139     margin = 20;
140 else
141 end
142
143 %%% For AOA lobe
144 AOAlobeAngularPowers = getLobePowers(lobeAOA,AOAlobeMaxPower_Lin,...
145     AOAlobeAngles,sigmaAOA,margin);
146
147 %%% For AOD lobe
148 AODlobeAngularPowers = getLobePowers(lobeAOD,AODlobeMaxPower_Lin,...
```

```
149      AODlobeAngles,sigmaAOD,margin);
150
151  %%%%%%%%%%%%%%%%%%%%%%%%%%%%%%%%%%%%%%%%%%%%%%%%%%%%%%%%%%%%%%%%%%%%%%%%%%%%
152  %%%%%%%%%%%%%%%%% END WIDEBAND STATISTICAL SIMULATOR %%%%%%%%%%%%%%%%%%%%%%%%
153  %%%%%%%%%%%%%%%%%%%%%%%%%%%%%%%%%%%%%%%%%%%%%%%%%%%%%%%%%%%%%%%%%%%%%%%%%%%%
```

```
1  function dist = getTRSep(dmin,dmax)
2  %%% Step 1
3
4  %%% Generates a uniform random variable distributed between dmin and dmax
5
6  dist = dmin + (dmax-dmin).*rand;
7
8  end
```

```
1  function [TRDistance envType] = getTRSep_envType(dmin,dmax)
2
3  %%% Step 1 bis:
4
5  %%% Generate a distance between 30 and 200 m
6  TRDistance = getTRSep(dmin,dmax);
7
8  %%% Estimate the LOS probability using the WINNER II LOS probability
9  %%% formula
10 P_LOS = min(18/TRDistance, 1)*(1-exp(-TRDistance/36)+exp(-TRDistance/36));
11
12 %%% Generate an instance of a uniform random variable between 0 and 1
13 X = rand;
14
15 %%% Depending on the value of X, assign LOS or NLOS environmnent
```

```
if X≤P_LOS
    envType = 'LOS';
elseif X>P_LOS
    envType = 'NLOS';
else
end


end
```

```
function Pr_Lin = getRXPower(dist,n,sigma,TXpower,d0)

%%% Step 2:

%%% combined TX-RX antenna gains (dB) - this is user-defined
AntGain = 49;

%%% constants
c = 3e8; %% speed of light (m/s)
f = 28e9; %% carrier frequency (Hz)
lambda = c/f; %% wavelength (m)

%%% free space path loss at d0 (dB)
PLref = 20*log10(4*pi*d0/lambda);

%%% absolute path loss at distance dist
PL = PLref + n*10*log10(dist/d0)+sigma*randn;

%%% total received power (dBm) at distance dist
Pr_dB = TXpower + AntGain - PL;

```

```
%%% total received omnidirectional power in mW
Pr_Lin = 10^(Pr_dB/10);

end
```

```
function [numberOfClusters,numberOfAOALobes,numberOfAODLobes] = getClusters_AOA_AOD_LOS(...
    lambda_cluster,lambda_aoa,lambda_aod)

    %%% Step 3: (LOS)


    %%% See Chapter 5, the procedure for generating number of time
    %%% clusters, the number of AOD and AOA spatial lobes in LOS
    %%% environments

    cluster_instance = round(exprnd(lambda_cluster))+1;
    aoa_instance = round(exprnd(lambda_aoa+1));
    aod_instance = poissrnd(lambda_aod+1);


    if cluster_instance ≥ 11

        x=rand;

        if x>.75

            cluster_instance =1;
        else
            cluster_instance = 2;
        end

```

```
26
27      else
28      end
29
30      if cluster_instance ==1
31
32          y = rand;
33
34          if y>.5
35              cluster_instance = 1;
36          else
37              cluster_instance = round(6*rand)+1;
38          end
39      else
40      end
41
42      if aoa_instance > cluster_instance
43          aoa_instance = cluster_instance;
44      else
45      end
46
47      if aoa_instance ≥ 7
48          aoa_instance = 2;
49      else
50      end
51
52      if aoa_instance == 1
53
54          x = rand;
55
56          if x<.33
57              aoa_instance = 4;
58          elseif x≥ .67
```

```
59              aoa_instance = 5;
60          else
61          end
62
63      else
64      end
65
66      if aod_instance > cluster_instance
67          aod_instance = cluster_instance;
68      else
69      end
70
71      if aod_instance ≥ 5
72
73          x = rand;
74
75          if x<.5
76              aod_instance = 1;
77          elseif x≥.5
78              aod_instance = 4;
79          else
80          end
81
82
83      else
84      end
85
86      if aod_instance == 2
87          aod_instance = 3;
88      else
89      end
90
91
```

```
92      numberOfClusters = max(1,cluster_instance);
93      numberOfAOALobes = max(1,aoa_instance);
94      numberOfAODLobes = max(1,aod_instance);
95
96  end
```

```
1   function [numberOfClusters,numberOfAOALobes,numberOfAODLobes] = getClusters_AOA_AOD_NLOS(...
        lambda_cluster,lambda_aoa,lambda_aod)
2
3       %%% Step 3: (NLOS)
4
5       %%% See Chapter 5, the procedure for generating number of time
6       %%% clusters, the number of AOD and AOA spatial lobes in NLOS
7       %%% environments
8
9       cluster_instance = poissrnd(lambda_cluster-.5);
10      aoa_instance = poissrnd(lambda_aoa+1.5);
11      aod_instance = poissrnd(lambda_aod+2);
12
13      if cluster_instance == 1
14
15          y = rand;
16
17          if y>.8
18
19              cluster_instance = 8;
20
21          else
22          end
23
24
```

```
25      else
26      end
27
28
29      if cluster_instance == 3
30
31            y = rand;
32
33          if y>.85
34
35              cluster_instance = 9;
36
37          else
38          end
39
40
41      else
42      end
43
44      if cluster_instance ≥ 10
45          cluster_instance = 7;
46      else
47      end
48
49
50
51      if aoa_instance > cluster_instance
52          aoa_instance = cluster_instance;
53
54          if aoa_instance ≥ 7
55
56              aoa_instance = 5;
57
```

```
58          else
59          end
60      else
61      end
62
63
64      if aoa_instance ≥ 7
65
66          aoa_instance = 5;
67
68      else
69      end
70
71      if aoa_instance == 3
72
73          x = rand;
74
75          if x<.2
76              aoa_instance = 1;
77          else
78          end
79
80      else
81      end
82
83
84
85      if aod_instance > cluster_instance
86          aod_instance = cluster_instance;
87
88          if aod_instance ≥ 6
89              aod_instance = 5;
90          else
```

```
91          end
92
93      else
94      end
95
96      if aod_instance ≥ 6
97          aod_instance = 5;
98      else
99      end
100
101     if aod_instance == 4
102         aod_instance = 1;
103     else
104     end
105
106     if aod_instance == 3
107
108         x = rand;
109
110         if x<.25
111             aod_instance = 1;
112         else
113         end
114
115     else
116     end
117
118
119     numberOfClusters = max(1,cluster_instance);
120     numberOfAOALobes = max(1,aoa_instance);
121     numberOfAODLobes = max(1,aod_instance);
122
123
```

```
124 end
```

```
1  function numberOfClusterSubPaths = getNumberOfClusterSubPaths(meanNumberOfClusterSubPaths,...
       numberOfClusters)
2
3      %%% Step 4:
4
5      %%% See Chapter 5, the procedure for generating the number of cluster
6      %%% subpaths.
7
8      %%% No difference between LOS and NLOS
9
10
11     %%% initialize array containing the number of cluster subpath in each time
12     %%% cluster
13     numberOfClusterSubPaths = zeros(numberOfClusters,1);
14
15     %%% for loop generates N numbers
16     for index=1:numberOfClusters
17
18         %%% generate an instance
19         a = round(exprnd(meanNumberOfClusterSubPaths));
20
21         %%% if greater than 10, set to 1
22         if a≥10
23             a = 1;
24         else
25         end
26
27         %%% the max() operation is to avoid instances = 0
28         numberOfClusterSubPaths(index) = max(a,1);
```

```
29
30      end
31
32
33
34  end
```

```
1   function rho_mn = getIntraClusterDelays(numberOfClusterSubPaths)
2
3       %%% Step 5: (both LOS and NLOS)
4
5       %%% initialize the structure that will contain the intra cluster delays
6       rho_mn = struct;
7
8       %%% number of clusters
9       numberOfClusters = size(numberOfClusterSubPaths,1);
10
11      %%% for loop iterates N times for each cluster
12      for clusterIndex=1:numberOfClusters
13
14          %%% number of sub-paths in current cluster
15          numberOfComponents = numberOfClusterSubPaths(clusterIndex);
16
17          %%% generate a set of component delays
18          arrayTemp = 5*(1:numberOfComponents);
19
20          %%% field name
21          str = ['c',num2str(clusterIndex)];
22
23          %%% store the components
24          rho_mn.(str) = sort(arrayTemp - min(arrayTemp));
```

```
25
26
27      end
28
29  end
```

```
1   function tau_n = getClusterExcessTimeDelays(meanClusterExcessTimeDelay,numberOfClusters,...
        rho_mn,envType)
2
3   %%% Step 6
4
5   %%% See Chapter 5, the procedure for generating cluster excess time delays
6
7   if strcmp(envType,'NLOS')==true
8       %%% delay proportionality constant
9       r_scaling = 0.25;
10
11      %%% initialize cluster delays
12      tau_n = zeros(1,numberOfClusters);
13
14      %%%% generate cluster delays as exponential
15      tau_n_prime = exprnd(r_scaling*meanClusterExcessTimeDelay,[1 numberOfClusters]);
16
17      %%% normalize
18      tau_n_double_prime = sort(tau_n_prime - min(tau_n_prime));
19
20      temp = rho_mn.c1(end);
21      %%% this for loop starts at the 2nd cluster index because the first
22      %%% cluster index is always 0
23      for clusterIndex = 2:numberOfClusters
24
```

```
25          %%% add the last cluster sub-path delay of the previous cluster to
26          %%% the current cluster delay for no overlap in multipath
27          %%% components. the 10 ns arises from 2*2.5+2.7. Additional 2.3 ns
28          %%% for extra margin
29          tau_n(clusterIndex) = tau_n_double_prime(clusterIndex)+temp+10;
30
31          %%% cluster sub-path delays of the previous cluster
32          rho_m = rho_mn.(['c',num2str(clusterIndex)]);
33
34          %%% keep track of the last intra-cluster delay
35          temp = tau_n(clusterIndex)+rho_m(end);
36
37      end
38
39  elseif strcmp(envType,'LOS')==true
40      %%% delay proportionality constant
41      r_scaling = .41;
42
43      %%% initialize cluster delays
44      tau_n = zeros(1,numberOfClusters);
45
46      %%%% generate cluster delays as exponential
47      tau_n_prime = sort(exprnd(r_scaling*meanClusterExcessTimeDelay,[1 numberOfClusters]));
48
49      tau_n_double_prime = tau_n_prime - min(tau_n_prime);
50
51      for clusterIndex = 1:numberOfClusters
52
53          tau_temp = tau_n_double_prime(clusterIndex);
54
55          %%% truncate at 1800 ns
56          tau_n_double_prime(clusterIndex) = min(tau_temp,800);
57      end
```

```
58
59      temp = rho_mn.c1(end);
60      %%% this for loop starts at the 2nd cluster index because the first
61      %%% cluster index is always 0
62      for clusterIndex = 2:numberOfClusters
63
64          %%% add the last cluster sub-path delay of the previous cluster to
65          %%% the current cluster delay for no overlap in multipath
66          %%% components. the 10 ns arises from 2*2.5+2.7. Additional 2.3 ns
67          %%% for extra margin
68          tau_n(clusterIndex) = min(tau_n_double_prime(clusterIndex)+temp+10,800);
69
70          %%% cluster sub-path delays of the previous cluster
71          rho_m = rho_mn.(['c',num2str(clusterIndex)]);
72
73          %%% keep track of the last intra-cluster delay
74          temp = tau_n(clusterIndex)+rho_m(end);
75
76      end
77
78
79
80  else
81  end
82
83
84
85  end
```

```
function clusterPowers_Lin = getClusterPowers(tau_n,Pr_Lin,alpha,beta,mu,sigma,envType)


%%% Step 7: (both LOS and NLOS)

%%% number of clusters
numberOfClusters = size(tau_n,2);

%%% minimum cluster power level: -100 dBm
minClusterPower_dB = -100;

%%%% per cluster shadowing
Z = mu+sigma*randn([1 numberOfClusters]);

if strcmp(envType,'LOS')


    %%% cluster ratios
    clusterPowerRatios = alpha*exp(-tau_n/(2.5*beta)).*10.^(Z/10);


elseif strcmp(envType,'NLOS')


    %%% cluster ratios
    clusterPowerRatios = alpha*exp(-tau_n/beta).*10.^(Z/10);


else
end

```

```
%%% normalize cluster ratios such that their sum equals 1
clusterPowerRatios = clusterPowerRatios/sum(clusterPowerRatios);

%%% multiply the ratios by the total received power (in linear units)
clusterPowers_Lin = Pr_Lin*clusterPowerRatios;

%%% elements whose powers are greater than -100 dBm
indGreaterThanMinClusterPower = 10*log10(clusterPowers_Lin)<minClusterPower_dB;

%%% assign elements whose power levels are less than -100 dBm, the value of
%%% -100 dBm
clusterPowers_Lin(indGreaterThanMinClusterPower) = 10^(minClusterPower_dB/10);

end
```

```
function subPathPowers_Lin = getSubPathPowers(rho_mn,clusterPowers_Lin,alphaSubPath,...
    betaSubPath,muSubPath,sigmaSubPath)

%%% Step 8: (both LOS and NLOS)

%%% number of clusters
numberOfClusters = size(clusterPowers_Lin,2);

%%% initialize the structure that will contain component powers
subPathPowers_Lin = struct;

%%% minimimum detectable signal
minThreshold_dB = -105;

for clusterIndex = 1:numberOfClusters

```

```
16      %%% current intra-cluster delays
17      rho = rho_mn.(['c',num2str(clusterIndex)]);
18
19      %%% number of components in current cluster
20      numberOfComponents = size(rho,1);
21
22      %%% per sub path shadowing
23      U = muSubPath+sigmaSubPath*randn([1 numberOfComponents]);
24
25      %%% generate sub path ratios
26      subPathRatios = alphaSubPath*exp(-rho/betaSubPath).*10.^(U/10);
27
28      %%% normalize ratios
29      subPathRatios = subPathRatios/sum(subPathRatios);
30
31      %%% current cluster power
32      clusterPower =  clusterPowers_Lin(clusterIndex);
33
34      %%% store current power levels
35      powerTemp = clusterPower*subPathRatios;
36
37      %%% elements whose powers are less than -105 dBm
38      indSmallerThan100 =10*log10(powerTemp)<minThreshold_dB;
39
40      %%% see those elements to the threshold of -105 dBm
41      powerTemp(indSmallerThan100) = 10^(minThreshold_dB/10);
42
43      %%% store sub path powers
44      subPathPowers_Lin.(['c',num2str(clusterIndex)])=powerTemp;
45
46
47
48  end
```

```
49
50
51  end
```

```
function t_mn = getAbsolutePropTimes(dist,tau_n,rho_mn)

    %%% Step 9: (both LOS and NLOS)

    %%% initialize structure that will contain propagatin times
    t_mn = struct;

    %%% number of clusters
    numberOfClusters = size(tau_n,2);

    %%% speed of light (m/s)
    c = 3e8;

    %%% absolute propagation time of first arrival in ns
    t0 = dist/c*1e9;

    for clusterIndex = 1:numberOfClusters

        %%% cluster excess delay
        tau = tau_n(clusterIndex);

        %%% intra cluster excess delays
        rho = rho_mn.(['c',num2str(clusterIndex)]);

        %%% recover absolute propagation times of arrival
        t_mn.(['c',num2str(clusterIndex)]) = t0+tau+rho;

    end


end
```

```
function meanLobePointingAngles = getLobeMeanPointingAngles(numberOfLobes)


    %%% Step 10:


    %%% define lobe indices
    lobeIndex = 1:numberOfLobes;


    %%% discretize the azimuth plane in the same number of lobes
    theta_min = 360*(lobeIndex-1)/numberOfLobes;
    theta_max =  360*lobeIndex/numberOfLobes;


    %%% initialize the mean lobe angles to 0
    meanLobePointingAngles = zeros(numberOfLobes,1);


    %%% generate a mean lobe angle that is uniformly random in each section of the
    %%% azimuth plane, and find the close neighbor to 10.
    for lobeIndex=1:numberOfLobes


        %%% generate the random angle
        angle = theta_min(lobeIndex)+(theta_max(lobeIndex)-theta_min(lobeIndex))*rand;


        %%% store the angle
        meanLobePointingAngles(lobeIndex) = roundn(angle,1);
    end


end
```

```
function lobeMaxPower_Lin = getLobeMaxPowers(lobeAOA,clusterPowers_Lin,envType)

%%% Step 11:

%%% initialize the lobe max powers
lobeMaxPower_Lin = zeros(size(lobeAOA));

numberOfLobes = size(lobeAOA,1);
numberOfClusters = size(clusterPowers_Lin,2);

%%% lobe indices
lobeIndices = 1:numberOfLobes;

%%% sort the cluster powers for easier assignment
clusterPowers_Lin_Sorted = sort(clusterPowers_Lin);

%%% assign the L strongest clusters to the L lobes
lobeMaxPower_Lin(lobeIndices) = clusterPowers_Lin_Sorted(lobeIndices);

%%% clusters that have not yet been assigned
remainingClusterPowers = clusterPowers_Lin_Sorted((numberOfLobes+1):end);

%%% if there are remaining clusters, then do this if statement
if numberOfClusters ≠ numberOfLobes

    %%% number of remaining clusters to assign
    J = numberOfClusters - numberOfLobes;

    for jIndex = 1:J

        %%% generate a random index ranging from 1 to numberOfLobes
        remainingClusterIndex = 1+(numberOfLobes-1)*round(rand);
```

```
33
34          %%% add the remaining cluster to the current lobe
35          lobeMaxPower_Lin(remainingClusterIndex) = lobeMaxPower_Lin(remainingClusterIndex) +...
                remainingClusterPowers(jIndex);
36
37      end
38
39  else
40  end
41
42  %%% define the threshold margin depending on the environment type
43  if strcmp(envType,'LOS')
44      margin = 10;
45  elseif strcmp(envType,'NLOS')
46      margin = 20;
47  else
48  end
49
50  %%% find the power threshold (dB)
51  polarThreshold = 10*log10(max(lobeMaxPower_Lin)) - margin;
52
53  %%% find the elements whose powers are below the threshold
54  indLess = find(10*log10(lobeMaxPower_Lin)<polarThreshold);
55
56  %%% set powers below threshold to 5 dB above threshold power
57  if ~isempty(indLess)
58      lobeMaxPower_Lin(indLess) = 10^((polarThreshold+5)/10);
59  else
60  end
61
62
63  end
```

```
function numberOfAngularSegments = getNumberOfAngularSegments_AOA(meanAngularSpread,...
    sigmaAngularSpread,numberOfLobes,envType)

%%% Step 12: (for both LOS and NLOS)

if strcmp(envType,'NLOS')==true

    numberOfAngularSegments = zeros([1 numberOfLobes]);
    for index = 1:numberOfLobes

        LAS = roundn(meanAngularSpread+sigmaAngularSpread*randn,1);
        numberOfAngularSegments_temp = max(LAS,10);
        numberOfAngularSegments(index) = min(numberOfAngularSegments_temp,90)/10;

    end

elseif strcmp(envType,'LOS')==true

    numberOfAngularSegments = zeros([1 numberOfLobes]);
    for index = 1:numberOfLobes

        LAS = roundn(meanAngularSpread+sigmaAngularSpread*randn,1);
        numberOfAngularSegments_temp = max(LAS,10);
        numberOfAngularSegments(index) = min(numberOfAngularSegments_temp,140)/10;

    end
else
end
end
```

```
function numberOfAngularSegments = getNumberOfAngularSegments_AOD(meanAngularSpread,...
    sigmaAngularSpread,numberOfLobes,envType)

if strcmp(envType,'NLOS')==true

    numberOfAngularSegments = zeros([1 numberOfLobes]);
    for index = 1:numberOfLobes

        LAS = roundn(meanAngularSpread+sigmaAngularSpread*randn,1);
        numberOfAngularSegments_temp = max(LAS,10);
        numberOfAngularSegments(index) = min(numberOfAngularSegments_temp,80)/10;

    end


elseif strcmp(envType,'LOS')==true

    numberOfAngularSegments = zeros([1 numberOfLobes]);
    for index = 1:numberOfLobes

        LAS = roundn(meanAngularSpread+sigmaAngularSpread*randn,1);
        numberOfAngularSegments_temp = max(LAS,10);
        numberOfAngularSegments(index) = min(numberOfAngularSegments_temp,60)/10;

    end
else
end
end
```

```
function lobeAngles = getLobeAngles(numberOfAngularSegments,lobeAOA)

%%% Step 13: (for LOS and NLOS)

%%% number of lobes
numberOfLobes = length(lobeAOA);

%%% initialize structure that will contain the lobe angles
lobeAngles = struct;

for lobeIndex = 1:numberOfLobes

    %%% number of angular segments
    numberOfSegments = numberOfAngularSegments(lobeIndex);

    %%% current lobe AOA
    AOA = lobeAOA(lobeIndex);

    if mod(numberOfSegments,2) == 1 %% odd

        %%% indices about the main angle
        k_min = -(numberOfSegments-1)/2; k_max = (numberOfSegments-1)/2;

    elseif mod(numberOfSegments,2) == 0 %% even

        X = rand;

        if X<.5
            x = 0;
            y = 1-x;
        elseif X>=.5
            x = 1;
```

```
33              y = 1-x;
34          else
35          end
36
37
38          %%% indices about the main angle
39          k_min = -numberOfSegments/2+y; k_max = numberOfSegments/2-x;
40
41
42
43
44      else
45      end
46
47      %%% store lobe angles
48      lobeAngles.(['L',num2str(lobeIndex)]) = AOA + 10*(k_min:k_max);
49
50  end
51
52  end
```

```
1   function lobeAngularPowers = getLobePowers(lobeAngle,lobeMaxPower_Lin,s,sigma,margin)
2
3   %%% Step 14
4
5   %%% number of lobes
6   numberOfLobes = length(lobeAngle);
7
8   lobePowers = struct;
9
10  maxSegmentPower = -100; %% dBm
```

```
11
12 for lobeIndex =1:numberOfLobes
13
14     %%% lobe AOA
15     AOA = lobeAngle(lobeIndex);
16
17     %%% max power in the lobe
18     P0 = lobeMaxPower_Lin(lobeIndex);
19
20     %%% lobe angles
21     currents = s.(['L',num2str(lobeIndex)]);
22
23     %%% number of segments in the lobe
24     numberOfSegments = size(currents,2);
25
26     %%% deviations from AOA
27     lobePowers_Temp = zeros(numberOfSegments,1);
28
29     %%% find segment powers
30     for segmentIndex = 1:numberOfSegments
31
32         %%% current lobe angle
33         currentAngle = currents(segmentIndex);
34
35         %%% deviation away from AOA
36         ΔTheta = abs(AOA - currentAngle);
37
38         %%% Lobe segment shadowing
39         Z = 6*randn;
40
41         %%% If directly on boresight of lobe, the ratio is 1
42         if ΔTheta == 0
43
```

```
44              lobeRatio = 1;
45
46          elseif ΔTheta ≠ 0 %%% away from lobe boresight
47
48              %%% lobe segment ratio
49              lobeRatio = exp(-ΔTheta^2/(2*sigma^2))*10^(Z/10);
50
51          else
52          end
53
54          %%% lobe segment power
55          lobePowers_Temp(segmentIndex) = P0*lobeRatio;
56
57      end%%% end of segmentIndex for loop
58
59      max_temp = max(10*log10(lobePowers_Temp));
60
61      if max_temp > maxSegmentPower
62          maxSegmentPower = max_temp;
63      else
64      end
65
66      %%% store all lobe powers
67      lobePowers.(['L',num2str(lobeIndex)]) = lobePowers_Temp;
68
69  end%%% end of lobeIndex for loop
70
71  threshold_dB = maxSegmentPower - margin;
72
73  for lobeIndex = 1:numberOfLobes
74
75      power_temp = lobePowers.(['L',num2str(lobeIndex)]);
76
```

```
77      indLower = 10*log10(power_temp)<threshold_dB;
78
79      power_temp(indLower) = 10^((threshold_dB+1)/10);
80
81      lobePowers.(['L',num2str(lobeIndex)]) = power_temp;
82
83
84  end
85
86
87  %%% assign output of this function
88  lobeAngularPowers = lobePowers;
89  end
```

Bibliography

[1] Nokia Solutions and Networks, "2020: Beyond 4G: Radio Evaluation for the Gigabit Experience," 2011.

[2] Wikipedia. Radio spectrum. [Online]. Available: //en.wikipedia.org/wiki/Radio_spectrum#IEEE_US

[3] K. Allen, R. Ott, E. Violette, and R. Espeland, "Height-gain study for 23 km links at 9.6, 11.4, and 28.8 Ghz," *Antennas and Propagation, IEEE Transactions on*, vol. 30, no. 4, pp. 734–740, Jul 1982.

[4] E. Violette, R. Espeland, R. DeBolt, and F. Schwering, "Millimeter-wave propagation at street level in an urban environment," *Geoscience and Remote Sensing, IEEE Transactions on*, vol. 26, no. 3, pp. 368–380, May 1988.

[5] F. Schwering, E. Violette, and R. Espeland, "Millimeter-wave propagation in vegetation: experiments and theory," *Geoscience and Remote Sensing, IEEE Transactions on*, vol. 26, no. 3, pp. 355–367, May 1988.

[6] G. Vannucci and R. Roman, "Measurement results on indoor radio frequency re-use at 900 mhz and 18-ghz," in *Personal, Indoor and Mobile Radio Communications, 1992. Proceedings, PIMRC '92., Third IEEE International Symposium on*, Oct 1992, pp. 308–314.

[7] H. Droste and G. Kadel, "Measurement and analysis of wide band indoor propagation characteristics at 17 ghz and 60 ghz," in *Antennas and Propagation, 1995., Ninth International Conference on (Conf. Publ. No. 407)*, vol. 2, Apr 1995, pp. 288–291 vol.2.

[8] Y.-P. Zhang and Y. Hwang, "Measurements of the characteristics of indoor penetration loss," in *Vehicular Technology Conference, 1994 IEEE 44th*, Jun 1994, pp. 1741–1744 vol.3.

[9] G. Kalivas, M. El-Tanany, and S. Mahmoud, "Millimeter-wave channel measurements with space diversity for indoor wireless communications," *Vehicular Technology, IEEE Transactions on*, vol. 44, no. 3, pp. 494–505, Aug 1995.

[10] N. Moraitis and P. Constantinou, "Propagation study in urban environment at 25 and 40 ghz," in *Vehicular Technology Conference, 2001. VTC 2001 Spring. IEEE VTS 53rd*, vol. 1, 2001, pp. 298–302 vol.1.

[11] PN.837-1, ITU-R Recommendation, International Telecommunication Union, "Characteristics of precipitation for propagation modeling," 1997.

[12] P.676, ITU-R Recommendation, International Telecommunication Union, "Attenuation by atmospheric gases," 1997.

[13] A. Elrefaie and M. Shakouri, "Propagation measurements at 28 ghz for coverage evaluation of local multipoint distribution service," in *Wireless Communications Conference, 1997., Proceedings*, Aug 1997, pp. 12–17.

[14] S. Seidel, "Radio propagation and planning at 28 ghz for local multipoint distribution service (lmds)," in *Antennas and Propagation Society International Symposium, 1998. IEEE*, vol. 2, June 1998, pp. 622–625 vol.2.

[15] K. V. Ravi and P. Soma, "Modeling of local multipoint distribution service (lmds) channel at 27.4 ghz millimeterwave bands," in *Microwave Conference, 1999 Asia Pacific*, vol. 3, 1999, pp. 702–705 vol.3.

[16] ——, "Analysis and modeling of local multipoint distribution service (lmds) channel," in *Global Telecommunications Conference, 1999. GLOBECOM '99*, vol. 1B, 1999, pp. 873–877 vol. 1b.

[17] C. Briso-Rodriguez, M. Vazquez-Castro, and J. Alonso-Montes, "28 ghz lmds channel measurements and modeling for parameterized urban environments," in *Microwave Symposium Digest, 2001 IEEE MTT-S International*, vol. 3, May 2001, pp. 2207–2210 vol.3.

[18] J. Murdock, E. Ben-Dor, Y. Qiao, J. Tamir, and T. Rappaport, "A 38 ghz cellular outage study for an urban outdoor campus environment," in *Wireless Communications and Networking Conference (WCNC), 2012 IEEE*, April 2012, pp. 3085–3090.

[19] T. Rappaport, E. Ben-Dor, J. Murdock, and Y. Qiao, "38 ghz and 60 ghz angle-dependent propagation for cellular amp; peer-to-peer wireless communications," in *Communications (ICC), 2012 IEEE International Conference on*, June 2012, pp. 4568–4573.

[20] T. Rappaport, F. Gutierrez, E. Ben-Dor, J. Murdock, Y. Qiao, and J. Tamir, "Broadband millimeter-wave propagation measurements and models using adaptive-beam antennas for outdoor urban cellular communications," *Antennas and Propagation, IEEE Transactions on*, vol. 61, no. 4, pp. 1850–1859, April 2013.

[21] P. Soma, Y. W. M. Chia, and L. Ong, "Modeling and analysis of time varying radio propagation channel for lmds," in *Radio and Wireless Conference, 2000. RAWCON 2000. 2000 IEEE*, 2000, pp. 115–118.

[22] E. Ben-Dor, T. Rappaport, Y. Qiao, and S. Lauffenburger, "Millimeter-wave 60 ghz outdoor and vehicle aoa propagation measurements using a broadband channel sounder," in *Global Telecommunications Conference (GLOBECOM 2011), 2011 IEEE*, Dec 2011, pp. 1–6.

[23] P. Tenerelli and C. Bostian, "Measurements of 28 ghz diffraction loss by building corners," in *Personal, Indoor and Mobile Radio Communications, 1998. The Ninth IEEE International Symposium on*, vol. 3, Sep 1998, pp. 1166–1169 vol.3.

[24] P. Papazian, G. A. Hufford, R. Achatz, and R. Hoffman, "Study of the local multipoint distribution service radio channel," *Broadcasting, IEEE Transactions on*, vol. 43, no. 2, pp. 175–184, Jun 1997.

[25] P. Papazian and Y. Lo, "Seasonal variability of a local multi-point distribution service radio channel," in *Radio and Wireless Conference, 1999. RAWCON 99. 1999 IEEE*, 1999, pp. 211–214.

[26] M. Chavero, V. Polo, F. Ramos, and J. Marti, "Impact of vegetation on the performance of 28 ghz lmds transmission," in *Microwave Symposium Digest, 1999 IEEE MTT-S International*, vol. 3, June 1999, pp. 1063–1066 vol.3.

[27] S. Perras and L. Bouchard, "Fading characteristics of rf signals due to foliage in frequency bands from 2 to 60 ghz," in *Wireless Personal Multimedia Communications, 2002. The 5th International Symposium on*, vol. 1, Oct 2002, pp. 267–271 vol.1.

[28] H. Xu, T. Rappaport, R. Boyle, and J. Schaffner, "Measurements and models for 38-ghz point-to-multipoint radiowave propagation," *Selected Areas in Communications, IEEE Journal on*, vol. 18, no. 3, pp. 310–321, March 2000.

[29] P. Soma, L. C. Ong, S. Sun, and M. Chia, "Propagation measurements and modeling of lmds radio channel in singapore," *Vehicular Technology, IEEE Transactions on*, vol. 52, no. 3, pp. 595–606, May 2003.

[30] H. Zhao, R. Mayzus, S. Sun, M. Samimi, J. Schulz, Y. Azar, K. Wang, G. Wong, F. Gutierrez, and T. Rappaport, "28 ghz millimeter wave cellular communication measurements for reflection and penetration loss in and around buildings in new york city," in *Communications (ICC), 2013 IEEE International Conference on*, June 2013, pp. 5163–5167.

[31] Y.-H. Kim, K.-S. Yang, and S.-H. Kim, "Scattering characteristics of surface roughness in frequency and incident angle dependent at millimeter-wave," in *Microwave Conference, 1999 Asia Pacific*, vol. 3, 1999, pp. 789–792 vol.3.

[32] C. Dillard, T. Gallagher, C. Bostian, and D. Sweeney, "Rough surface scattering from exterior walls at 28 ghz," *Antennas and Propagation, IEEE Transactions on*, vol. 52, no. 12, pp. 3173–3179, Dec 2004.

[33] ——, "28 ghz scattering by brick and limestone walls," in *Antennas and Propagation Society International Symposium, 2003. IEEE*, vol. 3, June 2003, pp. 1024–1027 vol.3.

[34] N. Hawkins, R. Steele, D. Rickard, and C. Shepherd, "Path loss characteristics of 60 ghz transmissions," *Electronics Letters*, vol. 21, no. 22, pp. 1054–1055, October 1985.

[35] R. Cole, H. Thomas, and G. Siqueira, "Two frequency coherence measurements on a 55ghz mobile radio link," *Electronic and Radio Engineers, Journal of the Institution of*, vol. 58, no. 6, pp. S140–S144, September 1988.

[36] G. Allen and A. Hammoudeh, "Frequency diversity propagation measurements for an indoor 60 ghz mobile radio link," in *Antennas and Propagation, 1991. ICAP 91., Seventh International Conference on (IEE)*, Apr 1991, pp. 298–301 vol.1.

[37] M. Bensebti, J. McGeehan, and M. Beach, "Indoor multipath radio propagation measurements and characterisation at 60 ghz," in *Microwave Conference, 1991. 21st European*, vol. 2, Sept 1991, pp. 1217–1222.

[38] P. Smulders and A. Wagemans, "Wideband indoor radio propagation measurements at 58 ghz," *Electronics Letters*, vol. 28, no. 13, pp. 1270–1272, June 1992.

[39] A. Plattner, N. Prediger, and W. Herzig, "Indoor and outdoor propagation measurements at 5 and 60 ghz for radio lan application," in *Microwave Symposium Digest, 1993., IEEE MTT-S International*, June 1993, pp. 853–856 vol.2.

[40] A. R. Tharek and J. McGeehan, "Propagation and bit error rate measurements within buildings in the millimeter wave band about 60 ghz," in *Electrotechnics, 1988. Conference Proceedings on Area Communication, EUROCON 88., 8th European Conference on*, Jun 1988, pp. 318–321.

[41] G. Allen and A. Hammoudeh, "60 ghz propagation measurements within a building," in *Microwave Conference, 1990. 20th European*, vol. 2, Sept 1990, pp. 1431–1436.

[42] H. Thomas, R. Cole, and G. Siqueira, "An experimental study of the propagation of 55 ghz millimeter waves in an urban mobile radio environment," *Vehicular Technology, IEEE Transactions on*, vol. 43, no. 1, pp. 140–146, Feb 1994.

[43] G. Lovnes, J. Reis, and R. Raekken, "Channel sounding measurements at 59 ghz in city streets," in *Personal, Indoor and Mobile Radio Communications, 1994. Wireless Networks - Catching the Mobile Future., 5th IEEE International Symposium on*, Sep 1994, pp. 496–500 vol.2.

[44] J. Kunisch, E. Zollinger, J. Pamp, and A. Winkelmann, "Median 60 ghz wideband indoor radio channel measurements and model," in *Vehicular Technology Conference, 1999. VTC 1999 - Fall. IEEE VTS 50th*, vol. 4, 1999, pp. 2393–2397 vol.4.

[45] D. Matic, H. Harada, and R. Prasad, "Indoor and outdoor frequency measurements for mm-waves in the range of 60 ghz," in *Vehicular Technology Conference, 1998. VTC 98. 48th IEEE*, vol. 1, May 1998, pp. 567–571 vol.1.

[46] A. Siamarou and M. Al-Nuaimi, "Wideband propagation measurements for future millimetre 60 ghz wireless lans," *Electronics Letters*, vol. 38, no. 16, pp. 918–920, Aug 2002.

[47] A. Siamarou, "Broadband wireless local-area networks at millimeter waves around 60 ghz," *Antennas and Propagation Magazine, IEEE*, vol. 45, no. 1, pp. 177–181, Feb 2003.

[48] S. Geng, J. Kivinen, and P. Vainikainen, "Propagation characterization of wideband indoor radio channels at 60 ghz," in *Microwave, Antenna, Propagation and EMC Technologies for Wireless Communications, 2005. MAPE 2005. IEEE International Symposium on*, vol. 1, Aug 2005, pp. 314–317 Vol. 1.

[49] S. Geng, J. Kivinen, X. Zhao, and P. Vainikainen, "Millimeter-wave propagation channel characterization for short-range wireless communications," *Vehicular Technology, IEEE Transactions on*, vol. 58, no. 1, pp. 3–13, Jan 2009.

[50] M. Peter, W. Keusgen, A. Kortke, and M. Schirrmacher, "Measurement and analysis of the 60 ghz in-vehicular broadband radio channel," in *Vehicular Technology Conference, 2007. VTC-2007 Fall. 2007 IEEE 66th*, Sept 2007, pp. 834–838.

[51] A. Maltsev, R. Maslennikov, A. Sevastyanov, A. Khoryaev, and A. Lomayev, "Experimental investigations of 60 ghz wlan systems in office environment," *Selected Areas in Communications, IEEE Journal on*, vol. 27, no. 8, pp. 1488–1499, October 2009.

[52] L. Correia and P. O. Frances, "A propagation model for the estimation of the average received power in an outdoor environment in the millimetre waveband," in *Vehicular Technology Conference, 1994 IEEE 44th*, Jun 1994, pp. 1785–1788 vol.3.

[53] G. R. MacCartney and T. S. Rappaport, "73 GHz millimeter wave propagation measurements for outdoor urban mobile and backhaul communications in new york city," in *International Conference on Communications (ICC), 2014 IEEE*, June 2014.

[54] S. Nie, G. R. MacCartney, S. Sun, and T. S. Rappaport, "28 Ghz and 73 Ghz signal outage study for millimeter wave cellular and backhaul communications," in *International Conference on Communications (ICC), 2014 IEEE*, June 2014.

[55] S. Nie, "Millimeter wave indoor propagation channel measurements and characterization at 73 ghz and coverage studies in dense urban environments," Master's thesis, May 2014.

[56] Z. Ghebrentensae, "Simulation of beacon-vehicle communications for drive applications," in *COST231, ReportTD(91)041*, Apr 1992.

[57] K. Gunmar, "Broadband technique for car to car communication at 60 ghz," in *COST231, ReportTD(91)041*, Jun 1991.

[58] C. Anderson and T. Rappaport, "In-building wideband partition loss measurements at 2.5 and 60 ghz," *Wireless Communications, IEEE Transactions on*, vol. 3, no. 3, pp. 922–928, May 2004.

[59] A. Alejos, M. Sanchez, and I. Cuinas, "Measurement and analysis of propagation mechanisms at 40 ghz: Viability of site shielding forced by obstacles," *Vehicular Technology, IEEE Transactions on*, vol. 57, no. 6, pp. 3369–3380, Nov 2008.

[60] T. Manabe, K. Sato, H. Masuzawa, K. Taira, T. Ihara, Y. Kasashima, and K. Yamaki, "Polarization dependence of multipath propagation and high-speed transmission characteristics of indoor millimeter-wave channel at 60 ghz," *Vehicular Technology, IEEE Transactions on*, vol. 44, no. 2, pp. 268–274, May 1995.

[61] T. Manabe, Y. Miura, and T. Ihara, "Effects of antenna directivity and polarization on indoor multipath propagation characteristics at 60 ghz," *Selected Areas in Communications, IEEE Journal on*, vol. 14, no. 3, pp. 441–448, Apr 1996.

[62] P. F. M. Smulders and A. Wagemans, "A statistical model for the mm-wave indoor radio channel," in *Personal, Indoor and Mobile Radio Communications, 1992. Proceedings, PIMRC '92., Third IEEE International Symposium on*, Oct 1992, pp. 303–307.

[63] C. R. 719-2, "Recommendations and reports of the ccir," in *ITU*, 1986.

[64] C. R. 721-2, "Recommendations and reports of the ccir," in *ITU*, 1986.

[65] B. Langen, G. Lober, and W. Herzig, "Reflection and transmission behaviour of building materials at 60 ghz," in *Personal, Indoor and Mobile Radio Communications, 1994. Wireless Networks - Catching the Mobile Future., 5th IEEE International Symposium on*, Sep 1994, pp. 505–509 vol.2.

[66] H. Xu, V. Kukshya, and T. Rappaport, "Spatial and temporal characteristics of 60-ghz indoor channels," *Selected Areas in Communications, IEEE Journal on*, vol. 20, no. 3, pp. 620–630, Apr 2002.

[67] N. Moraitis and P. Constantinou, "Indoor channel measurements and characterization at 60 ghz for wireless local area network applications," *Antennas and Propagation, IEEE Transactions on*, vol. 52, no. 12, pp. 3180–3189, Dec 2004.

[68] C. Anderson, T. Rappaport, K. Bae, A. Verstak, N. Ramakrishnan, W. Tranter, C. Shaffer, and L. Watson, "In-building wideband multipath characteristics at 2.5 and 60 ghz," in *Vehicular Technology Conference, 2002. Proceedings. VTC 2002-Fall. 2002 IEEE 56th*, vol. 1, 2002, pp. 97–101 vol.1.

[69] K. Sato, T. Manabe, T. Ihara, H. Saito, S. Ito, T. Tanaka, K. Sugai, N. Ohmi, Y. Murakami, M. Shibayama, Y. Konishi, and T. Kimura, "Measurements of reflection and transmission characteristics of interior structures of office building in the 60-ghz band," *Antennas and Propagation, IEEE Transactions on*, vol. 45, no. 12, pp. 1783–1792, Dec 1997.

[70] K. Sato, H. Kozima, H. Masuzawa, T. Manabe, T. Ihara, Y. Kasashima, and K. Yamaki, "Measurements of reflection characteristics and refractive indices of interior construction materials in millimeter-wave bands," in *Vehicular Technology Conference, 1995 IEEE 45th*, vol. 1, Jul 1995, pp. 449–453 vol.1.

[71] P. F. M. Smulders and L. Correia, "Characterisation of propagation in 60 ghz radio channels," *Electronics Communication Engineering Journal*, vol. 9, no. 2, pp. 73–80, Apr 1997.

[72] K. Sato, T. Manabe, T. Ihara, H. Saito, S. Ito, T. Tailaka, K. Sugai, N. Ohmi, Y. Murakami, M. Shibayama, Y. Konishi, and T. Kimura, "Measurements of reflection and transmission characteristics of interior structures of office building in the 60 ghz band," in *Personal, Indoor and Mobile Radio Communications, 1996. PIMRC'96., Seventh IEEE International Symposium on*, vol. 1, Oct 1996, pp. 14–18 vol.1.

[73] P. F. M. Smulders and A. Wagemans, "Frequency-domain measurement of the millimeter wave indoor radio channel," *Instrumentation and Measurement, IEEE Transactions on*, vol. 44, no. 6, pp. 1017–1022, Dec 1995.

[74] T. Manabe, K. Sato, and T. Ihara, "Measurement of complex refractive index of soda-lime glass at 60 ghz by vector-network-analyser-based scatterometer," *Electronics Letters*, vol. 28, no. 14, pp. 1354–1355, July 1992.

[75] L. Correia and P. Frances, "Estimation of materials characteristics from power measurements at 60 ghz," in *Personal, Indoor and Mobile Radio Communications, 1994. Wireless Networks - Catching the Mobile Future., 5th IEEE International Symposium on*, Sep 1994, pp. 510–513 vol.2.

[76] J. Lahteenmaki and T. Karttaavi, "Measurement of dielectric parameters of wall materials at 60 ghz band," *Electronics Letters*, vol. 32, no. 16, pp. 1442–1444, Aug 1996.

[77] A. Hayn, R. Bose, and R. Jakoby, "Multipath propagation and los interference studies for lmds architecture," in *Antennas and Propagation, 2001. Eleventh International Conference on (IEE Conf. Publ. No. 480)*, vol. 2, 2001, pp. 686–690 vol.2.

[78] 3GPP, "Spatial channel model for multiple input multiple output (mimo) simulations," Sept 2012.

[79] e. a. IST-WINNER D1.1.2P. Kyosti, "Winner II channel models," Sept 2007.

[80] G. Calcev, D. Chizhik, B. Goransson, S. Howard, H. Huang, A. Kogiantis, A. Molisch, A. Moustakas, D. Reed, and H. Xu, "A wideband spatial channel model for system-wide simulations," *Vehicular Technology, IEEE Transactions on*, vol. 56, no. 2, pp. 389–403, March 2007.

[81] T. S. Rappaport, "Wireless communications: Principles and practice, 2nd edition, pp 194, prentice hall communications engineering and emerging technologies series," 2002.

[82] R. Pirkl and G. Durgin, "Optimal sliding correlator channel sounder design," *Wireless Communications, IEEE Transactions on*, vol. 7, no. 9, pp. 3488–3497, September 2008.

[83] C. R. Anderson, "Design and implementation of an ultra-broadband millimeter-wavelength vector sliding correlator channel sounder and in-building multipath measurements at 2.5 and 60 ghz," *Master of Science*, 2002.

[84] W. G. Newhall, "Wideband propagation measurement results, simulation models, and processing techniques for a sliding correlator measurement system," *Master of Science*, 1997.

[85] ——, "A sliding correlator channel sounder for ultra-wideband measurements," *Master of Science*, 2007.

[86] J. Talvitie and T. Poutanen, "Self-noise as a factor limiting the dynamic range in impulse response measurements using sliding correlation," in *Spread Spectrum Techniques and Applications, 1994. IEEE ISSSTA '94., IEEE Third International Symposium on*, Jul 1994, pp. 619–623 vol.2.

[87] G. Martin, "Wideband channel sounding dynamic range using a sliding correlator," in *Vehicular Technology Conference Proceedings, 2000. VTC 2000-Spring Tokyo. 2000 IEEE 51st*, vol. 3, 2000, pp. 2517–2521 vol.3.

[88] T. Rappaport, S. Sun, R. Mayzus, H. Zhao, Y. Azar, K. Wang, G. Wong, J. Schulz, M. Samimi, and F. Gutierrez, "Millimeter wave mobile communications for 5G cellular: It will work!" *Access, IEEE*, vol. 1, pp. 335–349, 2013.

[89] Y. Azar, G. Wong, K. Wang, R. Mayzus, J. Schulz, H. Zhao, F. Gutierrez, D. Hwang, and T. Rappaport, "28 ghz propagation measurements for outdoor cellular communications using steerable beam antennas in new york city," in *Communications (ICC), 2013 IEEE International Conference on*, June 2013, pp. 5143–5147.

[90] S. Sun and T. S. Rappaport, "Multi-beam antenna combining for 28 ghz cellular link improvement in urban environments," in *Communications (ICC), 2013 IEEE International Conference on*, December 2013.

[91] S. Sun, G. R. MacCartney, M. K. Samimi, S. Nie, and T. S. Rappaport, "Millimeter wave multi-beam antenna combining for 5g cellular link improvement in new york city," in *Communications (ICC), 2013 IEEE International Conference on*, June 2014.

[92] S. Sun, "Antenna diversity combining and beamforming at millimeter wave frequencies," Master's thesis, May 2014.

[93] K. Schaubach, I. Davis, N.J., and T. Rappaport, "A ray tracing method for predicting path loss and delay spread in microcellular environments," in *Vehicular Technology Conference, 1992, IEEE 42nd*, May 1992, pp. 932–935 vol.2.

[94] K. Schaubach and I. Davis, N.J., "Microcellular radio-channel propagation prediction," *Antennas and Propagation Magazine, IEEE*, vol. 36, no. 4, pp. 25–34, Aug 1994.

[95] S. Seidel and T. Rappaport, "A ray tracing technique to predict path loss and delay spread inside buildings," in *Global Telecommunications Conference, 1992. Conference Record., GLOBECOM '92. Communication for Global Users., IEEE*, Dec 1992, pp. 649–653 vol.2.

[96] ——, "Site-specific propagation prediction for wireless in-building personal communication system design," *Vehicular Technology, IEEE Transactions on*, vol. 43, no. 4, pp. 879–891, Nov 1994.

[97] G. Durgin, N. Patwari, and T. Rappaport, "An advanced 3d ray launching method for wireless propagation prediction," in *Vehicular Technology Conference, 1997, IEEE 47th*, vol. 2, May 1997, pp. 785–789 vol.2.

[98] W. Lu and K. Chan, "Advanced 3d ray tracing method for indoor propagation prediction," *Electronics Letters*, vol. 34, no. 12, pp. 1259–1260, Jun 1998.

[99] J. McKown and J. Hamilton, R.L., "Ray tracing as a design tool for radio networks," *Network, IEEE*, vol. 5, no. 6, pp. 27–30, Nov 1991.

[100] C. Ho and T. Rappaport, "Wireless channel prediction in a modern office building using an image-based ray tracing method," in *Global Telecommunications Conference, 1993, including a Communications Theory Mini-Conference. Technical Program Conference Record, IEEE in Houston. GLOBECOM '93., IEEE*, Nov 1993, pp. 1247–1251 vol.2.

[101] M. R. Anderberg, "Cluster analysis for applications," 1973.

[102] J. A. Hartigan, "Clustering algorithms," 1975.

[103] M. G. Bulmer, "Principles of statistics, p. 154, the M.I.T. press," 1965.

[104] W. Tranter, K. Shanmugan, R. T.S., and K. L. Kosbar, "Principles of communication systems simulation with wireless applications, prentice hall communications engineering and emerging technologies series, 2004," 2004.